

Ph.D. THESIS TITLE:

INVESTIGATIONS OF DRY SAND BEHAVIOUR UNDER MOVING RIGID WHEELS

by: C.W. BOYD

ABSTRACT

INVESTIGATIONS OF DRY SAND BEHAVIOUR

UNDER MOVING RIGID WHEELS

a thesis, presented by:

Conor W. Boyd

in partial fulfilment for the Ph.D. degree

Department of Civil Engineering & Applied Mechanics
McGill University
Montreal, P.Q.

SUMMARY

In the past, an inadequate understanding of the dynamic soil response to the simplest vehicular load has hindered successful predictions of soft-soil vehicle performance. A new approach to this problem is described, whereby a Ciné Flash X-ray technique is used to study the translation paths, velocities, and accelerations, of small objects buried within the sand, as a function of depth and relative wheel position. This mensurational technique is described and the precision levels, of the derived radiographic information, defined.

The study is limited to two scaled driven rigid wheels, rolling on an initially loose, dry, fine grained sand, under a variety of parametric restraints. The essential description of the deformations that characterise the soil domain, under the centre-line of the rolling wheel, has been defined. Dynamic similitude is established and the scaling of deformations and soil dependent forces are examined.

INVESTIGATIONS OF DRY SAND BEHAVIOUR
UNDER MOVING RIGID WHEELS

by:

Conor W. Boyd

A thesis submitted to the Faculty of Graduate
Studies and Research in Partial Fulfilment of the
requirements for the degree of Doctor in Philosophy.

Department of Civil Engineering & Applied Mechanics,
McGill University,
Montreal, P.Q.

March 1967.

SUMMARY

In the past, an inadequate understanding of the dynamic soil response to the simplest vehicular load has hindered successful predictions of soft-soil vehicle performance. A new approach to this problem is described, whereby a Ciné Flash X-ray technique is used to study the translation paths, velocities, and accelerations, of small objects buried within the sand as a function of depth and relative wheel position. This mensurational technique is described and the precision levels of the derived radiographic information defined.

The study is limited to two scaled driven rigid wheels, rolling on an initially loose, dry, fine grained sand, under a variety of parametric restraints. The essential description of the deformations that characterise the soil domain under the centre-line of the rolling wheel has been defined. Dynamic similitude is established and the scaling of deformations and soil dependent forces are examined.

ACKNOWLEDGEMENTS

This thesis contains the results of the first part of a continuing study on the nature of soil response to vehicular loads. I wish to thank Professor R.N. Yong who, as Research Director, has provided sustained interest and support throughout the project and has offered many constructive suggestions during the preparation of this manuscript. Stephen J. Windisch has been a partner to every aspect of this work and has contributed many of the ideas incorporated in the development of the technique. For these and for countless hours of his free time I am deeply grateful.

I would also like to thank:

Mr. B. Cockayne and Mr. G. Matsell for their assistance in building the experimental facility;

Mr. R. Berlyn and Mr. Emile Kohler, of the Pulp and Paper Research Institute of Canada, for their generous assistance in the editing of the basic radiographic information on the P.P.R.I.C.'s IBM 1620 Computer;

Mr. L.J. Vrooman, Department of Mechanical Engineering, for his invaluable help in both the development and maintenance of the instrumentation, and to the Department of Mechanical Engineering for the loan of numerous items of equipment;

Professor D.R. Axelrad, Professor L.G. Jaeger, and Dr. J.F. Adie, of the Faculty of Engineering, for their time, ideas and interest;

Mrs. Margaret Gibbons for typing the manuscript;

The National Research Council of Canada for providing a scholarship;

The De Havilland Aircraft of Canada Ltd. for their financial support and for providing the test wheels used during this study;

Mr. T. A. Harwood, who as D.R.B. Project Officer was responsible for the contractual arrangements with the Defence Research Board of Canada.

This agency provided the research funding through the Department of
Defence Production.

TABLE OF CONTENTS

	Page
SUMMARY	i
ACKNOWLEDGEMENTS	ii
CONTENTS	iii
LIST OF TABLES.	vii
LIST OF ILLUSTRATIONS	vii
NOTATION INDEX.	ix
LIST OF ABBREVIATIONS	xi
 CHAPTER	
I INTRODUCTION	1
A) Some Basic Considerations of Soil Behaviour	2
B) Previous Theories Used to Predict Vehicle Performance	4
C) Mensurational Techniques Used In Previous Subsurface Investigations of the Soil-Vehicle Problem	7
Purpose and Scope of the Current Study	9
II THE EXPERIMENTAL FACILITY	11
A. Introduction	11
B. Specifications of the Overall Test Facility.	14
1. General Description	14
2. The Hydraulic System	14
3. The Dynamometer and Wheel Carriages	14
4. The Wheel Drive Mechanism	15
C. The Test Wheels and the Chosen Loading Parameters	15
1. Selection of the Test Wheels	15
2. The Selection of Wheel Loading Parameters	18
D. Instrumentation and Calibration	18
E. The Ciné Radiographic System.	20
1. Introduction	20
2. Radiographic Considerations	21
3. Description of Ciné Radiographic Equipment	24
III THE EXPERIMENTAL TECHNIQUE	26
A. Introduction	26
B. Sand Preparation and Tracer-Object Placing Technique	26
1. Properties of the Sand	26
2. The Sand Container	27
3. The Sand Preparation and Tracer-Object Placing Technique	27
C. The Wheel-, Tracer-Object-, Cassette-, Source-, Geometry	30

CHAPTER

Page.

D. The X-Ray Pulse Sequence. 33.

E. Transfer of Radiographic Data to Digitized Information. 34.

F. The Basic Reduction of Test Results. 37

 1. Introduction. 37

 2. Translation Path Computations. 38

 3. Velocity and Acceleration Computations. 41

G. A Discussion of the Reliability of the Derived Results and the Validity of the Invoked Assumptions. 45

 1. The Reliability of the Derived Translations. 45

 2. The Reliability of the Derived Velocities. 47

 3. The Validity of the Invoked Assumptions. 51

IV THE SURFACE & SUBSURFACE DISPLACEMENT OF SAND UNDER A VARIETY OF DRIVEN RIGID WHEEL LOADING PATTERNS. 52

A. Introduction. 52

B. Measurements of Soil Movement Beneath a Variety of Controlled Loading Patterns. 52

 1. Some Kinematic Considerations. 52

 2. Three Typical Displacement Patterns. 58

 3. An Analysis of Sand Displacement Patterns in Row 1. 63

 4. An Analysis of Soil Displacement Patterns in Row 4. 67

C. Rolling Wheel Sinkage. 69

D. Discussion of Results and Conclusions. 71

 1. The Influence of Side Wall & Lateral Constraint on the Measured Results. 71

 2. Conclusions. 73

V ENERGY CONSIDERATIONS 78

A. Introduction. 78

B. The Component of Energy Lost by the Wheel to the Soil. 78

 1. The Plane Motion of a Rigid Wheel. 78

 2. Energy Definitions & Concept of Rolling Resistance. 81

 3. The Similitude Parameters. 84

 4. Variations in the Recorded Torque Energy Coefficient η 85

C. Considerations of Energy Dissipation Within the Soil. 89

 1. Preliminary Considerations. 89

 2. The Dissipation Function, (V-10), and Some Experimental Results. 91a

D. A Summary Statement. 105

VI SUMMARY AND CONCLUSIONS 107

A. Summary. 107

B. Conclusions. 108

C. Claim to Original Work. 117

CHAPTER	Page.
VII . RECOMMENDATIONS FOR FURTHER STUDY	113
APPENDICES	115
APPENDIX I.	116
APPENDIX II	118
APPENDIX III.	152
APPENDIX IV	188
APPENDIX V.	190
BIBLIOGRAPHY	197

LIST OF TABLES

Table	Page.
II-1. Dynamic Similitude Scaling Ratios Used for Wheel Quantities.	16
II-2. The Essential Specifications of Flash X-Ray Unit	25
IV-1. The Experimental Design of the Main Test Series.	53
IV-2. Experimental Design of Supplementary Test Series..	54
V-1. Sample Determination of the Torque Scaling Ratio λ^u	88

LIST OF ILLUSTRATIONS

PLATE I	Photograph of Soil-Vehicle Test Facility.	12
PLATE II	Photograph of Soil-Vehicle Test Facility.	13
Fig. III-1	Schematic of Sand Placing Technique.	28
Fig. III-2	The Source-Tracer-Object-Wheel-Film-Geometry.	32
Fig. III-3	Schematic of Superposition Technique Used to Obtain Translation Paths Followed by Tracer-Objects in Any One Row.	39
Fig. III-4	The Translation Path Followed by Tracer-Objects Originally Placed at a Depth of 1.5", Test No.14.	40
Fig. III-5	Diagram for Explaining Rationale For Velocity Computations.	42
Fig. III-6	Diagram of Instantaneous Wheel Position Referenced to Radiographic Plate, and Tracer-Object Network; Positions.	45
Fig. III-7	Diagram to Illustrate Possible Sources of Error in Derivation of $\Delta s/\Delta t$ Component of Velocity.	48
Fig. IV-1	Schematic of Situation Described by O. Reynolds (1876).	55
Fig. IV-2	Rigid Wheel Towed on Non-Elastic Surface.	55
Fig. IV-3	Curtate Trochoid of Rigid Wheel on Deforming Soil.	57
Fig. IV-4	Translation Patterns of Tracer-Objects Under Wheel Centre Line for Test Number 11.	59
Fig. IV-5	Translation Patterns of Tracer-Objects Under Wheel Centre Line for Test Number 12.	60
Fig. IV-6	Translation Patterns of Tracer-Objects Under Wheel Centre Line for Test Number 13.	61
Fig. IV-7	Variation of Final Relative Coordinates (r,s), of First Row Tracer-Objects.	65
Fig. IV-8	Variation of Final Relative Coordinates (r,s), for Fourth Row Tracer-Objects.	68
Fig. IV-9	The Sinkage Ratio y_0/D , Showing the Scaled Slip Sinkage Phenomenon.	70
Fig. IV-10	Diagram defining Regions A & B	74

Fig. V-1	The Driven Wheel as a Free Body.	80
Fig. V-2	Variation of Torque Energy Coefficient, η , with Slip.	86
* Fig. V-3	Diagram of Test 29 Geometry.	92
Fig. V-4	Particle Velocity Fields.	95
Fig. V-5	Particle Acceleration Fields.	96
Fig. V-6	The Density Distribution for Test 29.	98
Fig. V-7	Component Frict/ μ Surfaces.	100
Fig. V-8	Diagram to Illustrate Considerations of Energy Losses Proportional to the Velocity Squared.	104

*

Addendum to list of illustrations
Fig. V-2a, Fig. V-2b, and Fig. V-2c.

NOTATION

b	= Wheel Width (ins.)
D	= Wheel diameter (ins.)
e	= voids ratio.
\dot{E}_{input}	= rate of energy lost to soil, by wheel, per unit distance travelled.
\dot{E}_{frict}	= rate of energy dissipated by the frictional mechanism described in Chapter V.
F	= drawbar pull (lbs.)
g	= acceleration due to gravity (ft/sec ²)
G	= differential wheel slip rate.
$K_c, K_\phi, n,$	= Bekker soil Parameters.
L	= horizontal distance travelled by wheel (ins.)
M	= Net Torque Moment developed by wheel (in.-lbs.)
m	= mass of wheel (poundals).
M.I.	= Moment of Inertia of Wheel.
p	= nominal ground pressure (lbs/sq.in).
Q	= Vector sum of all soil forces in the wheel contact region (lbs.)
R	= Rolling Resistance (as defined by Bernstein & Bekker).
R_{pq}	= Finite rotation tensor
r	= wheel radius (ins.)
s	= normal wheel slip rate.
t	= characteristic time (seconds).
Δt	= time delay between 2nd and 3rd Radiographic flashes.
\bar{u}	= average $\Delta x / \Delta t$ component of velocity (ins./sec.)
\bar{v}	= average $\Delta y / \Delta t$ component of velocity (ins./sec.)
V or $\dot{\bar{x}}$	= translational wheel velocity (ins./sec.)
W	= Vertical wheel load (lbs.)

- y_0 = equilibrium rolling sinkage (ins.)
- (x,y) = 'Absolute' Cartesian coordinate reference system.
- (r,s) = 'relative' Cartesian coordinate reference system.
- $\alpha_{1,2}$ = slopes of two lines in Fig. IV-7.
- δ_1 = coefficient of limiting friction between dry sand and polished Aluminum (dilatant and rolling effects eliminated).
- δ_2 = coefficient of limiting friction between dry sand and hard rubber (dilatant and rolling effects eliminated) (degrees).
- δ = coefficient of kinetic friction (degrees)
- η = coefficient of Torque Energy.
- θ = reference angles (degrees).
- λ = a) ratio of characteristic prototype to model wheel length.
or b) wavelength of X-radiation (Angstroms), or c) direction cosine matrix, or d) principal stretches.
- Λ = pull energy coefficient, or stretch tensor.
- μ = coefficient of sand-sand friction (including dilatant components).
- ρ = (mass) density of soil (pounds/mass/cu.in.)
- ρ' = a) Chudakov-Phillips coefficient of Rolling Resistance
or b) Dissipated energy coefficient (equivalent to a)).
- $\hat{\sigma}$ = best estimate of population standard deviation.
- ϕ = equivalent to μ .
- ψ = angle at wheel rim, between extended wheel radius and instantaneous vector of wheel rim velocity (degrees)
- ω = angular wheel velocity (radians/sec.)
- Ω = Power supplied to wheel (in.-lbs./sec.)
- $(\frac{\mu}{\rho})$ = Mass attenuation coefficient.
- $(\frac{\mu}{\rho})/\rho$ = Linear attenuation coefficient (reciprocal cms).
- ψ = Angle of finite rigid body rotation.

ABBREVIATIONS:

D.B.P. = Draw Bar Pull.

R.E.F. = Radiographic Equivalence Factor.

I.S.T.V.S. = International Society of Terrain Vehicle Systems.

S.F.D. = Source to Film Distance.

S.O.D. = Source to Object Distance.

CHAPTER I

INTRODUCTION

Historically there is evidence to support the claim that wheels were used for transportation purposes prior to 3,000 B.C. It is thus surprising that despite the long history of development, the increasing sophistication of vehicular transport, and the myriad demands of the user, very little is known about the soft soil performance of even the simplest vehicular loading device; namely, the rigid wheel. The soil appears to be the single most important factor - and yet the least understood one - affecting vehicle performance. Other factors include: variations in micro- and macro-topography, obstacle performance, seasonal and diurnal climatic changes, physiological effects of machine vibrations, etc., but these are considered as subservient to the soil problem.

The practical objective of soil-vehicle research is the effective prediction of vehicular performance. Invariably the criterion of performance is the ability of a vehicle to develop a tractive effort greater than that required for forward motion on a smooth horizontal soil surface. The 'excess' tractive energy is a measure of the vehicle's ability to perform useful drawbar work or may be interpreted in other ways; e.g. hill-climbing capacity. At the present time there is no theoretical or empirical technique of successfully predicting the performance of a given vehicle on the simplest soil medium; which may be considered as a homogeneous, non stratified, soil with a smooth horizontal surface.

A survey of the related literature reveals that in only a few cases have attempts been made to determine the behaviour of soils beneath a vehicular load. The considerable 'weight' of research effort has been concentrated

on the measurement of the system parameters and variables above the soil surface. Since purely surficial measurements can reveal virtually no information on the mechanisms, or behaviour, of the soil to a vehicular forcing function, a considerable amount of speculation has arisen concerning the 'soil' component of the soil-vehicle system. Although some of the reasons for this speculation stem from inadequate information of the subsurface soil behaviour, the problem is confounded by the difficulties inherent in describing (a) the stress-strain behaviour of soils, (Drucker, 1961), (b) a suitable yield criterion (Yong and Osler, 1966), and (c) the vehicular forcing function, (Leflaive, 1966). Attempts to predict vehicle performance using empirical relationships, have thus been made in order to bridge the gap between theory and practice. However these attempts have only met with limited success, (Reece, 1965).

For a consideration of previous related research it is convenient to subdivide the subsequent discussion into three sections:

- A) Some basic considerations of Soil Behaviour.
- B) Previous theories used to predict Vehicle Performance.
- C) Mensurational techniques used in previous subsurface investigations of the Soil-Vehicle problem.

In order to restrict the discussion, the case of a rigid driven wheel rolling on a dry loose sand will be considered as the reference soil-vehicle system. This conveniently reduces the problem to the simplest realistic case, where such influences as tire carcass stiffness, inflation pressure, track tension, etc., can be temporarily laid aside.

A) Some Basic Considerations of Soil Behaviour

From a theoretical standpoint the problems associated with accounting for the dynamic soil reaction beneath a driven rigid wheel are considerable.

The absence of suitable stress-strain relationships presents a serious obstacle to a theoretical development. Stress-displacement curves obtained from triaxial and direct-shear devices can not be related to other conditions if the distribution of either stress or strain is unknown. For static analyses a notable advance has been made by Arthur et al (1964) who determined the strains below 'yield' within a soil mass behind a model retaining structure, and related the strain fields to stress fields using a stress-strain relationship derived from a direct shear device. In this context 'yield' is defined as the onset of soil flow; that is, large relative inter particle movements. However 'yield' in the plasticity context refers to non recoverable deformations, which in soils can and do occur under small loads. This behaviour is analogous to a work hardening phenomenon in metals, and the stress state associated with flow is defined as 'failure'. Yong and Osler (1966) have emphasized that the specification of a 'failure' criterion becomes essential if the conditions beneath the wheel are to be rationally analysed. The problem is indeed complex since this dynamic soil régime is characterised by stress-states resulting in non-linear soil displacements with flow, by rotations of the principal stress axes and by significant material property changes (associated with significant volume changes). The specification of a locus that defines the stress state, in principal stress space, corresponding to the onset of flow is not yet possible for the general case - as a study of the available literature reveals conflicting experimental results, (Boyd, Japp, Leitch, 1966). An analysis of the results of Habib (1953), Kirkpatrick (1957), Shibato and Karube (1965), Wu, Loh and Malvern (1963), Haythornthwaite (1960), Cornforth (1964), and Yong and McKyes (1967) revealed that the widely used Mohr-Coulomb parameters provide a conservative estimate of the stress state corresponding to the onset of 'flow'. Once flow is established the necessary governing relation-

ships that describe the flow phenomenon are - ideally - required. For certain well defined limiting cases flow relationships have been developed, (Yong and Japp, 1967) and (Savage, 1966), but unfortunately these are not directly applicable to more complex situations at the present time.

Since the loading pattern is transient the dynamic equilibrium of the soil system must necessarily be considered. That is, inertia effects must be considered when operative.

In summary, the absence of suitable mathematical relations describing the mechanical properties of soil does not permit a direct theoretical analysis to be made of the soil response to vehicular loading. However it is emphasized that if these essential 'tools' were available it would first be necessary to establish experimentally the stress and strain fields within the soil domain, the related soil translations and rotations, the corresponding volume changes and the extent of influence of the wheel.

B) Previous Theories Used To Predict Vehicle Performance.

The work of Bekker (1956), (1960), represents one of the few attempts to provide a coherent framework for the quantitative prediction of vehicle performance on both clay and sand soils. For the case of the reference rigid wheel - sand system Bekker's theory appears to be the only one available to predict the drawbar pull, the sinkage and the rolling resistance. The theory is based on the assumption that the soil pressure-sinkage relationship is of the form

$$p = \left[\frac{K_c}{b} + K_\phi \right] y^n \quad (I-1)$$

= pressure (lbs./sq.inch).

where: K_c , K_ϕ , and 'n' are considered as ^{true}~~time~~ soil parameters

b , is the wheel width

y , is the sinkage.

Although not dimensionally accurate it is based on the equation proposed by Bernstein (1913) : $p = Ky^n$.

The parameters K_c , K_ϕ and 'n' are determined experimentally from two plate penetration tests, and the assumption that a plot of p vs. y reduces to a linear log-log plot - see Bekker (1959) for a description of the method.

Unfortunately all these parameters appear to be functionally dependent on the size and shape of plate used and thus can not reasonably be considered as 'true' soil parameters, (Terzaghi and Peck (1948), Yong and Warkentin (1966)). The relationship (I-1) to prototype vehicles, thus requires considerable extrapolation of 'parameters' that are test dependent.

The second assumption made by Bekker is that the work expended by the wheel in rut formation is constant ^{for a given soil} and independent of wheel slip. He further assumed that this work could be equated to the work expended in forcing a plate vertically into the soil to a depth corresponding to the sinkage. Thus if R is the work lost irrecoverably to the soil per unit of distance travelled by the wheel, then for a rut length, l , Bekker assumed:

$$Rl = bl \int_{y=0}^{y_0} p dy = bl \int_{y=0}^{y_0} \left[\frac{K_c}{b} + K_\phi \right] y^n dy \quad (I-2)$$

where y_0 represents the equilibrium sinkage. This assumption is apparently the same as that made by Bernstein, (Reece, 1965), who also coined the term Rolling Resistance for R , which is seen to have the dimensions of Force. As will be explained in Chapter V, this fact has led to considerable confusion in the literature.

If the axle load of the wheel is denoted as W , and the wheel radius as r , Bekker has used equations (I-1) and (I-2) to derive an expression for the equilibrium wheel sinkage y_0 :

$$y_0 = \left[\frac{3W}{(3-n)(K_c + bK_\phi) \sqrt{2r}} \right]^{\frac{2}{2n+1}} \quad (I-3)$$

and for Rolling Resistance, R ;

$$R = \frac{1}{(n+1)(Kc + bK\phi)^{(1/2n+1)}} \left[\frac{3W}{(3-n)\sqrt{2F}} \right]^{\frac{2n+2}{2n+1}} \quad (I-4)$$

The derivation of both these equations, together with the simplifying assumptions, have been included as Appendix I. Using the assumption that the gross tractive effort may be equated to $W \tan \phi$, the approximation is then made that the drawbar pull force, F , may be equated to the algebraic difference between the gross tractive effort and the rolling resistance R , i.e.

$$F = W \tan \phi - R \quad (I-5)$$

where ϕ is the "angle of internal soil friction".

Equations (I-3), (I-4) and (I-5) represent the Bekker Theory for a driven rigid wheel on sand.

Experiments by Wills et al (1965) have shown that, for a towed wheel on sand, where equations (I-3) and (I-4) are applicable 'by assumption', Bekker's prediction of sinkage, y_0 , was reasonably accurate. However the prediction of Rolling Resistance, R , was shown to be spectacularly wrong. Measurements of R up to twice that of the predicted value were recorded. Since we chose to consider R as the energy expended per unit distance travelled it is clear that energy is expended in other mechanisms in addition to the assumed vertical soil deformation. Deformation in the horizontal plane must therefore be considered explicitly in subsequent analyses.

It will be noticed that equations (I-3) and (I-4) are independent of wheel slip, and thus neither account for nor explain the slip-sinkage phenomenon that is readily observed in the field with sandy soils. This phenomenon, characterised by increased sinkage with increasing slip rate, would indicate that both y_0 and R are strongly dependent on wheel slippage. Equation (I-5) is ^{here assumed to be} ~~explicitly~~ independent of slip rate but ^{in practice is found to be} ~~implicitly~~ dependent on it. The assumption is made that the soil behaves as a

Coulombic material. If this is temporarily accepted as a convenient assumption, then the full friction will only be mobilised by the soil as a result of strains induced by wheel slippage. This mechanism helps to explain the experimentally observed increase in drawbar pull, F , with normal slip rate - see Nicholson and Booker (1963) and Leflaive (1966). This equation must therefore be regarded as explicitly dependent on slip rate and, if valid, can only refer to the F , $W \tan \phi$, and R values corresponding to a given slip. The $W \tan \phi$ term represents an approximation since the load W , is assumed to act on a horizontal surface, and not over the actual curved interface of the wheel-soil contact region. From a practical standpoint the determination of a meaningful soil friction angle, ϕ , also presents problems, since ϕ appears to be dependent on strain and initial density, (Rowe, 1962).

In summary; it appears that equations (I-1) to (I-5) do not offer a promising avenue for predicting wheel performance, since they fail to account for the observed wheel performance.

C) Mensurational Techniques Used in Previous Subsurface Investigations of the Soil-Vehicle Problem.

One of the earliest attempts to measure the behaviour of soil under a rigid wheel was the work carried out by McKibben (1938). In this study McKibben traced the paths followed by lead shot, buried in a soil box with plate glass sides, under a slowly towed, rigid wheel. From these visual observations the translation paths showed a pronounced horizontal component, in contradistinction to the Bernstein-Bekker assumption, and the patterns in both clay and sand soils were seen to be similar.

Attempts to measure free field strains using electrical devices have been limited to regions in the soil mass where deformations are both linear and below 'yield', Selig et al (1961); their application is thus extremely

limited. Attempts to measure free-field stresses have been made, Freitag and Knight (1962), and have provided some useful qualitative information. However the practical problems of measuring just one component of stress, normal to one plane in the soil mass, are extraordinarily complex. The pressure "sensing" devices used by Freitag and Knight were found to both migrate and rotate during the stressing cycle imposed by a vehicle. Since the history of movement was not recorded during the stressing cycle the necessary corrections could not be made. There is also convincing evidence that the presence of the sensing device within the soil mass influences the pressure distribution, (Selig, 1964), so that it is unlikely that any corrections, for cell orientation, would provide meaningful quantitative stress values. Since it is necessary to obtain the principal and shear stresses to completely describe the stressing at any one 'point' in a soil medium, this approach to subsurface measurements is not promising.

The foregoing statements do not, in general, apply to stress measurements at a boundary.

More recently the experimental work of Wong and Reece (1966), provided some interesting qualitative information on the flow of sand beneath a driven, rolling, rigid wheel. Observations on the flow patterns were made using a plate glass sided soil box similar to McKibben's and were recorded photographically. Since no tracer technique was used, no record was made of component soil translations or velocities.

These four examples are representative of previous subsurface investigations of the mechanical properties and behaviour of soil under vehicular loads.

It is hoped that the preceding sections provide a general background to statement ~~the present state of the art~~. With the notable exception of the research reported in Section C), virtually nothing is known of the nature of soil

behaviour under vehicular loading. Since even these attempts were of a limited nature it becomes mandatory that an experimental investigation must precede theoretical or, due to the complexity of the problem, empirical predictions. Once the behaviour of the physical model is understood then the appropriate simplifying assumptions, or theoretical developments, can be made.

Purpose & Scope of the Current Study

A complete and rigorous description of the soil-vehicle system requires the specification of both the vehicle forcing function and the stress and strain histories of the dynamic soil régime.

The study reported herein is directed towards this ultimate objective, with the emphasis on a description of the dynamic soil response to controlled 'vehicular' loads. Because of the difficulties inherent with in-field stress measurements this investigation was directed towards a description of the soil response in terms of measured deformations and translations within the soil mass.

The purposes of the study may be summarised as:

- 1) To provide quantitative information on the dynamic response of soil to a variety of controlled wheel loads as one step towards the ultimate objective outlined above. The soil response is examined from measurements of translations and velocities of 'particles' within the soil mass, using a ciné Flash X-ray technique that provides much hitherto unavailable information.
- 2) To examine the assumptions invoked in the prediction of wheel performance, in the light of information provided by 1), above. In particular, to examine the concept of Rolling Resistance in the context of possible horizontal soil translations, ^{the} nature of the slip-

sinkage phenomenon, the influence of wheel slip on the gross tractive effort developed by the wheel-soil system, and the nature of the sub-surface soil deformations that result in the surficially measured wheel sinkage, y_0 .

- 3) To examine, from dynamic similitude studies, the practically desirable objective of extrapolating information from model wheel studies in the laboratory to prototype wheel performance in the field.

In order to restrict the study to sensible proportions the scope of the study is limited to the following cases:

- i) A 'vehicular' load described by two driven rigid wheels. The loading patterns were dynamically scaled combinations of five basic test parameters: a) Wheel size, b) Wheel translational velocity, c) Wheel slip rate, d) Wheel load, and e) nature of wheel rim surface material .
- ii) All tests were conducted on a dry, initially loose, fine grained sand.
- iii) Observations based on measurements of sand translations and velocities in a plane parallel to the wheel side wall and co-planar with the centre line of the rolling wheel.

CHAPTER II

THE EXPERIMENTAL FACILITY

A; INTRODUCTION

The experimental facility was previously located at the Canadian Army Research and Development Establishment Vehicle Mobility Laboratories, CARDE/VML, Quebec. A change in research emphasis has necessitated the major modifications described below and in Appendix II. Because of the decision to use wheeled loading patterns the CARDE tracked vehicle models have been temporarily shelved and the facility has been redesigned to ensure adequate parametric control of the forcing function. In this context the known loading pattern is considered as the independent component of the soil-wheel system, and the unknown soil response as the dependent component.

B; SPECIFICATIONS OF THE OVERALL TEST FACILITY

B1; General Description.

The soil bin, the dynamometer carriage frame and the hydraulic drive mechanisms are substantially the same as those described by Nicholson and Booker (1963). Although the study reported herein is restricted to investigations with single wheels, the original soil bin width of 6 ft. has been retained to permit subsequent studies on vehicular models. The bin is 4 ft. deep and was filled with a fine grained sand. Mounted on either side of the bin are Z rails to support and guide the dynamometer carriage; used both as an anchor 'vehicle' for wheel testing and for sand preparation. This carriage supports: the wheel and its flexure frame, the wheel drive housing, the sand hopper and an instrumentation box - referred to subsequently as switching box 'A'. This carriage is pulled along the bin Z rails by an endless double-link drag chain, located on either side of the bin and driven

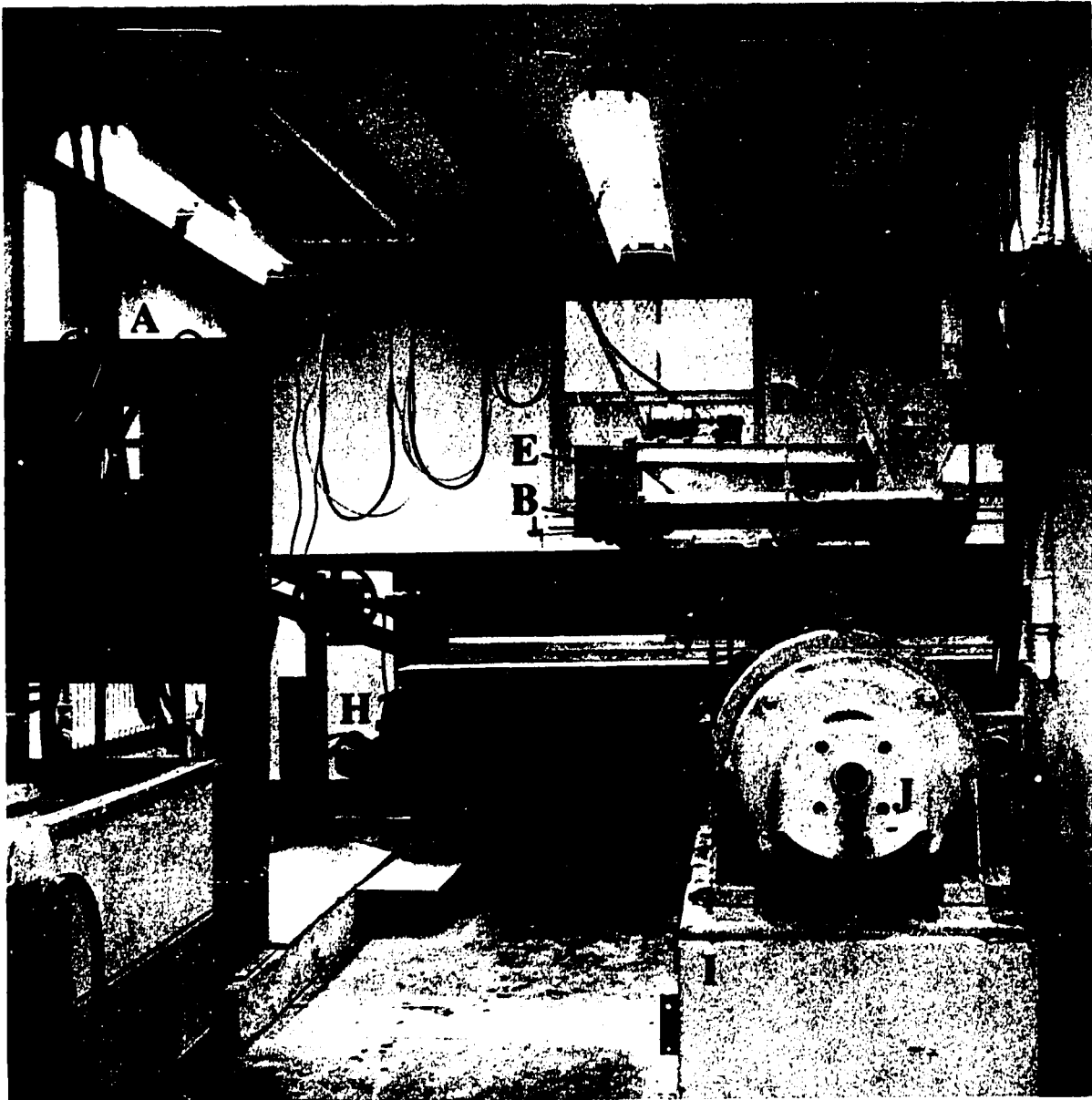


PLATE I

The following annotations apply to both Plates I and II :

A = hydraulic control panel, B = dynamometer carriage, C = wheel carriage, D = gear housing, E = switching box 'A', F = sand preparation hopper, G = soil bin, H = dynamometer carriage drive reducers, I = oil reservoir, J = Howell electric motor, K = flash X-ray control console, L = recording console, M = flash X-ray pulser, N = cassette holder, O = rheostat, P = telescopic drive shaft, W = test wheel, Q = sand 'container'!

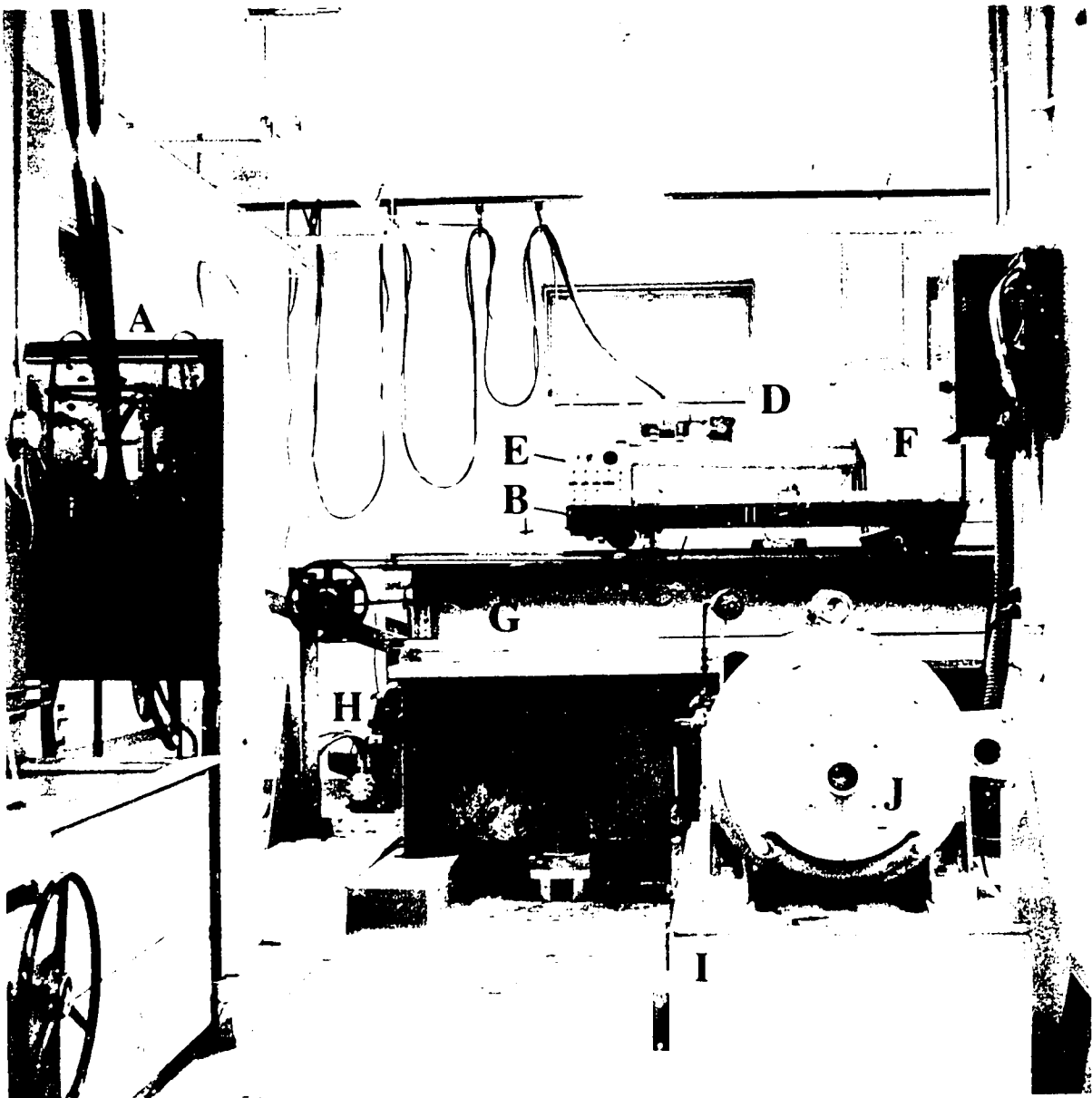


PLATE I

The following annotations apply to both Plates I and II .

A = hydraulic control panel, B = dynamometer carriage, C = wheel carriage,
 D = gear housing, E = switching box 'A', F = sand preparation hopper,
 G = soil bin, H = dynamometer carriage drive reducers, I = oil reservoir,
 J = Howell electric motor, K = flash X-ray control console, L = recording
 console, M = flash X-ray pulser, N = cassette holder, O = rheostat, P =
 telescopic drive shaft, W = test wheel, Q = sand container.



PLATE II



1

2

3

hydraulically via two worm and wheel reducers. The speed of the carriage can be regulated from 0 → 35 inches/sec., by hydraulic flow control. Both the electrical leads from the carriage mounted transducers to the recording console and from the D.C. wheel drive motor to the rheostat are supported by runners suspended from a guiding track on the ceiling.

The physical arrangement of the experimental facility is shown in Plates I and II, overpage. Plate II also shows the geometric arrangement of the essential X-ray equipment components.

B2; The Hydraulic System.

The circuitry and essential components are shown in detail in Appendix II-B2. The pump unit is set to provide a working pressure of 2000 p.s.i., and flow is controlled by temperature compensating Vickers valves. A limit switch control system provides a safety mechanism for stopping the carriage at either end of the soil bin by a circuit that includes a solenoid activated by-pass valve. This electrical circuit is also described in Appendix II-B2.

B3; The Dynamometer and Wheel Carriages.

The dynamometer carriage spanning the Z rails, acts as an 'anchor' vehicle for the wheel carriage assembly shown in Appendix II-B3. The inner - or wheel - carriage consists of a flexure frame within which the test wheel is mounted. The flexure frame assembly permits freedom of wheel movement vertically, prevents 'yawing' and 'rolling' motions and provides a means of measuring the drawbar forces via strain gauges mounted on the flexures. One of two sets of spring steel flexures was used depending on the drawbar forces anticipated. In order to ensure that the flexure frame was horizontal, a support was made that accommodated both different wheel sizes and a range of anticipated sinkages. This support also provided the means of attaching the wheel carriage to the Dynamometer carriage.

B4; The Wheel Drive Mechanism.

In order to satisfy the requirements for dynamic similarity, severe restrictions are imposed on the choice of a drive mechanism. As shown in the following section, a ratio of λ^4 is used for scaling applied wheel torque, from considerations of the wheel parameters alone. Here, λ denotes the ratio of a characteristic prototype to model wheel length. This ratio imposes considerable demands on the power range of the wheel drive unit, and for a given drive unit restricts λ to small values. However, for the wheel sizes chosen a variable-speed, constant torque, shunt wound 1/2 horse power D.C. motor - with a 29:4 reduction ratio - proved satisfactory. It should be noted that this reduction ratio and an imposed upper limit on angular wheel velocity of 2.5 rads/sec. prevented the maximum rated Horse Power from being developed. A schematic of the driving mechanism is given in Appendix II-B4, together with diagrams of the drive chain housing. The telescopic drive shaft connecting the drive unit to the test-wheel axle permitted freedom of vertical wheel movement. In order to minimise the sinusoidal variations of drive velocity, from the universal joints, the drive housing was mounted on supports that permitted vertical adjustment.

C; THE TEST-WHEELS AND THE CHOSEN LOADING PARAMETERS.

C1; Selection of the Test Wheels.

Having restricted the choice of a vehicular load to the case of rigid wheels a scaling criterion was required for model studies. However, without a knowledge of the soil behaviour the system parameters are undefined and so it was necessary to consider the vehicle parameters alone in the initial formulation. From an analysis of the results an inspectional analysis (Birkhoff, 1961) is made to include - or account for - the soil reaction.

The equivalence of the Froude Number, V^2/gl , was assumed for scaling

time dependent variables; where the gravitational force, g , is necessarily constant for both model and prototype. A second assumption used in the derivation of the scaling ratios was that the density of both prototype and model wheel materials was the same. Using these two assumptions the scaling ratios for dynamic similitude were obtained. Details of the Buckingham Π formulation are included in Appendix II-C1, and a listing of the wheel scaling ratios is shown in Table II-1, below:

<u>QUANTITY</u>	<u>RATIO</u>
Angles, densities, Accel. due to gravity - - - -	1
Angular accelerations - - - - -	λ^{-1}
Angular velocities - - - - -	$\lambda^{-1/2}$
Translational Velocities, Time intervals, - - -	$\lambda^{1/2}$
Linear Dimensions, nominal pressures, - - - -	λ
Area - - - - -	λ^2
Volumes, Forces, Mass - - - - -	λ^3
(Horse Power, Rate of Doing Work)*1 - - - -	$\lambda^{7/2}$
(Moments of Force, Work, Energy)*1 - - - -	λ^4
Mass Inertia - - - - -	λ^5

TABLE II-1: DYNAMIC SIMILITUDE SCALING RATIOS USED FOR

WHEEL QUANTITIES

where λ = ratio of characteristic prototype to model length, e.g. wheel diameter.

*1 = denotes those terms whose magnitude and ratio are dependant on the nature of the soil reaction.

Those terms not marked by the superscript *1, can be specified completely in the chosen loading pattern, as they are independent of the surface on which the wheel rests. However the range that any of these ratios can take is limited by the supporting experimental facility. As an example: the ciné-

radiographic system imposes an upper limit on the translational wheel velocity of ≈ 10 inches/second, whereas the hydraulic circuitry imposes a practical lower control limit of 3 inches/second on this parameter. Also the ciné-radiographic technique provides an upper limit to the wheel diameter, when using the equipment described in Section II-E, for reasons that are described later.

In order to meet the requirements of Table II-1 and keep within the limits imposed from considerations of the supporting mechanical facility, the instrumentation and the ciné-radiographic system, two wheels were chosen for the study. The largest wheel - referred to as the 'prototype' - measured 13.5 inches in diameter by 3.75 inches wide, and the 'model' wheel was at 2:3 scale. Both wheels were supplied by the DeHavilland Company of Canada Ltd. and were manufactured from aluminum. A photograph of these wheels, together with a listing of the specifications, has been included in Appendix II-C1.

The practical difficulties of ensuring equivalent distributions of mass in both model and prototype, in a situation where it was decided to study the influence on soil behaviour of different loads on the same wheel, did not permit the mass inertia ratio to be satisfied. All scaling of wheel loads was achieved by external application of dead-loads above the wheel axle. However, this single deviation from the scaling scheme does not reduce the wheel-soil system to the kinematic case (Sedov, 1959) and it may be assumed, from considerations in Chapter V, that the external wheel forces are homologous; that is, that dynamic similitude is achieved.

It is of interest to note that the ratios of Table II-1 are identical to those developed by Blagoveshchensky (1954) for scaling ship motions. However, these ratios are significantly different from those proposed by Nuttall (Bekker, 1956) for previous model vehicle studies on soils.

C2: The Selection of Wheel Loading Parameters.

For this study five loading parameters were chosen in order to examine the soil behaviour beneath a variety of wheel loads. These were:

- 1) Wheel Size, D_i ($i = 1, 2$)
- 2) Wheel Load, W_i ($i = 1, 2$)
- 3) Applied Torque, M_i ($i = 1, 2, 3$)
- 4) Rim surface texture, δ_i ($i = 1, 2$)
- 5) Translational Wheel Vel., \dot{x}_i or v_i ($i = 1, 2$)

where there is no summation over the subscripts. The wheel sizes, loads and translational velocities were controlled in accordance with the ratios of Table II-1. The applied Torque Parameter is related to slip rate, the two being directly proportional, where slip rate is defined as:

$$a) \text{ Normal Slip rate} = S = (\omega r - \dot{x}) / \omega r$$

$$\text{and } b) \text{ Differential Slip rate} = G = (\omega r - \dot{x}) / \dot{x}$$

where ω = angular wheel velocity radians/sec.

r = wheel radius, inches

and \dot{x} = translational wheel velocity, inches/sec.

In the subsequent discussion normal slip rate will invariably be considered, and the numerical values taken on by the subscripts will be listed.

D; INSTRUMENTATION AND CALIBRATION.

Six wheel loading variables were measured continuously during each test.

These were:

	CHANNEL NO.
1) Driving torque to Wheel (inch-lbs.)	1
2) Drawbar pull on Rt.hand Flexure (lbs.)	2
3) Drawbar pull on L.hand Flexure (lbs.)	3
4) Wheel Sinkage (inches)	4

CHANNEL NO.

- | | |
|--|---|
| 5) Angular Wheel Velocity (rads./sec.) | 5 |
| 6) Translational Carriage Velocity (inches/sec.) | 6 |

The devices used for the above measurements, together with their circuitry and calibrations are included in Appendix II-D. The torque device (Windisch, 1967) was located on the carriage end of the telescopic drive shaft. Thus the torque input to the wheel could be measured with some precision since the losses to the wheel carriage bearings may be considered negligible.*

In order to accommodate the range of torques and drawbar pull values anticipated, yet provide sensitive measurements over a wide range, the central strain gauged component of the torque measuring device (Windisch, 1967) and the two flexures were replaceable.

The transducers in the circuits of Channels 1 to 5 inclusive were located on the moving wheel and dynamometer carriage, together with the associated power supplies and switching circuits of Box 'A' - see Plate I. The signals from these devices were passed via a suspended moving cable assembly - see Plates I and II - to the recording console. An ultra violet light recorder provided the output for all the variables listed above. All calibrations were carried out using the 'black box' technique described in detail in Appendix II-D. This same Appendix includes sample calibration curves.

During the early part of the study attempts were made to measure stresses normal to the wheel surface, by embedding a small piezo-electric pressure transducer** in the wheel rim. Because of technical difficulties with the

* Supplementary tests showed that a torque of approximately 4 in-ozs. was necessary to induce rotation with the 9" diam. wheel and a superimposed axle load of 20 lbs. With lower axle loads, wheel motion and carriage vibrations, this value probably represents a conservative estimate.

** Kistler model GOIL transducer with 1/4" diameter sensitive area. The charge amplifier model No. was 555B-50.

in-line charge amplifier the attempt had to be abandoned.

In order to control the slip rate, and thus the applied Torque to the wheel, a voltmeter was wired in parallel to Channel 5 and a calibration of voltage output to angular wheel velocity was made - see Appendix II-D. This enabled approximate slip rate control by continuous rheostat adjustment during each test. However, the indeterminate nature of soil wheel dependence on slip, tachometer generator fluctuations, and the transition from the 'approach' to the 'prepared' region as each test proceeds, all combine to prevent rigid control of this parameter.

E; THE CINE-RADIOGRAPHIC SYSTEM.

E1; Introduction.

In Chapter I the speculation surrounding the nature and mechanism of soil behaviour beneath a rigid wheel was emphasised. Recent technological advances have provided a variety of mensurational devices whose application to the field of soil mechanics is largely unexplored. These tools include radioactive tracing, hypersonic devices and Flash X-Ray equipment. A Flash X-ray unit being used prior to this study in the Mechanical Engineering Dept. of McGill, led to the suggestion by Mr. L. J. Vroomen that it might offer potential for examining the soil-vehicle problem. Exploratory studies carried out with the cooperation of the Radiological unit at CARDE supported this suggestion and the technique described in Chapter III was developed. It should be noted that any non-destructive device that offers a means of examining dynamic phenomena in an opaque material offers considerable potential in the field of soil-mechanics.

Recent developments in Field emission (Dyke, 1963), have made it possible to record these transient phenomena in a variety of opaque media with high information rates. Field emission - as opposed to thermionic emission -

enables a 'Flash' of X-Radiation to be emitted from a cold cathode with a short pulse duration (exposure time) and high intensity. There is thus little analogy with medical - hot cathode - X-ray units.

A literature survey reveals that the only precedent in 'soil-mechanics' was the exploratory study by Bloedow (1962) who successfully penetrated five inches of dry sand, but did not apply the technique to any specific problem.

In the following section only the basic design considerations and equipment specifications are included.

E2; Radiographic Considerations.

Since a radiograph is a shadow-graph on photographic film exposed to X-rays, it was necessary to determine the radiographic resolution, contrast and density required to detect the movement of particles embedded in the soil.

The absorption, (attenuation), of X-rays is a function of the thickness, the density, but, most important of all, the atomic nature of the test medium. Unfortunately there is no analytical method of determining the total attenuation of X-rays and only first approximations of total effective penetration can be obtained from known empirical relationships. Some of the more important factors accounting for this situation are:

- i) That theoretical studies have been concerned primarily with mono-energetic X-ray sources whereas the 300 KV source chosen for the study emits a multi-energetic, though bounded, radiation (McMaster, 1959).
- ii) At 300 KV, the photoelectric effect and Compton - and Rayleigh - scattering account for most of the absorption in soils. When one considers the randomness of the resulting secondary radiation, or Bremsstrahlung, and the stochastic nature of the inter- and intra-'atomic' movements in a heterogeneous two - or three - phase soil

system the total attenuation cannot at present be predicted from theoretical considerations.

- iii) The wide beam geometry, 30° , of the chosen X-ray emitter does not satisfy the condition of narrow-beam geometry used in many of the theoretical attenuation component calculations - see Richtmeyer and Kennard (1947), McMaster (1959), Evans (1955).

However, despite these limitations a first order approximation has been obtained from Victoreen's (1948), (1949), mass attenuation coefficients and from some simplifying assumptions. This method, included in Appendix II-E, relates the mass attenuation coefficients of a material, whose linear attenuation coefficients are known, to the attenuation coefficients of the soil. From this information radiographic equivalence factors, R.E.F.'s, have been derived for sand-air and sand-water systems as a function of source to film distance, S.F.D., and void ratio, e . These R.E.F. values have provided a most satisfactory first approximation of anticipated soil penetration - (proved by subsequent experimentation).

Since maximum penetration consistent with acceptable limits of geometry and object definition was considered a prerequisite, a minimum S.F.D. of 16.5 inches has been used for all testing. The geometry of the radiographic cassette, the sand filled region, and the X-ray source thus impose a maximum thickness of sand absorber of 7.25 inches - perpendicular to the plane of the cassette. This takes into account the attenuation caused by the lateral confining plates and permits acceptable radiographic contrast and tracer-object definition.

In order to follow the movement of soil particles with X-rays, as a function of position and time, it is necessary to embed tracer-objects in the soil mass. The fundamental requirement that the embedded object possess properties identical to those of the soil - size, compressibility, etc. -

is difficult, if not impossible, to satisfy. The net result is invariably a compromise that attempts to satisfy as many of the fundamental requirements without detracting from the usefulness of the test technique.

Using a Flash X-ray technique, it is possible to eliminate the intrusive effects of leads - associated with electrical mensurational devices. It is not possible however to satisfy the condition of soil-object density equality. The reason for this is based on the attenuation requirements. Within the effective wave-length range of the 300KV unit, namely $.0413\text{\AA}$ to $c.25\text{\AA}$, there is only a slight variation in the mass attenuation coefficients of all elements in the periodic table - and thus, implicitly, of all compounds. Thus it is only the influence of density, within this wave-length range, that creates the condition of differential linear absorption that is necessary for buried object identification. It may be shown, again by using Victoreen's results, that under the above conditions a 1 mm. thickness of lead produces differential film densities greater than the minimum distinguishable visible limit of two percent. Since maximum penetration has been specified, the generally accepted maximum penumbral image width of 0.25 mm. has to be forgone, as this would dictate an S.F.D. greater than 8 feet (McMaster, 1959). However this does not present a major problem since the centre of a cross may be identified almost independently of the penumbral image. A second source of image unsharpness, caused by secondary radiation, or Bremsstrahlung, is less easy to control.

The outcome of these considerations was a three dimensional cross with six orthogonal arms - each of length 3 mm. - giving a maximum dimension of 7 mm. Each arm is 1 mm. in diameter. This shape and size make it possible to measure both translations and rotations, with an accuracy that will be discussed in a later Section. These tracer-objects were made from a composition of 94% lead and, to reduce the malleability, 6% Antimony. Details of the fabrication and assembly of these tracer-objects are included in Appendix

II-E.

The possibility that differential inertia effects might occur, caused by an object to sand density ratio of 4.2, has been examined experimentally. Using a coloured sand tracer technique, and gelatin fixation, no measurable differential inertia effects were observed under controlled vertical loading, at strain rates of 30 inches per second. This adds experimental support to the requirement that the buried objects move 'with', rather than 'through', the surrounding sand - see Appendix II-E.

The requirements of maximum penetration and good tracer-object definition are, in large measure, dependent on the film and screening techniques used. Experimentation with a variety of films and screens led to the choice of Kodak Royal Blue Medical Film, 8" x 10", and DuPont, calcium tungstate, fluorescent intensifying screens. General Electric Supermix chemicals were used with development times corresponding to the maximum contrast listings. For double exposure on the same radiograph a single .002 inch Ilford lead screen was placed in the cassette, on the source side of the X-ray film, to reduce the cumulative effects of Bremsstrahlung.

E3; Description of Ciné Radiographic Equipment.

A schematic of the X-ray system is contained in Appendix II-E. The essential feature of this system is that it can pulse a successive train of up to 10 exposures, at 300KV, at a maximum rate of two pulses per second. Specifications of the essential features of the McGill unit are listed in Table II-2, below. All components of the Flash X-ray train were supplied by the Field Emission Corporation of McMinnville, Oregon.

TABLE II-2. ESSENTIAL SPECIFICATIONS OF FLASH X-RAY UNIT

Model Number	730/233
Output Voltage (Kilovolts)	300
Output Current (amps)	1400
Output impedance (ohms)	215
Pulse Width (microseconds)	0.1
Peak Power (megawatts)	420
Source Diameter (mm.)	4.0
Dose rate at tube surface (r/sec.)	1×10^8
Penetration of Aluminum (inches)	6.0 (at 1 ft.S.F.D.)

CHAPTER III

THE EXPERIMENTAL TECHNIQUE

A. INTRODUCTION.

The method of measuring translations, rotations, velocities and accelerations of a co-planar tracer-object network, located in a sand mass beneath the centre-line of a rigid wheel, forms the subject of this Chapter.

In the field of Soil-Mechanics, where X-rays have been used almost exclusively in spectroscopic applications, there are only a few examples of thermionic X-ray emitters being used to study deformations occurring within a soil mass. Roscoe et al (1963), describe an X-ray method for studying plane-strains, occurring in a soil mass behind a retaining wall, and refer to previous studies by Gerber (1929) and Davis & Woodward (1949). More recently a similar low kilovoltage thermionic emitter was used by Wilson and Kizywicki (1965), to measure deformations that occurred in an organic soil (moisture content \approx 600%) under a rigid wheel moving at 24 inches per minute - in what appeared to be the first X-radiographic application to the soil-vehicle problem.

However quite different demands are imposed on the mensurational device when one attempts to measure deformations occurring in mineral soils under 'dynamic' wheel loads. The technique described herein is developed for these conditions, and has been made possible by the recent development of small high powered field emitters, (Dyke, 1964). Appendix III contains detailed supporting information relevant to this Chapter.

B. SAND PREPARATION AND TRACER-OBJECT PLACING TECHNIQUE.

B1: Properties of the sand.

The soil bin contains over 40 tons of crushed silica sand supplied by Canadian Silica Corporation Ltd., St. Jerome, Quebec. This angular sand has

a specific gravity of 2.67 and a void ratio, e , range of: $e_{\text{loose}} = 0.905$, $e_{\text{dense}} = .58$. This corresponds to a density range of: $\rho_{\text{loose}} = 1.40$ to $\rho_{\text{dense}} = 1.69$, where ρ = mass density in gms/cc. These ranges were determined using Kolbuszewski's (1948) pouring techniques. A grain size analysis has been plotted ~~as the distribution~~ and is included in Appendix III-B - where it can be seen that the sand is predominantly fine grained.

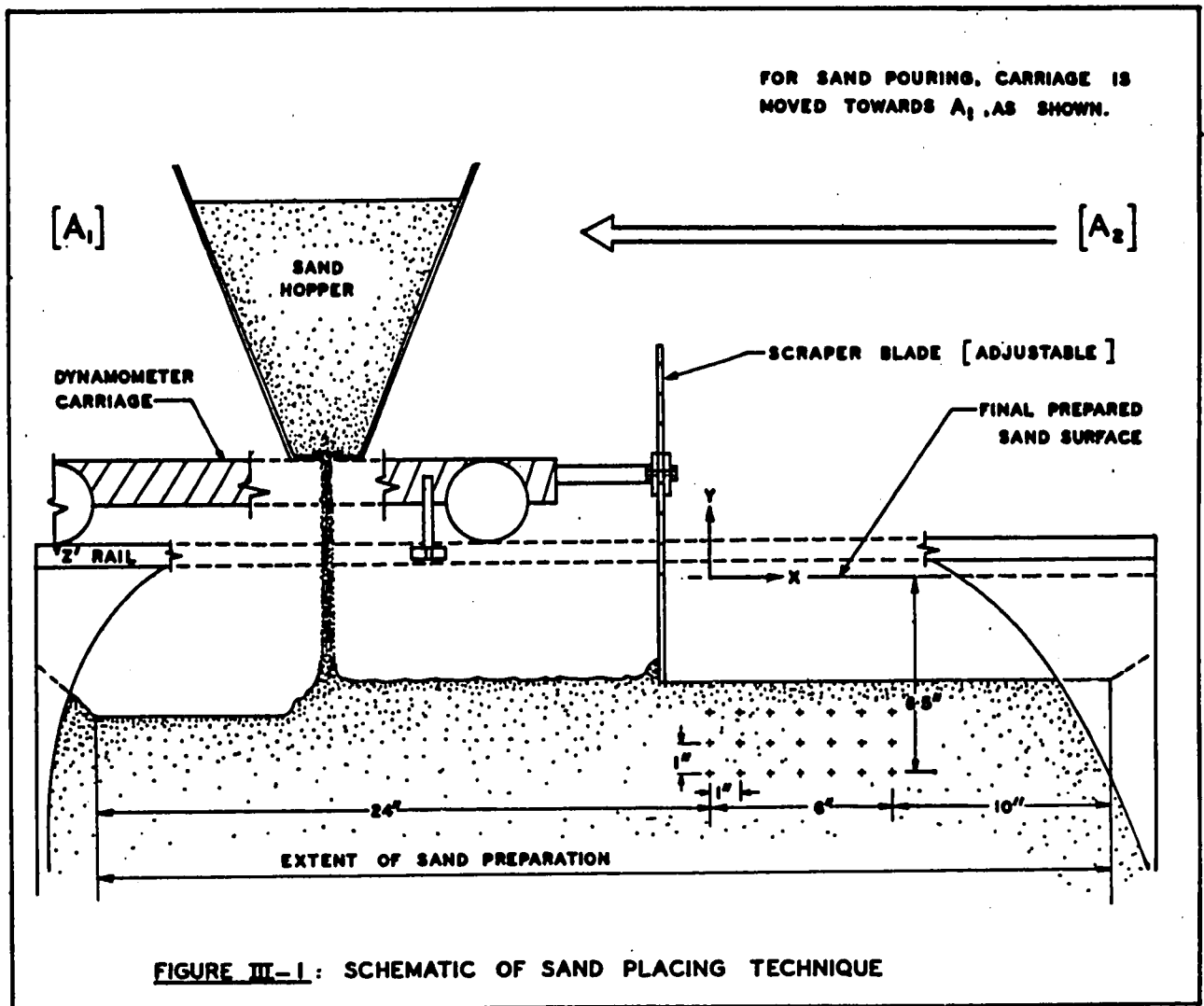
B2; The Sand Container.

The X-rays produced by the 730/233 unit can effectively penetrate 7.25 inches of sand perpendicular to the plane of the Cassette. This 'dictates' the side wall spacing of the region where soil behaviour can be examined. The 30° cone produced by the X-ray source, together with the 16.5 inch S.F.D., restricts the area of study to approximately 7 inches by 7 inches in the plane of the wheel centre line. However to reduce end effects and to ensure a steady-state loading pattern, the sand is prepared for a distance of 40 inches parallel to the side walls. The sand container dimensions are thus 7.25" x 40" x 48". The side walls of the container were polished aluminum for the majority of tests, although a supplementary series of tests was undertaken using 1/4" plate-glass side walls to evaluate the influence of the side walls on the measured soil translations. The location of the 'sand container' is shown in Plate II.

B3; The Sand Preparation and Tracer-Object Placing Technique.

The essential requirement for sand preparation and for tracer-object placing was considered to be repeatability. In order to obtain this the following technique was devised:

A sand hopper, shown in both Plates I and II, was mounted on the dynamometer carriage, as illustrated diagrammatically in Figure III-1, below:



The dynamometer carriage speed, regulated by the flow control values, was adjusted so that the sand flow rate provided the required depth of sand, to satisfy the following sequence:

- i) The 'sand container' was excavated to a depth of approximately 6.1/2 inches, and then levelled to this depth by a scraper blade mounted to the dynamometer carriage.
- ii) A template, measuring 7.25 x 12 inches, with 7 cross shaped holes spaced one inch centre to centre and in a line corresponding to the centre-line of the test wheels - see figure III-2- , was

placed on the levelled sand surface. One tracer-object was placed in each of these holes with a pair of tweezers, and care was taken not to disturb these tracer-objects once placed. The template was then removed.

- iii) The scraper-blade was then raised one inch and the carriage moved to location (A₂) - see figure III-1. The sand cut-off blade was removed to start flow and the carriage moved towards position (A₁). The carriage speed was adjusted to ensure that just over 1 inch of sand was poured. The corresponding flow control valve settings are listed in Appendix II-B2. On reaching position (A₂) the cut-off blade was used to stop flow, and the carriage was halted.
- iv) The next layer of tracer-objects was placed at the 5.5 inch depth using the template as in ii), above, ensuring a coplanar network spacing. The entire process is then repeated for successive layers.
- v) After placing the sixth row of tracer-objects a 1.5 inch layer of sand is placed using the value settings listed in Appendix II-B2, and the appropriate scraper blade settings.

In order to obtain the translation paths and tracer-object velocities an assumption of superposition is invoked in a later section. The validity of this assumption is largely dependent on the precision with which the tracer-object matrix can be positioned.

An analysis of the accuracy of the placing technique, Appendix III-B3, shows that for a representative test the variability of the tracer-object placing about the mean row depth is less than $\pm .022$ inches at the 95 per cent confidence level.

The average inter-row spacing for the same test was 1.042 inches. These values include components of variation contributed by the data reduction technique, discussed in Sections F and G of this Chapter.

Variations in the column spacing, or x coordinate, are of little consequence since any variation is accommodated by the subsequent analysis.

A complementary experiment was carried out to determine the variation in density, with depth and height of sand drop, of the poured sand. The greatest variation in density, ρ , occurred in the surface to 1.5 inch depth, from a surface value of $\rho = 1.43$ gm/cc to a 1.5 inch value of $\rho = 1.46$ gm/cc. The in situ density range between the 1.5" and 6.5" depth was seen to be negligible, and averaged $\rho = 1.49$ gm/cc. The actual method used to derive these values, together with additional experimental results, is described in Appendix III-B3. The curves contained in this Appendix do not account for minor density variations caused by scraper action, the boundary influence, etc.. Attempts to measure these, using in situ chemical fixation techniques all proved unsatisfactory; the chemicals used included Canadian Cyanamide AM 9, Paraffin and gelatin. However, on the basis of the results reported in Appendix III-B3 only minor density variations, caused by these extraneous influences, might reasonably be expected between the top and bottom row of the tracer-objects.

The average density of 1.49 gm/cc., within this depth range, represents a reasonably loose packing arrangement as the minimum density of the sand is 1.40 gms/cc. Thus the preparation technique results in a stratified sand system with three distinct layers characterised by different densities:

- i) The top layer: surface to 1.5" depth: $1.43 \leq \rho < 1.49$ gm/cc.
- ii) The middle layer: 1.5" to 6.5" depth: $\rho \approx 1.49$ gms/cc.
- iii) The bottom layer: $> c. 6.5"$ depth : $\rho > 1.49$ gms/cc
as undisturbed during sand preparation.

C. THE WHEEL-, TRACER-OBJECT-, CASSETTE-, SOURCE-, GEOMETRY.

The physical arrangement of the flash X-ray pulser, the sand container and the cassette holder is shown on Plate II. However, the relationship of

these components to the wheel and the tracer-object network is shown in Figure III-2, overpage.

It will be noticed from this figure that the tracer-objects are placed with their "arms" in the coordinate directions. This enables easier detection of rotations about the Y and Z axes and also permits more precise location of the image centres on each series of radiographs.

The wheel positions relative to the undisturbed tracer-object network are also shown on Figure III-2. These positions correspond to the relative wheel position when the two intermediate Ciné radiographic exposures are taken. The two X-ray pulses are synchronised so that the complete velocity, and translation history of the tracer-objects may be obtained for each test. This is achieved experimentally by adjusting distances x_1 and x_2 , and examining the radiograph obtained, for a given loading pattern, from the two consecutive pulses. The time delay from triggering to firing may be considered the same for both triggering devices, and is in the order of 10^{-6} secs.

The duration of the X-ray flash is 10^{-7} sec, and since this is 10^6 times as fast as the effective loading time of the wheel all motions within the soil may be considered as "stationary" for the instant of each flash. The circuitry of the triggering devices is shown in Appendix II-E, but it should be noted that the minimum time delay between two consecutive pulses with the McGill flash X-ray unit is 0.5 seconds. Since x_1 could not exceed 5.5 inches for the range of loading patterns considered, this imposed an upper limit to the translational wheel speed of 11 inches/second.

The Cassette holder contained four lead reference markers permanently attached on the inner side of the Aluminum plate located nearest the source. A fifth triangular lead marker was also placed on this plate in the position corresponding to the optical centre. This position was located with a

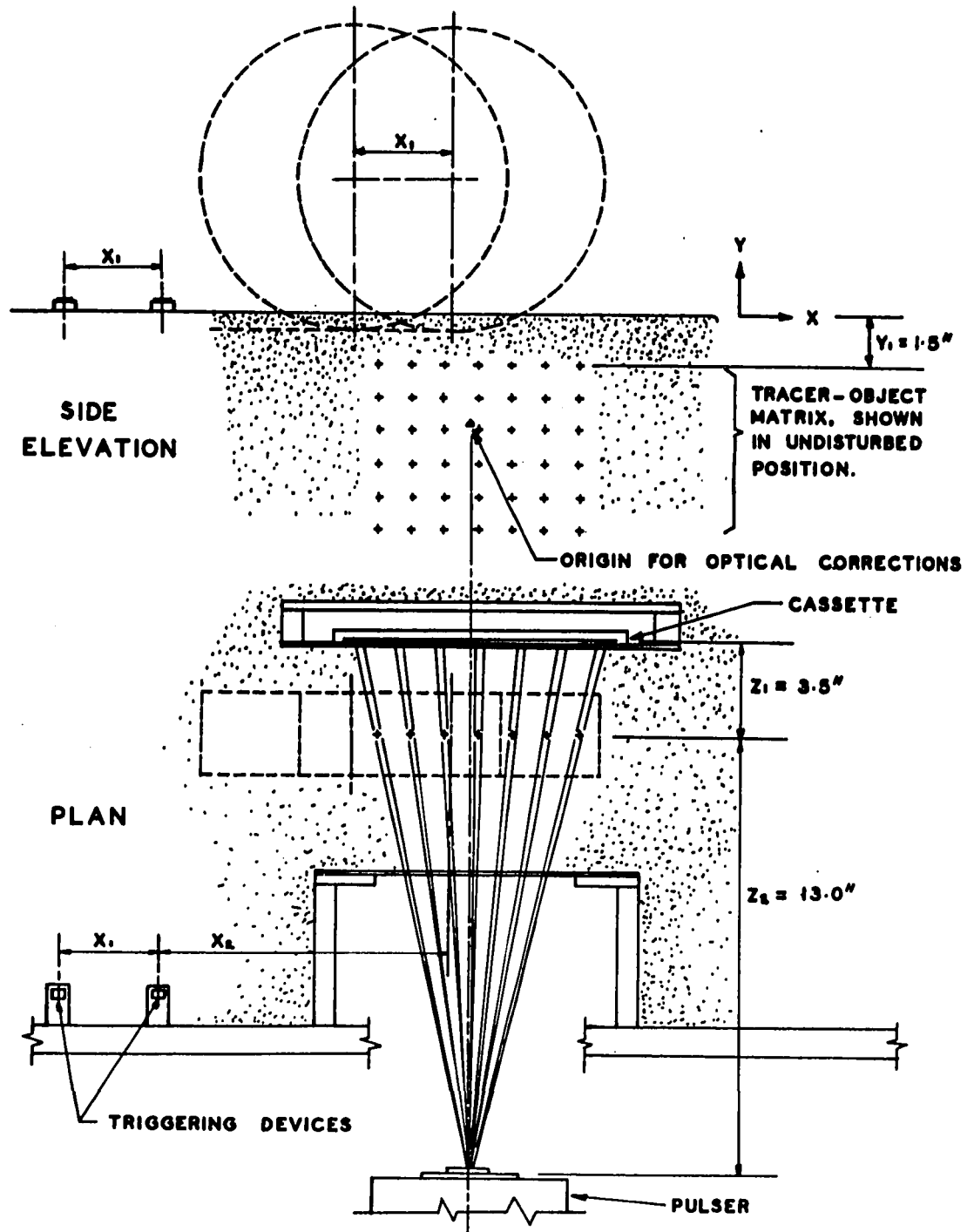


FIGURE III-2 : THE SOURCE - TRACER-OBJECT - WHEEL - FILM GEOMETRY .

theodolite and is the point from which all optical corrections are made. All five reference points form images on the radiograph, and thus one source of Cassette placement variation is accommodated. An upper 'spring' type fitting ensures that the Cassette is at a constant distance, $Z_1 + Z_2$, from the X-ray source. The importance of locating the Cassette in the same position for each X-ray pulse (or pulses) is paramount, since variations in the Cassette positioning result in displacements of the images not caused by tracer-object movements. These 'fictitious displacements' have been discussed in some detail by Roscoe et al (1963).

D. THE X-RAY PULSE SEQUENCE.

For each test a series of four X-ray pulses were fired. The sequence may be broken down as follows:

- i) The first pulse was fired after the soil preparation had been completed, in order to establish the initial position of the tracer-object network. After one exposure the first Cassette was removed. At this stage the dynamometer carriage and wheel were stationary and at a distance of some 12 feet from the centre-line of the X-ray pulser.
- ii) A second, loaded, Cassette was then placed in the holder and the wheel, under controlled loading conditions, was passed over the prepared region. A spring loaded arm on the wheel carriage triggered two consecutive ciné pulses synchronised to two preselected wheel positions. The actual delay between consecutive pulses is dependent on the spacing x_1 - see figure III-2 - and the translational carriage velocity. This Cassette contained a .002 inch lead screen to reduce the Bremsstrahlung effects from two exposures. The Cassette was removed once the wheel was some six feet beyond the centre-line of the X-ray pulser.

- iii) A third Cassette was used to determine, with a fourth - and final - pulse, the final position of the tracer-object network.

E. TRANSFER OF RADIOGRAPHIC DATA TO DIGITIZED INFORMATION.

The need to reduce the basic radiographic information of some 70 tests, required for the overall study, led to the development of a semi-automatic data reduction system. This was considered essential since a minimum number of 300 radiographic 'bits' of information per test, was required for subsequent computer calculations.

A contact print of the initial radiograph, for test number 14, is shown in Appendix III-E, as a typical radiograph. The tracer-object network and the identification marker images can be clearly seen, as can the image of the optical centre 'triangle'. In order to combine the radiographic information from four exposures, per test, the following procedure was carried out:

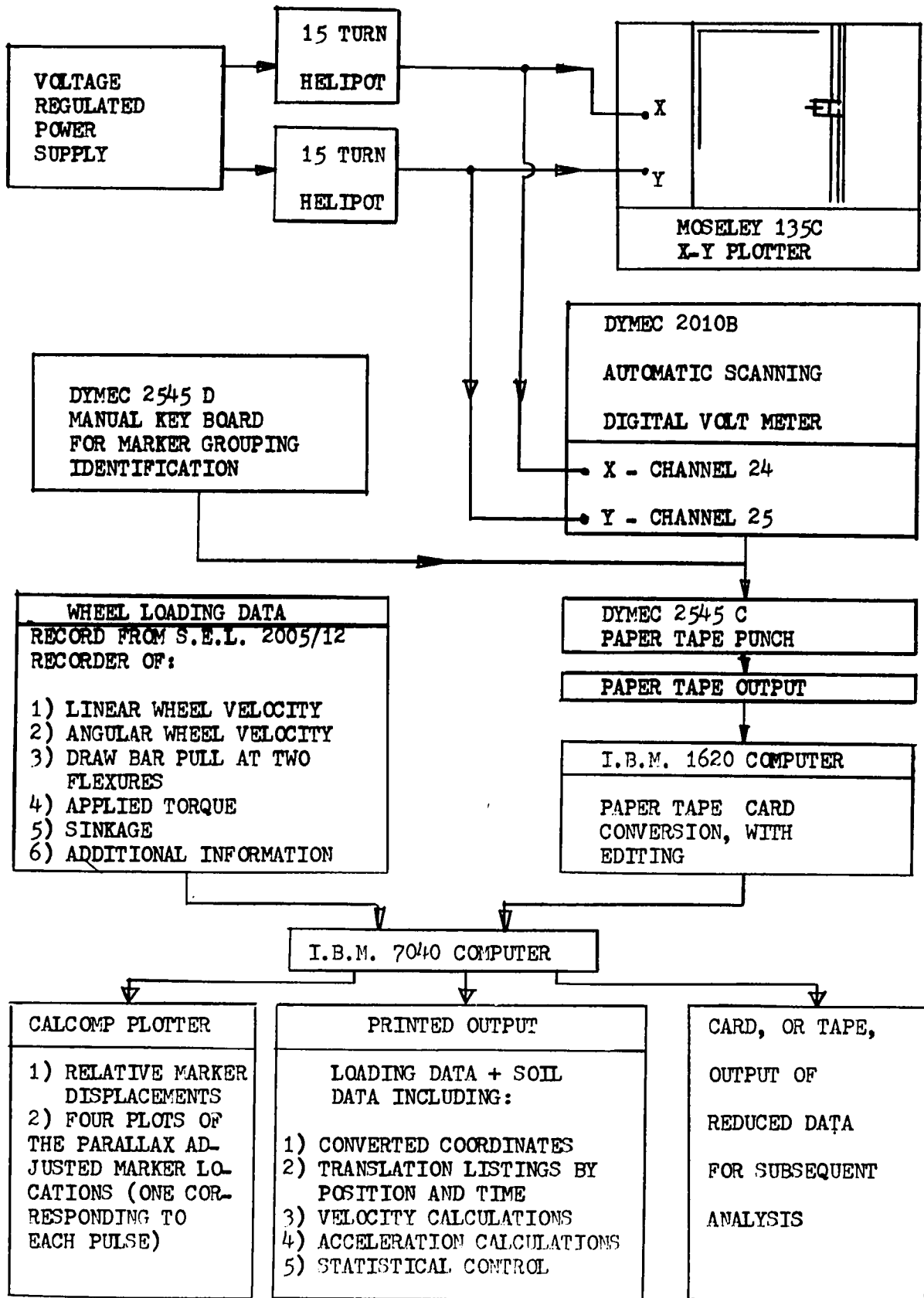
Each radiograph was placed on a light table and a Matex acetate sheet placed over each reference grid, aligned, and the image centres were then transferred to a common base. The translucent properties of the Matex facilitated this basic data transfer as the differential object-sand image density was often close to the minimum distinguishable limit - a compromise necessitated by maximum penetration requirements. A less translucent piece of graph paper was then placed over the acetate sheet and aligned so that the initial tracer-object network rows coincided with the horizontal grid lines. The information was then transferred to the graph paper. This additional step was necessary to align the coordinates of the image locations for the subsequent reduction to digital voltage meter, D.V.M., values.

The precise coordinates of each image location were then obtained as digitized voltage values using an X-Y plotter, the Mechanical Engineering Dymec D.V.M. system and two heliopotentiometers connected as shown in Appendix

III-E. This semi-automatic data reduction technique was developed by Mr. J. L. Vrooman of the Mechanical Engineering Dept., McGill University. The graph paper was fixed in position on the X-Y plotter and the carriage needle was moved manually, by adjusting the heliopots., to each image location and the voltages corresponding to the coordinates were recorded. The linearity of voltage output is shown in Appendix II-D.

A manual keyboard in the Dymec system made it possible to reference the recorded, punched, D.V.M. output. A four digit number was assigned to each set of images of the same tracer-object. The first two digits corresponded to the test number and the last two to the matrix number as shown in Appendix III-E, for Test 14. The coordinates of the optical centre were referenced as XX99, (where XX denoted the test number).

The 'eight level' paper tape output from the Dymec was edited using the P.P.R.I.C.'s 1601 I.B.M. computer which also provided the card output necessary for subsequent computations on the McGill Computing Centre's IBM 7044. Details of this editing are included in Appendix III-E. The Flow graph, overpage, shows the sequence of operations described in this section and their relationship with the following section, III-F.



FLOW GRAPH FROM SECTION III-E

F. THE BASIC REDUCTION OF TEST RESULTS.

F1. Introduction.

In order to obtain meaningful information of the translation-, velocity-, and acceleration- history of sand behaviour beneath a given loading condition it was necessary to reduce the radiographic and loading information to a meaningful format.

Two programs were written to obtain the following information:

- i) The calibrated wheel loading information.
- ii) The precise coordinates of the four co-planar tracer-object network locations corresponding to their positions at the time of each X-ray pulse. This includes the necessary reduction of all radiographic information from the plane of the X-ray film to the plane of the tracer-objects, by an optical correction - discussed in Appendix III-F. This Cartesian reference framework was arbitrarily termed the 'absolute coordinate' (x, y) system.
- iii) A listing of the coordinates of the second, third and fourth image locations relative to their respective initial tracer-object location. The resulting 'relative coordinate', (r, s), Cartesian reference framework is convenient for computing the translation paths on a row by row basis and is also required for subsequent velocity calculations.
- iv) As a criterion for checking the reliability of results from any one test a statistical control section was included. The chosen statistics were the relative coordinates of the tracer-objects corresponding to their final positions, by row, at the time of the fourth X-ray pulse.
- v) The velocity components by row, as a function of cumulative loading

time and relative and absolute coordinates.

- vi) The acceleration components by row as a function of cumulative loading time.

Because deformations beneath the 9" diameter wheel were less than those occurring under the 13.5" diameter wheel it was only possible to resolve four images per tracer-object for the top three rows of objects in tests with the model wheel - as opposed to satisfactory optical resolution for six rows under the larger wheel. Because the subscript notation had to be adjusted accordingly, two computer programs were written: the first listed as "Soil-Vehicle Study I", S.V.S.I., was used in reducing results from the model wheel tests, whereas S.V.S.III was used for the corresponding prototype wheel data reductions. A listing of S.V.S.I is included as Appendix III-F, together with explanatory notes.

The assumptions implicit in the above calculations are:

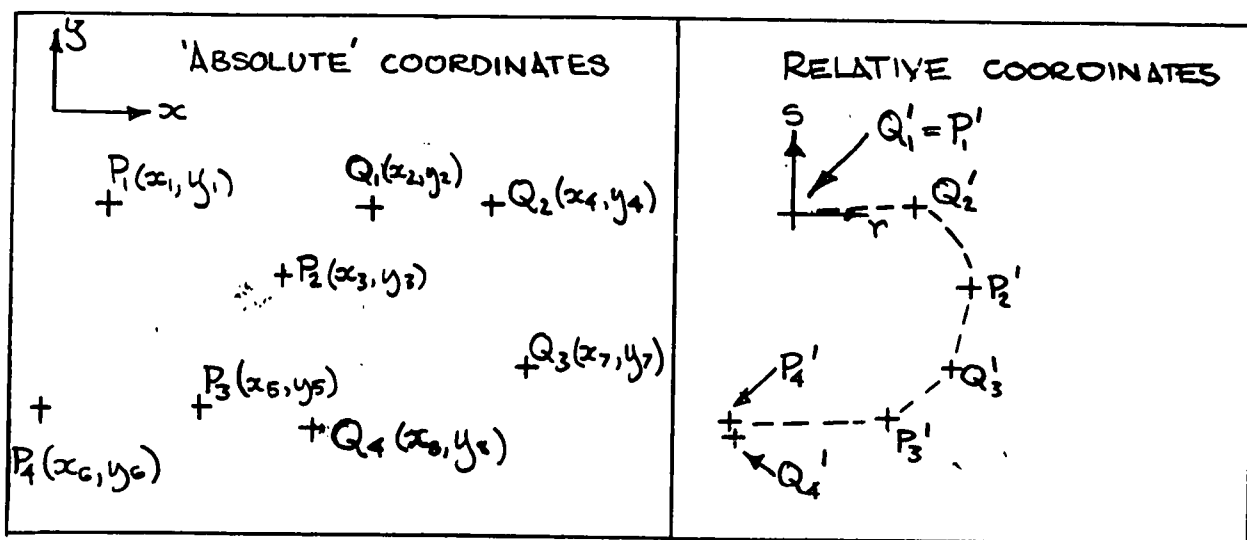
- (1) The mass of sand in any one layer strains homogeneously under a steady-state loading pattern.
- (2) There is no relative movement between the sand grains and the lead and antimony tracer-objects.
- (3) The network of tracer-objects remains co-planar with the centre line of the wheel, for the entire test duration.

A discussion of the validity of these assumptions is contained in Section III-G3, at the end of this Chapter.

F2. Translation Path Computations.

The above assumptions are invoked to determine the path described by a tracer-object located in any given row. The path can not be drawn directly from the four known locations of a given tracer-object, because the increments between each location are too large. However, by superposing the

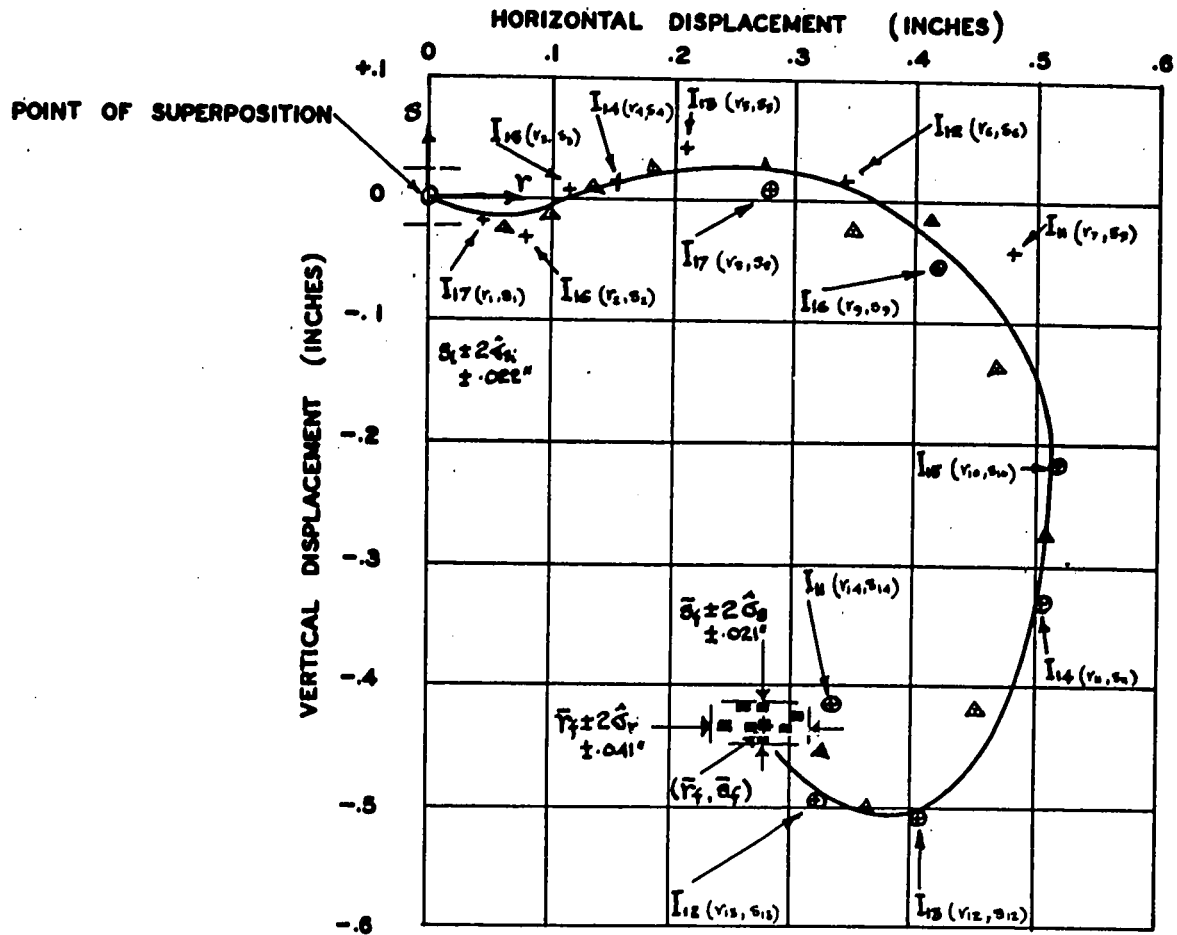
initial tracer-object locations for any one row, and using the relative coordinates - rather than the absolute coordinates - the resulting increments are sufficiently small to describe a continuous translation path. A diagram of this procedure is shown below as Figure III-3.



where: P_N and Q_N are two tracer objects located in the same row. ($N = 1, 2, 3$ or 4 refers to the location of P or Q at the instant of the first, second, third or fourth X-ray flash, respectively). P'_N and Q'_N are the corresponding 'relative' coordinate locations of the tracer-objects P and Q . e.g. Q'_1 and P'_1 have the relative coordinates $(0, 0)$, Q'_2 has the relative coordinates $((x_4 - x_2), (y_4 - y_2))$, P'_2 has the relative coordinates $((x_3 - x_1), (y_3 - y_1))$, etc.

Figure: III-3 SCHEMATIC OF SUPERPOSITION TECHNIQUE USED TO OBTAIN TRANSLATION PATHS FOLLOWED BY TRACER-OBJECTS IN ANY ONE ROW.

In this Figure only two tracer-objects, P and Q , are shown although in practice seven tracer-objects per row are superposed to obtain 14 intermediate locations along the translation path. In Figure III-4 an example from the results of Test 14 - see Appendix III-F - is shown. The path described by tracer-objects, initially placed 1.5" beneath the undisturbed sand surface, during the total stressing cycle has been plotted from the optically corrected relative coordinate values.



NOTATION: I_{ij} = TRACER-OBJECT LOCATIONS (i = ROW, j = COLUMN) RELATIVE TO COMMON ORIGIN, BY SUPERPOSITION
 + = LOCATION DERIVED FROM 2ND RADIOGRAPHIC FLASH
 ⊙ = " " " 3RD " "
 ⊞ = " " " 4TH " "
 Δ = RELATIVE COORDINATES OF VELOCITY TERMS

FIGURE III-4: THE TRANSLATION PATH FOLLOWED BY TRACER-OBJECTS ORIGINALLY PLACED AT A DEPTH OF 1.5", TEST No. 14.

The scatter of the initial and final tracer-object positions is shown for the 95% confidence limit - where the associated small sample standard deviations have been corrected using the Bessel approximation for the best estimate of the population standard deviation, $\hat{\sigma}$. This Figure illustrates the importance of correctly synchronising the wheel position and X-ray Flash to obtain the complete translation path history, with the necessary overlap of radiographic information.

F3. Velocity and Acceleration Computations.

The technique of computing velocities from the radiographic information derived in this testing differs significantly from that used in the visio-plasticity methods of Thomsen, Yang and Kobayashi (1965) for studying metal flow. Using their technique an analogous situation would be represented by taking two radiographs in rapid succession and then obtain the velocity vectors from a division of the difference between successive positions of any tracer-object by the time interval between X-ray pulses. With the X-ray facility installed for the testing reported herein, a minimum time delay between successive pulses of 0.5 seconds renders this analogous method unfeasible for the range of wheel velocities used.

Thus in order to obtain meaningful velocity information the simple expedient of converting a 'space' base to a 'time' base was used. This procedure is described with the aid of Figure III-5. below, and the following rationale:

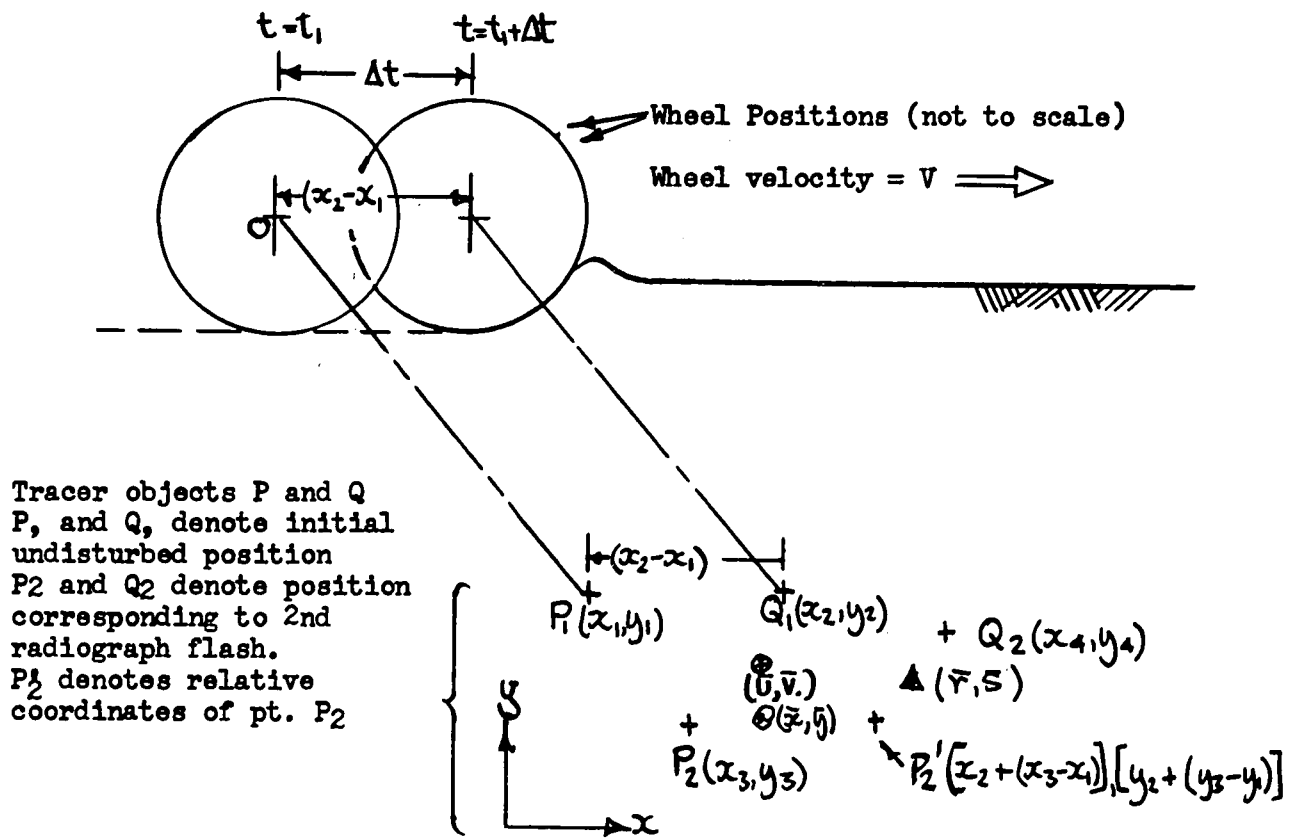


Figure III-5. Diagram for explaining rationale for Velocity Computations.

With reference to Figure III-5:

- i) At instant $t = t_1$, let tracer-object P occupy location $P_2 (x_3, y_3)$ and tracer object Q location $Q_2, (x_4, y_4)$.
- ii) At time $t_1 + \Delta t$, where $\Delta t = (x_2 - x_1)/V$, the wheel centre, O, would be in the same position relative to the undisturbed position of Q, i.e. Q_1 , as it was to position P_1 at time t_1 .
- iii) From assumptions (1), above, the position of tracer-object Q at time $t + \Delta t$ should correspond to the relative position P_2' , where P_2' represents the relative coordinates of P_2 , i.e. $((x_3 - x_1), (y_3 - y_1))$ transferred to position $((x_2 + (x_3 - x_1)), (y_2 + (y_3 - y_1)))$. That is, in time Δt the tracer-object has hypothetically moved from position Q_2 to P_2' .
- iv) The horizontal component of velocity, in this case denoted by \bar{U} , where

$$\bar{u} = \frac{\Delta x}{\Delta t} = \frac{((x_2+(x_3-x_1)) - x_4)}{\Delta t} \quad (\text{III-1})$$

The vertical component of velocity, in this case denoted by \bar{v} ,

$$\bar{v} = \frac{\Delta y}{\Delta t} = \frac{((y_2+(y_3-y_1)) - y_4)}{\Delta t} \quad (\text{III-2})$$

which from the above assumptions acts at position

$$\bar{x} = \frac{x_1+x_2}{2} + \frac{(x_2+(x_3-x_1)) - x_4}{2} + (x_4-x_2) = \frac{(x_3+x_4)}{2} \quad (\text{III-3})$$

$$\bar{y} = \frac{y_1+y_2}{2} + \frac{(y_2+(y_3-y_1)) - y_4}{2} + (y_4-y_2) = \frac{(y_3+y_4)}{2} \quad (\text{III-4})$$

where \bar{x} and \bar{y} refer to the 'absolute' cartesian reference system.

v) The velocity components can also be expressed in terms of the 'relative' coordinate system, described in the previous subsection.

With reference to Figure III-5 it can be seen that the relative coordinates of Q_2 are $((x_4-x_2), (y_4-y_2))$ and thus \bar{u} and \bar{v} are unchanged since the increments of x and y are identical to those in equations (III-1) and (III-2), respectively. The corresponding relative coordinates of \bar{u} and \bar{v} , designated as \bar{r} , \bar{s} , are:

$$\bar{r} = \frac{(x_3-x_1) - (x_4-x_2) + (x_4-x_2)}{2} = \frac{x_3-x_1+x_4-x_2}{2} \quad (\text{III-5})$$

$$\bar{s} = \frac{(y_3-y_1) - (y_4-y_2) + (y_4-y_2)}{2} = \frac{y_3-y_1+y_4-y_2}{2} \quad (\text{III-6})$$

From a computing standpoint it was considered easier to determine the components of velocity in the 'relative' Cartesian frame, (r,s) , and then convert to the 'absolute' Cartesian frame, (x,y) , from the relationship

$$\bar{x} = \frac{(x_1+x_2)}{2} + \bar{r} \quad (\text{III-7})$$

$$\text{and } \bar{y} = \frac{(y_1+y_2)}{2} + \bar{s} \quad (\text{III-8})$$

for the particular case illustrated in Figure III-5.

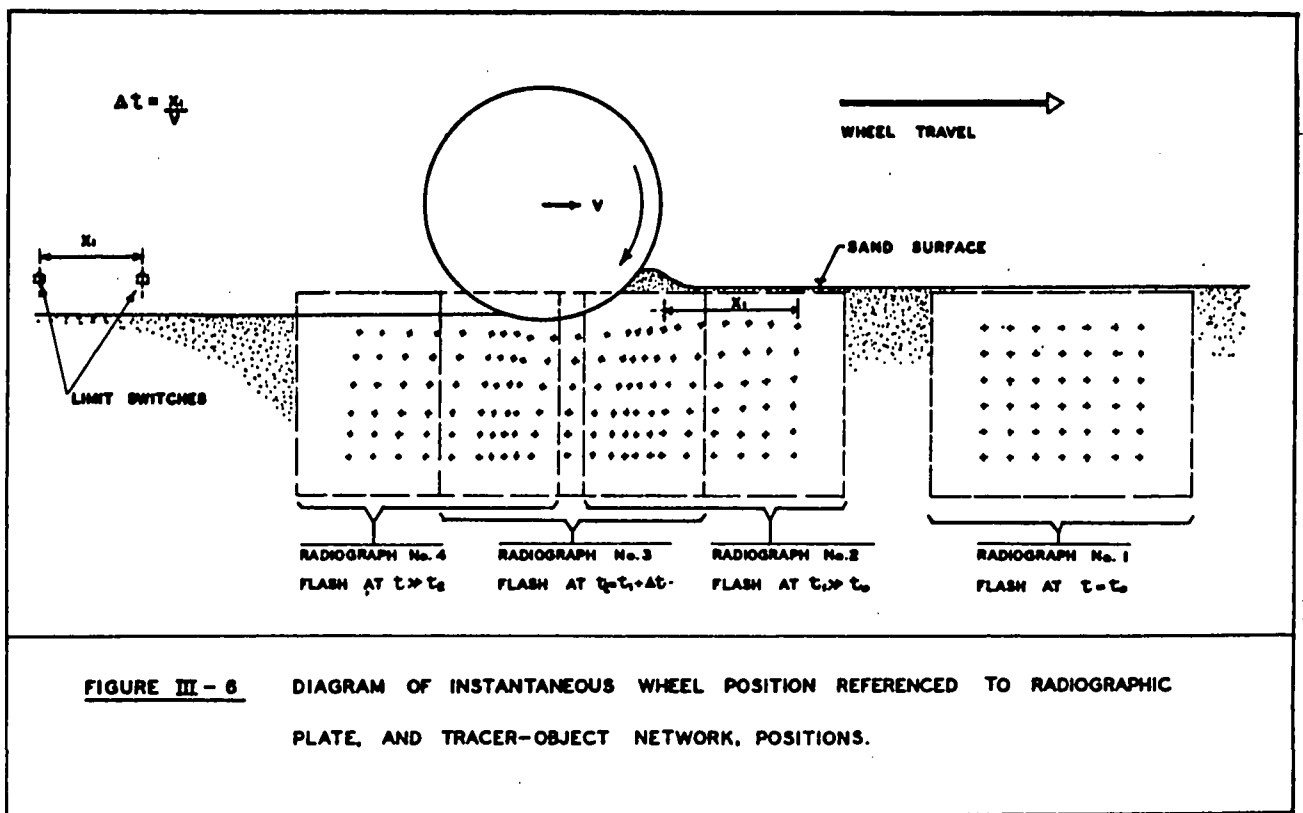
This formulation has been generalised for both programs used in the analysis, and can be followed through step by step from the program listing in Appendix III-F. Figure III-4 illustrates the coordinate positions of the 12 velocity computations for the 1.5" row translations of Test No. 14. From this information the velocity components along the path can be plotted. However to plot these components as a function of the cumulative loading time or in terms of the 'absolute' coordinate reference system the time interval between the second and third radiographs is used. This time interval, Δt , is obtained from the known spacing between the limit switches and the known translational velocity of the carriage. In Figure III-6, below, the position of the recorded tracer-object locations relative to an instantaneous position of the wheel is shown with reference to the tracer-object network locations. The importance of correct experimental synchronisation of Pulses is emphasised, as a continuous record of the entire translation history was considered desirable. In practice, as shown in Figure III-6, it was not possible to achieve this with the soil-wheel systems chosen for the testing reported herein. It was, however, possible to 'overlap' or 'abutt' radiographic information from the second, third and fourth radiographs. This particular combination was chosen because of the higher component velocity and translation magnitudes within this range.

These computations may be used with appropriate modifications, to describe the velocity history of the sand beneath a rigid wheel in both the Eulerian and Lagrangian systems; although only the Eulerian formulation will be developed in Chapter V.

This statement is limited to the velocity histories examined within the boundaries imposed by the mensurational technique.

The VELOC subroutine of the Computer Programs, included in Appendix III-F, also includes instructions for computing Acceleration components by

finite difference techniques, similar to those described above for the velocity computations. These instructions were included solely to obtain an idea of the order of magnitude of the acceleration terms. The acceleration print out should therefore be examined only in this light. For the detailed acceleration computations used in Chapter V graphical methods have been used and thus will be discussed later.



G. A DISCUSSION OF THE RELIABILITY OF THE DERIVED RESULTS AND THE VALIDITY OF THE INVOKED ASSUMPTIONS.

1. The reliability of the Derived Translations.

Three distinct sources of error can influence the reliability of the derived translations:

- i) Any geometric variation in the placing of the Cassettes, the location of the field emission source, the placing of individual tracer-objects in a position away from the network plane or in the data transfer technique, results in measured radiographic displacements not caused by movements of the tracer-objects.
- ii) Variations resulting from the possible inapplicability of the three assumptions listed in Section III-F. This potential source of variation could result from two possible situations: a) that the assumptions were valid, but the necessary conditions were not realised experimentally (e.g. inhomogeneities resulting from the sand preparation technique), or b) that the assumptions were invalid.
- iii) The assumption of tracer-object superposition applied to tracer-objects in the same row but not at the same mean depth.

An itemised analysis of the magnitudes of source i) variations of image locations, reduced to the tracer-object plane, is included as Appendix III-G. The maximum realistic displacement from this source is seen to be approx. $\pm .04$ inches at the 95 percent confidence level. This magnitude of variation could be reduced considerably by increasing the source-to-object distance, Z_2 , - see Figure III-2. However, for the same limiting test conditions this could only be achieved with a higher kilovoltage, capacity, pulser.

For the majority of tests the measured range of displacements, at the same confidence level, was considerably smaller than the $\pm .04$ inch limits of source i). It is thus difficult to isolate the magnitude of source ii) variations for displacement differences $\leq .04$ inches. However, for variations $> .04$ inches it appears that the applicability of the Section III-F assumptions must be questioned. In practice these large variations only occur in soil regions near the wheel at high slip rates - see Chapter

IV - and apparently result from non-homogeneous deformations in the soil layers near the surface.

The third source of variation, iii), can only be considered within the framework of the assumptions of Section III-F. The principle of superposition is only strictly applicable when the tracer-objects of any one row are initially located at exactly the same depth, \bar{y} . From Appendix III-B the precision of object placement for any depth \bar{y} was seen, for one test, to be $\bar{y} \pm .022$ inches at the 95% confidence level. This source of variability is difficult to isolate since object placement away from the tracer-object network plane could possibly account for this variation - see Appendix III-G.

Turning from these generalities to the specific case of test number 14 - Appendix III-F - the final relative tracer-object coordinates exhibited displacement variations $< .025$ inches (95% level) in all but one case. For the translation pattern of the top row tracer-objects, plotted as Fig. III-4, the scatter of the final relative coordinate positions is seen to represent $\approx 15\%$ and $\approx 8\%$ of the gross translations in the r and s directions respectively. This test is considered as representative of the complete test series.

G2. The Reliability of the Derived Velocities.

The computation of velocity is based on a finite difference technique, that is considerably more 'sensitive' to displacement variations than are the translation computations.

In Section III-F an analogous viscoplasticity technique was described for obtaining velocity components. In this technique only three main sources of variability influence the derived velocities:

- i) as for Source i) in Section III-G1 above.
- ii) as for Source ii) in Section III-G1 above.

iii) The accuracy of measuring the appropriate time increment.

Using the method of velocity determination described in Section III-F, another source of variation influences the accuracy of the results:

iv) Deviations from an assumed row level, \bar{y} , which from the assumed superposition causes corresponding deviations in the δs increment used in evaluating the $\delta s / \delta t$ term (this source is equivalent to that in Section III-G1-iii).

The first two sources, listed above, have been shown previously to lead to measured deviations usually less than $\pm .040$ inch at the 95 percent level. However source iv) variations, although not completely separable from source i) variations, are usually of a lower magnitude and will be discussed with reference to Figure III-7.

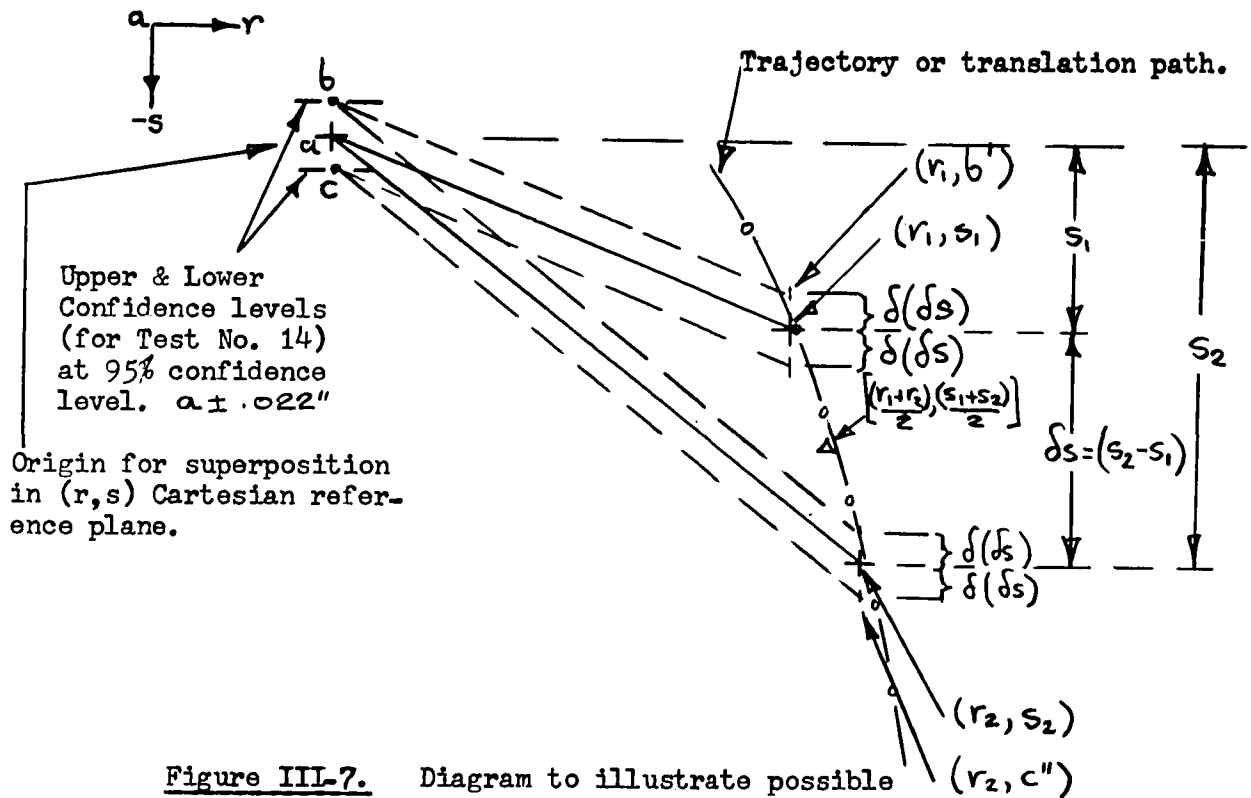


Figure III-7. Diagram to illustrate possible sources of error in derivation of $\delta s / \delta t$ component of velocity.

Only the possible variation of one component of velocity, resolved in the, s, direction of the r,s reference plane will be considered as the $\delta r / \delta t$ component variations are of a similar nature.

With reference to Figure III-7, the $\delta s / \delta t$ component of velocity at the coordinates $((r_1+r_2) / 2, (s_1+s_2) / 2)$, is computed as $(s_2-s_1) / \delta t$. This is only correct if the following conditions apply:

- a) The tracer-object was in the network plane and was located at the mean row depth, \bar{y} , and thus from superposition may be assumed to have started from pt. 'a' in Figure III-7.
- b) The geometry of the Cassette and source conformed to the assumed in situ locations.
- c) The time increment δt was computed from exact wheel translational velocity and initial tracer-object location, information.

In the extreme case this situation may not be exactly represented and because of the finite difference technique large variations in calculated velocities can result from small variations of a), b) or c). The most extreme situation may be emphasised with reference to Figure III-7. If the initial position of (r_1, s_1) had corresponded to an ordinate value of $\bar{y} + .022''$ in the absolute (x,y) reference frame, the equivalent initial position in Figure III-7 should be 'b' and thus (r_1, s_1) should be (r_1, b') . Similarly if the initial position of the tracer-object corresponding to (r_2, s_2) was $(x, \bar{y} - .022'')$, the corresponding position of (r_2, s_2) would be (r_2, c^{11}) . For this case the computed velocity would be;

$$\begin{aligned} & ((s_2 - \delta(\delta s)) - (s_1 + \delta(\delta s))) / \delta t \\ & \text{or } ((s_2 - s_1) + 2\delta(\delta s)) / \delta t. \text{ or } (\delta s + 2\delta(\delta s)) / \delta t. \end{aligned}$$

Since $2\delta(\delta s) = .044''$ at the 95% confidence level, δs must be greater than $.044''$ if the variation in velocity computations is to be $< 100\%$.

Reference to the printed output of Test No. 14, included in Appendix III-F

shows that δs is seldom $> .044''$.

For these reasons, and accepting that the above example represents an extreme situation, the accuracy of velocity determinations is seen to depend largely on the averaging techniques used to obtain velocity values for subsequent calculations.

It should be noted that the time increment, δt , is subject to consistent error for any one test, since the calibrated wheel translational velocity, V , is constant for each test.

From an analysis of possible errors in the velocity calculations it would appear that large displacement increments, δs , would minimize the error magnitude. Unfortunately large δs values result in averaging errors not considered under any of the source of variation headings listed above. One is thus concerned with a compromise that is in turn, dependent on the accuracy of the radiographic technique. The overall accuracy can thus only be improved by reducing the variability caused by all sources listed.

G3. The Validity of the Invoked Assumptions.

The validity of the assumptions listed in Section III-F may be examined from the above discussion of the derived translations and from results of complementary tests. As previously stated there is experimental evidence to support the assumption that the tracer-objects move 'with' rather than 'through' the sand - see Appendix II-E. The translation patterns of the tracer-objects are thus considered to be representative of actual sand translation patterns. From an experimental standpoint the accuracy of the measurement technique is considered acceptable. When the measured deviations are less than the bounds of the source 1) variation, the assumptions of Section III-F are considered acceptable. When the measured deviations are outside this range the basic assumptions are not necessarily invalidated, but require a different inter-

pretation. As an example: at high slip rates the tracer-object rows near the sand surface 'enjoy' characteristically different - but recognisable - translation patterns, within a given row. The basis for Assumption (3) is thought to rest in the ~~axisymmetric~~ nature of the loading pattern. However the possibility of deviations from Assumption (1) and (3) will be discussed in detail, when necessary, in the subsequent analyses.

CHAPTER IV

THE SURFACE AND SUBSURFACE DISPLACEMENT OF SAND UNDER A VARIETY OF DRIVEN RIGID WHEEL LOADING PATTERNS.

A. INTRODUCTION

As emphasised in the first Chapter, there has been considerable speculation surrounding the question of how soil behaves under a moving wheel. This situation has developed from a diversity of theoretical studies unsupported by experimental investigations. There are, however, two notable exceptions; specifically the experimental work of McKibben (1938) and Wong and Reece (1966). McKibben made some detailed measurements of the translation patterns of tracer-objects placed adjacent to glass plates, in sand, under a towed rigid wheel. The more recent work of Wong and Reece, has been in the study of initially dense sand movement beneath driven rigid wheels. Using a photographic technique, and a glass sided box they have determined the mode of deformation directly beneath a rolling rigid roller, (8.1/4 inch diameter). This method is useful to determine general trends of gross longitudinal soil transportation phenomena, but does not provide detailed measurements of these and other aspects of soil behaviour, to be discussed in this Chapter.

In the following sections some of the results from a series of experiments, designed to investigate the influence of wheel - translational (ground) velocity, - slip-rate, - load, and - rim surface material. on the sand behaviour beneath the longitudinal centre line of the wheel, are examined. In conjunction with this the influence of scaling the wheel loading variables, on these same soil parameters, is also studied.

Due to the physical arrangement of the side walls, the sand contained

therein, and the geometry of the wheel, any measurements under the centre line of the wheel, (x,y) plane, must account for the influence of sand flow and translation in the Z direction. Since the test series to be described was conducted in this quasi three dimensional setup, a supporting test series was conducted to establish the soil behaviour in the two dimensional case. In order to obtain radiographic continuity, the same effective thickness of sand was retained and a pair of additional glass plates was installed at a separation just greater than the width of the wheel under test. Another series of supporting tests was conducted to determine the influence of replacing the Aluminum retaining walls with glass plates. The results of both supporting test series are considered in the following analysis.

A synopsis of the essential features of the experimental design is included in Table IV-1, below:

MODEL WHEEL $D_1 = 9"$ Diameter					PROTOTYPE WHEEL: $\lambda D_1 = 13.5"$ Diameter				
TEST NO.	TEST W	SPECIFICATION V	M	δ	TEST NO.	TEST W	SPECIFICATION V	M	δ
4	W_1	V_2	M_2	δ_1	39	$\lambda^3 W_1$	$\sqrt{\lambda} V_1$	M_1^*	δ_1
5	W_1	V_2	M_3	1	40	"	"	M_2^*	"
6	W_1	V_2	M_1	1	41	"	"	M_3^*	"
8	W_1	V_1	M_2	1	42	"	$\sqrt{\lambda} V_2$	M_1^*	"
9	W_1	V_1	M_3	1	43	"	"	M_2^*	"
10	W_1	V_1	M_1	1	44	"	"	M_3^*	"
11	W_1	V_1	M_1	δ_2	45	"	$\sqrt{\lambda} V_1$	M_2^*	"
12	W_1	V_1	M_2	2	46	"	"	M_1^*	"
13	W_1	V_1	M_3	2	47	"	"	M_3^*	"
14	W_1	V_2	M_1	2	48	"	"	M_1^*	δ_2
15	W_1	V_2	M_2	2	49	"	"	M_2^*	"
16	W_1	V_2	M_3	2	50	"	"	M_3^*	"
19	W_2	V_1	M_1	2	51	"	$\sqrt{\lambda} V_2$	M_1^*	"
20	W_2	V_1	M_2	2	52	"	"	M_2^*	"
21	W_2	V_1	M_3	2	53	"	"	M_3^*	"
22	W_2	V_2	M_1	2	54	$\lambda^3 W_2$	"	M_1^*	"
23	W_2	V_2	M_2	2	55	"	"	M_2^*	"
24	W_2	V_2	M_3	2	56	"	"	M_3^*	"
					57	"	$\sqrt{\lambda} V_1$	M_1^*	"
					58	$\lambda^3 W_2$	"	M_3^*	δ_2

TABLE IV-1 The Experimental Design of the Main Test Series.

where: λ , represents ratio of characteristic prototype to model length = 3:2
 $V_{1,2}$ represents wheel translational velocity $V_1 < V_2$
 $W_{1,2}$ represents weight of wheel plus axle load $W_1 < W_2$
 $\delta_{1,2}$ represents static friction angle of wheel rim surface and sand
 where $\delta_1 = 21^\circ$ (polished aluminum) and $\delta_2 = 34^\circ$ (hard Rubber)
 $M_{1,2,3}$ Torque Moment, $M_1 < M_2 < M_3$
 $M^*_{1,2,3}$ Torque developed by Prototype wheel where the scaling ratio
 is 'dictated' by the interaction of wheel and sand.

The specifications of the two supporting experimental series are contained in a second table, IV-2, using the same notation.

DESCRIPTION OF SUPPLEMENTARY SERIES	TEST NO.	TEST SPECIFICATION				δ
		D	W	V	M	
<u>I. 2-Dimensional Test Series</u> , with additional glass plates spaced 2.5/8" apart analogous to Tests 14, 15, 16.	29	D ₁	W ₁	V ₂	M ₁	δ_2
	30	D ₁	W ₁	V ₂	M ₂	δ_2
	31	D ₁	W ₁	V ₂	M ₃	δ_2
II. Exptl. Set-up as for Tests of Table IV-1, but 1/4" glass plates placed adjacent to aluminum walls of sand container - see fig. III-	33	D ₁	W ₁	V ₂	M ₁	δ_2
	34	D ₁	W ₁	V ₂	M ₂	δ_2
	35	D ₁	W ₁	V ₂	M ₃	δ_2

TABLE IV-2. Experimental Design of Supplementary Test Series.

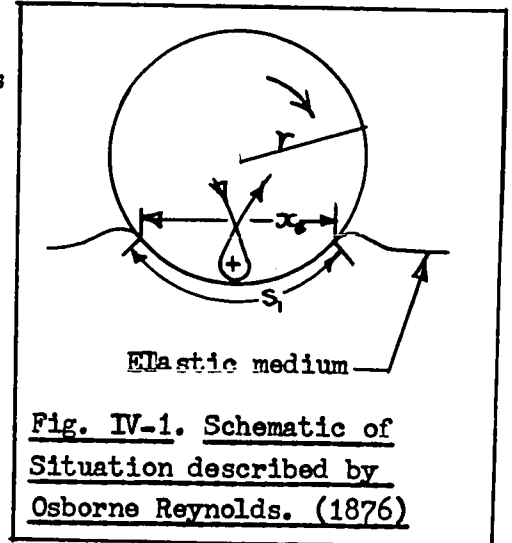
The numerical values of the controlled parameters D, W, and V, and the developed torques, M, are listed for each test number appearing in Tables IV-1 and IV-2, together with the recorded surficial variables, in Appendix IV-A1. Slight variations in the wheel diameters, D, caused by the addition of a hard rubber layer, for δ_2 , were accommodated by adjusting the ratio λ accordingly.

B. MEASUREMENTS OF SOIL MOVEMENT BENEATH A VARIETY OF CONTROLLED LOADING PATTERNS.

1. Some Kinematic Considerations.

Reynolds (1876) was one of the first to investigate the phenomenon of a rolling wheel on an elastic medium. With reference to fig. IV-1, the case

of an undeforming wheel rolling on an elastic surface is illustrated. Reynolds experiments showed that for this particular situation the horizontal distance, x_s , is less than the corresponding peripheral distance, s_1 , due to the elastic extension of the surface. Thus for one revolution the forward displacement of the axle will be less than the wheel circumference. In this case the instantaneous centre of rotation is located above the wheel rim - as shown - and thus

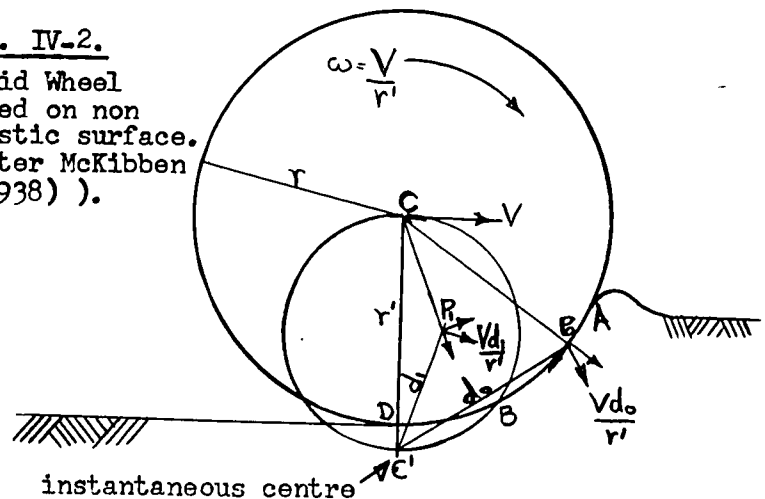


any point on the rim describes a curtate trochoid. Since the motion of any point on the rim in contact with the soil has - for this case - a clockwise component of motion, backward motion of the elastic medium is facilitated by a no-slip condition occurring along some portion of the contact zone. This prevents accumulation of compressed material in front of the rolling wheel.

McKibben (1938) appears to be one of the first to consider the kinematics of a rigid wheel rolling on a non elastic surface. This contribution may be summarised with the aid of Fig. IV-2. The magnitude of the Velocity vector

at any point P is $\frac{Vd}{r'}$ where V is the translational velocity of pt. C, d is the distance from P to C' and r' is the distance CC'. If the point P is located on the circle CC' the vector direction is

Fig. IV-2.
Rigid Wheel
Towed on non
elastic surface.
(After McKibben
(1938)).



parallel to the wheel radius on which it is located. If the point P is located inside this circle, P_1 , the velocity direction has a counter-clockwise component perpendicular to the radius on which it is located. However if the point P is located outside the circle, e.g. point P_0 , it has a component vector direction acting clockwise and perpendicular to the radius on which it acts. This means that in the region of wheel-soil contact AB the rim surface will have clockwise components of motion resisted by counter-clockwise soil reactions that tend to retard motion. In the region DB clockwise components of soil reaction will be encountered. For this reason the region BD is often referred to as the skid zone, when it exists. For the case of driven wheels, not considered by McKibben, the same situation can be represented in the negative slip zone. However with positive slips the instantaneous centre of rotation, $r' = V/w$, is located above the wheel rim and thus all velocity components perpendicular to the rim surface are clockwise.

From an analytical approach Poletayev (1964) has suggested that the wheel-soil interface may be subdivided into three characteristic zones of - slip, - cohesion, and - skid. The extent of any one zone has been expressed as a function of the soil-wheel rolling frictional value, δ' , and the angle ψ , where ψ is the angle between the radius to any point on the rim - on the soil-wheel interface - and the wheel velocity vector at that point:

Skid zone	$C_1^\circ < \psi < -\delta'$	where C_1 and C_2 are dimensionless
Cohesive zone	$-\delta' < \psi < \delta'$	constants dependent on the boundary
Slip zone	$\delta' < \psi < C_2^\circ$	cond'ts., and proportional to sinkage.

However Poletayev's predictions of the trajectories of particles initially on the soil surface bear little relation to those trajectories observed experimentally, by McKibben (1938), Berlyn (1961) and Sitkei (1966). The same criticism may be made of the cycloidal trajectory proposed by Vincent (1960).

The path traced by a point on the rolling wheel's rim surface has the

coordinates

$$\left. \begin{aligned} x &= r \left(\frac{\pi\theta}{180} (1-s) + \sin \theta \right) \\ y &= r (1 + \cos \theta) \end{aligned} \right\} \text{(IV-1)}$$

where the axes are as shown in Fig. IV-3 below.

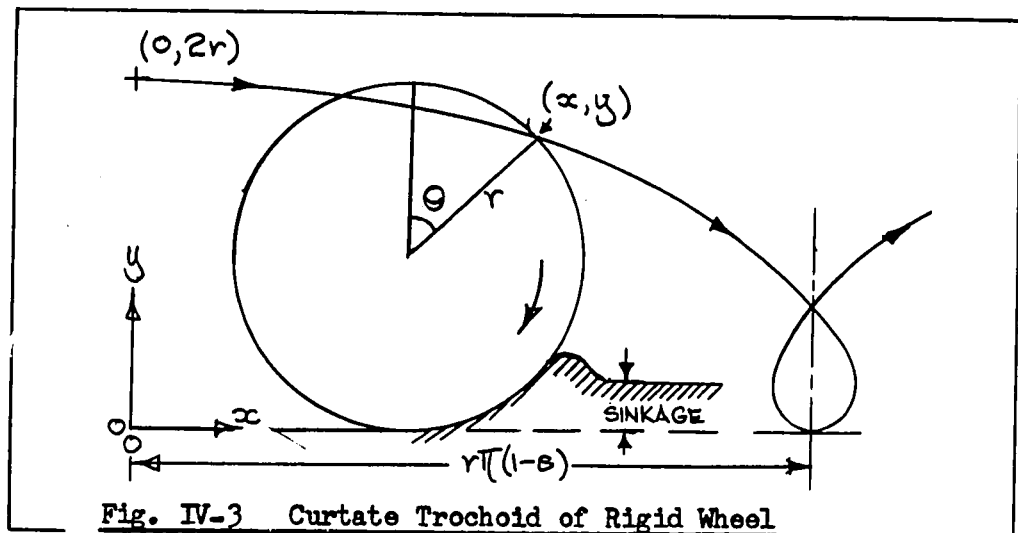


Fig. IV-3 Curtate Trochoid of Rigid Wheel on Deforming Soil (Positive Slip Cond. Shown).

It will be noted from this figure that for normal slip, s , the wheel advance per revolution will be $2r\pi(1-s)$. Thus the wheel advance is ~~in-~~ greater than $2r\pi(1-s)$ ~~less than~~ $2r\pi(1-s)$ ~~versely proportional for slip in the~~ $(0\% \leq s < 100\%)$ range and ~~directly prop-~~ ~~ortional~~ in the negative slip range ($s < 0\%$).

In synopsis it should be said that although something is known about the kinematics of a rigid wheel virtually nothing is known about the kinematics of the soil on which this wheel rolls. In consequence the following questions arise:

- 1) What are the characteristic features of soil displacement beneath a driven rigid wheel under a prescribed loading pattern and how do the displacements vary as a function of radial distance from the wheel?
- 2) Is this characteristic displacement pattern dependent on changes

of the wheel loading pattern? That is to say: what is the specific influence of wheel-load, - rim surface texture, - translational velocity, and - slip rate?

- 3) What is the specific influence of wheel size on the measured displacements?

With the aid of experimental information gained from the radiographic results of the tests of Tables IV-1 and IV-2, these questions can, in part, be answered.

B2. Three Typical Displacement Patterns.

The translation patterns of dry sand beneath the centre line of a 9.25" diameter, hard rubber coated, δ_2 , wheel rolling at an average speed of 4.83 ins. per sec., under three slip conditions are shown in figures IV-4, IV-5, and IV-6. The wheel load, W_1 , was in all cases 24.2 lbs. In all figures the trochoids followed by a point on the wheel rim have been plotted: prolate in the case of Test No. 11 for a negative slip condition and curtate for the positive slip conditions of Tests 12 and 13. The instantaneous centres of rotation and the wheel rim velocity vectors are also included in all figures. It should be noted that the translational wheel velocity, V , and the rotational angular velocity, ω , are considered constant for each test. This assumption is valid for the steady state conditions of the loading pattern in the region of study.

Under these three loading patterns the coordinates of the tracer object locations, taken from S.V.S.I. output, have been plotted. The line, or path, connecting the two object locations is an averaged composite of the plotted translations. The variation in final tracer-object location is shown by a shaded zone where measured variations had Bessel corrected Standard deviations, $\hat{\sigma}$, greater than 0.0125 inches. The final tracer object

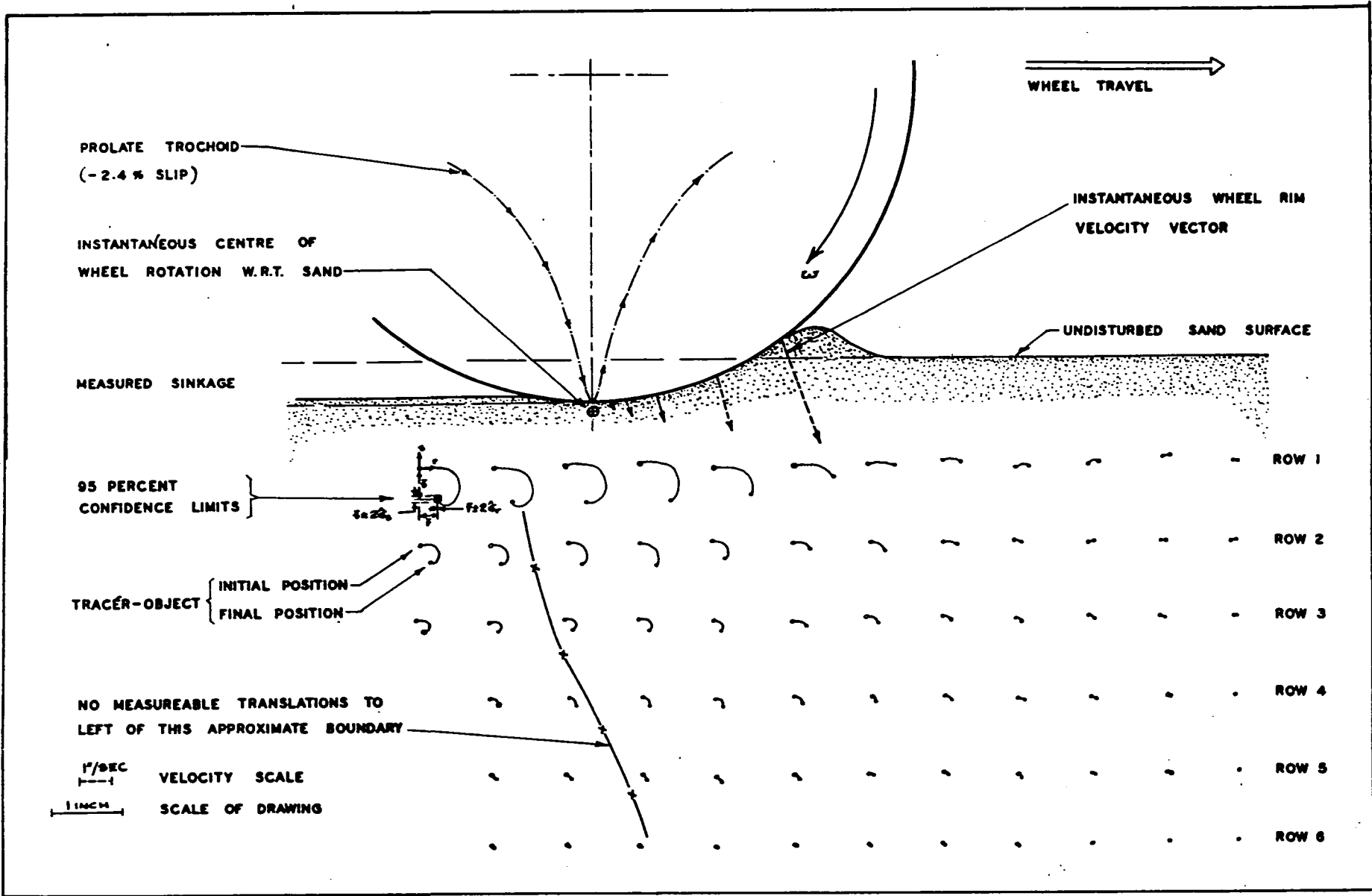


FIGURE IV-4: TRANSLATION PATTERNS OF TRACER-OBJECTS UNDER WHEEL CENTRE-LINE FOR TEST NUMBER II.

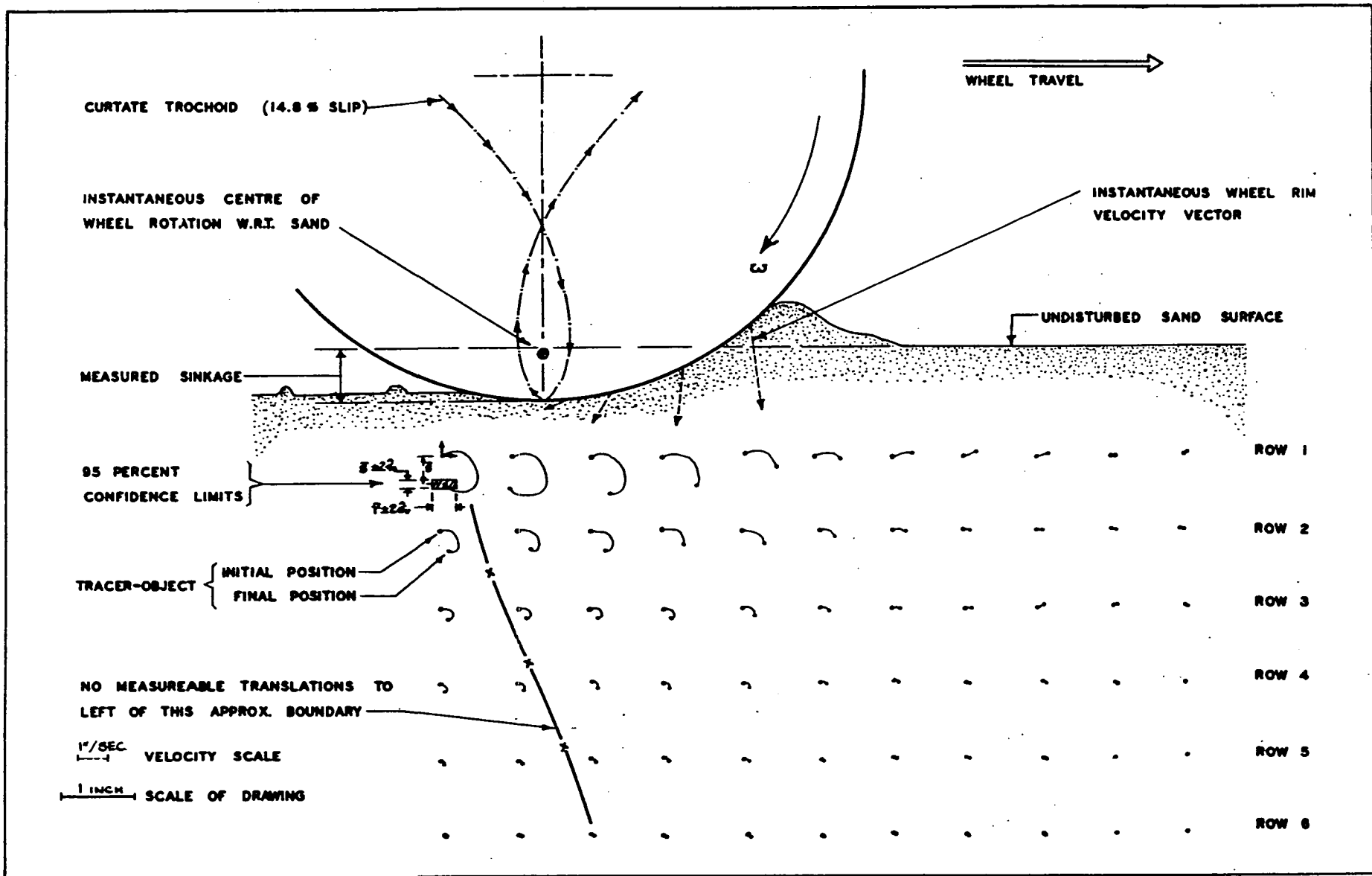


FIGURE IV-5: TRANSLATION PATTERNS OF TRACER-OBJECTS UNDER WHEEL CENTRE-LINE FOR TEST NUMBER 12

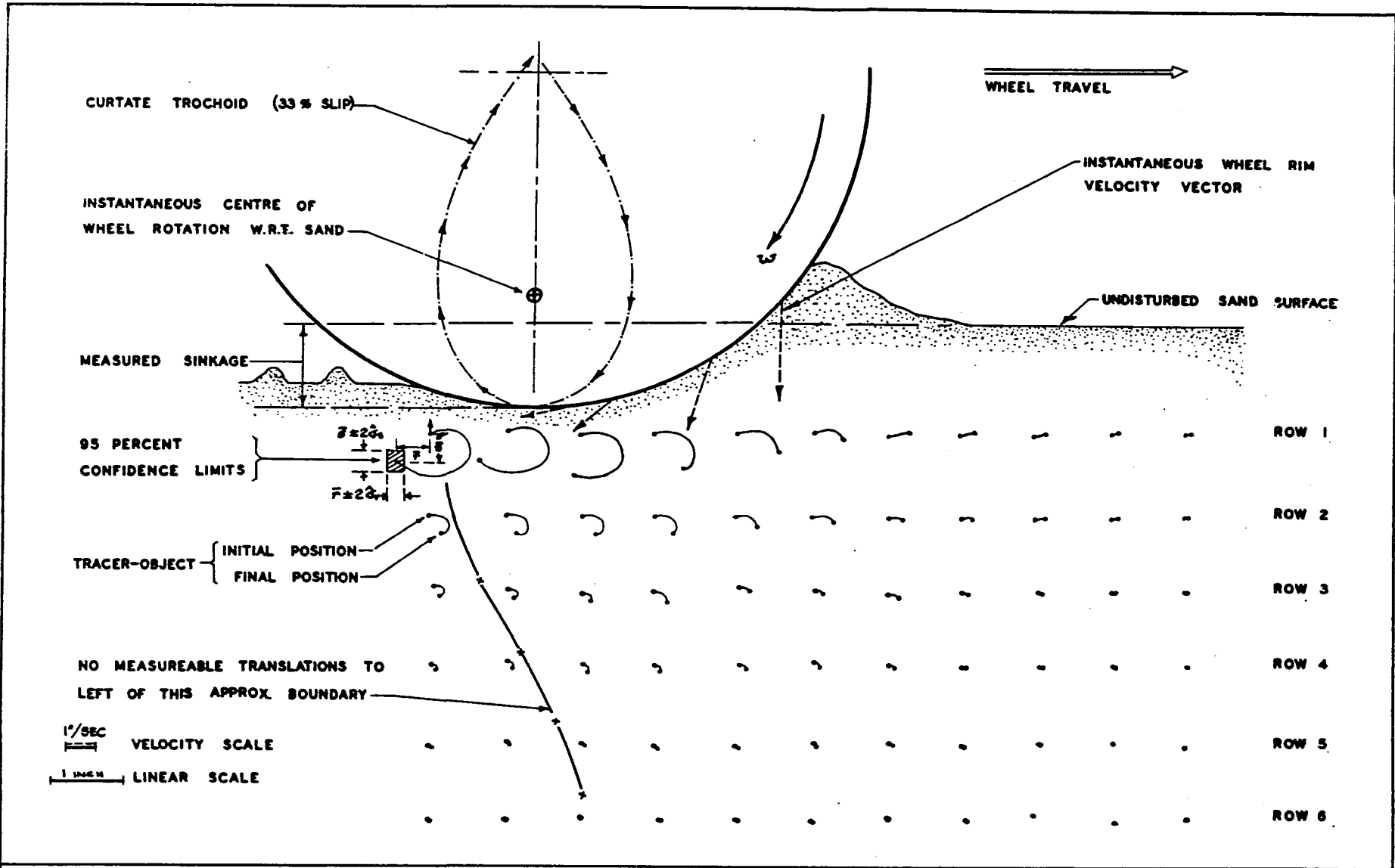


FIGURE IV-6: TRANSLATION PATTERNS OF TRACER-OBJECTS UNDER WHEEL CENTRE-LINE FOR TEST NUMBER 13

location was attained for all points to the left of an approximate boundary shown in all figures. This boundary is, of course, a function of the resolution of the measurement technique. The shaded zones have been drawn with rectangular boundaries although in reality the corners should be curved and not square. It was observed that raised ridges, perpendicular to the plane of wheel rolling, were left behind the wheel in the rut for positive normal slip loading patterns. These ridges of sand increased in frequency, though not in magnitude, as the positive normal slip increased. These ridges resulted from the development of shear planes in the near-surface layers of the sand, manifested in the subsurface translation patterns and in corresponding, measured, wheel torque fluctuations. Partial rut recovery occurred in all cases.

The ridges in the case of test No. 12 occurred at intervals of $c1.5'' \rightarrow 2''$ and for Test No. 13 at intervals of $c1.25'' \rightarrow 1.5''$.

An examination of the translation paths in different rows shows very similar translation patterns, for the three tests, for all corresponding rows below the first. This similarity is borne out statistically in Section IV-B3, with reference to the final tracer object locations. The top row 'experiences' quite different translational histories. The initial translation is similar for the three tests in that it 'experiences' an upward component of movement and follows a similar path until negative component increments, in the $-r$ direction, are 'experienced'. At this stage the patterns change for the three tests. The average displacement of the final tracer-object position, relative to the initial position, and plotted as (\bar{r}, \bar{s}) in the (r, s) coordinate reference plane have essentially similar \bar{s} values for the three tests but significantly different \bar{r} values. This phenomenon is discussed with reference to all the other tests in Section IV-B3.

In this test series there appears to be a boundary located between Rows 1 and 2, below which the influence of slip has little - or no - effect. Above this boundary there is an appreciable influence of slip rate ^{recognized in the resulting} on the translation patterns. Since the \bar{s} components of each corresponding row may be considered of the same magnitude below this boundary - from Section IV-B3- it is evident that as the slip rate increases there must be an increasing amount of soil transported from in front of, to behind, the rolling wheel if the increased sinkage is to be accounted for. It should be noted that the measured sinkage of test No. 11 (-2.4% normal slip) was .591 inches and of Test No. 13 (+33.35% normal slip) was 1.01 inches, and that the bow-wave attained a steady-state magnitude. The longer translation path in Row 1 and the significantly different \bar{r} values would thus be consistent with this observed sinkage phenomenon and the pattern of the wheel rim velocity vectors at maximum wheel sinkage (for the three tests, individually).

With these general observations as a framework the translation patterns under the loading ranges listed in Tables IV-1 and IV-2, can be studied.

B3. An Analysis of Sand Displacement Patterns in Row 1.

Tracer-objects placed at an initial depth of 1.5 inches are referred to as first Row objects. The final translation history of these objects is examined in this section, as a function of the loading patterns described in Tables IV-1 and IV-2. Since the actual 'translation path' is derived at by subjective interpretation, the statistics of $\bar{r} \pm 2\hat{\sigma}_r$ and $\bar{s} \pm 2\hat{\sigma}_s$ have been used as a standard of comparison; - where (\bar{r}, \bar{s}) are the averaged final relative row coordinates and $(\hat{\sigma}_r, \hat{\sigma}_s)$ are the corresponding best estimates of the population standard deviations. This statistic in each case, incorporates all errors resulting from a) the radiographic technique, b) the superposition assumption, and c) any inhomogeneities resulting from the sand preparation

technique. Thus the only variation not accounted for is that of "between-test" differences in the assumed 1.5 inch depth of object placing. This variation is not large - see Appendix III-B3. - and will be assumed to vary normally about a mean of 1.5 inches.

Figure IV-7A has been plotted from the $\bar{r} \pm 2\hat{\sigma}_r$ results of the main experimental tests and the two supporting test series. The loading information corresponding to each test number can be seen in Appendix IV-A1. The following observations can be made from this Figure, and are confined to the range of Parameters, D, W, V, M, and δ used in this study.

- 1) The final tracer-object position, $\bar{r} \pm 2\hat{\sigma}_r$, was for both wheels strongly dependent on the applied Torque, M, (or slip rate). The trend is shown by a curve drawn through the averaged $\bar{r} \pm 2\hat{\sigma}_r$ values (positive slip only). It is clear that the results of low positive slip displacements, in this row, at the 95 per cent confidence limits do not overlap with the abscissal values of the 95% confidence bands of the same statistic at high positive normal slip rates. The slope of the trend line is shallower ($\alpha_2 < \alpha_1$) for the prototype wheel, as might be expected. That is, the position of the first row relative to the large wheel corresponds to an equivalent row at a depth less than 1.5" under the scaled model wheel (i.e. at a depth of $1.5"/\lambda$). In this 'equivalent' row both forward (positive \bar{r}) and backward (negative \bar{r}) values would be greater and thus the shallower angle α_2 .

The final tracer object position is thus in front (positive r) of the initial position for normal slips less than c9%, under the initial position (zero r) for slips in the c(8% < s < 20%) region and behind the initial position for slips c \geq 20%. There is no significant difference in the zero r, normal slip cross over point

LEGEND: AS FOR FIGURE III-8

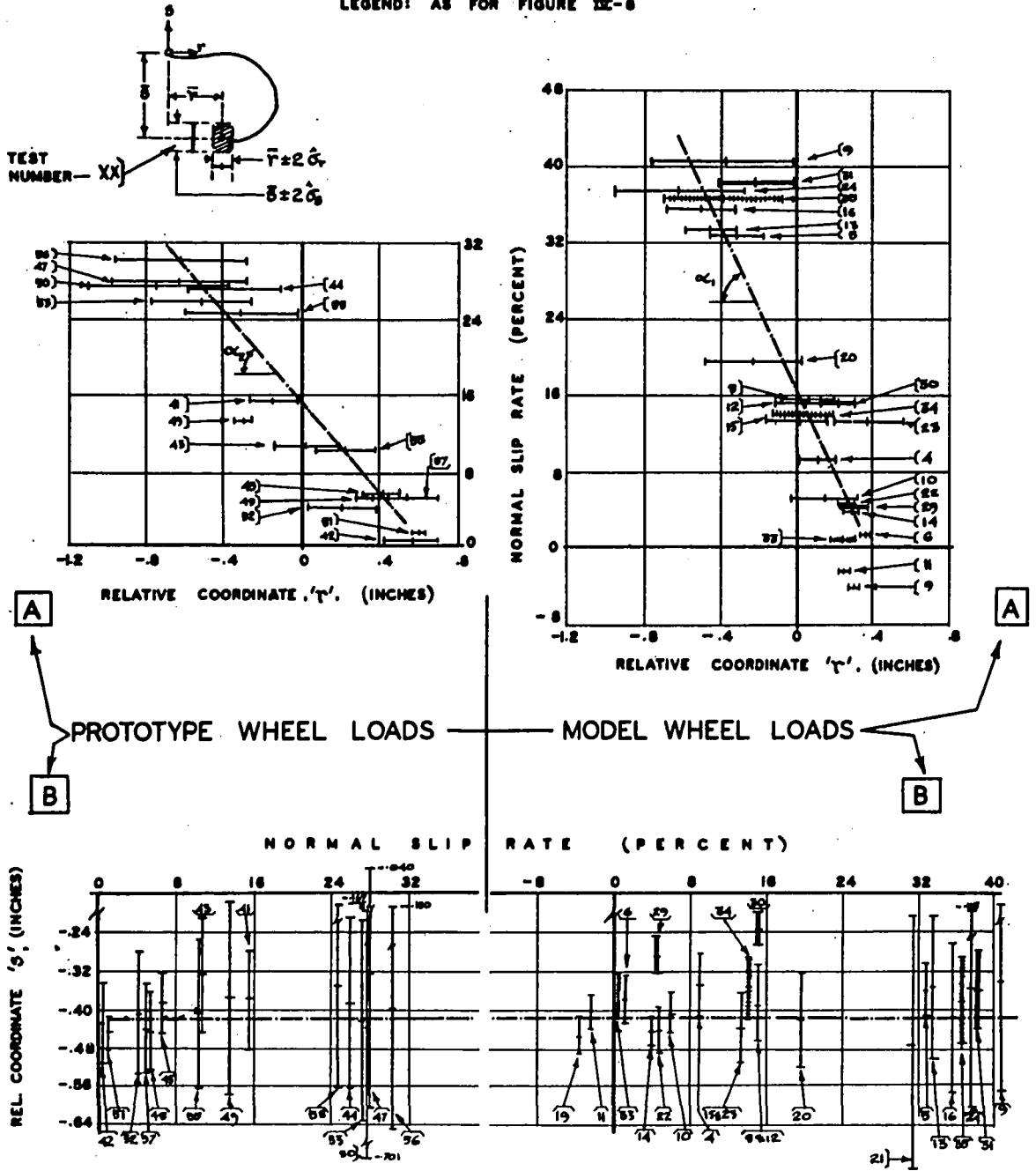


FIGURE IV-7: VARIATION OF FINAL RELATIVE COORDINATES (r, s), OF FIRST ROW TRACER-OBJECTS, SHOWING:

IV-7A $\bar{r} \pm 2\sigma_r$ RESULTS

IV-7B $\bar{s} \pm 2\sigma_s$ RESULTS.

for the two wheels tested.

- 2) The $\bar{r} \pm 2\hat{\sigma}_r$ values appear to be uninfluenced by the translational wheel velocities (v_1, v_2) and ($\sqrt{\lambda} v_1, \sqrt{\lambda} v_2$) the material of the wheel rim (hard rubber, δ_2 , polished aluminum, δ_1) or the wheel loading range tested - for each wheel - (w_1, w_2 and $\lambda^3 w_1, \lambda^3 w_2$)
- 3) The substitution of glass side walls in the Series II supplementary tests had no significant effect on the chosen statistic for the small wheel, D_1 .
- 4) The series I supplementary tests followed the same trend as that followed by the quasi three dimensional test series. (Test No. 30 to be discussed later).

Figure IV-7B has been plotted from the corresponding $\bar{s} \pm 2\hat{\sigma}_s$ values for all tests, and the following observations can be made:

- 1) That, for the main test series, a horizontal line can be drawn that intercepts the 95 per cent confidence bands of all tests. This line, at $s = -0.416''$, is common to both the results of the prototype and model wheel tests. Thus a sample from all populations is common to all tests in the series.
- 2) There is no evidence that the parametric variation of V , or δ , - for the ranges tested - influence the statistic of $\bar{s} \pm 2\hat{\sigma}_s$.
- 3) At low normal slip values the magnitude of the standard deviation, $\hat{\sigma}_s$, tends to be smaller than at high positive slip values, under both wheels, and greater under the prototype than under the model wheel. The noted ridges left in the rut after the passage of a wheel, at positive slip rates, attest to the fact that characteristically different subsurface displacements are expected to occur near the surface. These characteristically different modes of trans-

lation are observed from the radiographs and obviously lead to $\hat{\sigma}_s$ values at high positive slip rates and to $\hat{\sigma}_s$ values under the prototype wheel. Again the 1.5 inch depth under the prototype wheel is analogous to a $(1.5^n/\lambda)$ depth under the model wheel.

- 4) There is no apparent influence of the glass substitution, in the Series II supplementary tests.
- 5) The Series I supplementary tests resulted in characteristically smaller \bar{s} values at the low positive slip rates. Test No. 30 is not considered representative and will be discussed later.

The significance of the above observations is discussed in Section IV-D.

B4. An Analysis of Soil Displacement Patterns in Row 4.

The tracer-objects initially buried at a depth of 4.5 inches are referred to as Row 4, objects. This row was chosen as being typical of those rows beneath a boundary where slip rate appears to have no detectable influence on the mean final, relative, s coordinate, \bar{s} . The same statistic has been used for comparative purposes as that used in Section IV-B3 above.

Fig. IV-8A shows the variation in the chosen statistic for all tests with the model wheel, in this row. It will be noticed that the trend indicated in Section IV-B2 is followed closely by the other tests. Horizontal lines intercept all test variation populations. There is no apparent influence of any of the test variables on the final r coordinate value. The same statement applies to the s coordinate values with the exception of the supplementary Series I results, which show a slight slip rate influence.

In Figure IV-8B a similar plot has been made for all the Prototype tests and the same conclusions can be drawn as for Figure IV-8A. However the intercepts of the common horizontal lines are significantly different under the two wheels. It should be noted that the r value common to all Fig. IV-8A

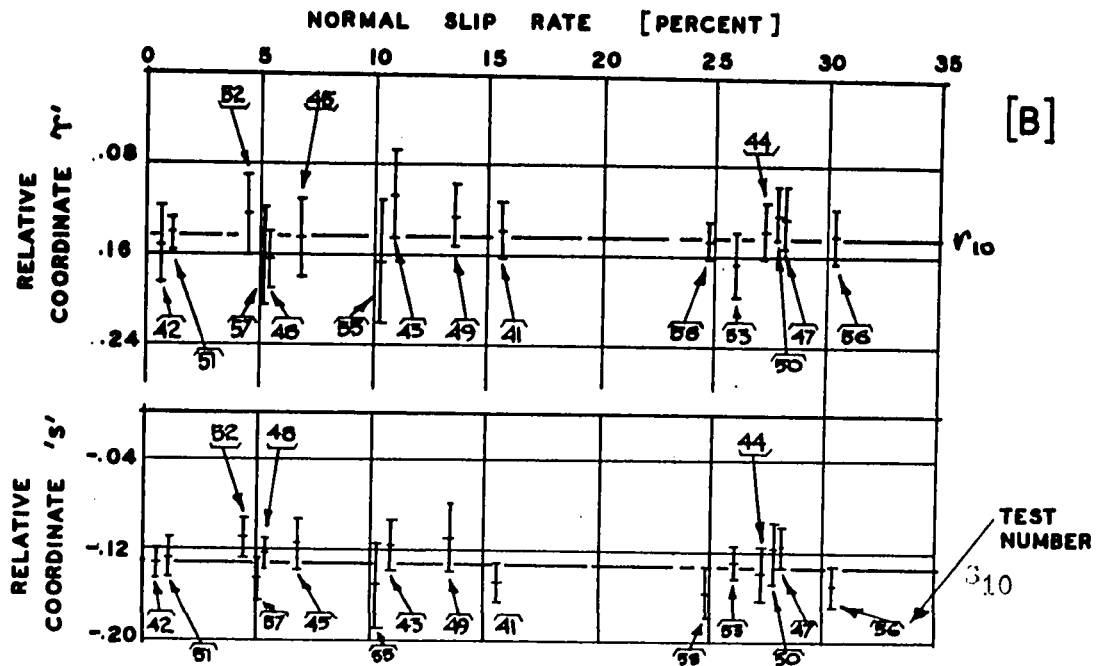
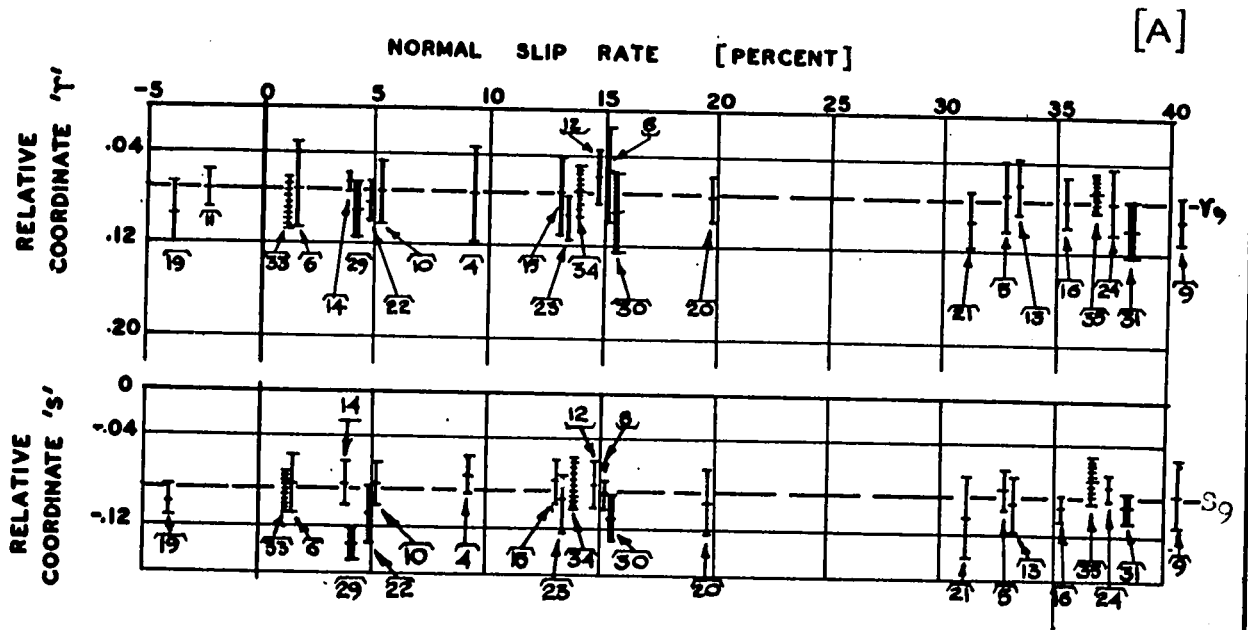
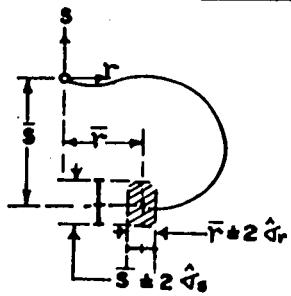


FIGURE IV-8: VARIATION OF FINAL RELATIVE COORDINATES $[\bar{r}, \bar{s}]$, FOR 4TH ROW TRACER-OBJECTS UNDER:
 'A', MODEL WHEEL LOADS
 'B', PROTOTYPE WHEEL LOADS.



LEGEND:
 ——— MAIN TEST SERIES
 ——— SUPPLEMENTARY SERIES I
 ■■■■■ SUPPLEMENTARY SERIES II
 } IN INCHES,
 } 95% CONFIDENCE
 } LEVEL

populations is only common to test No. 43 of the Figure IV-8B populations and only tests 21 and 49 overlap the common lines of the relative coordinate s . It is also worth noting that the 'common line' intercept on the s ordinate of Fig. IV-8B is equal to the scaling ratio λ , times the common time intercept, s , of Figure IV-8A (i.e. $s_{10} = \lambda s_9$). However for the r intercept, $r_{10} = 2r_9$ which represents a scaling ratio greater than $\lambda = 1.5$.

These results will be discussed in Section IV-D.

C. Rolling Wheel Sinkage.

The sinkage beneath the undisturbed ground level ($y = 0$), and measured before the recovery of the rut is referred to as the rolling, or dynamic, sinkage (and denoted y_0).

If y_0 is nondimensionalised the influence of scaling the wheel on the measured sinkage can be evaluated. These ratios are listed in Appendix V-B-1. The influence of variations in V , W , M , and δ , can also be studied on this basis. In Figure IV-9, y_0/D has been plotted against slip rate, for all the tests listed in Tables IV-1 and IV-2. It can be seen from this Figure that all the y_0/D values for both wheel sizes collapse into the same band of variation for all but the Series I tests. A study of the test specifications reveals no obvious trends to the variation within this band and thus, for the range tested, there appears to be no measurable influence of variations in V , δ or W for either wheel. However the influence of slip rate, or developed Torque, produces marked differences in the sinkage ratio, y_0/D . The two dimensional arrangement of Series I resulted in a quite different trend, that is discussed in section IV-D. It is considered significant that the scaling of sinkage - 'dictated' solely by the soil reaction - follows the linear scaling ratio, λ , adopted for the model study.

The line drawn through the plotted points has not been fitted mathe-

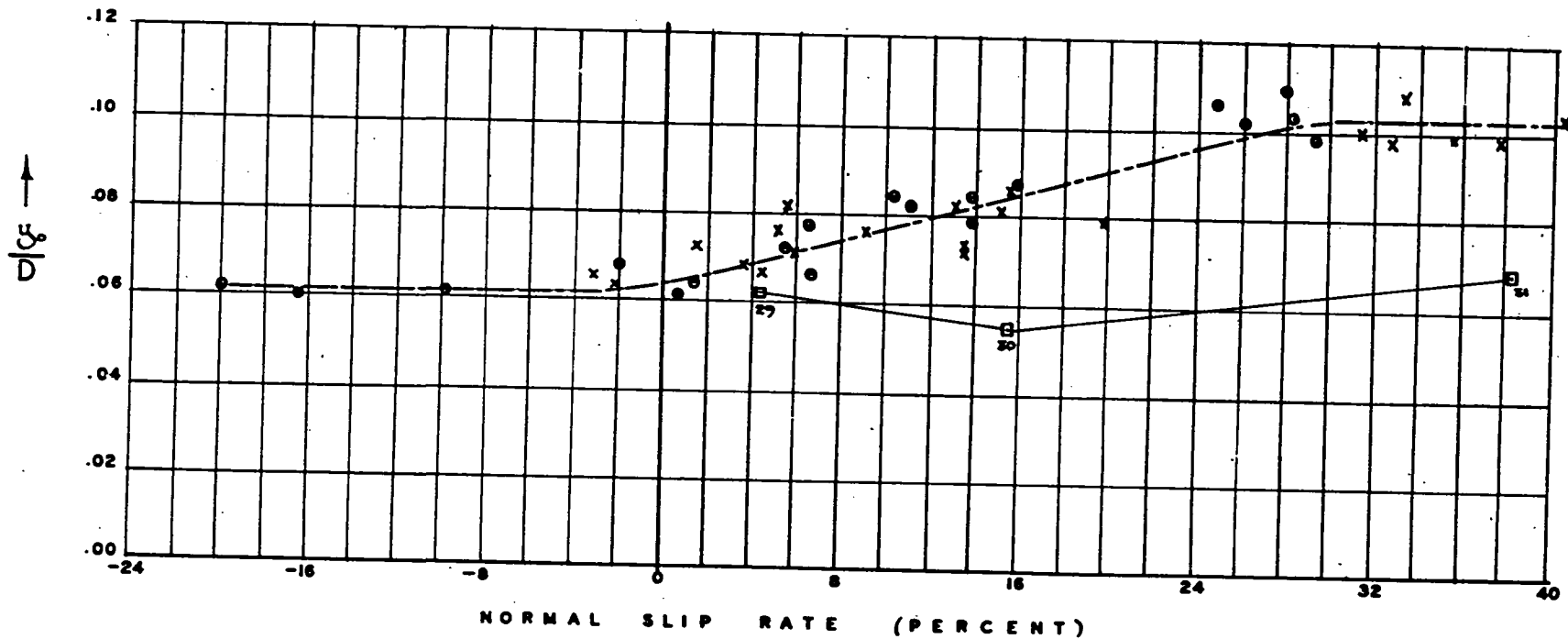


FIGURE IV-9: THE SINKAGE RATIO y/d . SHOWING THE SCALED SLIP-SINKAGE PHENOMENON.

LEGEND: ○ MAIN EXPERIMENTAL SERIES, PROTOTYPE WHEEL
 X " " " " " MODEL WHEEL + SUPPLEMENTARY SERIES II
 □ SUPPLEMENTARY SERIES I, (2D TESTS)

matically and is just included to demonstrate the trend of y_0/D vs. normal slip rate.

D. Discussion of Results and Conclusions.

D1. The Influence of the Side Wall and Lateral Constraint on the Measured results.

A comparison of all the plotted results in Section IV-B shows that there is no detectable influence on the chosen statistic resulting from the substitution of glass side walls - as opposed to Aluminum ones - for the quasi three dimensional set up. The results of the supplementary test Series II, followed the trends of the main test series, despite the frictional differences of glass and Aluminum, with dry sand.

The results of the supplementary Series I tests were, however, significantly different from the results of the main test series, both in magnitude and in the basic trends. Here the possible influence of lateral constraint on the translation path is confused by the possible side wall influence created by narrower separation of the constraining walls. Test No. 30 presents a case in point. The loading measurements of Test No. 30 - see Appendix IV-A1 - are considered atypical not only of all other tests reported herein but from the results of others, - see proceedings of 1st international I.S.T.V.S. meeting. The decrease in the recorded sinkage value, y_0 , for this test from a greater value at a lower slip rate is one manifestation of this atypicality - see Fig. IV-9. This would, in turn, affect the $\bar{s} \pm 2\hat{\sigma}_s$ value of Test No. 30, which when plotted in Fig. IV-7B shows a smaller $\bar{s} \pm 2\hat{\sigma}_s$ value than both tests 29 and 31. The results of Tests 29, 30 and 31 when plotted in Fig. IV-8A show a significant influence of the 2.D constraint at low slip rates and form a slip rate vs. $(\bar{s} \pm 2\hat{\sigma}_s)$ trend. However, the sinkages, y_0 , recorded for tests 29 and 31 only vary by 0.035 inches. It can thus be

concluded that the influence of the glass side walls in the 2-D tests produced differences in the measured displacements and sinkages that prevent a useful comparison of the two test series. These differences do not follow a simple 'distortion' relationship and thus must be attributed to the side wall influence.

A discussion of soil translation that occurs at right angles to the plane of the rolling wheel can more usefully be examined from another standpoint. Any Z component of translation will result in a corresponding image translation on the plane of the radiograph - see Appendix III-G-1. Since the tracer-object translations are 'assumed' to be confined to the (x,y) plane any actual Z component translation will appear as a component of variation buried in the \hat{V}_v or \hat{V}_c terms. The tracer-objects are, however, buried in the sand approximately coplanar to the centre-line of the rolling wheel. (i.e. the (x,y,0) plane). The wheel loading is thus ~~axi~~-symmetric. A detailed consideration of these facts and the sand preparation technique reveal no reason for a 'preferred' positive- or negative- Z component of translation from the (x,y,0) plane, at any depth. There is no evidence to suggest that these component Z translations should not be normally distributed about the mean relative final coordinate points (\bar{r}, \bar{s}) for any layer of tracer-objects. Considering the hypothetical case that the entire variation, \hat{V}_s or \hat{V}_r , resulted from \pm Z component translations this would restrict any conclusions to a study of the mean values (\bar{r}, \bar{s}) alone. If the results of Section IV-B are re-examined in this light the conclusions require only slight modification. However, it is quite apparent that the component variations \hat{V}_r and \hat{V}_s do not result solely from \pm Z component translations. The ridged appearance of the rut under positive slip rates attests to the fact that variation in the final s value of layers near the surface are not only anticipated, but measured - see $\bar{s} \pm 2 \hat{V}_s$ values in Fig. IV-7B.

Component variations resulting from all the sources discussed in Chapter III also contribute to the measured \hat{G}_r and \hat{G}_s values.

The conclusions that follow, have been generalised to accommodate the possibility of these $\pm Z$ component translations from the $(x,y,0)$ plane.

D2. Conclusions:

The mensurational technique described in Chapter III has, from the limited results described in this Chapter, provided considerable insight into the nature of soil behaviour under rigid wheels. The measurement of significant horizontal sand translations provides convincing evidence that the Bernstein-Bekker assumption, of equation (I-2), is unjustified. Rolling resistance, R , is not only dependent on horizontal sand translations but also on the wheel slip. From the preceding results, it is clear that applied wheel slip-rate must be considered explicitly in any theoretical or empirical prediction of vehicular performance. However the influence of slip-rate only extends to a limited depth beneath the rolling wheel. The entire slip-sinkage phenomenon shown quite graphically in Figure IV-9, is thus accommodated within this limited depth.

In order to examine the nature of subsurface sand translations that result in the surficially measured sinkage, y_0 , and in order to explain the slip-sinkage phenomenon, it is convenient to define an arbitrary boundary. This boundary is a plane, parallel to the undisturbed sand surface and occurring at a depth, y_s ; where y_s is the maximum depth to which slip rate can exert an influence on the measured tracer-object translation patterns. The sand translations above this boundary are characteristically different to those at depths greater than y_s .

With reference to Figure IV-10, Region A thus includes sand translations that result from shear induced flow beyond 'yield'. Where 'yield' was

defined in Chapter I as the onset of significant inter-particle displacements. ('Significant', in this context is qualified by the limiting precision of the measurement technique and observations at a macroscopic level). Region B is characterised by translation patterns that are independent of slip-

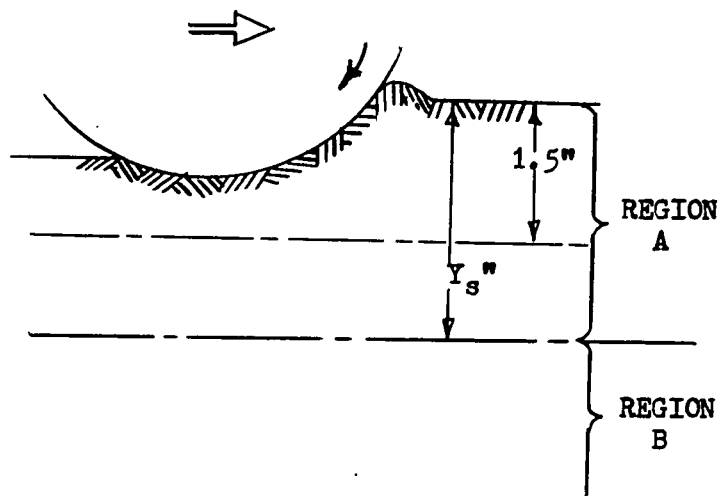


Figure IV-10 Diagram Defining
Regions 'A' and 'B'

rate, within the imposed experimental limitations described in Chapter III. However, the essential diagnostic features of both regions are summarised below:

Region A.

- i) The translation paths described by tracer-objects are dependent on the magnitude of wheel slip within this region, but independent of parametric changes in W , δ , and V - for the range tested.
- ii) The relative coordinate, \bar{r} , of the final tracer-object position is proportional to the slip rate, s , in the following way, (for tracer-objects originally placed at a depth of 1.5"):

for $s \leq c 9\%$, $\bar{r} > 0$	}	See Figure IV-7.
for $c9\% < s < c20\%$, $\bar{r} = 0$		
for $s \geq c20\%$, $\bar{r} < 0$		
- iii) Both $\hat{\nabla}_r$ and $\hat{\nabla}_s$ increase as normal slip rate increases.

This reflects the nonhomogeneous strains resulting from shear induced 'yield' and flow within this region. The observed

transverse ridges across the wheel rut are surficial manifestations of these non-homogeneous flow patterns.

Region B.

- i) The translation paths are independent of parametric variations in slip rate, s , and in W , δ , or V - for a given wheel size. Thus the relative coordinate, \bar{r} , of the final tracer-object position, is independent of slip rate within this region.
- ii) Both $\hat{\gamma}_r$ and $\hat{\gamma}_s$ are characteristically independent of slip rate, thus reflecting the homogeneity of strains within this region. Relative inter-particle movements within this region result in particle rearrangement and overall 'consolidation', as opposed to large movements characteristic of flow.
- iii) The relative coordinate, \bar{s} , within this region was dependent on the wheel used. For the fourth row tracer-objects the magnitude of \bar{s} common to all the test populations corresponding to the prototype wheel was equal to λ , (the scaling ratio), times the common \bar{s} value for all the model wheel tests. This observation did not apply to the Region A translations where the ^{analogous} common line was found to be the same for $\bar{s} \pm 2 \hat{\gamma}_s$ populations under both model and prototype wheels.

The actual depth y_s , was found to lie at 1.5" \rightarrow 2.5" for tests with the model wheel and at a depth of 2.5" \rightarrow 3.5" for tests with the prototype wheel - or approximately at .75b".

Having defined these two distinct regions it is possible to consider the slip sinkage phenomenon; that is, Figure IV-9. From this Figure the sinkage ratio, y_o/D , is seen to vary with wheel slip only within the region ($c4\% \leq s \leq c24\%$). At slip rates above and below this range a constant, though different, ratio is attained. It is thus apparent that the increased sinkage

in the ($c4\% \leq s \leq 24\%$) range is accommodated completely by sand movement in Region A, since Region B translations are independent of slip.

In the ($s \leq 4\%$) slip region the measured, r , coordinate of the final tracer-object position is seen from Figure IV-7A to be characteristically independent of slip in the Region A. This observation, coupled with the invariant equilibrium sinkage, y_0 , supports the hypothesis that sand movements characteristic of Region B actually extend into Region A for this slip range. This is confirmed, in part, by the representative translations of Test No. 11, plotted as Fig. IV-4, where $s = -2.4\%$.

When slip rate is increased in the ($c4\% \leq s \leq c24\%$) range the ratio y_0/D increases almost linearly. The subsurface translations are seen from Figure IV-7 to describe slip rate dependent translations in the horizontal, r , coordinate direction. This increased sinkage is explained ^{in part} by the measured increase in longitudinal soil transportation from in front of, to behind, the wheel. As slip increases, within this range, the discontinuities of flow created by an associated increase in the number of shear failure surfaces becomes evident in the \hat{G}_r and \hat{G}_s values, and the increasing frequency of the ridges appearing in the rut.

At slip rates greater than $c24\%$ no significant variation in final horizontal coordinate, \bar{r} , was observed, however the increased magnitude of both \hat{G}_r and \hat{G}_s reflect increased variation in the shear 'failures' within Region A, and behind the wheel - see Figure IV-6.

An examination of the translation patterns reveals that vertical components of translation, $(\bar{s} \pm 2 \hat{G}_s)$, appear to follow the linear scaling ratio adopted for the wheel scaling within the Region B. Since the measured sinkage, y_0 , followed this ratio it is thus evident that Region A translations result in the same ratio λ , although this can not be measured in terms of $\bar{s} \pm 2 \hat{G}_s$ - see Figure IV-7. The explanation for this 'effective'

scaling in Region A must thus be explained in terms of sand transportation - or excavation - from in front of, to behind, the wheel.

Horizontal translation components did not follow the λ ratio of the scaled wheels. This observation has considerable bearing on the scaling of torque in the wheel-sand system, on Rolling Resistance as a variable quantity and on energy-dissipation mechanisms, that will all be considered in the following Chapter.

It should also be noted that the translation patterns described by McKibben (1938) are significantly different to those shown in Fig. IV-4 under a driven wheel at a low negative slip. McKibben's test wheel was towed at a similar slip value yet the translations contained only forward components (positive Δr) of horizontal translation. Thus the translation patterns beneath a driven and a towed rigid wheel at a similar slip value are seen to be radically different.

CHAPTER V

ENERGY CONSIDERATIONS

A. INTRODUCTION

Over the years various criteria have been used to evaluate vehicle performance. It is a fair generalisation that most of these criteria are based, either directly or indirectly, on considerations of energy terms. Since nearly all previous measurements of the soil-vehicle system have been restricted to the measurement of vehicle parameters, the energy terms have correspondingly been associated with the vehicle and not the soil.

In this Chapter the energy considerations are divided into two mutually dependent sections, namely a) considerations of the energy balance of the wheel and b) considerations of the possible mechanisms of energy dissipation within the soil. The concept of 'rolling resistance' is examined from a theoretical standpoint, and the scaling of soil-dependent energy terms is examined on the basis of experimental results.

B. THE COMPONENT OF ENERGY LOST BY THE WHEEL TO THE SOIL.

B1 The Plane Motion of a Rigid Wheel.

The forces and couples acting on the test wheels can perhaps best be described by considering the wheel as a free body, as in Fig. V-1.

For the conditions of these tests:

- 1) The wheel is assumed to be plane rolling in the $(x,y,z = \text{constant})$ plane, on a smooth-, level-, longitudinally homogeneous-, sand surface.
- 2) At the axle a driving torque, M , a vertical force, W , and a horizontal force, F , are applied. The couple, M , is considered as the

net applied couple acting at the hub; being the algebraic sum of the driving couple, M_d , and the bearing friction couple, M_b , acting on the axle. The force F is often referred to as the Draw Bar Pull and is considered positive when the wheel develops a tractive effort and negative when the wheel is towed. The force, W , represents the "load" acting through the centre of gravity of the wheel.

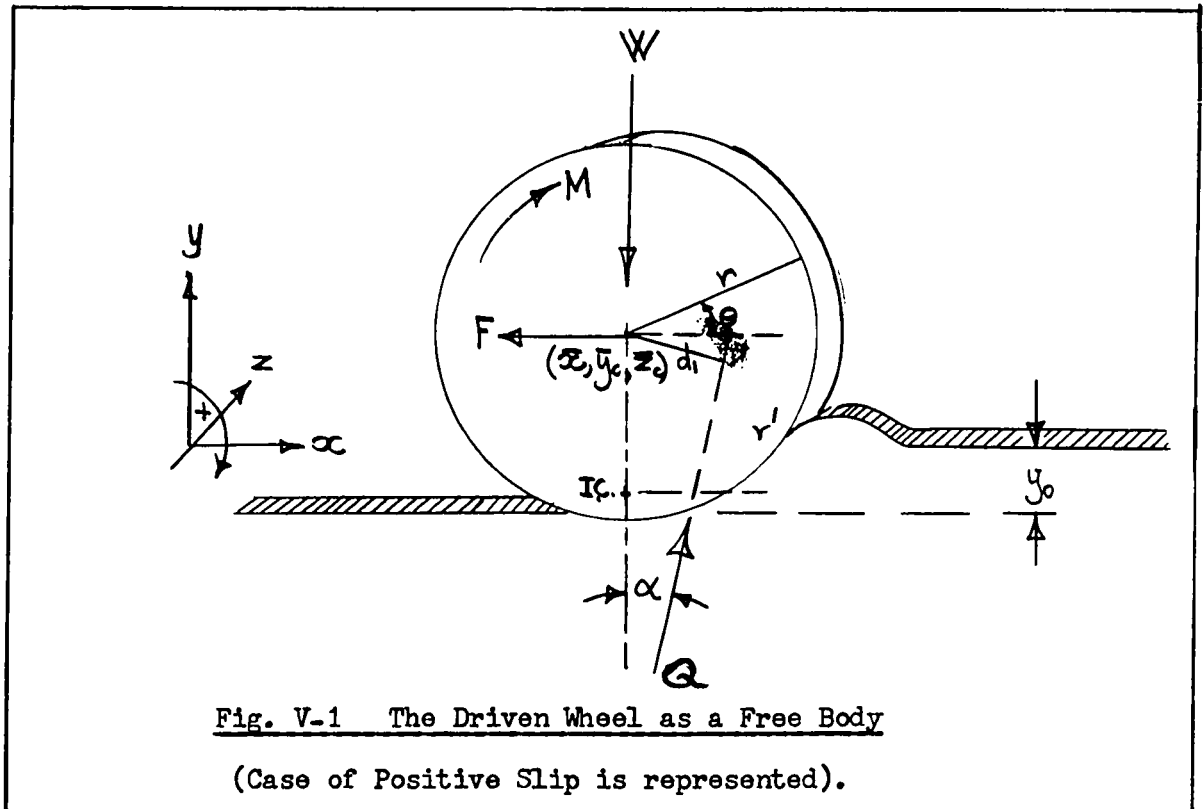
In the associated literature a force, Q , representing the vector sum of all the resultant soil reaction forces in the contact region, is added to complete the free body diagram. Although measurements of stresses on the wheel rim have been made by several researchers virtually nothing is known of the stress distribution within the soil that could be used to describe the force Q . Naturally a complete specification of the magnitude and direction of this resultant soil reaction would provide the essential information required for predicting wheel performance. Using the mensurational technique described in the previous Chapter it is possible to describe the deformations and translations occurring within the soil mass as a first stage towards the specification of Q . However the necessary stress-strain and stress-flow relationships are not presently available to specify the stresses from the measured deformations. It is for these reasons that the resultant soil reaction is assumed to act at a distance d_1 from the axle and at an angle α , from the vertical line through the axle. The direction of Q , shown in Fig. V-1, corresponds to the case of ^apositively slipping wheel with a developed drawbar pull.

- 3) The wheel is assumed to be rolling in a steady state condition where the vectors $\dot{\bar{x}}$ and $\dot{\bar{\theta}} = \omega$ (and thus slip-rate) are constant. Since the accelerations $\ddot{\bar{x}}$ and $\ddot{\bar{\omega}}$ are zero, and sinkage, y_0 , and slip

rates, s , are constant, time may be considered as a dummy variable.

The equations of motion for the plane rolling wheel:

$$\left. \begin{aligned} m\ddot{x} &= Q \sin \alpha - F \\ m\ddot{y}_c &= 0 = Q \cos \alpha - mg \\ I_{zz} \dot{\omega} &= M - Qd_1 \end{aligned} \right\} \quad (V-1)$$



where $m = W/g$ and I_{zz} is the moment of inertia about the axle, thus reduce to the equilibrium equations:

$$\left. \begin{aligned} Q \sin \alpha - F &= 0 \\ Q \cos \alpha - W &= 0 \\ \text{and } M - Qd_1 &= 0 \end{aligned} \right\} \quad (V-2)$$

Since $\ddot{x} = \ddot{\omega} = \text{zero}$.

The forces acting on the side wall of the wheel are neglected in this representation, but with this one restriction equations (V-2) are valid for any chosen loading combination or resultant soil deformation encountered in this testing.

B2. Energy Definitions and the Concept of Rolling Resistance.

The basic energy quantities have been considered by Bekker (1956), Leflaive (1966), Schuring (1966), and others, for the case of a driven rigid wheel. In the most general terms, three quantities can be considered:

- 1) The torque energy: This is the work done by the torque M , and may be positive or negative - see sign convention of Fig. V-1. In all cases considered herein this term is positive.
- 2) The Pull energy: This is the work done by the draw bar pull, F , and may be positive or negative depending on whether the wheel is developing a tractive effort or being towed.
- 3) The dissipated energy: This is the difference between the torque energy and the pull energy and is always positive. Since the wheel is rigid and $M = M_d + (-M_b)$, this energy is lost to the soil. It is, in fact, the component of energy that causes the resulting translations, rotations, volume changes and accelerations that constitute the soil reaction to the wheel loading. This term will be denoted as E_{input} .

From first principles the rate of energy input, or rate of energy dissipated to the soil from the wheel is

$$\dot{E}_{input} = M\dot{\omega} - F\dot{x} \quad (V-3)$$

where $M\dot{\omega}$ is the rate of torque energy input and $F\dot{x}$ is the rate at which energy is supplied or recovered (as a pull).

The rate of energy dissipation, \dot{E}_{input} , may be written as a function of slip. Since normal slip, s , is defined as $s = (1 - \dot{x}/v_r)$, equation (V-3) becomes:

$$\begin{aligned} \dot{E}_{input} &= M \left[\frac{\dot{x}}{r(1-s)} \right] - T\dot{x} \\ \text{or } \dot{E}_{input} &= \frac{\dot{x}}{r(1-s)} (M - Fr + Frs) = \frac{\dot{x}}{(1-s)} \left[(Fs + \frac{M}{r} - F) \right] \quad (V-4) \end{aligned}$$

Chudakov (1950), Phillips (1961) and others have suggested that the E_{input} term should be proportional to the wheel load, W , and have thus termed the proportionality constant, ρ' , the non-dimensional coefficient of Rolling Resistance. Thus:

$$\begin{aligned} E_{input}/\text{unit distance travelled by wheel} &= \rho' W \\ \text{or } \bar{E}_{input} &= \rho' W\bar{x} \end{aligned} \quad (V-5)$$

Both Phillips and Chudakov chose to consider the coefficient ρ' as analogous to the Coulombic frictional coefficient, since the ($E_{input}/\text{unit distance travelled}$) term has the dimensions of force. The fallacy of this argument may be seen from equation (V-4). By substitution,

$$\rho' W\bar{x} = \frac{\bar{x}}{(1-s)} (F_s + \frac{M}{r} - F) \quad \text{in Phillips' context} \quad (V-6)$$

The Coulombic relationship only holds when $s = 0$ and there is no applied torque (i.e. $M = 0$). Then:

$$\rho' W = -F \quad (V-7)$$

Schuring (1966) has made the claim that the Coulombic relationship (V-7) only holds for "full slip" conditions and thus points out the questionable nature of Equation (V-6). In practice it is questionable whether the Coulombic relationship is even approached in a sandy soil under any reasonable slip condition. Because $E_{input}/\text{unit distance}$, has the dimensions of a Force, Rolling Resistance has been regarded by many as a "Force". Not only is this incompatible with equations (V-2) but it has also led to much confusion in the associated literature. It is this writer's contention that the concept of "rolling resistance", per se, be dropped and that either " E_{input} per unit distance travelled by the wheel" or " \bar{E}_{input} " be adopted as more meaningful parameters of Vehicle performance. In comparing test results from scaled wheels it is convenient to express the energy components of equations (V-3) or (V-4) as dimensionless quantities. Leflaive (1966) has suggested the

following dimensionless relationship, by dividing all terms of equation (V-3) by $\frac{E_{input}}{Wx}$,

$$\frac{\frac{E_{input}}{Wx}}{\frac{E_{input}}{Wx}} = \frac{\frac{M_w}{Wx}}{\frac{M_w}{Wx}} - \frac{\frac{F}{W}}{\frac{F}{W}} \quad (V-8)$$

or $\rho' = \eta - \Delta$

Dissipated Energy Coefficient	Torque Energy Coefficient	Pull Energy Coefficient
-------------------------------------	---------------------------------	-------------------------------

Thus ρ' , although identical to Phillips (1961), coefficient of rolling resistance, will now be referred to as the energy that is not recovered mechanically per unit of Load per unit of distance travelled and referred to by Leflaive (1966) as the "dissipated energy coefficient".

Unfortunately it is not possible to evaluate the parameter ρ' , for all the tests listed in Chapter IV, as the drawbar pull flexure measurements did not prove to be entirely satisfactory. Reference to a sample Drawbar pull, D.B.P., output signal trace in Appendix II-C1-3 shows a characteristically large fluctuation. The reason for this is thought to rest in the fact that the wheel-frame-assembly is vibration sensitive, whereby minor fluctuations in the torque output and the angular wheel velocity result in an overcompensation in the D.B.P. signals. The net result is a mean D.B.P. value approaching zero pull for each flexure. It is evident that the U.S. Army Waterways Experiment Station researchers experienced similar mensurational problems during their early testing on sands, (personal communication with D.R. Freitag).

Fortunately, however, the torque energy coefficients, η , can be evaluated more precisely and can be compared: to provide a meaningful estimate of the scaling of forces in the wheel-soil system. It is first necessary to consider the basis for scaling the test wheel loads, as this has considerable bearing on the subsequent conclusions.

B3. The Similitude Parameters.

A successful scaling scheme is defined by four basic parameters, Sedov (1959), which provide the "necessary and sufficient" conditions for describing - in this case - the state of motion and régime of the soil-wheel system:

- 1) The scale parameter: represented in this case by the linear scaling ratio, λ .
- 2) The Kinematic parameters: these control the relationships of time, t , translational velocity, $\dot{\bar{x}}$, and angular wheel velocity, ω .
- 3) The dynamic parameters: the coordinates of the centre of gravity of the wheel; the moment of inertia I_{zz} , relative to coordinates at the axle passing through the centre of gravity; the vertical component of the given external force, ($W = mg$).
- 4) The physical constants: acceleration due to gravity, g , the sand-density, ρ , -preparation technique and -type.

In view of the speculation surrounding the nature of soil behaviour it was necessary to consider the wheel parameters alone in the initial formulation of the ratios - see Appendix II-C1-1. This is only justifiable if the resulting scaled loading patterns are run on the same soil medium, prepared in the same manner, for all tests (compared). There are some scaling ratios - for instance, those describing force - that are 'dictated' by the soil reaction and can not be completely described by considerations of the wheel parameters alone. It is thus essential that precise simulation of the loading patterns be made if valid conclusions are to be drawn on the 'soil-dependent' scaling ratios.

From the previous Chapters it is readily apparent that Sedov's conditions 1), 2) and 4) are met by the loading patterns described in Appendix IV-A1.

However, the fact that the spatial distribution of mass is not analogous in the model and prototype requires further consideration. The vertical component of force, W , has been scaled in accordance with the designated ratio of λ^3 , but this was achieved by mounting additional loads above the wheel axle and not by scaling the inertial moment I_{zz} by λ^5 . The centre of gravity of the wheel load may be considered to act through an homologous point in both model and prototype wheel, and thus satisfy the necessary scaling ratio. Equations V-2 contain neither angular or translational inertia terms as, for each test, both angular and translational velocities may be considered constant. Coupled with these considerations is the observed sand reaction to the wheel loading. For a given wheel and slip rate the translational paths of the tracer objects appear to be independent of the angular wheel velocity, ω . This is equivalent to saying that the vector summation of the interface soil reactions, Q , - see Fig. V-1 - is independent of the angular velocity, and thus of any effective rotational inertia term, $I_{zz}\omega$ for the range of loads tested. It is therefore concluded that, for the experimental test conditions used, the loading patterns meet the requirements of dynamic similitude and thus Sedov's condition 3) is effectively satisfied.

B4. Variations in the Recorded Torque Energy Coefficient, η .

The torque energy coefficients, η , have been calculated from results tabulated in Appendix IV-A1, for each test, and are listed in Appendix V-B-1. Since slip rate must be considered as a primary physical process the η values for each test have been plotted against the corresponding slip rate, s , in Figure V-2. From this figure it may be observed that:

- 1) All η values corresponding to the prototype wheel fall within a narrow band where η is shown to be dependent on slip rate, but - for the range

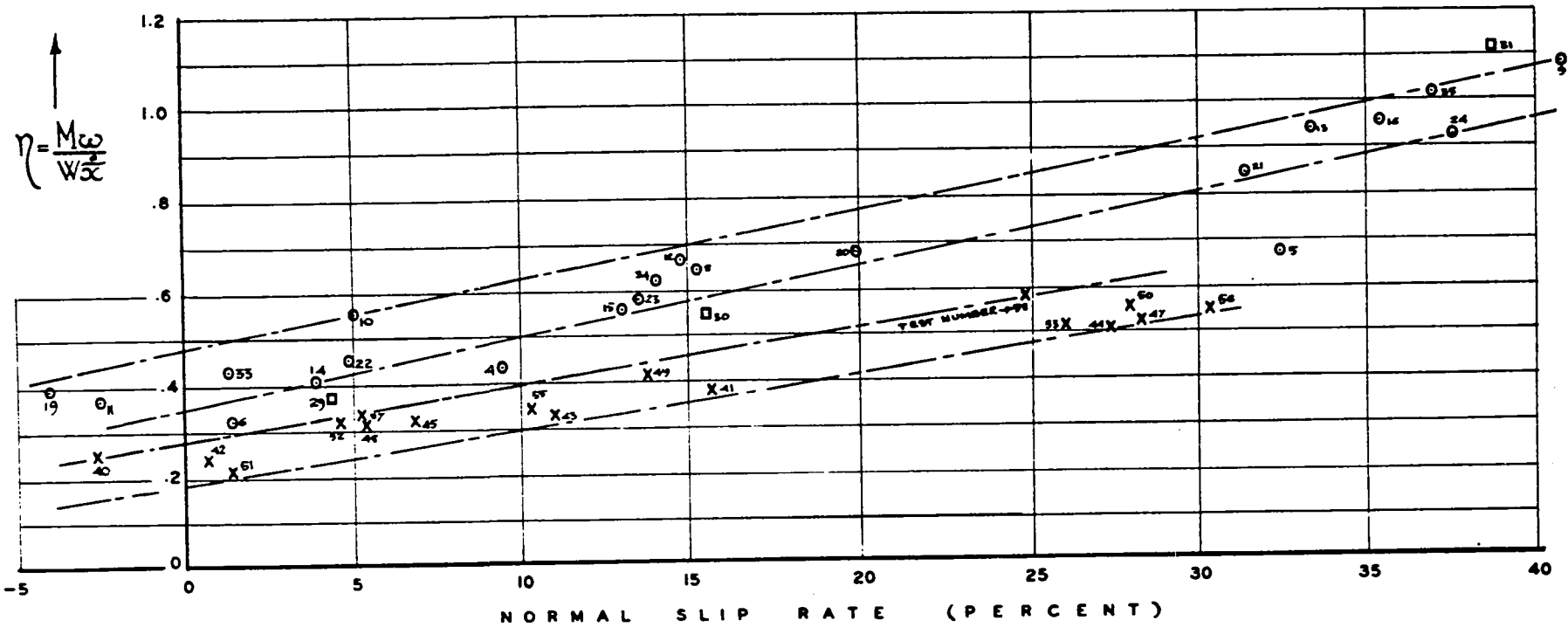


FIGURE V-2: VARIATION OF TORQUE ENERGY COEFFICIENT, η , WITH SLIP.

LEGEND: X MAIN EXPERIMENTAL SERIES, PROTOTYPE WHEEL
 O " " " , MODEL WHEEL + SUPPLEMENTARY SERIES II
 □ SUPPLEMENTARY SERIES I . 2D TESTS

tested - is independent of wheel surface material, δ , translational wheel velocity, V , and slight load variation, W .

- 2) The η values corresponding to the model wheel tests plot above the prototype wheel values and, with the exception of 6 tests, also fall within a well defined band. Three of these exceptions correspond to the two dimensional tests of Series I - Table IV-2. (The other three correspond to the $V_2 \delta_1$ test series). However, within this upper band the parameters of axle load, W , translational wheel velocity, V , or wheel rim surface material, δ , exert no significant influence on the developed torque, M .
- 3) Although the results from both wheels are dependent on the slip rate, s , the limiting-dotted-bands show a divergence between wheel sizes; i.e. they are not parallel.
- 4) The η values from the supporting Series II tests - see Table IV-2 - showed no recognizable influence resulting from the substitution of glass for aluminum as the side walls of the sand container.

These results clearly demonstrate the distorted scaling of "force" and "moment of force" that result from a consideration of the wheel parameters alone. The only 'soil dependent' parameter in the torque energy coefficient η , is the applied torque, M . If the developed torque of the prototype, M_p , followed the scaling scheme ($M_p = M_m \lambda^4$) the prototype η population would all reduce to the model η band. In practice however it is quite apparent that the scaling of torque corresponds to a lower power of the scaling ratio. Designating this relationship as:

$$\left[\begin{array}{l} \text{Torque developed} \\ \text{by prototype wheel} \end{array} \right] = \lambda^u \left[\begin{array}{l} \text{Torque developed} \\ \text{by model wheel} \end{array} \right] \quad (V-9)$$

for a given slip rate. The power, u , has been evaluated in Table V-1 below for two slip rates; namely at c5% and c20% slip, where $u = 2.8$ and 3.0 respectively.

TEST NO.	MODEL, m, or PROTOTYPE, p	η	W	ω	V or \bar{x}	SLIP(%)	M
22	m	.46	28.2	1.78	7.79	4.99	56.53
(22)*	p	.28	92*	1.46*	9.6*	4.99*	169*
20	m	.692	28.2	1.36	5.06	19.74	72.98*
(20)*	p	.465	92*	1.12*	6.18*	19.74*	237*
SCALING RATIO $\lambda = 1.48$			$\frac{W_p}{W_m} = \lambda^3$	$\frac{\omega_p}{\omega_m} = \frac{\omega_m}{\lambda}$	$V_p = V_m \sqrt{\lambda}$	$S_p = S_m$	$M_p = M_m \lambda^4$
<p>* = All items so marked have been calculated from observed η values - see Fig. V-2 and known scaling ratios.</p> <p>where: $u_i = \left\{ \frac{\text{Log}_{10} (M_{p_i}/M_{m_i})}{\text{Log}_{10} \lambda} \right\}$ for slip rate s_i</p> <p><u>$u_{.5} = 2.8$ for Test 22 ; c 5% slip</u></p> <p><u>$u_{.20} = 3.0$ for Test 20 ; c 20% slip</u></p>							

Table V-1 Sample Determination of the Torque Scaling Ratio, λ^u .

The scaling of forces follows a λ^{u-1} relationship and thus for the two slip rates arbitrarily chosen this force component is approximately λ^2 . The experimentally determined λ^2 relationship for scaling force is considered most significant as a λ^3 relationship would have resulted from ascribing a Coulombic behaviour to the sand. Here, however, it is necessary to distinguish between externally applied forces that are either a) independent of, or b) dependent on, the soil reaction.

In previous model studies, where plates and segments have been loaded vertically on sand soils, Schuring (1961), Hegedus (1965), and Wills (1966), have measured the penetrations corresponding to externally applied scaled (category a)) loads. In all cases they observed that for a λ^3 ratio of scaled load they obtained a penetration, sinkage, that followed the linear scaling ratio, λ . This same observation may be drawn from Figure IV-9,

where under an analogous zero sinkage condition the ratio y_0/D was shown to be the same for both wheels, within the limits of experimental accuracy.

However, the limitation of vertically loaded plate penetration tests is clearly emphasised by the results of the previous section. When the total soil reaction to wheel loading is examined, the scaling of some 'soil-dependent' forces are seen to follow a $c\lambda^2$ scaling ratio and not a λ^3 ratio - as predicted from plate bearing tests. Without a considerable degree of empiricism, the only viable plate bearing test would be one that reproduces the subsurface deformations and translations created by a driven rigid wheel. Since the translation patterns of soil movement are functionally dependent on both wheel slip and the method of load application - see Chapter IV - it is readily apparent that vertically loaded plate penetration tests do not even approximate the loading conditions of a wheel. Plate penetration tests with a horizontal component of load application, have been developed by Dickson (1963) and Reese (1966), to provide more information on the slip sinkage phenomenon. However, it is unlikely that either of these penetration tests produce translations within the soil, that are even similar to those occurring beneath a rolling, rigid wheel.

C. CONSIDERATIONS OF ENERGY DISSIPATION WITHIN THE SOIL

C1. Preliminary Considerations

From the definitions on page 81 the E_{input} term may be considered as that energy which is dissipated within the soil, since the energy losses in the wheel carriage bearings and in overcoming air resistance to wheel motion may be neglected under the loading conditions considered.

To undertake a rigorous analysis of the constituent components of this E_{input} term and quantitatively evaluate the magnitude of these component

dissipative mechanisms it is necessary to specify both the stress and strain fields occurring within the soil mass. Unfortunately there appear to be no viable constitutive equations available to relate stress and strain in this complex deformation process and for this reason the stress histories can not be deduced from measured deformations, in the absence of stress measurements. Thus it is not possible to quantitatively evaluate the \dot{E}_{input} term by following either the continuum approaches of Hill (1950), Prager (1961) or Ziegler (1963) or the particulate approaches of Rowe (1962), Horne (1965) or Barden and Khayatt (1966). In the context of the testing described previously any discussion of energy dissipation within the soil is necessarily speculative. However, although it is not possible to attempt to evaluate the contribution of each of the energy components that together constitute the \dot{E}_{input} term it is possible to speculate on the possible mechanisms of energy dissipation from considerations of soil behaviour beneath the test wheels. Here again it must be emphasised that the recorded deformation measurements were restricted to a plane with an upper boundary 1.5 inches from the undisturbed sand surface. Thus the following discussion of energy dissipation is based on the approximately two dimensional soil deformation history of a restricted region.

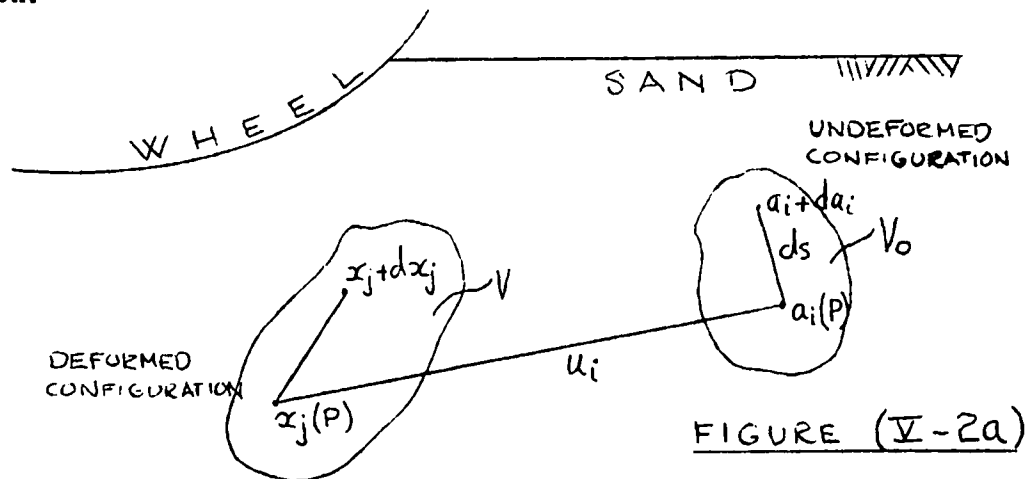
In dry sand, energy is dissipated when adjacent particles or assemblages of particles change their relative positions. In the following discussion an attempt is made to isolate some of the possible mechanisms of energy dissipation from a decomposition of the deformation and velocity gradients and from an examination of analogous components of dissipation. Despite the speculative nature of the following development it is hoped that a clearer understanding of the physical model may be realised and that a framework will be established for subsequent analysis - once stress information is made

available.

Before discussing the contributing mechanisms it is first necessary to establish a suitable coordinate reference system. In figure (V - 2a) the reference configuration of material particles P of the sand in the undeformed state are given by $a_i(P)$ in a generalised coordinate system. This configuration undergoes a rigid translation and deformation beneath the wheel and the material particles adopt the new - spatial - position $x_j(P)$ in a second coordinate system. Both of these configurations are related by a one-to-one mapping of points from the undeformed volume V_0 , to the points contained in the deformed volume V. That is:

$$a_i = a_i(x_j) \quad ; \quad x_j = x_j(a_i) \quad (V-a)$$

At this stage it should be emphasised that this representation of deformation is essentially different to that illustrated in figure III-6. Here the wheel may be thought of as rotating but not translating and the soil as being transported en masse (as if on an endless belt) at a velocity of magnitude equal to that of the wheel in Figure III-6, but in the opposite direction.



Since components of energy dissipation that depend on powers of the velocity of deformation will be discussed it is convenient - but not essential - to consider dissipation as a polynomial of the form:

$$D[\dot{x}_j(P)] = a + b[\dot{x}_j(P)] + c[\dot{x}_j(P)]^2 + \dots \quad (V-10)$$

where x_j are the generalised spatial coordinates, and the coefficients a , b , c , are associated with mechanisms of energy dissipation to be described below. Because we are concerned with the gradients of deformation and deformation rates - since energy is dissipated in relative sand motion - equation (V-10) serves only as a general statement of energy dissipation velocity dependence.

C2. The Dissipation Function (V-10) and Some Experimental Results

In his discussion of energy dissipation in a deforming assemblage of cohesionless particles, Horne (1966) concludes that solid body friction not only governs the overall behaviour of the assemblage but also acts as the primary dissipative mechanism. In this section frictional dissipation is considered under two categories: the first where the dissipative mechanism may be considered as quasi-static, and the second where friction contributes to a 'viscous-like', or deformation-rate dependent form of energy dissipation. This first category is contained in the "a" coefficient of equation (V-10) and is thus assumed to be independent of the rate of dissipation.

In order to consider the "a" coefficient in more detail it is first necessary to define, for an assemblage of sand particles, the assumptions of finite strain homogeneity, the coordinate reference system and a formalism for deriving the invariants of finite strain and finite rotation from measured deformation gradients.

Finite homogeneous strain has been defined by Jaeger (1962) as the special case of general strain where straight lines remain straight after straining and parallel lines remain parallel, though their direction may be altered. In addition, a sphere imagined to be embedded in the unstrained material at any point becomes an ellipsoid after straining. This ellipsoid is termed the strain ellipsoid and its axes are defined as the principal axes of strain. These assumptions appear to be justifiable for small assemblages of sand in

either region A and/or B - see Chapter IV - but not in the transition zone.

From the assumption of strain homogeneity it is possible to reduce the generalised coordinate systems of Figure (V-2a) to two simple Cartesian reference systems with origins, for the purpose of discussion, at the points a_i and x_j .

With reference to Figure (V-2a) the deformation of a vector da_i in a restricted two dimensional region is now examined. In the undeformed configuration a contiguous 'line' of sand particles laying between points a_i and $(a_i + da_i)$ may be visualised. In the deformed configuration these particles remain in a straight line, consistent with the assumptions of strain homogeneity, and lay between the points x_j and $(x_j + dx_j)$.

From equation (V-a):

$$dx_j = \frac{\partial x_j}{\partial a_i} da_i ; da_i = \frac{\partial a_i}{\partial x_j} dx_j \quad (V-b)$$

The deformation gradients, $\frac{\partial x_j}{\partial a_i}$ and $\frac{\partial a_i}{\partial x_j}$, may be decomposed into their constituent components of strain, rotation and translation, by invoking the polar decomposition theorem described by Toupin (1956), Truesdell and Toupin (1960), Coleman and Noll (1961) and Eringen (1962). This theorem states that any invertible deformation gradient may be written as the product of a symmetric positive definite tensor and an orthogonal tensor, or vice versa. This formulation of decomposition not only provides a framework for the analysis of finite deformations but also reduces the essential components to physically meaningful - and measureable - quantities. To relate the decomposition theorem to the physical model the geometric nature of homogeneous strain decomposition can be explained with the aid of Figure (V-2b).

In the plane of interest a circle in the undeformed state is deformed into an ellipse - consistent with the assumptions of strain homogeneity. With reference to Figure (V-2b) a circle with radius $ds = \sqrt{\delta_{ij} da_i da_j}$ and centred at

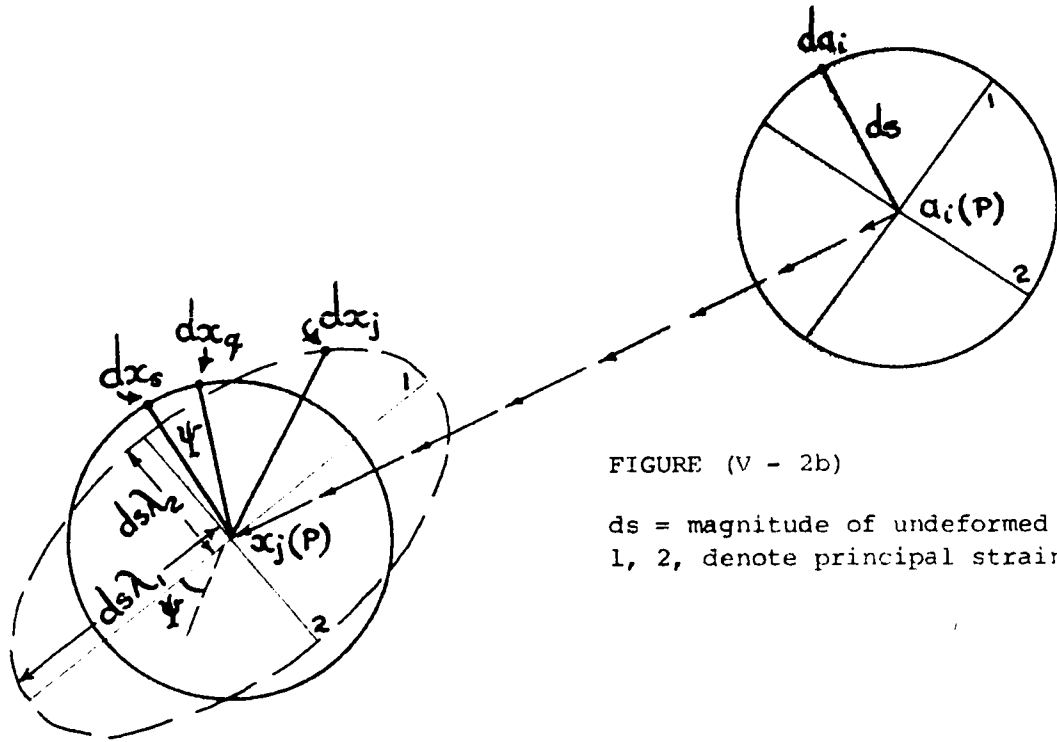


FIGURE (V - 2b)

ds = magnitude of undeformed vector da
 1, 2, denote principal strain direction

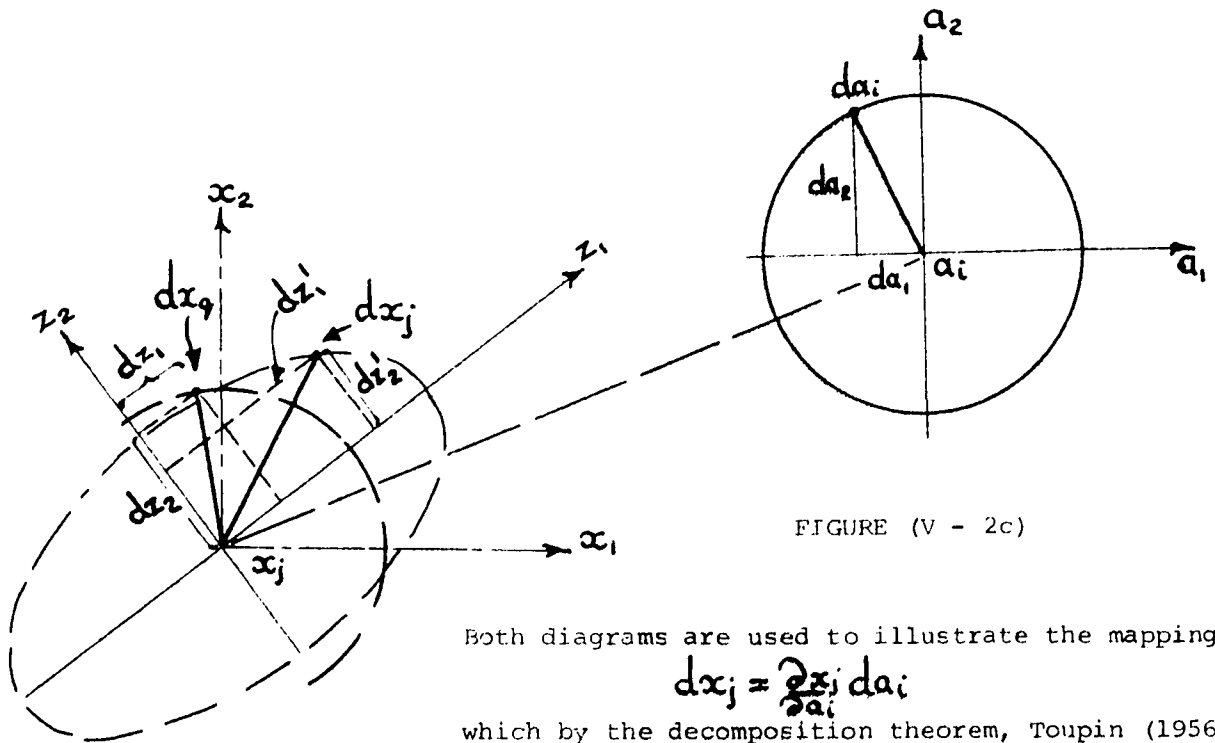


FIGURE (V - 2c)

Both diagrams are used to illustrate the mapping

$$dx_j = \frac{\partial x_j}{\partial a_i} da_i$$

which by the decomposition theorem, Toupin (1956),

$$dx_j = \lambda_{pj} \Delta_{pr} \lambda_{rq} R_{qs} S_{si} da_i$$

reduces to the form

The diagram is not to scale and is based on the physical situation illustrated in FIGURE (V - 2a).

a_i , is distorted into a spatial ellipse at x_j . Here δ_{ij} is Kronecker's delta. The theoretical justification for an ellipse may be found in the positive definite nature of the Cauchy-Green deformation tensors - see Eringen (1962).

The components of translation, rigid body rotation, pure strain, and volume change, are now considered individually with reference to the undeformed vector, da_i , and its final deformed position, dx_j .

- i) Translation: The particles of sand laying along the vector da_i are translated by a one-to-one mapping from the a_i to the x_j systems, i.e.

$$dx_s = \delta_{si} da_i \quad (V-c)$$

where δ_{si} is Kronecker's delta.

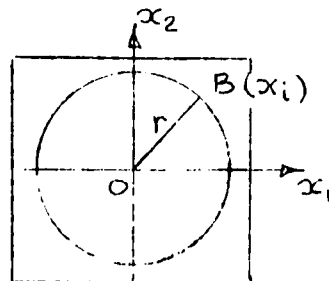
- ii) Rigid Body Rotation: The principal axes of strain are shown diagrammatically, Figure (V-2b), to have undergone a rigid body rotation of Ψ degrees. The finite rotation tensor, R_{qs} , defined by Spain (1956) and Jeffreys and Jeffreys (1967), can be reduced to the two dimensional form:

$$R_{qs} = \{ \cos \Psi \delta_{qs} - \sin \Psi \epsilon_{qrs} n_r \}$$

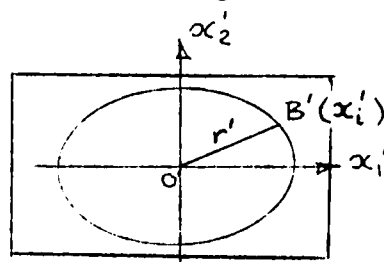
where ϵ_{qrs} is the Levi-Civita density; $q=s=1, 2$ or 3 , $r=3$. Using this tensor the principal strain axes of the circle may be brought into alignment with those of the ellipse and consequently the line element dx_s is rigidly rotated Ψ degrees, i.e.

$$dx_q = R_{qs} dx_s \quad (V-d)$$

- iii) Pure Strain, or stretch: Consider the diagram below:



Unstrained State



Strained State

If the length of the unstrained line OB is r , and that of the strained line OB' is r' then the stretch of line r is defined as $\lambda = \frac{r'}{r}$. If the principal axes of strain are orientated as shown above then $x'_1 = x_1 \lambda_1$ and $x'_2 = x_2 \lambda_2$ where λ_1, λ_2 are defined as the principal stretches, ($\lambda_1 > \lambda_2$). It can be shown - see Eringen (1962) - that the principal stretches, or the semi axes of the strain ellipse, are equivalent to the reciprocal of the square root of Cauchy's finite deformation tensor eigenvalues, for the formulation illustrated in Figure (V-2b). In the situation described the principal strain axes are not colinear with the reference axes - see Figure (V-2c). If z_1 and z_2 represent the principal stretch axes in this figure and dx_q represents the coordinates of the translated and rigidly rotated vector da_i , in the (x_1, x_2) coordinate system, it is first necessary to refer the dx_q to the (z_1, z_2) system. By the simple linear transformation:

$$dz_r = \lambda_{rq} dx_q \quad (V-e)$$

where λ_{rj} is a two dimensional array of direction cosines. The dz_r are then deformed by pure stretch to form the vector components dz'_p by contraction with the stretch tensor Δ_{pr} : i.e.

$$dz'_p = \Delta_{pr} dz_r \quad (V-f)$$

where $\Delta_{pr} = \begin{bmatrix} \lambda_1 & 0 \\ 0 & \lambda_2 \end{bmatrix}$

Note that unless the dz_r lay along the principal axes of strain this stretch will incur a further rotation. The dz'_p are then transformed linearly to the (x_1, x_2) coordinate system by using the transpose of the direction cosine matrix to give the final position of the deformed vector - see Figure (V-2c)

$$dx_j = \lambda_{pj} dz'_p \quad (V-g)$$

iv) Area and Volume change: The area of the ellipse in Figure (V-2b) is $\pi\lambda_1\lambda_2 ds^2$, whereas the area of the undeformed circle is πds^2 . Thus the product $\lambda_1\lambda_2$, is identically equivalent to the relevant Jacobian of this deformation and $(\lambda_1\lambda_2-1)\pi ds^2$ represents the change of area in deformation. It may be shown that the corresponding volume change, $\lambda_3=1$, is $(\lambda_1\lambda_2-\frac{4}{3})\pi ds^3$. It is therefore obvious that the third invariant of the stretch tensor, Δ_{pr} , is in fact the relevant Jacobian.

Collecting terms in the equations (V-c, -d, -e, -f, and -g) the components of translation, rotation and stretch can be grouped together to give one equation describing the mapping of da_i to dx_j : i.e. $dx_j = \frac{\partial x_j}{\partial a_i} da_i$

$$\text{or } dx_j = \lambda_{pj} \Delta_{pr} \lambda_{rq} R_{qs} \delta_{si} da_i \quad (\text{V-h})$$

Both the stretch tensor, Δ_{pr} , and the finite rotation tensor R_{qs} , can be evaluated directly using a variant of the radiographic technique described in Chapter III. For the assumptions of strain homogeneity to be valid the tracer-object grid should be finer than that chosen for the experiments reported in this thesis and for this reason the invariant fields of the two tensors can not be determined at this time. However there are no theoretical difficulties, other than those described by Roscoe, Arthur et al (1963), associated with the use of a considerably finer grid. It should be noted that the rotation of the tracer-objects in the deformation process provide a check on the rigid body rotation Ψ derived from the decomposition of the deformation gradients.

Equation (V-h) has been developed as an example of one representation of the decomposition of deformation. It should, however, be emphasised that

the theorem of decomposition may be used for both material and spatial coordinate reference systems and that the mapping is independent of the order of application of translation, rotation or stretch. A proof of this statement may be found in a theorem by Toupin (1956). The introduction of this formalism for finite deformation analysis is seen as an essential step towards a complete analysis of energy dissipation, by rate independent mechanisms. In the absence of stress information it is only possible to discuss some of the mechanisms contributing to the "a" coefficient of equation (V-10), and here only in a qualitative way.

First by considering the deformation of an assemblage of sand particles the isolation of rigid body rotations and pure strains immediately separates volumetric and surface components of energy dissipation in a manner analogous to Prager's (1961), continuum approach. Frictional dissipation of energy resulting from relative sand motions within the assemblage results from a stretch, or pure strain, situation whereas in the case of rigid body rotations relative particle movement only occurs on the surface of the rotating assemblage. As Horne (1966) discusses, energy is not only dissipated in solid-body friction resulting from inter-particle motions but also in cracking, crushing and possibly plastic deformation of the constituent sand particles. To what extent these latter mechanisms contribute to energy dissipation under the loading conditions considered is not certain, although Horne considered their contribution small enough to be ignored. Since the history of deformation of an elemental volume can be traced and decomposed it is possible to separate recoverable from irrecoverable volume changes. Thus, once stress information is available, the above analysis of strain will permit separation of the elastic or 'elastic-like' strain energy component from the net energy supplied.

Since both the soil translations and the measured wheel torque appeared to be independent of the translational wheel velocities used it is evident that the "a" term of the polynomial (V-10) accounts for most of the energy expended in the tests reported herein.

The second coefficient, "b", on the right hand side of equation (V-10) accounts for those dissipative mechanisms that are proportional to the first power of the velocity, or rate of deformation, gradients. In discussing this coefficient it is convenient to restrict the discussion to results of the two dimensional test No. 29, as this allows for the extrapolation of measurements under the centre line of a wheel - see shaded area in Figure (V-3) - to adjacent parallel planes extending to the containing side walls. The following formulation is with reference to the spatial coordinates, x_j , which have taken the form $x_1 = x$, $x_2 = y$ and $x_3 = z$. A typical subsystem, defined as an assemblage of particles, is illustrated in Figure (V-3) insert. It should be noted that the influence of the containing side walls on the measured translation patterns and thus on the velocity and acceleration histories, will be assumed negligible in this development. This is

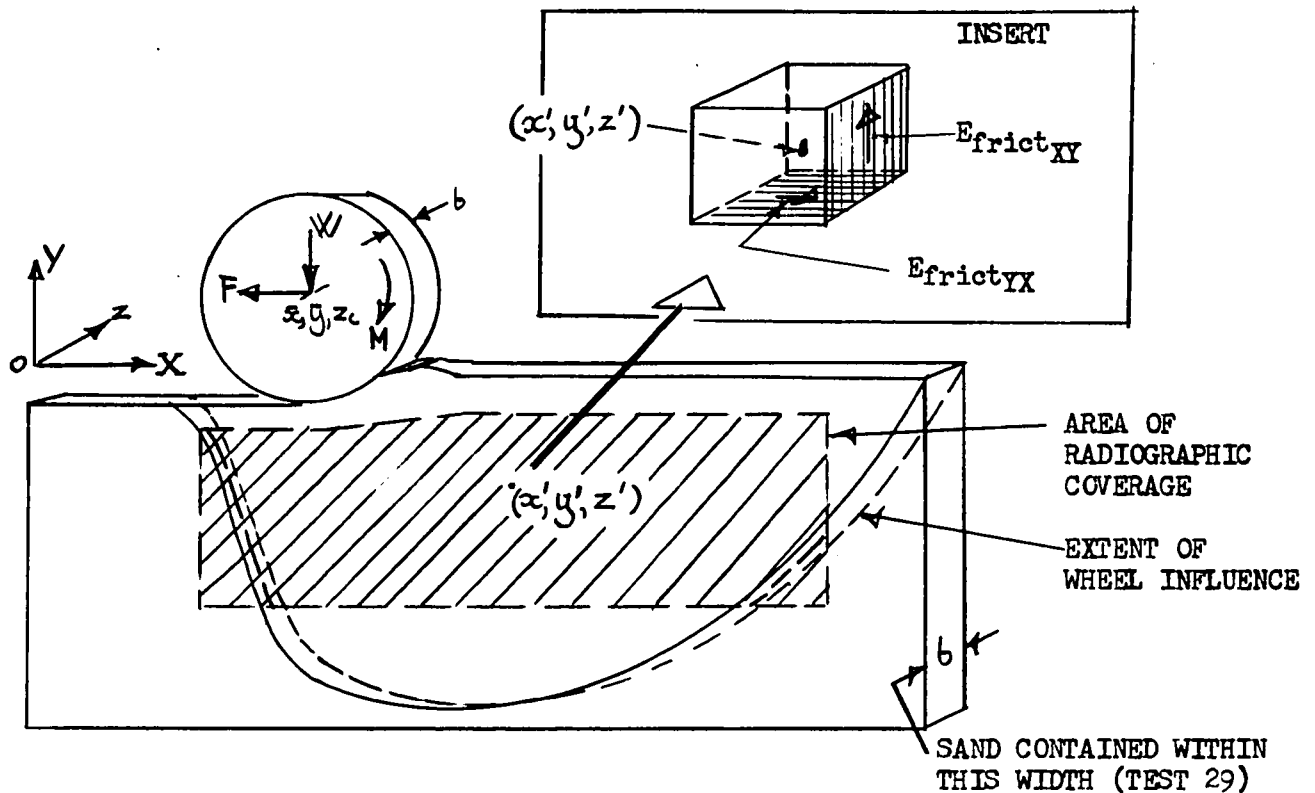


Fig. V-3 Diagram of Test 29 Geometry

a convenient assumption that does not necessarily follow from the discussion of Chapter IV.

Having already defined the subsystem: an elemental volume dV , with mass centre (x', y', z') will be considered with reference to Fig. V-3, above. The rate of energy loss due to the displacement of frictional forces will be termed, \dot{E}_{frict} . Considering the elemental cube shown, above, an expression for \dot{E}_{frict} can be derived using some simplifying assumptions. If it is assumed that the averaged accelerations of the mass are $\bar{\ddot{x}}$ and $\bar{\ddot{y}}$ (where $\bar{\ddot{z}} = 0$) then the forces normal to the Y and X faces of the cube are $\bar{\rho} \bar{\ddot{y}}' dV$ and $\bar{\rho} \bar{\ddot{x}}' dV$ respectively - where $\bar{\rho}$ is the instantaneous mean density of the elemental volume. If μ_{XY} and μ_{YX} are the frictional coefficients on the x and y facing surfaces of the cube then the friction forces acting along these faces are $\mu_{XY} \bar{\rho} \bar{\ddot{x}}' dV$ and $\mu_{YX} \bar{\rho} \bar{\ddot{y}}' dV$ respectively. The distance

moved by these forces is for $M_{XY} \bar{\rho} \frac{\partial \dot{x}}{\partial x} dV$, $\frac{\partial \dot{y}}{\partial x} dx$ and for the force on the Y facing surface is $\frac{\partial \dot{x}}{\partial y} dy$. Thus the rate of energy dissipation due to Friction forces is, on the two surfaces:

$$\left. \begin{aligned} \dot{E}_{\text{frict}_{XY}} &= M_{XY} \bar{\rho} \frac{\partial \dot{x}}{\partial x} dV \frac{\partial \dot{y}}{\partial x} dx \\ \text{and } \dot{E}_{\text{frict}_{YX}} &= M_{YX} \bar{\rho} \frac{\partial \dot{y}}{\partial y} dV \frac{\partial \dot{x}}{\partial y} dy \end{aligned} \right\} \quad (\text{V-11})$$

respectively - see insert to Fig.(V-3)

The coefficient 'b' in equation (V-10) is seen to be proportional to the density, and accelerations of the elemental volumes as well as to the velocity gradients and the frictional properties of the cube surface. If (V-11) is converted to a finite difference form it is possible to evaluate all but the frictional coefficients, using the experimental results obtained from the methods of Chapter III. Rowe (1954), (1962), (1963) and others, have shown that the frictional coefficient of a particulate medium is dependent on the density (or packing), the strain and the principal stress ratio of the subsystem. For this reason it is unlikely that $M_{XY} = M_{YX}$, and probable that the M_{XY} and M_{YX} values vary considerably for different subsystems. This precludes a numerical evaluation of equations (V-11). However the velocity, acceleration, and density distribution with respect to a fixed spatial coordinate system (X,Y,Z) and an instantaneous wheel position (\bar{x}, \bar{y}, z_c) can be evaluated.

Using a fixed reference coordinate system the instantaneous velocity and acceleration fields are referred to an instantaneous wheel position and the formulation is Eulerian. A change of variable from an Eulerian to a Lagrangian system may be obtained by evaluating the relevant Jacobian, (Jeffreys and Jeffreys, 1962). However the Soil Vehicle Programmes, I and III, were written to account for an Eulerian formulation.

The component velocity fields were obtained from the 'smoothed' velocity

vs. cumulative time curves plotted from the computer output. This 'smoothing' is necessary in view of the Chapter III discussion on the accuracy of the velocity computations. Since the absolute coordinates (x,y,z) are also plotted against a cumulative time base, the component velocities may be plotted with respect to an instantaneous wheel position by 'row'. The component \dot{x} and \dot{y} fields are obtained from graphical interpolation of the 'row' information. The component acceleration fields \ddot{x} and \ddot{y} , are plotted in a similar way to the velocity fields; the basic acceleration against cumulative time information being derived from the graphical differentiation of the velocity vs. cumulative time plots.

Appendix V-C-1 contains the x and y component velocities and accelerations, plotted by row against cumulative loading time, for test 29. The component velocity and acceleration fields, with respect to an instantaneous wheel position, are included as Figures (V-4) and (V-5). These figures give some idea of the complexity of the dynamic sand behaviour beneath a rolling rigid wheel - in addition to providing a basis for the evaluation of equation (V-11).

To determine the density distribution some additional assumptions are made. It is first assumed that with a negligible side wall influence, the translation patterns of sand particles in the two dimensional loading arrangement of Test No. 29, are essentially coplanar. Under this circumstance the area changes in the tracer object matrix provide a basis for estimating the density distribution, i.e. $\rho = \rho(x,y)$. Since mass is conserved:

$$\left\{ \rho_0 V_0 \right\}_{t=t_0} = \left\{ \rho_i V_i \right\}_{t=t_1} \quad (\text{where } i = 1, 2, 3) \quad (\text{V-12})$$

with no summation over i; where at time $t=t_0$ the tracer-object matrix is in its undisturbed (initial) position and at time $t=t_1$ has been exposed to the wheel forcing. The subscript i corresponds to the tracer object matrix

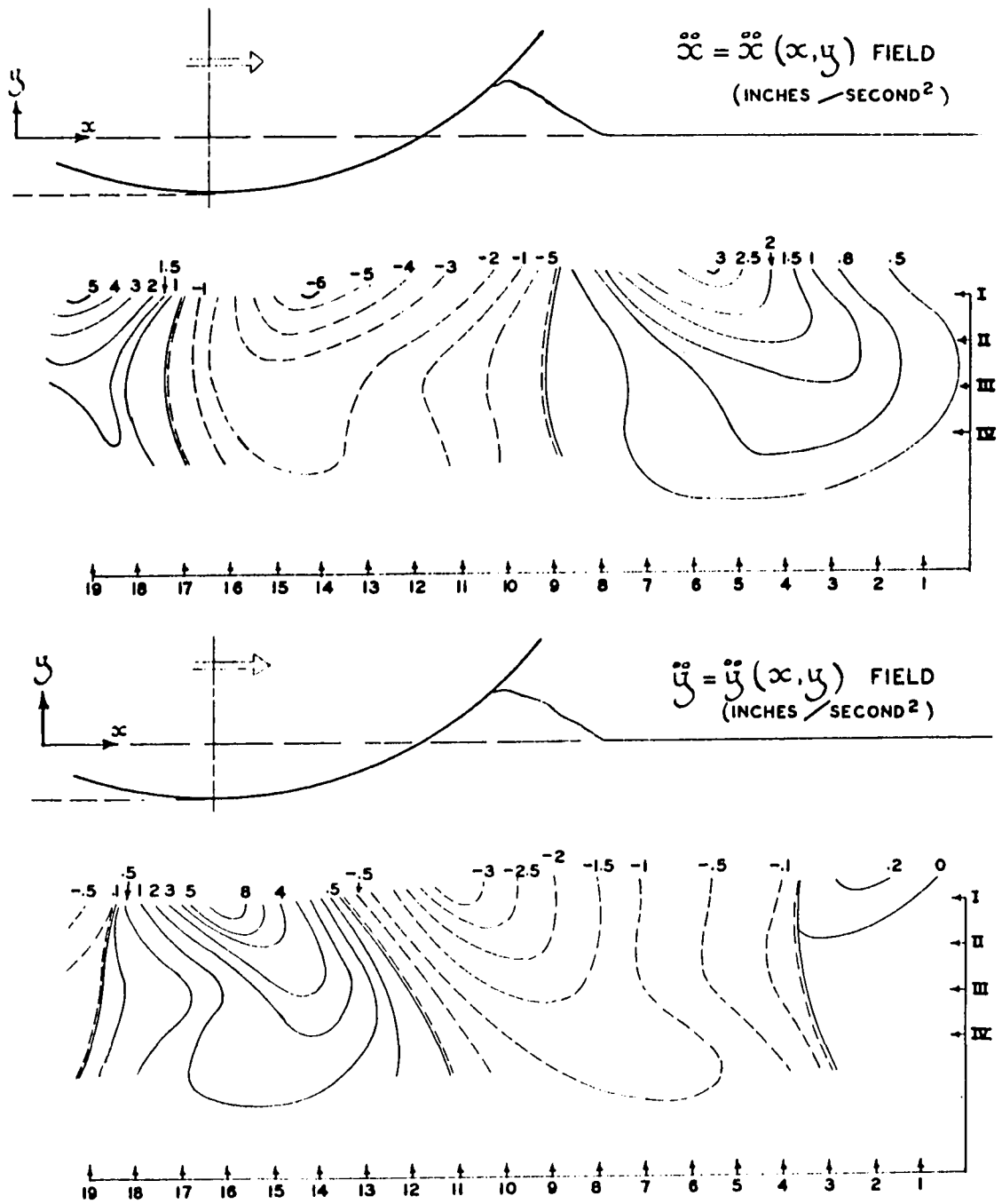


FIGURE V-5: PARTICLE ACCELERATION FIELDS

TEST 29 RESULTS, WITH REFERENCE GRID
USED TO EVALUATE EQUATION (V-10)

1 INCH

locations of the second third and fourth sequential X-ray pulses. Volume is denoted by, V . Because of the assumed two dimensional behaviour the density ρ_1 can be related to the area change of the tracer-object matrix i.e.

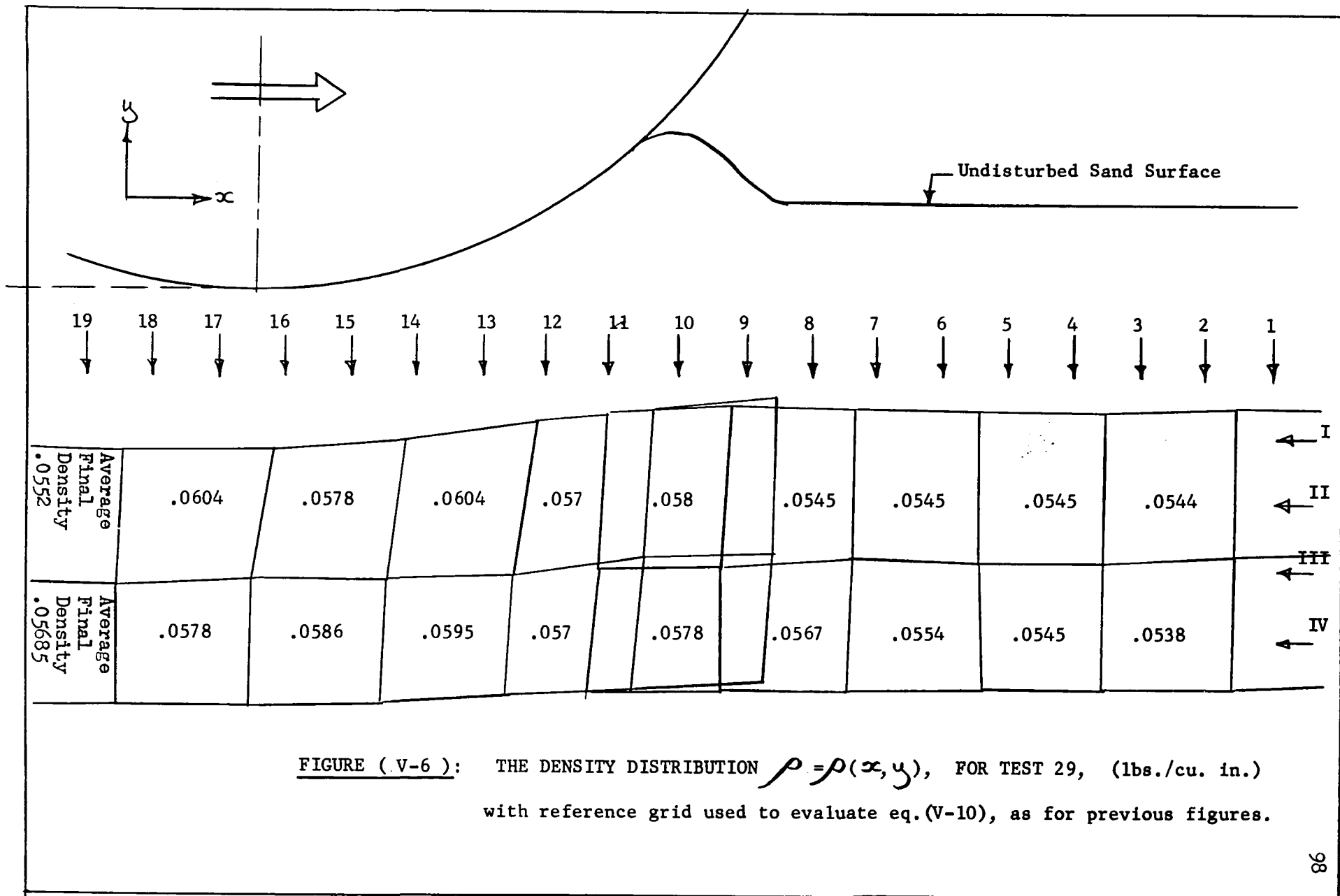
$$\rho_1 = \rho_0 \frac{V_0}{V_1} = \rho_0 \frac{A_0}{A_1} \quad (V-13)$$

for any one element of the matrix. (A_1 represents the area corresponding to V_1). The initial area A_0 of any 'element' of the matrix is related to the three corresponding areas $A_1 = 1, 2, 3$ and the instantaneous wheel position. Thus, since the averaged initial sand mass density $\rho_0 = 1.49 \text{ gms/cc} = 0.0539 \text{ lbs(mass)/cu.in.}$, - see Appendix III-B3-2 - the ρ_1 values, and thus the spatial distribution of density $\rho = \rho(x, y)$ can be evaluated. It is again emphasised that this is the instantaneous mass distribution. Since the spacing of the tracer object matrix is approximately $1'' \times 1''$ the area 'elements' are large and the resulting distribution results in rather gross averaging identified by abrupt boundaries. However, refinements associated with assuming curved, rather than straight, boundaries are not considered justifiable at this stage, and the distribution determined from the above technique is used. The tracer-object matrices corresponding to the four sequential X-ray pulses are included as Appendix V-C-2. The resulting distribution is shown as Figure (V-6), with respect to the instantaneous wheel position.

The density variations are seen from this figure to be greater in the $1.5'' \rightarrow 2.5''$ depth of sand than they are in the $2.5'' \rightarrow 3.5''$ layer. However the final averaged densities in the lower layer were found to be slightly greater than the corresponding value for the layer nearer the wheel.

Approximating equation (V-11) by a finite difference form:

$$\left. \begin{aligned} \dot{E}_{\text{frict}_{XY}} &\approx \mu_{xy} \bar{\rho} \frac{\partial \dot{V}}{\partial x} \frac{\Delta y}{\Delta x} \Delta x \\ \dot{E}_{\text{frict}_{YX}} &\approx \mu_{yx} \bar{\rho} \frac{\partial \dot{V}}{\partial y} \frac{\Delta x}{\Delta y} \Delta y \end{aligned} \right\} \quad (V-14)$$



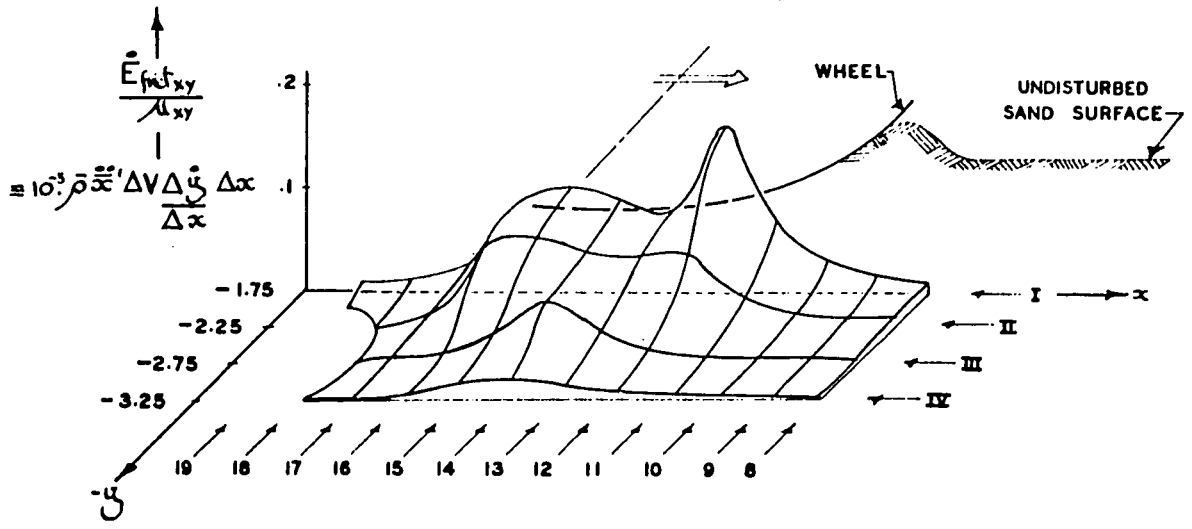
all but the μ values can be evaluated, from figures (V-4,5 & 6).

It is convenient to consider elemental volumes of .25 inches cubed (= .015725 cu.ins.) with centres located in a matrix .5" x .5" in the plane under the centre line of the wheel ($x, y, z = \text{constant}$). Thus each ΔV extends .125" on either side of this plane in the $\pm Z$ directions. For easy reference the x and y coordinates of these elemental volume centres has been coded using 4, $y=\text{constant}$ rows, labelled I, II, III and IV, and 19 $x=\text{constant}$ columns, labelled 1 \rightarrow 19 inclusive. This reference scheme is included in Figures (V-4, -5 and -6) so that the information contained therein may be related in order to evaluate equation (V-14). Since the product of frictional force and deformation rate represents a dissipation term, \dot{E}_{frict} , both accelerations and decelerations only have meaning as positive quantities, thus $\left| \frac{d^2x}{dt^2} \right|$ and $\left| \frac{d^2y}{dt^2} \right|$ are used in this evaluation. Also the velocity component sign convention* dictates the direction in which the frictional force acts but, whether positive or negative, the work associated with this deformation rate is always positive.

Using the information contained in Figures (V-4, -5 and -6) the $\dot{E}_{\text{frict}_{XY}} / \mu_{XY}$ terms have been evaluated for the matrix positions discussed above and are tabulated in Appendix V-C-3. The units of these terms are: in.lbs./sec, since the coefficient μ is dimensionless. However, since the distribution of μ_{YX} and μ_{XY} is unknown it is necessary to consider the rate of energy dissipation, under the centre line of the rolling wheel, as \dot{E}_{frict} surfaces unmodified by the frictional coefficient, i.e. the $\dot{E}_{\text{frict}_{XY}} / \mu_{XY}$ and the $\dot{E}_{\text{frict}_{YX}} / \mu_{YX}$ surfaces, which have been plotted, and appear overpage as Figure (V-7). Although the actual \dot{E}_{frict} surfaces will be different the

* The sign convention follows from the 'absolute' coordinate reference axes chosen for the basic data reduction, see for example: Fig. V-3.

(A): THE $\dot{E}_{frict_{xy}}/\mu_{xy}$ SURFACE



(B): THE $\dot{E}_{frict_{yx}}/\mu_{yx}$ SURFACE

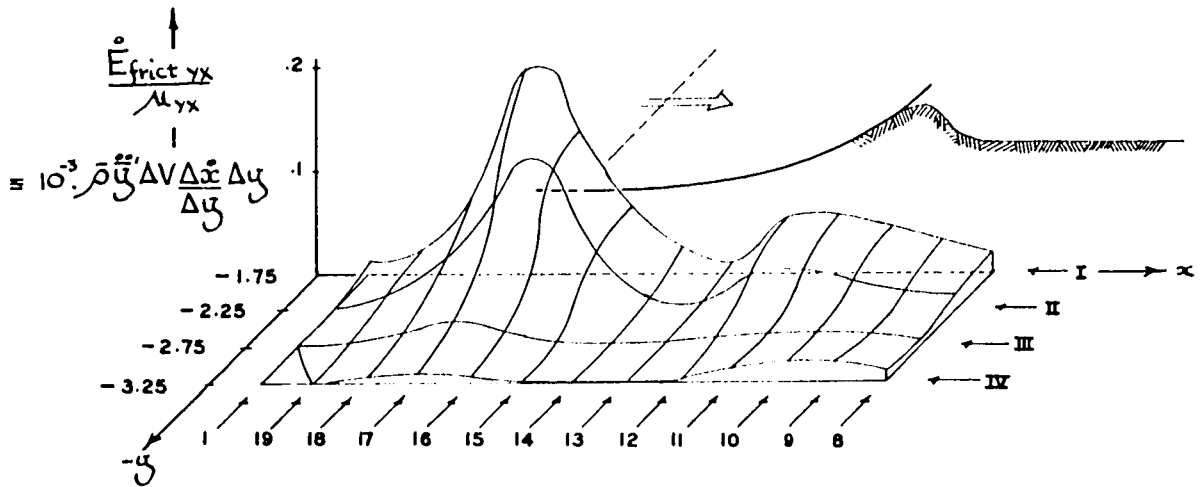


FIGURE V-7: COMPONENT \dot{E}_{frict}/μ SURFACES PLOTTED ON THE TRACER-OBJECT PLANE FOR TEST 29, WITH RESPECT TO AN INSTANTANEOUS WHEEL POSITION AND REFERENCE GRID.

(NOTE $\mu_{yx} = \mu_{xy}(x, y)$)

following observations have been generalised to accommodate such differences:

- 1) For both surfaces the energy dissipation, \dot{E}_{frict} , decreases with distance from the instantaneous wheel position. This situation might be anticipated from figure (V-4) where the velocity (deformation) gradients - and thus relative sand particle movements - are seen to be greater nearer the wheel. The \dot{E}_{frict} terms are seen to be negligible at depths greater than 3.25" beneath the undisturbed sand level - for test 29. Since \dot{E}_{frict} terms also fall off rapidly for 'column' reference positions less than 7 (i.e. 1 \rightarrow 6), the surface has not been extended in this direction.
- 2) The vertical component of frictional energy, $\dot{E}_{frict_{xy}}$, is dissipated almost entirely directly beneath the wheel - and not ahead of it. In this region the relative vertical particle movements, $\Delta \dot{y} / \Delta x$, as well as the forces ($\propto \frac{\sigma}{x}$), are greater. Also note that the peak $\dot{E}_{frict_{xy}}$ value on Figure (V-7)(a) occurs at Matrix location I-12. This location corresponds to the 'valley' of the Figure (V-7)(b) surface, where peak $\Delta \dot{y} / \Delta x$ gradients and near zero $\Delta \dot{x} / \Delta y$ gradients occur.

This region - column 12, Fig. (V-7) - is associated with the transition zone between sand movement in the direction of wheel travel (columns 11 \rightarrow 1 inclusive) and sand movement in the reverse direction (columns 12 \rightarrow 19).
- 3) The horizontal component of energy, $\dot{E}_{frict_{yx}}$, is dissipated in two distinct regions, separated by the transition zone described above. The increase in the $\dot{E}_{frict_{yx}}$ term to the right of this transition zone has no equivalent in the \dot{E}_{xy} surface since the $\Delta \dot{x} / \Delta y$ gradients are larger in this region than the $\Delta \dot{y} / \Delta x$ gradients. That is, the soil translation is predominantly

horizontal in this region, and since the x component velocities increase on approaching the wheel, and sand surface, the $\dot{E}_{frict_{YX}}$ term increases accordingly. However, in the zone to the left of Column 12 the $\dot{E}_{frict_{YX}}$ terms increase in magnitude since both the forces and gradients are greater.

- 4) A summation of the two energy surfaces shows that by far the most frictional dissipation occurs directly beneath the wheel, in the Column 12 \rightarrow 19 region. It will be noted that the densities in this region - Figure (V-6) - are greatest and thus the dilatant frictional component of the M_{XY} and M_{YX} terms can be expected to be greater in this region than in regions of lower density.
- 5) Even assuming an \dot{E}_{frict} surface with $M_{XY} = M_{YX} = 1$, the total rate of energy dissipation for the region studied, summed over the volume contained within the containing side walls of test 29, is still less than one half of one percent of the \dot{E}_{input} term. It is therefore unfortunate that no soil measurements were made above the 1.5" depth, so that the extended surfaces of Figure V-7 could be used to provide an estimate of the total \dot{E}_{frict} term. However it is evident that the \dot{E}_{frict} terms can be expected to increase in the region bounded by Row I and the sand surface.

Although it is possible to derive an expression for the rate of change of Kinetic energy - for the shaded region of Fig. V-3 - it is difficult to justify using the absolute, rather than the algebraic, sum of the components because of the difficulty of separating 'recoverable' from 'irrecoverable' terms. However the greatest component of dissipation is probably encompassed by the irrecoverable terms.

Having discussed the $b(\dot{x}_1)$ term, three terms remain: the coefficient 'a'

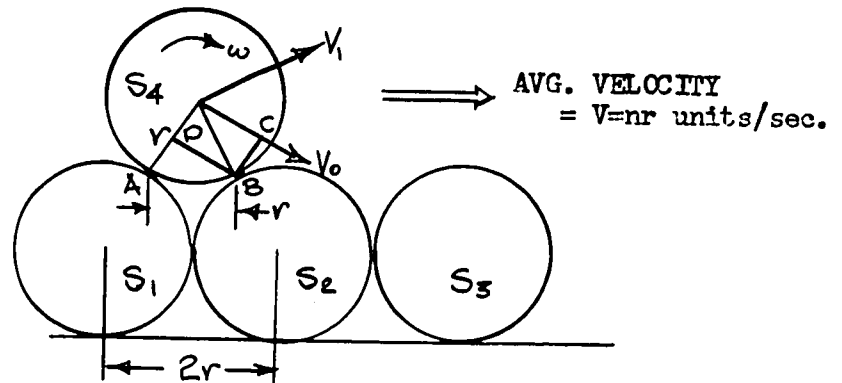
In the above analysis the displacements through which the frictional forces act are assumed to be colinear with the associated force. This would be true only for non dilatant deformation, at a critical voids ratio value, (Drucker (1954) and Rowe (1962)), and thus the analysis must be viewed with this reservation.

Having discussed the first two terms on the right hand side of equation (V-10) one additional term, $c [\dot{x}_j(p)]^2$ remains. By using the velocity or rate of deformation gradient to provide the rate dimension, energy losses proportional to the square of velocity may be accounted for in this third term. From a mechanistic viewpoint the $c [\dot{x}_j(p)]^2$ term can include losses from inelastic collision of the sand particles and also losses from overcoming dilatant effects. Although both phenomena are difficult to evaluate quantitatively an idealisation of the losses due to dilatant influences is considered useful.

An analogous situation has been developed by Inglis (1951), who considered the energy losses due to the passage of a rigid wheel over a series of pot-holes. Consider three hypothetical spherical sand grains S_1 , S_2 , S_3 , that are stationary and a fourth grain, S_4 , which is moving over the

FIGURE (V-8)

Diagram to illustrate considerations of energy losses proportional to the velocity squared.



stationary surface, without slip, at a mean velocity V - see Fig. (V-8). If the spherical grains are inelastic, V_0 is the velocity of sphere S_4 before striking point B, and V_1 the velocity after impact, then the corresponding angular velocities of this sphere are $\omega_0 = V_0/r$ and $\omega_1 = V_1/r$. On impact there is no change in the moment of momentum about B, thus if I = moment of inertia of sand grain S_4 and M the corresponding mass:

$$\begin{aligned} M V_0 \overline{BC} + I \frac{V_0}{r} &= M V_1 r + I \frac{V_1}{r} \\ \therefore V_0 \left[M \frac{r}{2} + \frac{I}{r} \right] &= V_1 \left[M r - \frac{I}{r} \right] \\ \therefore V_1 &= \frac{[M r/2 - I/r]}{[M r - I/r]} V_0 \end{aligned} \quad (V-15)$$

Since the kinetic energy loss per $2r$ horizontal distance travelled by S_4 , is

$$E_3 = \frac{1}{2} (M r^2 + I) (V_0^2 - V_1^2)$$

which, from equation (V-15), becomes

$$E_3 = \frac{1}{2} (M r^2 + I) \left[1 - \left\{ \frac{M r/2 - I/r}{M r - I/r} \right\}^2 \right] V_0^2 \quad (V-16)$$

K

or

Thus if S_4 travels at a mean velocity of $V = nr$ units per second, the rate of energy dissipation becomes

$$\dot{E}_3 = \frac{nr}{2r} \cdot K V_0^2 = \frac{n}{2} K V_0^2 \quad (V-17)$$

which is clearly seen to be proportional to the square of the velocity just before impact.

In reality the sand particles are obviously not spherical and relative displacement is not maintained at a constant average velocity $V = nr$. However velocity gradients are plainly evident and thus losses of a similar nature probably occur.

The polynomial nature of the dissipation function (V-10) is thus seen to be realistic from a qualitative standpoint. It is unfortunate that the step to an explicit quantitative statement of energy dissipation, numerically equivalent to the \dot{E}_{input} term, can not be made at this stage.

D. A SUMMARY STATEMENT OF CHAPTER V

From the previous sections of this Chapter, it is evident that only one side of the basic energy equation is known. Although it is possible to write an expression for, and experimentally evaluate, that energy dissipated by a rolling wheel, it has not been found possible to evaluate the precise mechanisms of dissipation within the soil mass. This difficulty stems largely from the observed fact that the sand does not behave as an 'ideal' material. In addition, many of the necessary conditions, required for an evaluation of the theoretical dissipation functions, are not met by the conditions of sand behaviour under a moving wheel load. The measured net volume changes - up to 8% -, the absence of any stress measurements and the difficulty of defining a stress-strain relationship to adequately define the dynamic régime beneath a moving wheel, are seen as major obstacles to the practical evaluation of a meaningful dissipation function.

Despite these limitations, the measurements of velocity and acceleration fields within a soil mass have made it possible to examine for the first time - to the best of this writer's knowledge - the complexity of the soil reaction to a moving rigid wheel load. Using this information one mechanism although not the primary contributing one, of energy dissipation is examined in some

detail - namely the \dot{E}_{frict} term. From considerations of other possible mechanisms of energy dissipation, it appears that a polynomial, in powers of soil velocities, might provide a meaningful dissipation function.

CHAPTER VI
SUMMARY & CONCLUSIONS

A. Summary

In the past the speculation surrounding the question of how soils behave under vehicular loads has provided a constant obstacle to the development of meaningful predictions of vehicular performance. For this reason an experimental approach was considered as a mandatory prerequisite, and the specific case of a driven rigid wheel, rolling on an initially loose dry sand has been studied. In order to examine the dynamic subsurface soil response a Cine-Flash X-ray technique was developed, to circumvent many of the inadequacies of previous experimental investigations, and to provide a basis for realising the objectives of this study - outlined in Chapter 1.

This technique is seen to have considerable potential in this application as it provides a method of measuring the previously unknown translation patterns and velocity - and acceleration - fields within a soil mass subjected to a wheel forcing function. This advance on previous experimental investigations is seen as one step towards successful predictions of vehicular performance based on an understanding of the subsurface soil behaviour. It is, however, readily apparent that the history of stress states must be specified before this ultimate objective can be realised. The essential description of the characteristic deformations that occur within the soil domain has been defined in this study, as one stage in the development of appropriate constitutive equations. This appreciation of the physical model has been used to examine certain superficially observed phenomena, to appraise previous assumptions, and to study soil-wheel similitude relations.

E. Conclusions

The following conclusions are restricted to the limiting conditions that define the soil-wheel system, namely:

- i) a vehicular load described by two rigid scaled wheels under the parametric restraints listed in Tables IV-1 and IV-2;
- ii) a dry, initially loose, fine grained sand; and
- iii) observations based on measurements whose precision levels have been specified in Chapter III.

The conclusions are listed below under three headings relating to the tripartite division of the objectives outlined in Chapter I:

I. Conclusions relating to soil behaviour.

- a) The complex patterns of sand translation beneath a variety of controlled wheel loads have been measured in a region co-planar with the wheel centre line. Representative particles are seen to 'enjoy' both horizontal and vertical movements, and to reflect two distinct mechanisms of soil behaviour depending on whether the particle lies within Region A or B - see Figure IV-10. Region A, extending from the surface to a depth of approximately $3/4$ the wheel width, is characterised by translation patterns that are influenced by the magnitude of wheel slip. The horizontal component of sand translation is shown to be significantly effected by wheel slip, whereas the vertical component only reflects a 'magnitude of variation' dependence on this parameter, within Region A. Region B, extending below this upper region, is characterised by yield deformations below failure that are independent of any parametric variations in the loading pattern, for either of the two wheels tested.

- b) Wheel slip rate was seen to be the only parameter to produce a measurable influence on the translation patterns, and the developed wheel torque, for a given wheel. Parametric variations in: a) translational wheel velocity, ($3 \text{ ins/sec} \leq V \leq 10.5 \text{ ins/sec}$); b) the rim surface material, (polished aluminum and hard rubber); and c) axle loads, ($\pm 20\% W$); produced no measurable influence on either of these quantities. Slip rate must therefore be considered as a primary physical process.
- c) The energy lost to the soil by a driven rigid wheel can be specified, although a quantitative evaluation of the constituent mechanisms is not possible at the present time. This situation arises from the absence of information on the stress history of loading. However, as one essential step towards this quantitative evaluation of energy terms, a framework for the analysis and decomposition of finite deformations is presented. An example of one such decomposition is illustrated and the translations, rigid body rotations and stretch invariants are isolated both conceptually and in a physical sense. Possible mechanisms of energy dissipation that are dependent on first and second powers of deformation rate or velocity gradients are introduced and in one case examined in some depth.
2. Conclusions relating the results to the assumptions of previous theories.
- a) It has been shown by Leflaive (1966) and Schuring (1966), that the energy lost per unit distance travelled by the wheel is a more meaningful interpretation of the traditional Bernstein (Reece, 1966) concept of Rolling Resistance, R . In his formulation of an expression for Rolling Resistance, Bekker has assumed that this energy

loss can be: a) equated to the energy expended in purely vertical components of deformation, equation (I-2), and b) expressed functionally as equation (I-4), which is independent of wheel slip. Both expressions are contradicted by the experimental results reported in the previous chapters. It is readily apparent that energy is expended in the horizontal translation of soil, although the precise mechanism of dissipation can not be specified at the present time. Since horizontal soil translations occur and are proportional to slip in the ($c0\% \leq \text{slip} \leq c30\%$) region it is concluded that the \dot{E}_{input} term is dependent on the applied wheel slip rate.

- b) The slip-sinkage phenomenon was observed from surficial measurements of the rolling sinkage, y_0 , - see Figure IV-9. Observations based on sub-surface measurements reveal that for the slip sinkage region ($c0\% \leq \text{slip} \leq 30\%$) the magnitude of sand flow from in front of to behind the wheel is directly proportional to the slip rate - being accommodated completely within Region A.

The Bekker assumption of a unique equilibrium sinkage for any one soil-wheel system, equation (I-3), is thus clearly inadequate.

3. Conclusions related to the results of the scaling studies.

- a) From plate bearing tests, and the Bernstein-Bekker formulation, equation (I-2), Schuring (1961) concluded that forces in a sand-wheel system were scaled to the third power of the linear scaling ratio λ ; i.e. as λ^3 . This observation is in conflict with the results reported in Chapter V, which show that at least some soil dependent forces are scaled to the second power of the linear scaling ratio λ , since the driving torque was scaled in a $c \lambda^3$ ratio.

For this reason it appears essential to distinguish between those forces in the sand-wheel system that are a) dependent on, and b) independent of, the soil reaction. This inspectional analysis reveals that the scaling of soil-dependent forces can not be obtained from:

- i) considerations of the wheel variables alone, and
- ii) from ascribing a Coulombic behaviour to the soil.

The observed non-Coulombic scaling of the torque energy parameter,

η , will in all probability extend to the non dimensionalised drawbar pull-slip relationship since the drawbar pull coefficient,

Δ , is itself dependent on the soil-dependent forces.

Thus considerably more research emphasis is required if model vehicle studies are to be extrapolated to field conditions.

- b) Because the vertical plate and segment loading tests of Schuring (1961), Hegedus (1965) and Wills (1966) have been limited to the zero slip condition the study of sinkage, y_0 , under dynamically scaled wheels can provide considerably more information. These previously reported plate bearing tests had shown that for loads scaled with a ratio λ^3 , a linear scaling of sinkage was obtained in sand soils. (Here, λ denotes the ratio of a characteristic prototype to model plate dimension). In the scaled wheel loads, reported on herein, it was found that the linear scaling ratio, λ , was also followed by the rolling sinkage, y_0 , for the entire slip range studied, - see Figure IV-9. This is considered an important conclusion from the standpoint of extrapolating the measured surface deformations from model studies.

An analysis of the total component translations in Region B revealed that the vertical component also 'enjoyed' deformations scaled in accordance with this linear scaling ratio. These component trans- were, however, independent of applied wheel slip rate.

- c) The value of vertically loaded plate bearing tests is questioned, in that they provide no information on slip-rate dependent behaviour. It is also considered unlikely that the modified plate bearing tests of Dickson (1963) or Reece (1966) can reproduce translation patterns within the soil that are similar to those occurring under a driven wheel, and for this reason their application is necessarily limited.
- d) A comparison of the translation patterns that occur under wheels driven at a similar negative slip rate to McKibben's (1938), towed wheels reveals significant differences. The widely used practice of relating powered wheel performance, via scaled plate tests, to towed wheel performance, although at identical slip rates, therefore appears to be questionable.

C. Claim to Original Work.

The development of the Cine Flash X-ray technique, with the acknowledged assistance of others, has made it possible to study the non-linear translations, the velocities and the accelerations that occur within the sand under a variety of controlled wheel loads. The quantitative description of the soil response, under the centre-line of a driven rigid wheel, has thus been defined for the first time in terms of these variables. This is seen as an essential step towards the prediction of soft-soil wheel performance, and is used as a basis for examining previous theories.

To the best of this writer's knowledge, dynamic similitude of the soil-wheel system has been established for the first time, thus permitting a rational analysis of both scaled deformations and scaled forces.

CHAPTER VII

RECOMMENDATIONS FOR FURTHER STUDY

The following recommendations, based on this research, are considered to be integral steps in the development of successful predictions of vehicular performance:

- 1) That a two phase research program be followed: the first phase directed towards an extension of the experimental technique and the second phase directed towards a complementary theoretical development. Phase 1) should include:
 - i) Measurements of the subsurface translations in the surface to 1.5" depth, in the plane of the rolling wheel centre-line. This will require modifications to the existing facility.
 - ii) Measurements of the three dimensional translation patterns of tracer-objects initially placed in planes exposed to an asymmetric stressing condition. The development of a stereoscopic Ciné Flash X-ray system - using an additional pulser and an augmented power supply - is seen as one means of achieving this.
 - iii) The modification of the wheel flexure frame to provide reliable drawbar pull measurements, in order to evaluate the dissipated energy coefficient, ρ' , from known values of the D.B.P. coefficient, Λ . This would provide essential information on the scaling of ρ' , for an evaluation of the Chudakov-Phillips assumption - see Chapter V.
 - iv) More detailed investigations of the sand preparation technique and the in situ density changes.
- Phase 2) would necessarily be directed towards the development of approp-

riate constitutive equations to describe the complex deformations occurring beneath a driven wheel. A complete mathematical description of the soil response must not only account for such items as a) three dimensional translations that result from 'yield' both below and beyond (i.e. flow) failure; b) non-unique stress strain relationships; c) large, non-recoverable, volume changes resulting from both deviatoric and isotropic stresses; d) non-unique physical properties (e.g. dilatant dependent frictional parameters), to mention a few; but must also provide a solution. This phase is, in consequence, extremely complex.

- 2) That the scope of the experimentation be extended to other soil conditions; including silts and clays, under a representative range of moisture contents.
- 3) That the similitude relations explored in this study be examined over a wider range of wheel sizes, and thus at larger values of the linear scaling ratio, λ .
- 4) That, if greater precision is required from the mensurational technique, the dimension Z_2 - Fig. III-2 - be increased by the use of a higher Kilo-voltage Pulser unit. The justification for this statement is found in Appendix III-G-1.

APPENDICES

APPENDIX I

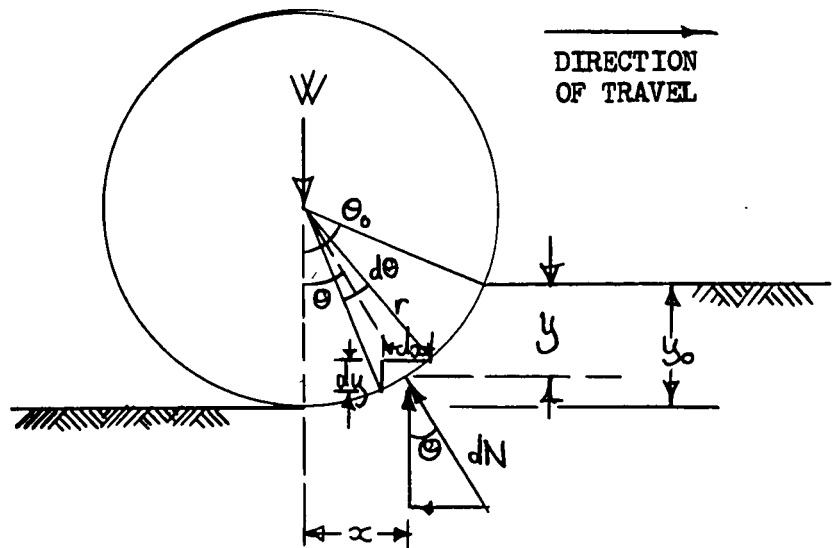
The Derivation of Equations (I-3) and (I-4)

FIGURE (I-A)

Notation for a Plane Rolling wheel (zero-slip).

b = width of wheel.

Note $dy = r d\theta \sin \theta$



Bekker assumed that the soil reaction was purely radial, dN , and equal to the normal pressure beneath a horizontal footing at the same depth.

Repeating equations (I-1) and (I-2), with the same assumptions:

$$p = \left\{ \frac{K_c}{b} + K_\phi \right\} y^n \quad (\text{I-1})$$

$$R = b \int_0^{y_0} \left(\frac{K_c}{b} + K_\phi \right) y^n dy \quad (\text{I-2})$$

From Figure (I-A), since $dN = pbrd\theta$

$$R = \int_0^{\theta_0} (pbr) \sin \theta d\theta \quad (1)$$

$$W = \int_0^{\theta_0} (pbr) \cos \theta d\theta \quad (2)$$

from (1)

$$R = \int_{y=0}^{y_0} b \left\{ \frac{K_c}{b} + K_\phi \right\} y^n dy = \frac{b \left\{ \frac{K_c}{b} + K_\phi \right\} y_0^{n+1}}{n+1} \quad (3)$$

From the geometry of Fig. (I-A)

$$x^2 = (2r - (y_0 - y))(y_0 - y)$$

or for small sinkages the approximation

$$x^2 = 2r(y_0 - y), \quad \text{i.e.} \quad 2x dx = -2r dy \quad (4)$$

is used in the evaluation of equation (2) in terms of the sinkage. That is:

$$W = \int_{x=0}^{\sqrt{y_0(2r-y_0)}} b \left\{ \frac{K_c}{b} + K_\phi \right\} y^n dx = b \left\{ \frac{K_c}{b} - K_\phi \right\} \int_{y=0}^{y_0} \frac{\sqrt{2r} y^n}{2\sqrt{(y_0-y)}} dy. \quad (5)$$

To integrate equation (5) let $s^2 = y_0 - y$ and thus $dy = -2s ds$ and

$$W = \sqrt{2r} b \left\{ \frac{K_c}{b} + K_\phi \right\} \int_{s=0}^{s=\sqrt{y_0}} (y_0 - s^2)^n ds \quad (6)$$

Taking the first two terms of the expanded $(y_0 - s^2)^n$ series

i.e. $y_0^n - n y_0^{n-1} s^2 + \dots$

$$W = b \left\{ \frac{K_c}{b} + K_\phi \right\} \frac{\sqrt{2r}}{3} y_0^{n+\frac{1}{2}} (3-n) \quad (7)$$

from (7)

$$y_0 = \left[\frac{3W}{(3-n)(K_c + bK_\phi)\sqrt{2r}} \right]^{\frac{2}{2n+1}} \quad (I-3)$$

and from (3)

$$R = \frac{1}{(n+1)(K_c + bK_\phi)^{\frac{1}{2n+1}}} \left[\frac{3W}{(3-n)\sqrt{2r}} \right]^{\frac{2n+2}{2n+1}} \quad (I-4)$$

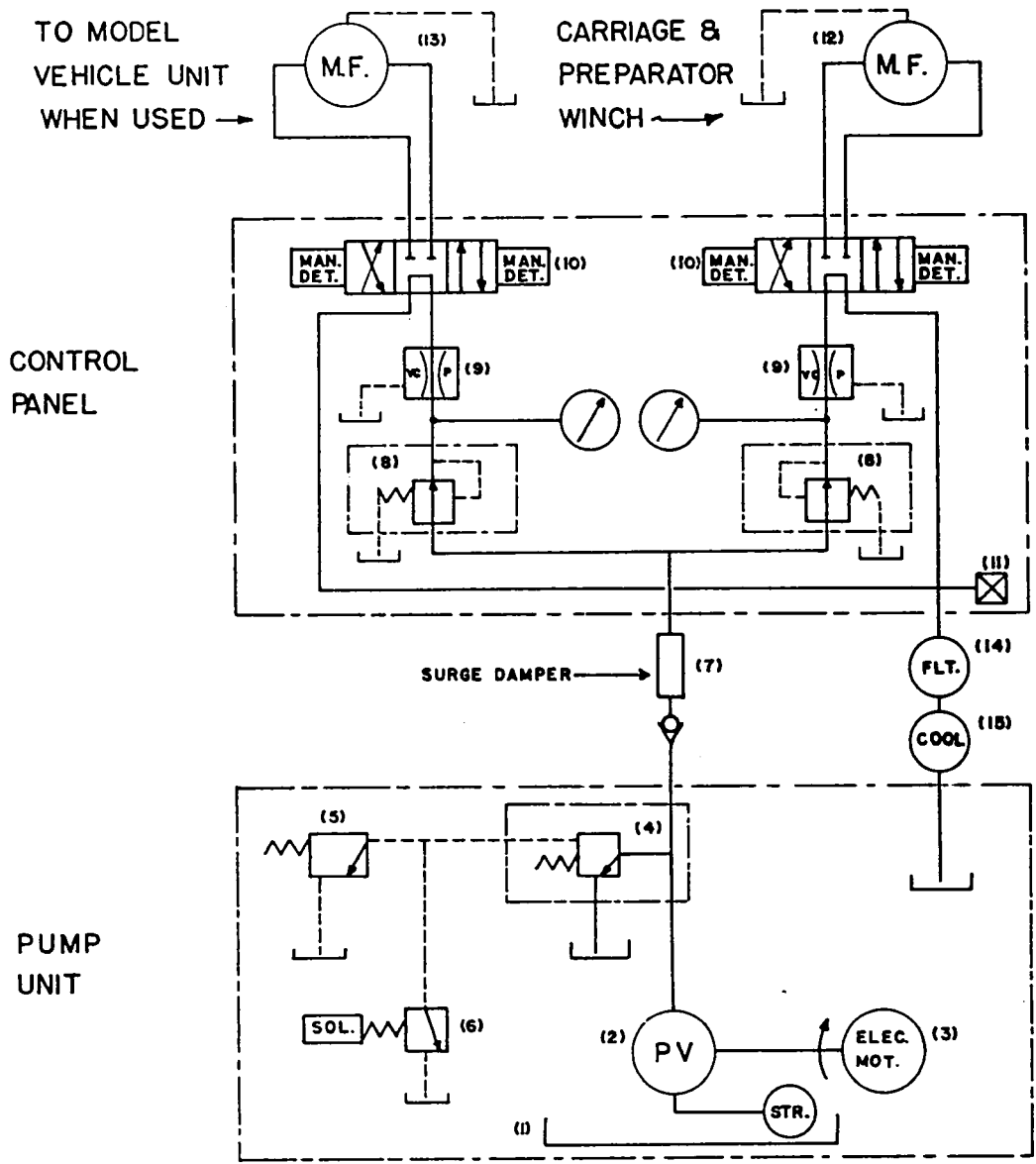
APPENDIX II

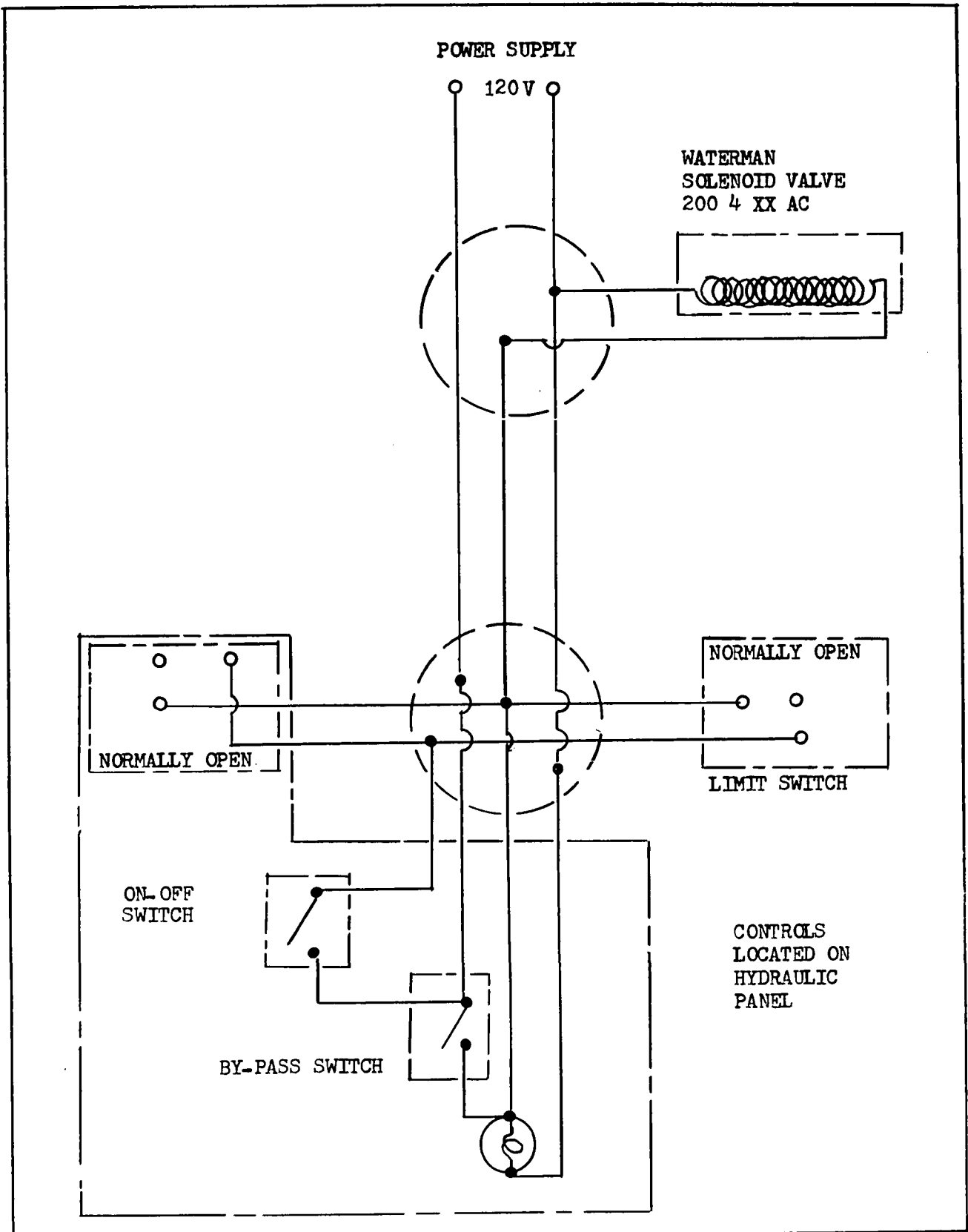
	Page.
II-B2-1	Hydraulic Circuitry of Soil-Vehicle Test Facility. 120
II-B2-2	The Electrical Circuitry of Hydraulic System. 121
II-B2-3	Flow Control Valve Settings. 136
II-B3	The Wheel Carriage Design. 122
II-B4	Schematic of Wheel Drive and Gear Housing. 123
II-C1-1	The Derivation of the Wheel Scaling Ratios. 124
II-C1-2	Wheel Specifications. 127
II-C1-3	Photograph of Test Wheels and Sample SEL2005/12 Output for Test No. 14. 128
II-D-1	Electric Signal Circuitry of Soil-Vehicle Facility. 129
II-D-2	Additional Information on Electric Signal Circuitry of Test Facility. 130
II-D-3	Calibration Equations for Complete Test Series. 132
II-D-4	The Calibration Procedure. 134
II-D-5	Sample Calibration of Angular Wheel Velocity and Carriage Velocity. 137
II-D-6	Sample Calibration of Sinkage and Torque. 138
II-D-7	Sample Calibration of Drawbar Pull Flexures. 139
II-D-8	Sample Calibration of Dymec-XY Plotter System and Voltmeter for Slip Rate Control. 140
II-E2-1	The Derivation of Radiographic Equivalence Factors for Two-Phase Sand Systems. 141
II-E2-2	The Fabrication of Tracer Objects. 148

APPENDIX II (Cont'd.)

	Page.	
II-E2-3	A Complementary Study to Determine Whether the Tracer-Objects Move Relative to the Sand Surrounding Them.	149
II-E2-4	Schematic of Ciné-Radiographic System.	151

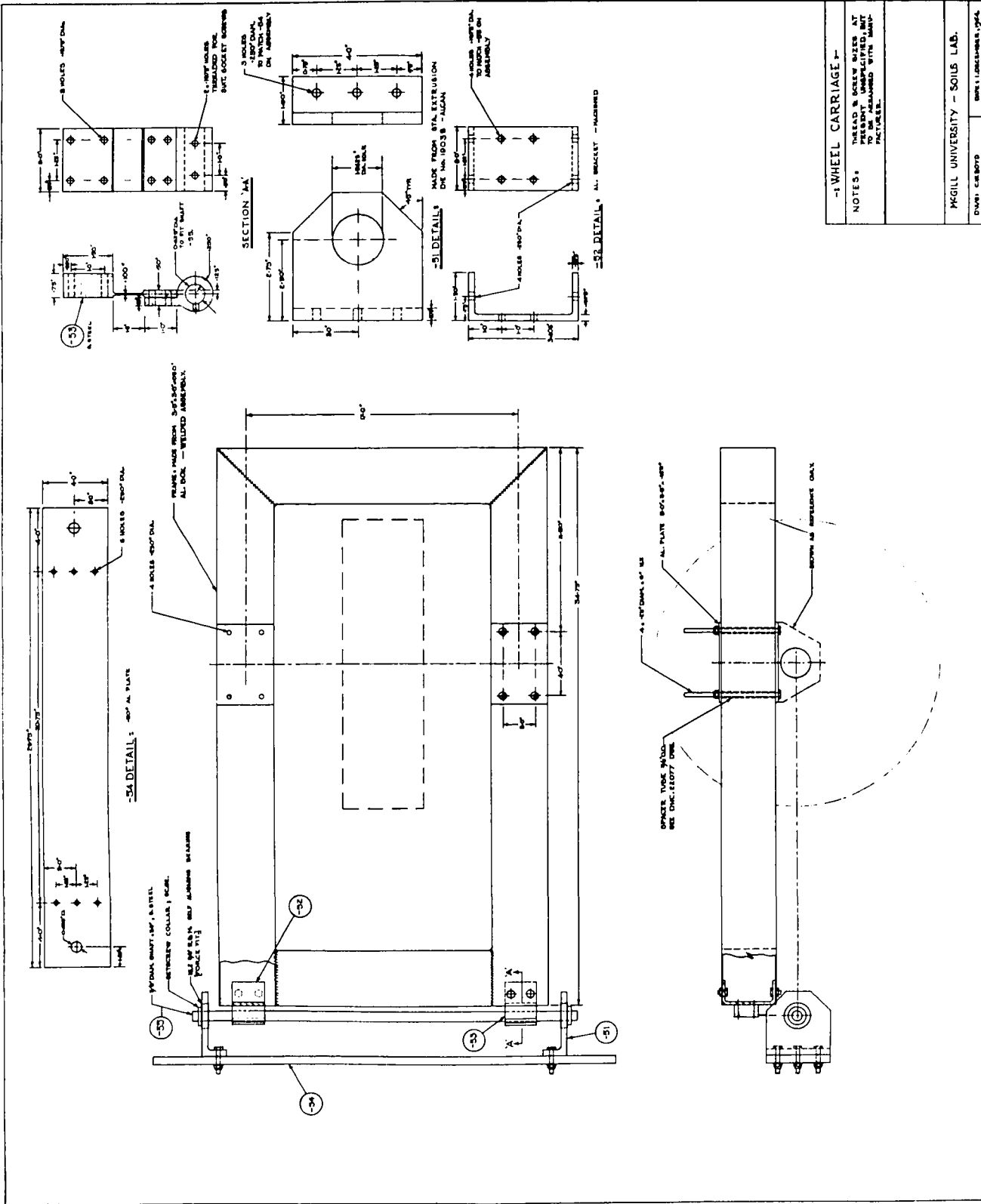
COMPONENT LIST	
1	RESERVOIR DENISON
2	PUMP BA.202.574.B DENISON
3	MOTOR, ELEC. 30.3FB TYPE N HOWELL ELECTRIC
4	VALVE, RELIEF, 3511-707-X DENISON
5	VALVE, NEEDLE, VICKERS
6	VALVE, SOL'D 200-4-XX AC WATERMAN
7	SURGE DAMPER E.112 P-16 DENISON
8	VALVE, PRES. RED. FCG. 02.1000-31 VICKERS
9	VALVE, FLOW CONT. 3512170.X VICKERS
10	VALVE, DIRECTIONAL, 143 P 3HO-3 BARKSDALE
11	VALVE, MANUAL
12	MOTOR, HYDRAULIC. LMH-125 LUCAS-ROTAX
13	MOTOR, HYDRAULIC. 1A4 LUCAS-ROTAX
14	FILTER CUNO ENG.
15	COOLER E502. EY. YOUNG
HYDRAULIC CIRCUITRY OF SOIL-VEHICLE TEST FACILITY	
DRAWN BY: C.W. BOYD 16.1.64	





APPENDIX II-B2-2

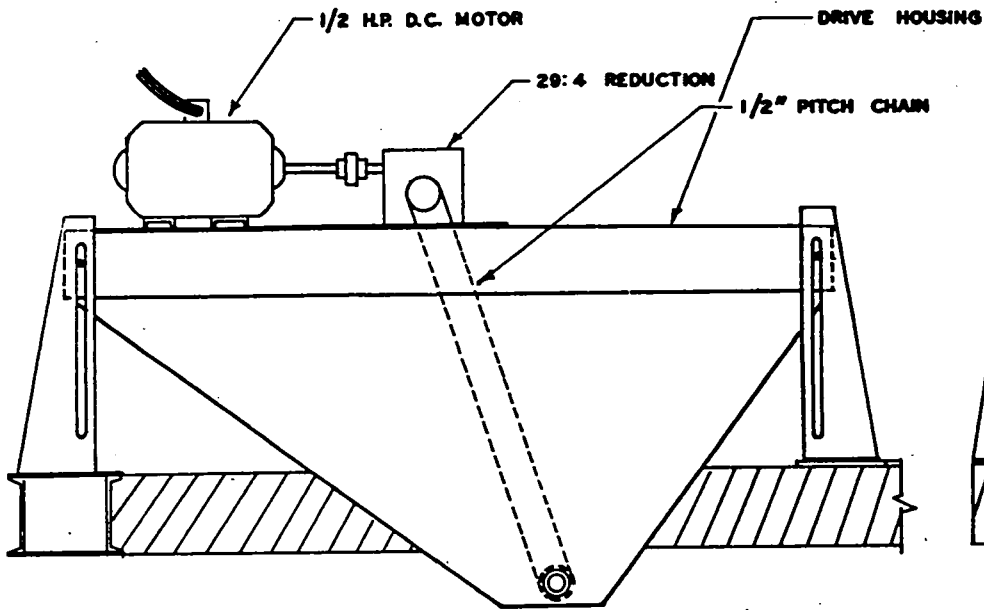
THE ELECTRIC CIRCUITRY OF HYDRAULIC SYSTEM



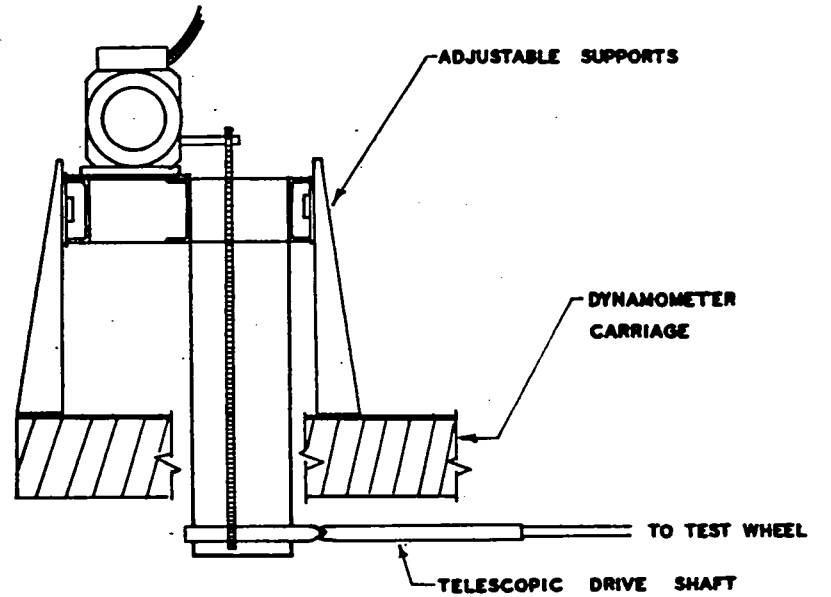
-1 WHEEL CARRIAGE -

NOTES:
 1. THREAD & SCREW SIZES AT PRESENT UNSPECIFIED, BUT MUST BE OBTAINED WITH MANUFACTURER.

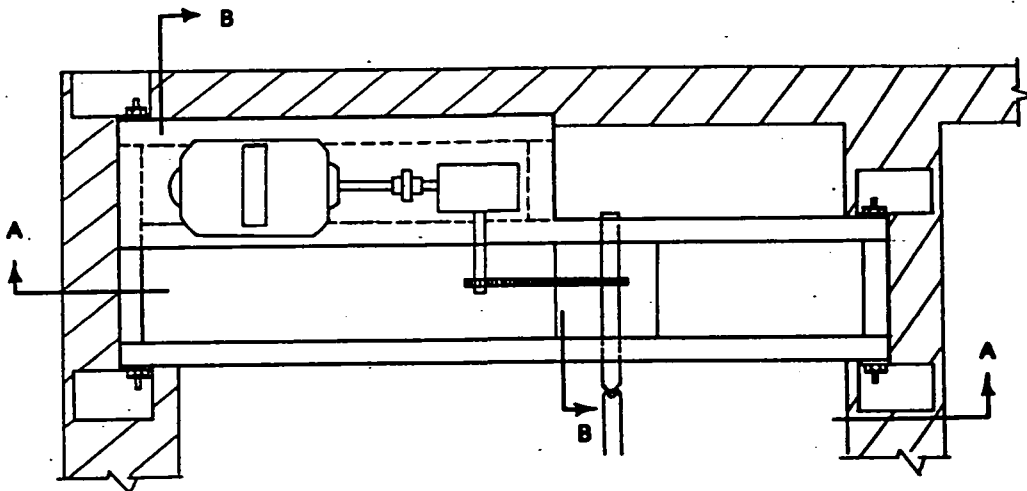
McGILL UNIVERSITY - SOILS LAB.
 DWG. CS-8070



SECTION A-A



SECTION B-B



APPENDIX II B4

SCHMATIC OF WHEEL DRIVE
ASSEMBLY & GEARING.

APPENDIX II-C1-1THE DERIVATION OF THE WHEEL SCALING RATIOS

The following, n , variables were considered in the derivation of the scaling ratios:

- D = characteristic length, inches.
 t = characteristic time, seconds.
 Ω = power supplied to wheel, in.lbs./sec.
 P = nominal ground pressure, p.s.i.
 ω = angular wheel velocity radius^{ans}/sec.
 V = translational wheel velocity, ins./sec.
 $M.I.$ = moment of inertia.
 M = moment of force (Torque), in.-lbs.
 F = characteristic force, lbs.
 W = wheel load, lbs.

It is also assumed that both accelerations, g , and specific densities, ρ , are equivalent for model and prototype.

$$\text{i.e. } \begin{aligned} \zeta_m &= \zeta_p & \text{where subscripts 'm' and 'p' denote} \\ \rho_m &= \rho_p & \text{model and prototype respectively.} \end{aligned}$$

From the above variables the following dimensional matrix may be constructed.

	K_1	K_2	K_3	K_4	K_5	K_6	K_7	K_8	K_9	K_{10}	
	W	F	M	$M.I.$	V	ω	P	Ω	t	D	
M	1	1	1	1	0	0	1	1	0	0	Dimensional Matrix
L	1	1	2	2	1	0	-1	2	0	1	
T	-2	-2	-2	0	-1	-1	-2	-3	1	0	

APPENDIX II-C1-1 (Cont'd.)

Since the third order determinant, involving the exponents of the dimensions of variables Ω , t and D , is nonzero, the rank, r , of the matrix is 3.

Thus a complete set of dimensionless products contains $(n-r)$ or $10-3$, i.e. 7 components, (Langhaar, 1951).

From Buckingham's π theorem, any product of the n variables has the form:

$$\pi = W^{K_1} F^{K_2} M^{K_3} \text{M.I.}^{K_4} V^{K_5} \omega^{K_6} P^{K_7} \Omega^{K_8} t^{K_9} D^{K_{10}}$$

Substituting the dimensions of each variable in the above equation one obtains the exponents of M , L and T in terms of the unknown K values and their coefficients. These exponents are used to obtain the solution matrix from the above dimensional matrix, since by substitution:

$$K_8 = -K_1 - K_2 - K_3 - K_4 - K_7$$

$$K_9 = -K_1 - K_2 - K_3 - 3K_4 + K_5 + K_6 - K_7$$

$$K_{10} = K_1 + K_2 - K_5 + 3K_7$$

and the Solution matrix becomes

	K_1	K_2	K_3	K_4	K_5	K_6	K_7	K_8	K_9	K_{10}
π_1	1	0	0	0	0	0	0	-1	-1	1
π_2	0	1	0	0	0	0	0	-1	-1	1
π_3	0	0	1	0	0	0	0	-1	-1	0
π_4	0	0	0	1	0	0	0	-1	-3	0
π_5	0	0	0	0	1	0	0	0	1	-1
π_6	0	0	0	0	0	1	0	0	1	0
π_7	0	0	0	0	0	0	1	-1	-1	3

One thus obtains the seven independent π terms

$$\pi_1 = \frac{WD}{\Omega t} ; \quad \pi_2 = \frac{FD}{\Omega t} ; \quad \pi_3 = \frac{M}{\Omega t} ; \quad \pi_4 = \frac{(\text{M.I.})}{\Omega t^3}$$

$$\pi_5 = \frac{Vt}{D} ; \quad \pi_6 = Dt ; \quad \pi_7 = \frac{PD^3}{\Omega t}$$

Since it has been assumed that gravitational accelerations can not realistically be scaled, and that the Froude number for both model and prototype must be equivalent, then:

$$\left[\frac{v^2}{gD} \right]_m = \left[\frac{v^2}{gD} \right]_p \quad (\text{where } g_m = g_p)$$

$$\frac{D_p}{D_m} = \frac{(t^2)_p}{(t^2)_m} \quad \text{or} \quad \frac{t_p}{t_m} = \sqrt{\lambda}$$

$$\text{where } \lambda = \frac{D_p}{D_m}$$

Since densities have not been scaled

$$\frac{W_p}{W_m} = \frac{(\rho V)_p}{(\rho V)_m} = \frac{D_p^3}{D_m^3} = \lambda^3$$

Thus the following scaling ratios may be obtained from the seven π terms:

$$\pi_1 = \left[\frac{WD}{\Omega t} \right]_p = \left[\frac{WD}{\Omega t} \right]_m \quad \therefore \frac{\Omega_p}{\Omega_m} = \lambda^3 \cdot \frac{1}{\lambda^{7/2}} = \lambda^{7/2}$$

$$\pi_2 = \left[\frac{FD}{\Omega t} \right]_p = \left[\frac{FD}{\Omega t} \right]_m \quad \therefore \frac{F_p}{F_m} = \lambda^{7/2} \cdot \frac{1}{\lambda} \cdot \lambda^{1/2} = \lambda^3$$

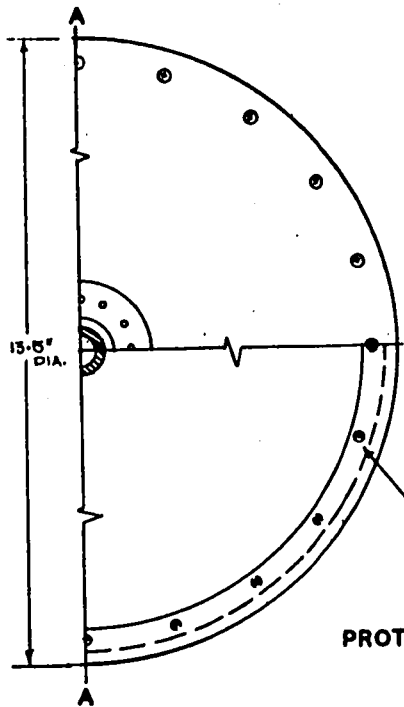
$$\pi_3 = \left[\frac{M}{\Omega t} \right]_p = \left[\frac{M}{\Omega t} \right]_m \quad \therefore \frac{M_p}{M_m} = \lambda^{7/2} \cdot \lambda^{1/2} = \lambda^4$$

$$\pi_4 = \left[\frac{(M.I.)}{\Omega t^3} \right]_p = \left[\frac{(M.I.)}{\Omega t^3} \right]_m \quad \therefore \frac{(M.I.)_p}{(M.I.)_m} = \lambda^{7/2} \cdot \lambda^{3/2} = \lambda^5$$

$$\pi_5 = \left[\frac{Vt}{D} \right]_p = \left[\frac{Vt}{D} \right]_m \quad \therefore \frac{V_p}{V_m} = \lambda \cdot \frac{1}{\lambda^{1/2}} = \lambda^{1/2}$$

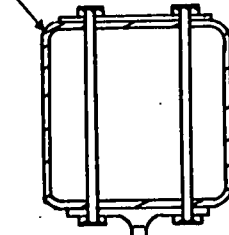
$$\pi_6 = [\omega t]_p = [\omega t]_m \quad \therefore \frac{(\omega)_p}{(\omega)_m} = \frac{1}{\lambda^{1/2}} = \lambda^{-1/2}$$

$$\pi_7 = \left[\frac{PD^3}{\Omega t} \right]_p = \left[\frac{PD^3}{\Omega t} \right]_m \quad \therefore \frac{P_p}{P_m} = \lambda^{7/2} \cdot \frac{1}{\lambda^3} \cdot \lambda^{1/2} = \lambda$$



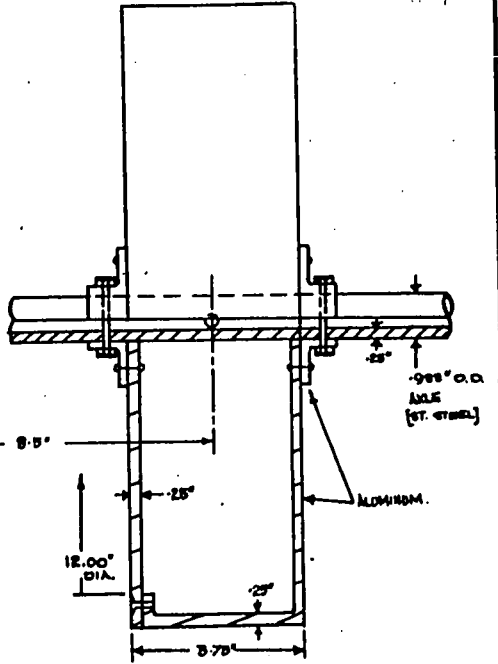
SIDE ELEVATION

FLEXURE FRAME

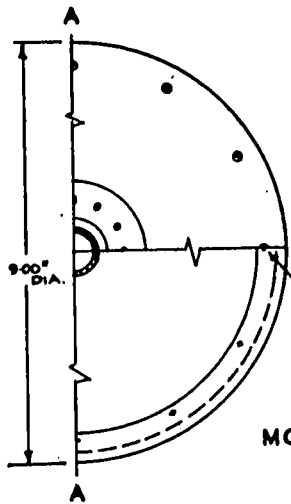


20 HOLES C/C [SPACED AT 18°] ON 12.5" DIA.

PROTOTYPE WHEEL

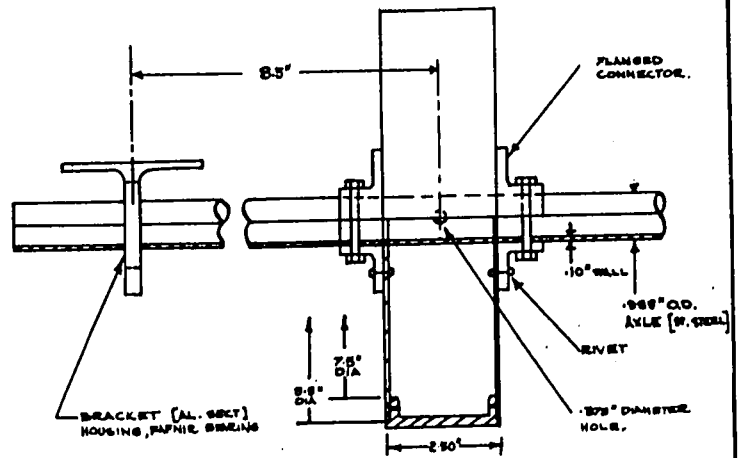


SECTION A-A



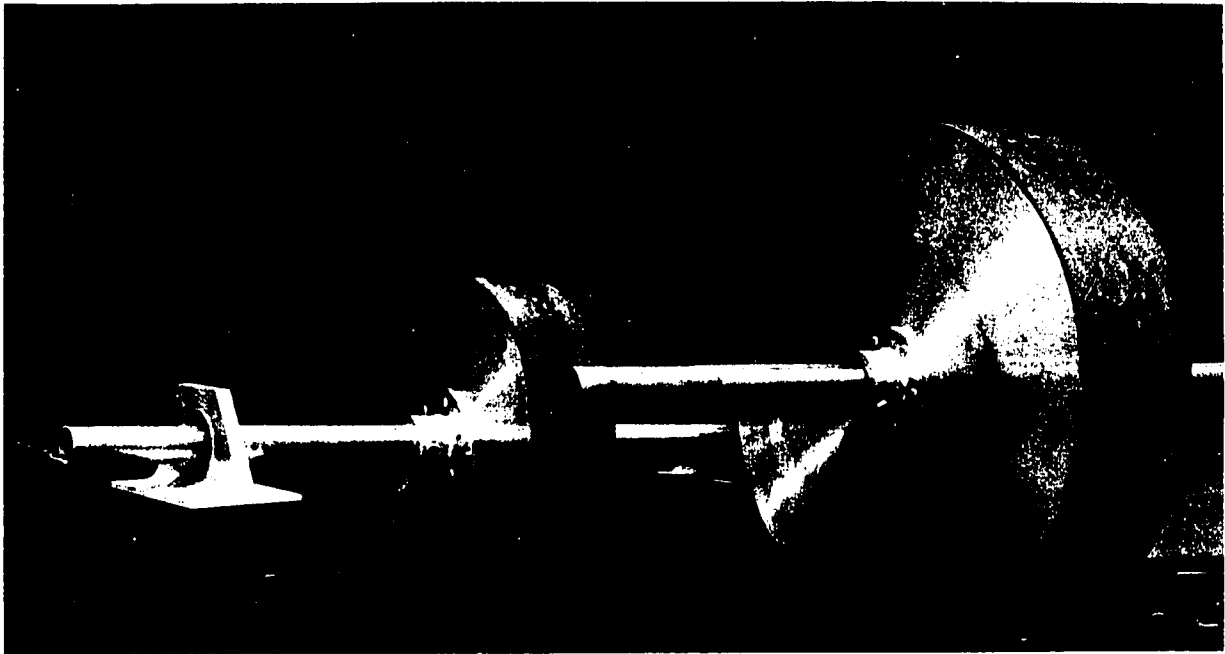
MODEL WHEEL

12 HOLES C/C [SPACED AT 30°] ON 9" DIA.

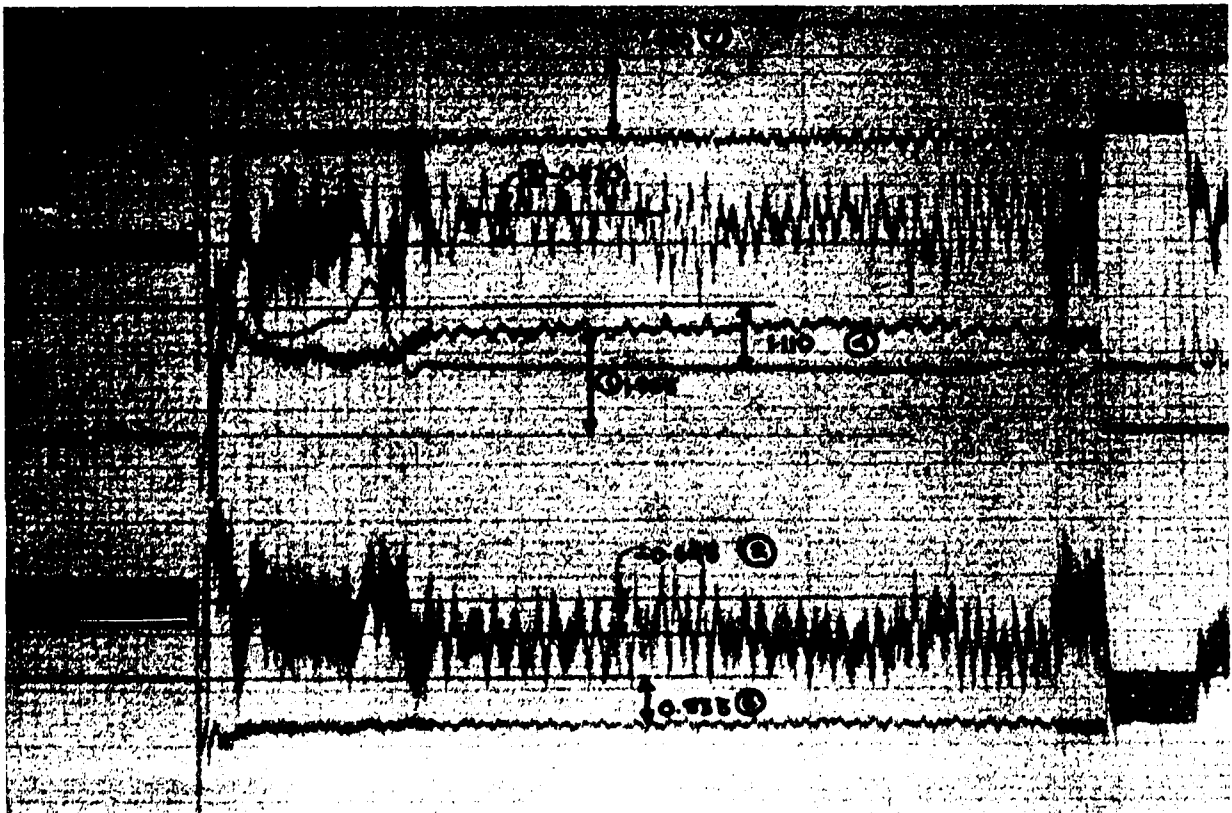


APPENDIX II - CI - 2 : WHEEL SPECIFICATIONS

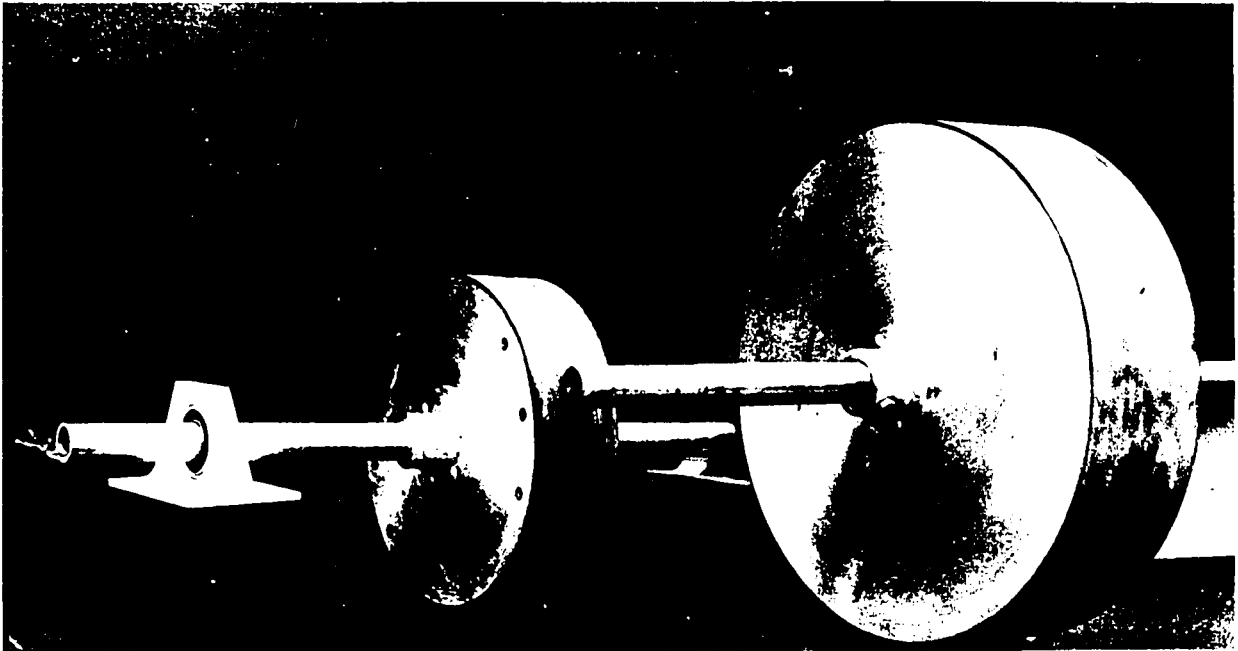
FROM DE HAVILLAND DRAWINGS: DHC22077 & DHC22079



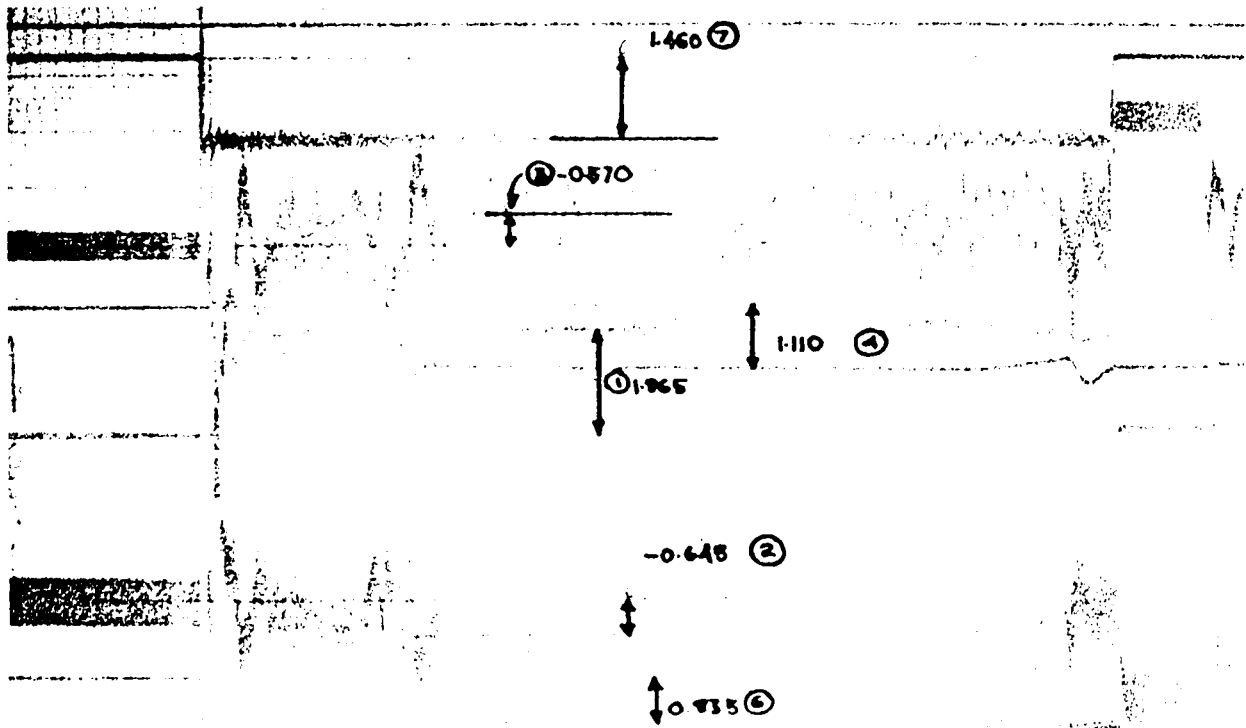
THE 9" AND 13.5" DIAMETER TEST WHEELS (see Appendix II-CI-2)



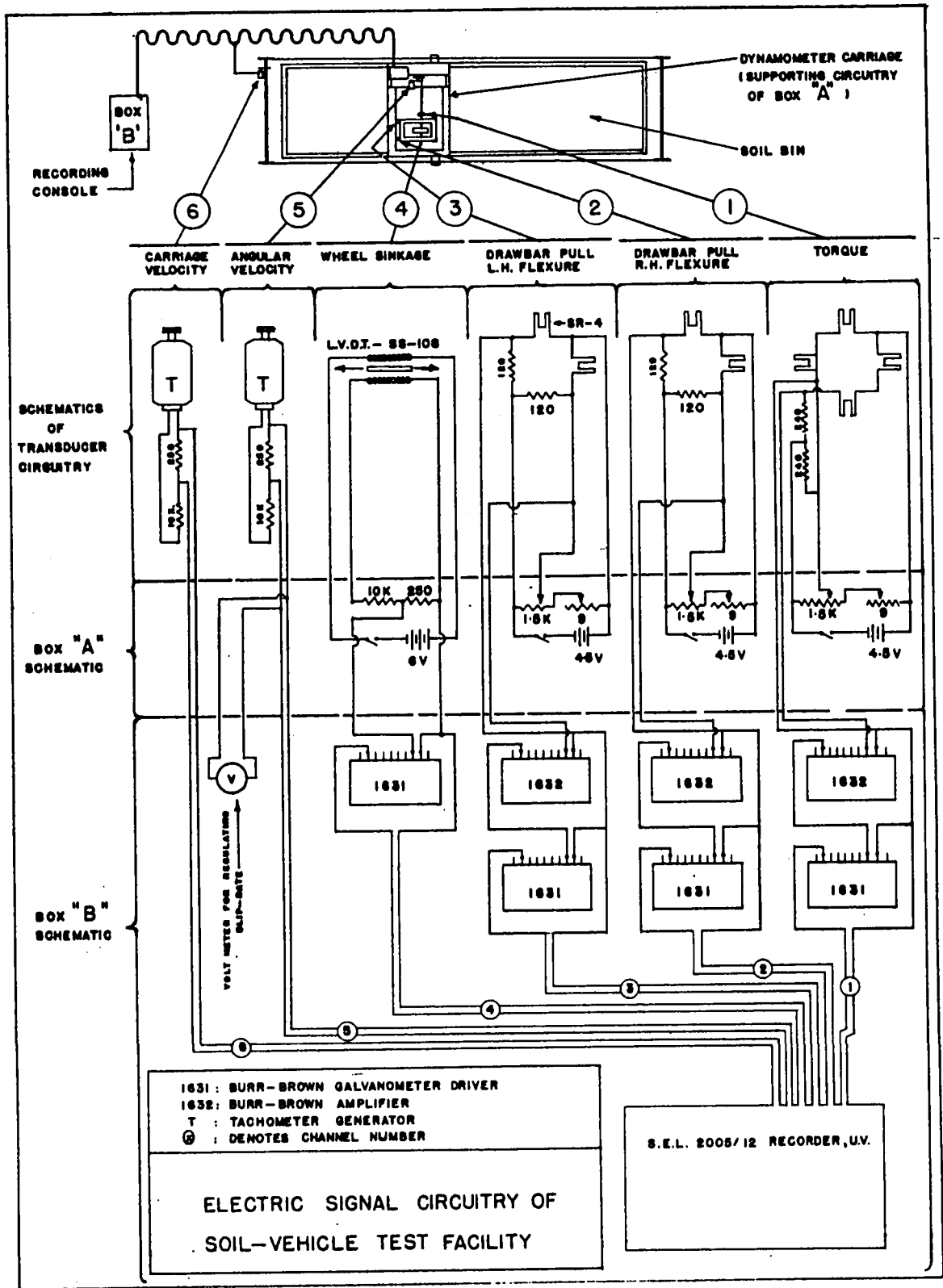
SAMPLE S.E.L. 2005/12 RECORDER OUTPUT, SHOWING TEST No. 14 TRACES.
Where ⊗ represents channel number.



THE 9" AND 13.5" DIAMETER TEST WHEELS (see Appendix II-CI-2)



SAMPLE S.E.L. 2005/12 RECORDER OUTPUT, SHOWING TEST No. 14 TRACES.
Where ⊗ represents channel number.



ELECTRIC SIGNAL CIRCUITRY OF SOIL-VEHICLE TEST FACILITY

APPENDIX II-D-2ADDITIONAL INFORMATION ON ELECTRIC SIGNAL CIRCUITRY OF TEST FACILITY

CHANNEL	1	2 AND 3	4
MEASUREMENT	TORQUE	DRAWBAR PULL	SINKAGE
MANUFACTURER OF DEVICE (& MODEL NO.)	L & T INSTRUMENTS CO., MONTREAL (To our specifications).	L & T INSTRUMENTS MONTREAL (To our specifications).	L.G. COLLINS CORP. LONG BEACH, CAL. (LVDT No. SS-108)
DEVICE SPECS.	See Windisch (1967) wheatstone, temperature compensated, bridge circuit with augmented output. 4 strain gauges: Budd C6-141-B	Spring Steel. two sets. Wheatstone bridge circuit, temperature compensated) augmented output. 2 strain gauges/ flexure. Budd C6-141-B.	L.V.D.T. 3" extension. Linear motion transducer. S/N. (4526)
SLIP RINGS	TYPE SR10M Michigan Scientific.	N.A.	N.A.
POWER SUPPLY TO DEVICE	4.5 volt dry cell + Zena diode. (Santarzantype V.R.4.5)	4.5 volt dry cell + Zena diode. (Santarzantype V.R.4.5)	6 volt dry cell + Zena diode (Santarzantype V.R.6.0)
PREAMPLIFIER (& SETTING)	BURR BROWN CORP. Galvanometer driver model 1632 (X2)	as for Channel 1 Burr Brown 1600-12R Power Supply	N.A.
AMPLIFIER (& SETTING)	Burr Brown Corp. model 1631 (X100)	as for Channel 1 Burr Brown 1600-12R Power Supply	as for Channel 1
S.E.L. GALVANOMETERS (NATURAL FREQ.) (SENSITIVITY)	C 300 240 c/s .12 ma/cm.	C 300 240 c/s .12 ma/cm.	C 300 240 c/s .12 ma/cm.

APPENDIX II-D-2 (Cont'd.)

ADDITIONAL INFORMATION ON ELECTRIC SIGNAL CIRCUITRY OF TEST FACILITY

CHANNEL	5	6
MEASUREMENT	ANGULAR VEL.	CARRIAGE VEL.
MANUFACTURER OF DEVICE (& MODEL NO.)	INSTRUMENT MOTORS CORP., STANFORD, CONN. (L23.023.4056)	INSTRUMENT MOTORS CORP., STANFORD, CONN. (L23.023.4056)
DEVICE SPECS.	Tachometer Generator. 3V(D.C.)/100 r.p.m. Max output: 5 watts	(As for channel 5)
SLIP RINGS	N.A.	N.A.
POWER SUPPLY TO DEVICE	N.A.	N.A.
PREAMPLIFIER (& SETTING)	N.A.	N.A.
AMPLIFIER (& SETTING)	N.A.	N.A.
S.E.L. GALVANOMETERS (NATURAL FREQ.) (SENSITIVITY)	C 300 240 c/s .12 ma/cm.	C 300 240 c/s .12 ma/cm.

APPENDIX II-D-3CALIBRATION EQUATIONS FOR COMPLETE TEST SERIES

In the following listings the circumflex, over the dependent variable, denotes the best estimate relationship. This is in all cases based on a least sum of squares criterion. The non 'Y' component of the dependent variable denotes the variable notation used in the subsequent S.V.S.I computer program. The independent variable 'X' refers to the galvanometer deflection of the U.V. Recorder (in centimeters):

Angular Velocity:

$$\hat{Y}_A = .001 + .327X \text{ revs/sec. (for tests 01} \rightarrow \text{10 inch)}$$

$$\hat{Y}_A = -.008 + .335X \text{ revs/sec. (for tests 11} \rightarrow \text{58 inch)}$$

Translational Carriage Velocity:

$$\hat{Y}_B = .36 + 5.1X \text{ ins/sec. (for tests 01} \rightarrow \text{58 inch)}$$

Drawbar Pull Flexure - Left Hand Side:

$$\hat{Y}_C = .039 + 3.496X - .388X^2 + .103X^3 \text{ lbs. (for tests 01} \rightarrow \text{35 inch)}$$

$$\hat{Y}_C = .2125 + 13.4994X - 1.844X^2 + 2.1166X^3 \text{ lbs. (for tests 36} \rightarrow \text{58 inch)}$$

Drawbar Pull Flexure - Right Hand Side:

$$\hat{Y}_D = .159 + 2.752X - .002X^2 + .023X^3 \text{ lbs. (for tests 01} \rightarrow \text{35 inch)}$$

$$\hat{Y}_D = -2.8729 + 19.3514X \text{ lbs. (for tests 36} \rightarrow \text{58 inch)}$$

Sinkage:

$$\hat{Y}_E = .048 + .513X \text{ inches (for tests 01} \rightarrow \text{35 inch)}$$

$$\hat{Y}_E = .02897 + .2368X + .0311X^2 - .0025X^3 \text{ inches (for tests 36} \rightarrow \text{58 inch)}$$

Torque:

$$\hat{Y}_F = -.0981 + 1.885X + .0433X^2 \text{ Ft.-lbs. (loading, for tests 01 and 02)}$$

APPENDIX II-D-3 (Cont'd.)

$$\hat{Y}_F = .07967 + .867X + .2222X^2 \text{ Ft.-Lbs. (unloading, for tests 01 and 02)}$$

$$\hat{Y}_F = .00208 - 1.0633X + 9.6112X^2 - 10.4387X^3 + 5.1347X^4 - 1.1718X^5 \\ + .1006X^6 \text{ inch-lbs. (loading for tests 03 } \rightarrow \text{ 35 inch)}$$

$$\hat{Y}_F = - 2.2123 + 82.0738 \text{ inch-lbs. (loading for tests 36 } \rightarrow \text{ 58 inch)}$$

DIGITAL VOLT METER (DYMEC) TRANSFER

where the independent variable, V, refers to voltage.

ABSCISSAL CALIBRATIONS:

$$\hat{X} = 1.01V \text{ inches (for tests 01 } \rightarrow \text{ 28 inch)}$$

$$\hat{X} = .184 + .792V - .0003V^2 \text{ inches (for tests 29 } \rightarrow \text{ 58 inch)}$$

ORDINATE CALIBRATIONS:

$$\hat{Y} = - .1745 + 1.2135V - .0898V^2 + .0156V^3 \text{ inches (for tests 01 } \rightarrow \text{ 28 inch)}$$

$$\hat{Y} = - .4059 + 1.3614V - .1595V^2 + .0184V^3 - .0008V^4 \text{ inches (for tests} \\ \text{ 29 } \rightarrow \text{ 58 inch).}$$

APPENDIX II-D-4THE CALIBRATION PROCEDURERECORDER CHANNEL 1; APPLIED WHEEL TORQUE

The mechanical torque measuring device is described in detail by Windisch (1967). The telescopic drive shaft was first disconnected and the wheel was locked rigidly to a firm immovable base. A steel lever arm was locked into the torque device drive shaft aperture, and a known moment was applied by a system of pulleys, hangers and weights. The U.V. galvanometer deflection was then recorded for a series of controlled applied moments. A representative calibration curve is included as Appendix II-D-6, where a pronounced hysteresis loop is observed on unloading. The plotted points represent an average of three loading-unloading cycles. This hysteresis resulted from internal mechanical friction within the torque device, which under the dynamic conditions of the actual testing is reduced by the vibrations of the wheel carriage-drive mechanism assembly.

RECORDER CHANNELS 2 and 3; DRAW BAR PULL

The wheel was placed on an aluminum plate and the wheel carriage levelled by adjusting the support fixture. After disconnecting one flexure the connected one was loaded with a wire and pulley system; steps being taken to ensure symmetric loading; the U.V. galvanometer trace deflection was then recorded against known load increments and the results plotted as in Appendix II-D-7. A similar process was repeated for the second flexure. The I.B.M. CURFIT subroutine being used to obtain the least sum of squares, best fit, polynomial. Virtually no hysteresis was noticed on unloading.

RECORDER CHANNEL 4; SINKAGE

APPENDIX II-D-4 (Cont'd.)

A pair of vernier calipers was attached to the L.V.D.T. and the U.V. galvanometer trace deflection was recorded for known L.V.D.T. extensions. The calibration was of the first degree, as anticipated, and a sample calibration is included in Appendix II-D-6. It should be noted that a no-sinkage L.V.D.T. setting is used for the zero adjustment of the galvanometer trace.

RECORDER CHANNEL 5: ANGULAR WHEEL VELOCITY

This calibration was obtained simply by recording the time taken for ten wheel revolutions, at a constant rheostat setting, and noting the corresponding galvanometer trace deflection. The procedure was then repeated for 14 other rheostat settings. Appendix II-D-5 contains a sample calibration.

RECORDER CHANNEL 6: TRANSLATIONAL WHEEL VELOCITY

After setting the flow control valves to a constant value the time taken for the dynamometer carriage to travel a distance of 20 feet was recorded together with the corresponding galvanometer trace deflection. This was repeated three times for a total of 14 flow control settings, and plotted in Appendix II-D-5. It should be noted that the valve settings shown in Appendix II-D-5 are unreliable estimates of wheel velocity as the setting varied widely for a constant wheel translational speed. This necessitated trial checks before each test, based on the more reliable galvanometer deflections.

VOLTMETER REGULATION OF SLIP RATE

This simply consisted of calibrating the tachometer generator output from Channel 5, against the Channel 5 galvanometer deflection. The calibration results are shown in Appendix II-D-8.

THE X-Y PLOTTER - DYMEC SYSTEM

The power supply, Dymec and X-Y plotter were given 30 minutes to

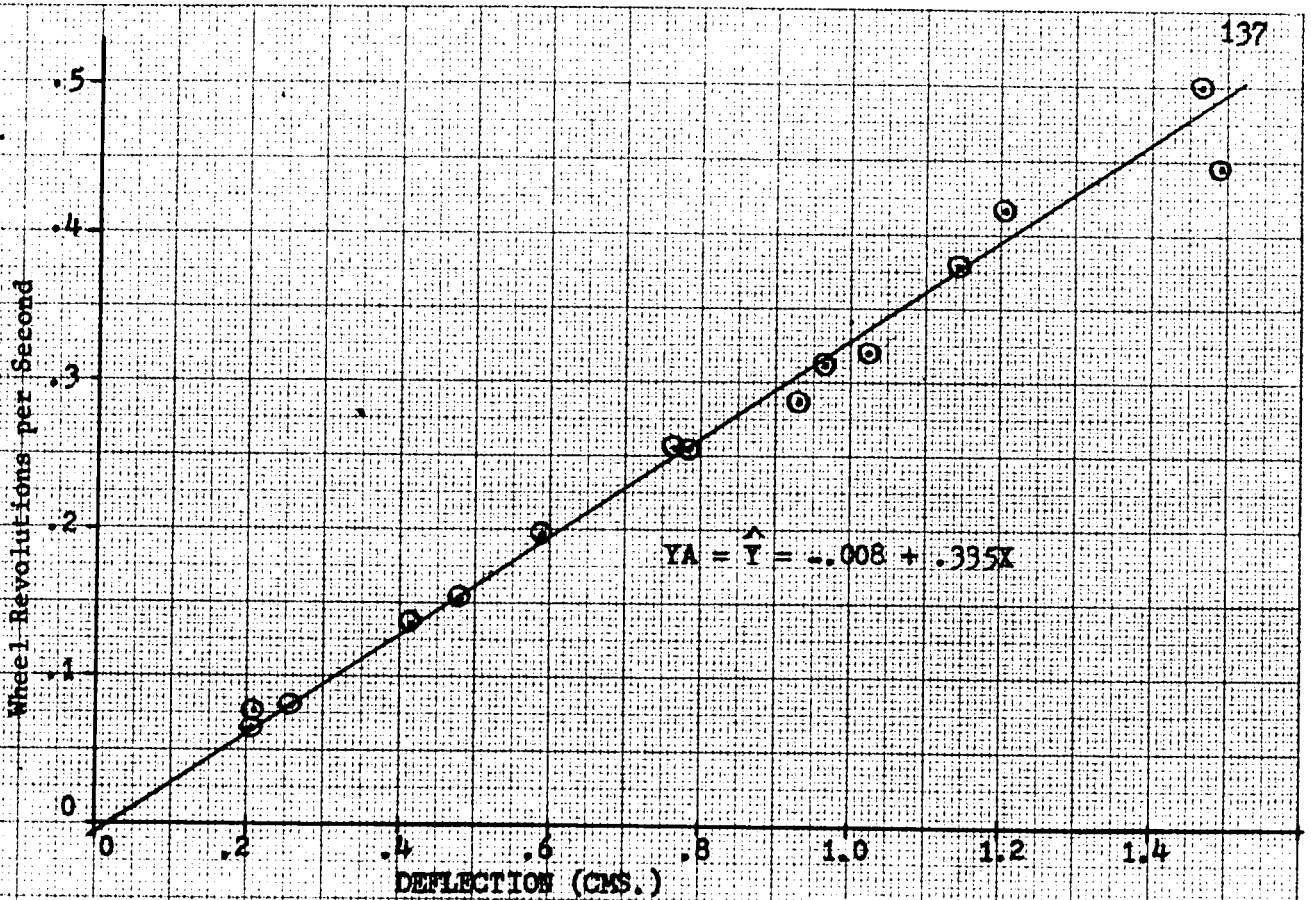
APPENDIX II-D-4 (Cont'd.)

stabilize. A grid with half inch orthogonal spacings was placed on the X-Y plotter, the bridge needle was placed on a given ordinate, and half inch abscissal increments were punched on to tape. The potentiometer controlling the ordinate value was left untouched for this first phase. An analogous procedure was carried out to obtain the ordinate calibrations. The tape was interpreted and the calibrations made. The linearity of output is illustrated in Appendix II-D-8.

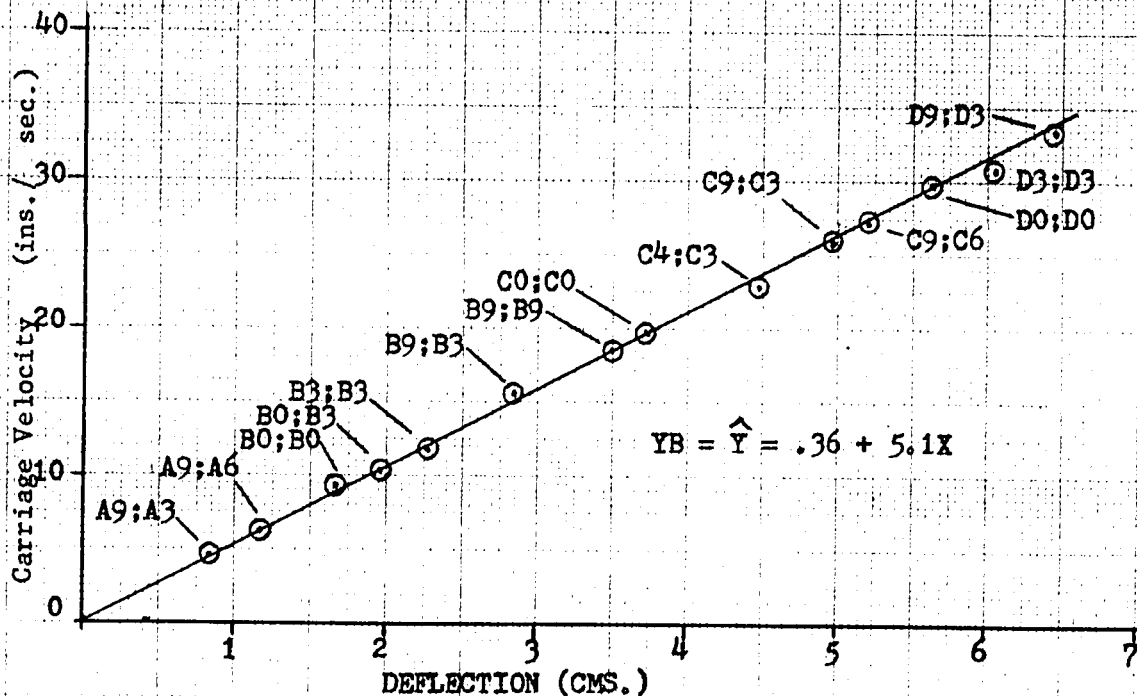
APPENDIX II-B2-3

Flow control valve settings for soil preparation:

For 1" increments	Left hand valve setting:	A-2	
	Right hand valve setting:	E 10.5	
For 1.5" increments	Left hand valve setting:	A-2	Forward
	Right hand valve setting:	E 10.5	
	Left hand valve setting:	A-2	Reverse
	Right hand valve setting:	E 50	

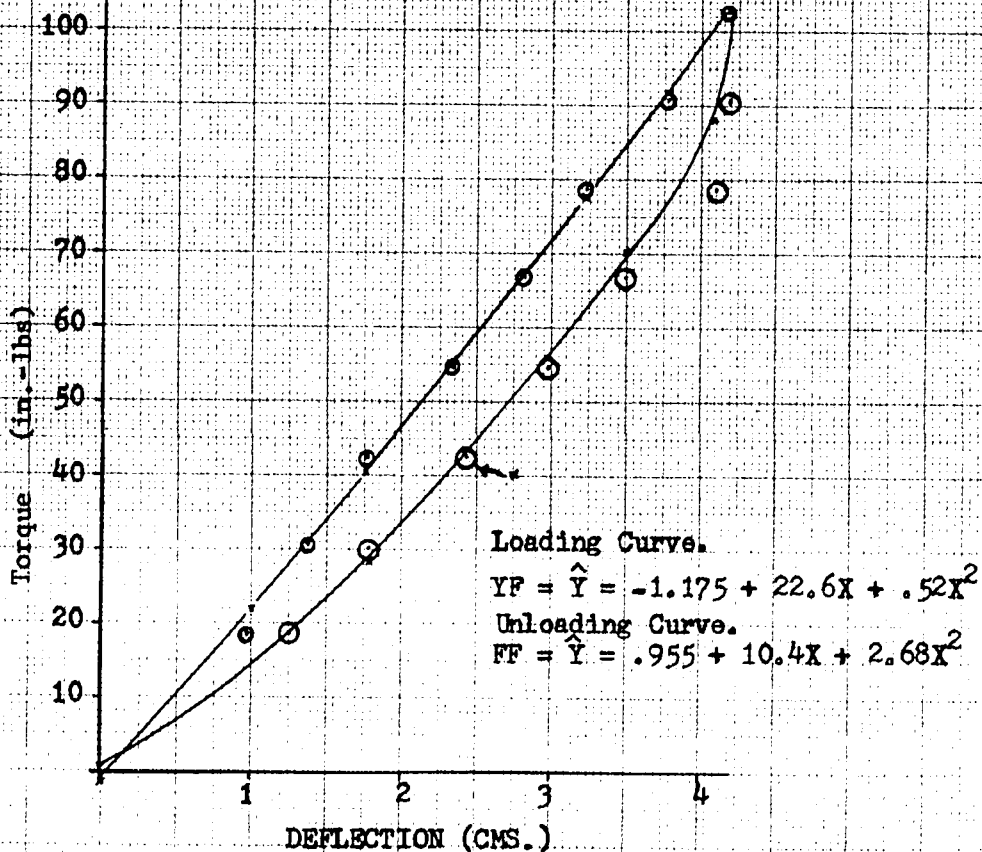
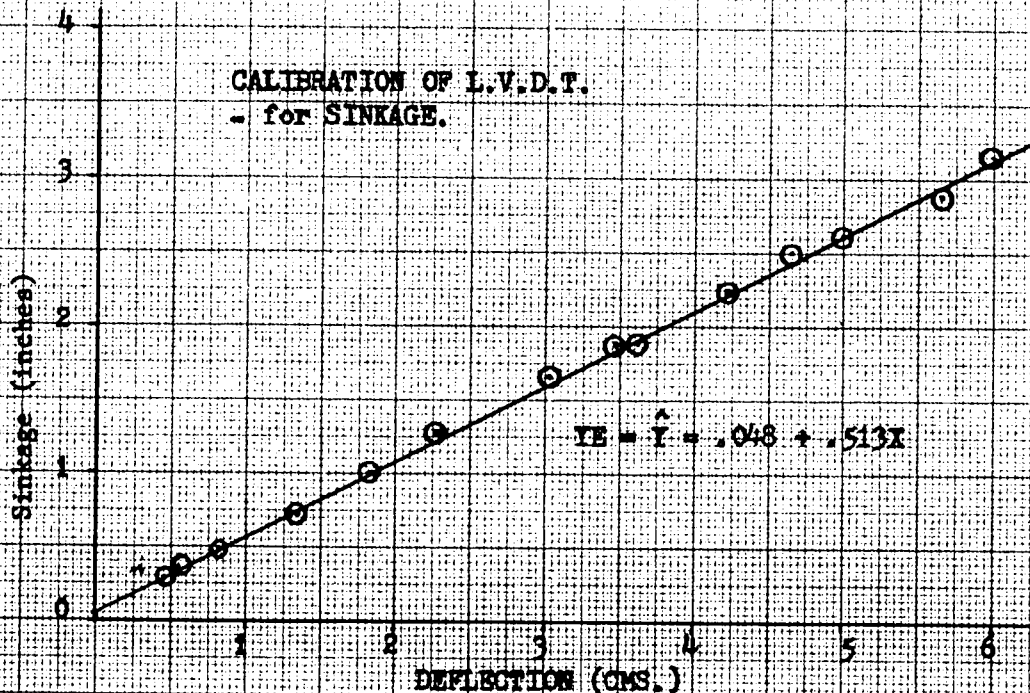


CALIBRATION OF ANGULAR WHEEL VELOCITY.



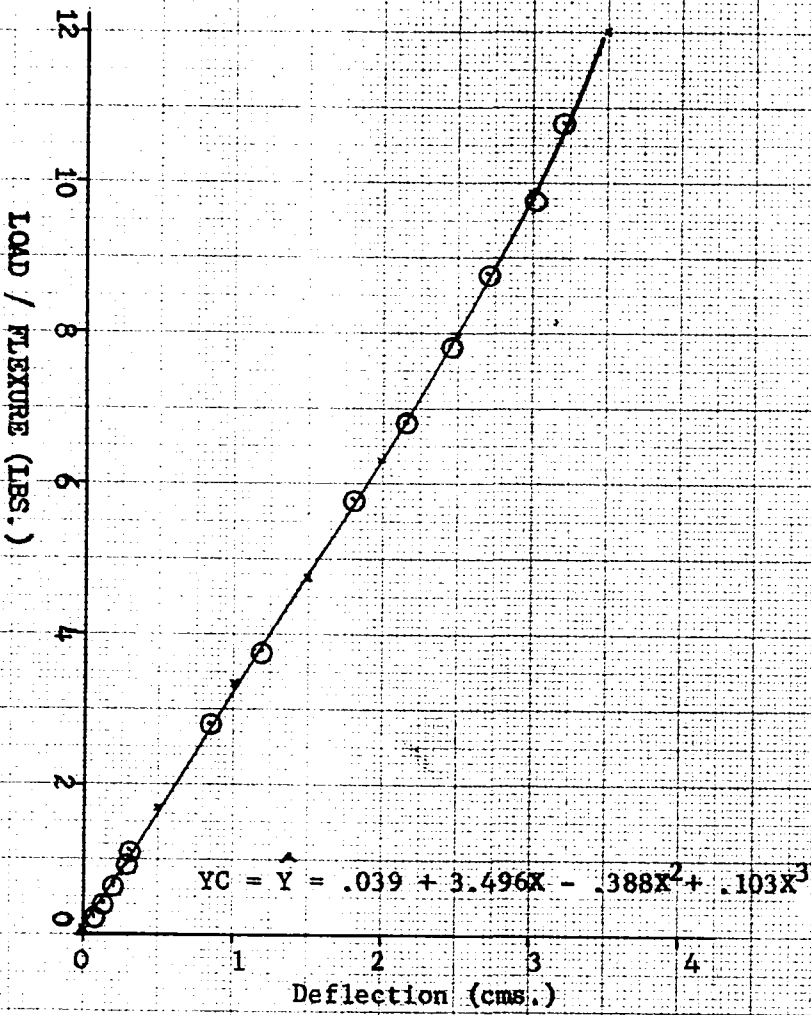
CALIBRATION OF CARRIAGE VELOCITY

CALIBRATION OF L.V.D.T.
- for SINKAGE.

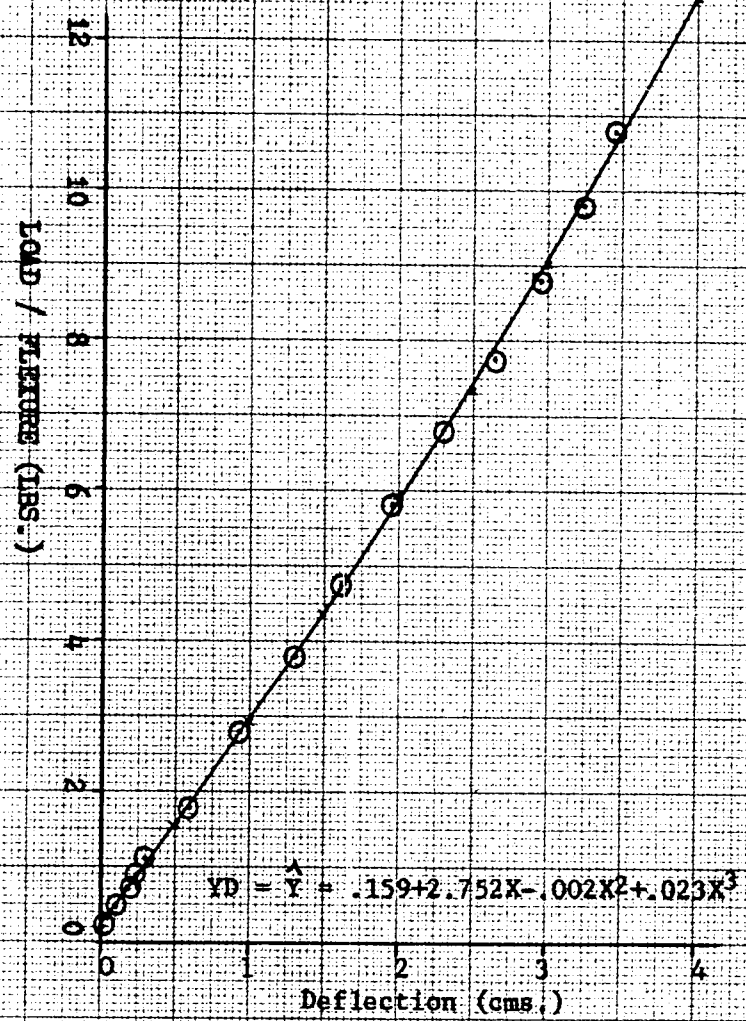


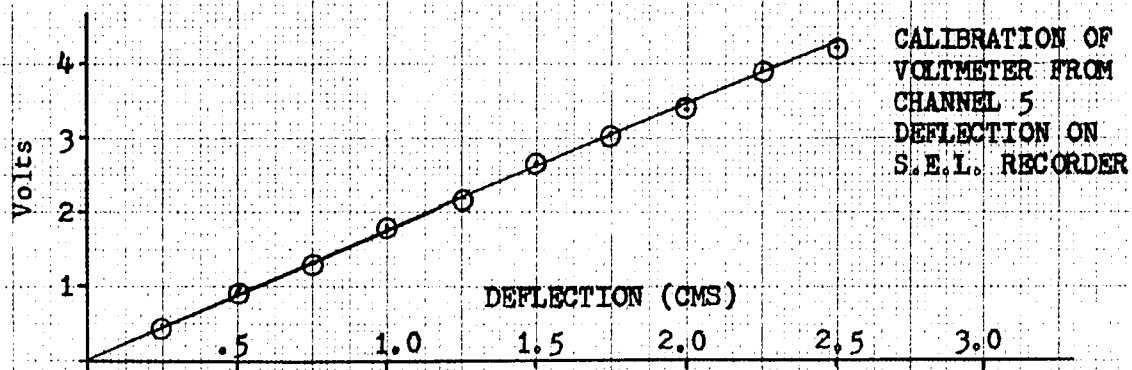
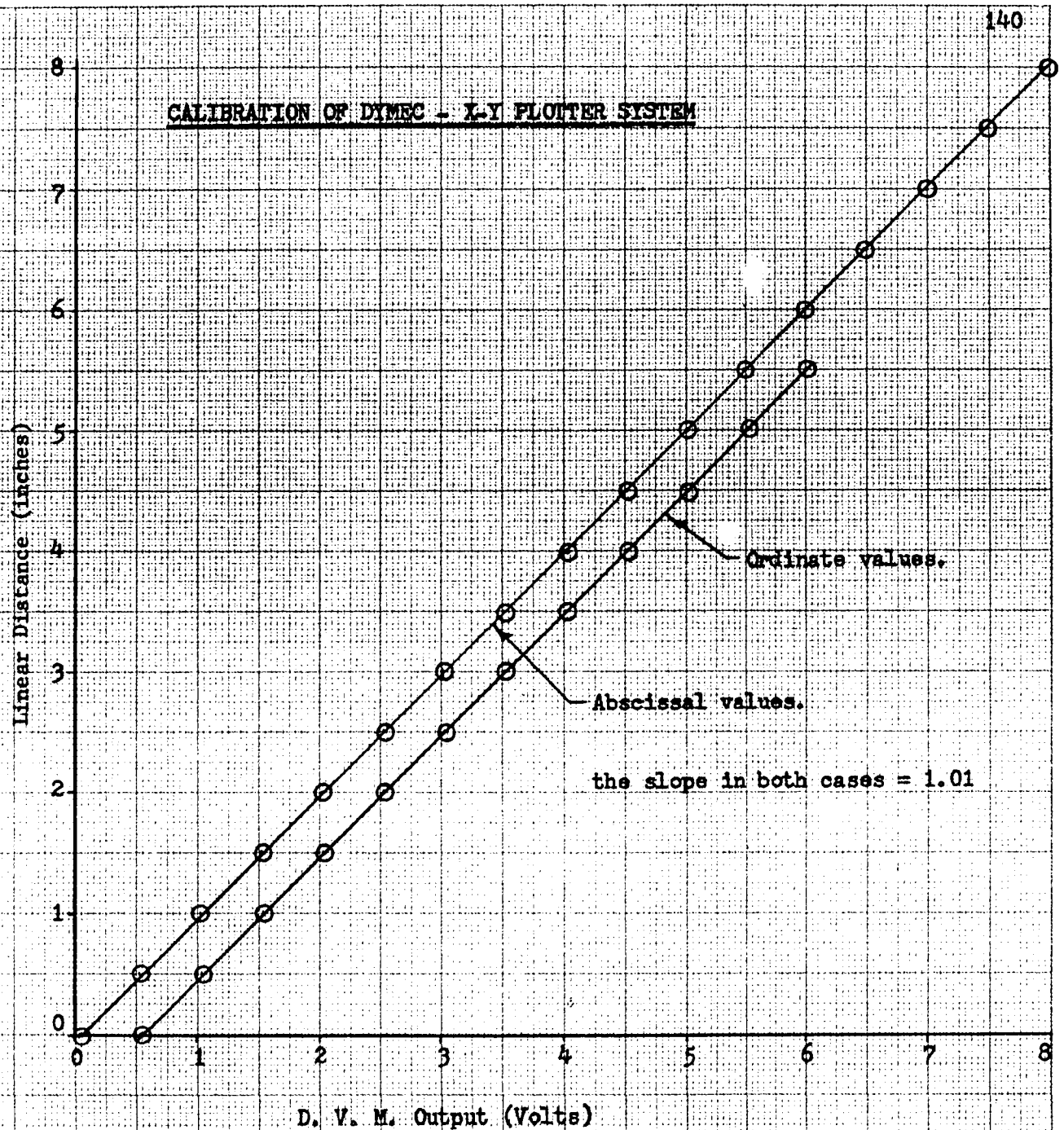
CALIBRATION OF MECHANICAL TORQUE DEVICE.

Calibration of Left Hand Flexure



Calibration of Right Hand Flexure





APPENDIX II-D-8 SAMPLE CALIBRATION OF DYMEC - X-Y PLOTTER SYSTEM AND VOLTMETER FOR SLIP RATE CONTROL.

APPENDIX II-E2-1

THE DERIVATION OF RADIOGRAPHIC EQUIVALENCE

FACTORS FOR TWO-PHASE SAND SYSTEMS

Two systems will be considered in detail below, namely a sand-air and a sand-water system. It is a simple extension of the following approach to calculate Radiographic Equivalence Factors, R.E.F.'s, for a three phase soil-air-water system, providing one has a measure of the degree of saturation of the test specimen.

If the void ratio, e , is known then it may be assumed that a sand-air or sand-water system is composed of equivalent volume components of pure sand, SiO_2 , and pure air or water; as shown in figure (1) below:

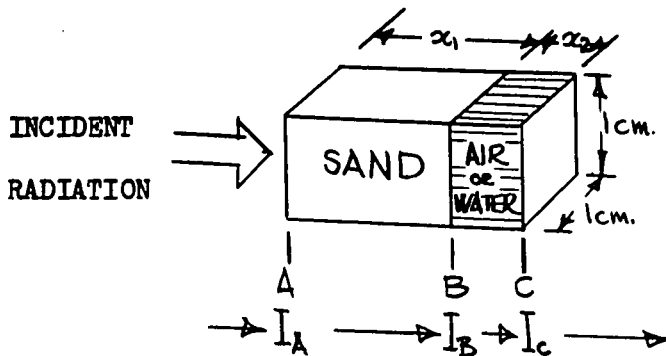


Figure (1):
Elementary volume of two phase soil system.

INTENSITY OF X-RADIATION
 $I_A > I_B > I_C$

From the Basic Exponential attenuation law - see Richtmeyer and Kennard (1947):

$$I_B = I_A e^{-\left(\frac{\mu}{\rho}\right) \rho x_1} \tag{1}$$

where:

I_A = Incident Photon Intensity (mono energetic).

I_B = Intensity of Mono-energetic Photon Beam, having passed through a thickness of material, x_1 at B.

$\left(\frac{\mu}{\rho}\right)$ = Mass Attenuation Coefficient.

$\left(\frac{\mu}{\rho}\right) \rho$ = Linear Attenuation Coefficient, where ρ is the material density (units of reciprocal cms.)

APPENDIX II-E2-1 (Cont'd.)

The intensity of a mono-energetic X-ray beam at B is thus:

$$I_B = I_A e^{-\left(\frac{\mu}{\rho}\right)_{\text{SiO}_2} \rho_{\text{SiO}_2} \cdot x_1} \quad (2)$$

and at C:
$$I_C = I_B e^{-\left(\frac{\mu}{\rho}\right)_{\text{air}} \rho_{\text{air}} \cdot x_2} \quad (3)$$

Substituting Eq. (2) in (3) gives:

$$I_C = I_A e^{-\left[\left(\frac{\mu}{\rho}\right)_{\text{SiO}_2} \rho_{\text{SiO}_2} \cdot x_1 + \left(\frac{\mu}{\rho}\right)_{\text{air}} \rho_{\text{air}} \cdot x_2\right]} \quad (4)$$

But since

$$\left(\frac{\mu}{\rho}\right)_{\text{SiO}_2} = \left(\frac{\mu}{\rho}\right)_{\text{Si}} \cdot \frac{28}{60} + \left(\frac{\mu}{\rho}\right)_{\text{O}_2} \cdot \frac{32}{60} \quad (5)$$

from the mass attenuation of a compound - see for example Compton & Allison (1935) - and $\left(\frac{\mu}{\rho}\right)_{\text{air}}$ may be found from Victoreen's (1949), tables, equation (4) becomes:

$$I_C = I_A \exp - \left[\left\{ \left(\frac{\mu}{\rho}\right)_{\text{Si}} \cdot \frac{28}{60} + \left(\frac{\mu}{\rho}\right)_{\text{O}_2} \cdot \frac{32}{60} \right\} \rho_{\text{SiO}_2} \cdot x_1 + \left(\frac{\mu}{\rho}\right)_{\text{air}} \rho_{\text{air}} \cdot x_2 \right] \quad (6)$$

The mass attenuation coefficients for all elements, on the periodic chart, together with those of water and air have been calculated by Victoreen (1949) for a range of wavelengths below the K_{α} absorption edge. The range of wavelengths of interest in the present study were 'dictated' by the 300 KV flash X-ray unit used in this study.

The minimum wavelength, λ_{min} , was 0.0413\AA being dependent only on the applied voltage (300 K.V.) and derived from the Planck-Einstein relationship. The maximum wavelength is controlled in the Field Emission units by the long wavelength filters covering the X-ray tubes. From Buchard's (1962) study it appears that λ_{max} of $.20\text{\AA}$ represents a reasonable upper wavelength limit for the subsequent calculations.

APPENDIX II-E2-1 (Cont'd.)

A peak intensity at 0.08\AA has also been assumed. Using this wavelength range ($.042\text{\AA} < \lambda < .20\text{\AA}$), the components of equation (6) have been computed and are listed in Table I, which also includes the appropriate linear attenuation coefficients for Aluminum. The information from Columns VIII \rightarrow XI, inclusive, is plotted as Figure (2) in order to demonstrate the strong dependence of absorption on incident X-ray wavelength.

TABLE I. Evaluation of Equation (6) Components as a Function of Incident Wavelength, λ .

					LINEAR ATTEN. COEFS.					
					MASS ATT'N. COEFS.					
I	II	III	IV	V	VI	VII	VIII	IX	X	XI
λ (Å)	$(\frac{\mu}{\rho})_{Si}$	$(\frac{\mu}{\rho})_{Si} \cdot \frac{28}{60}$	$(\frac{\mu}{\rho})_O$	$(\frac{\mu}{\rho})_{O} \cdot \frac{32}{60}$	$(\frac{\mu}{\rho})_{SiO_2}$	$(\frac{\mu}{\rho})_{air}$	$(\frac{\mu}{\rho})_{water}$	$(\frac{\mu}{\rho})_{SiO_2} \cdot (2.7)$	$(\frac{\mu}{\rho})_{Al} \cdot (2.7)$	$(\frac{\mu}{\rho})_{air} \cdot (.0012)$
.042 = λ min.										
.08	.1417	.0661	.1342	.0718	.1379	.1337	.1486	.371	.366	.00016
.12	.1788	.0835	.1529	.0815	.1650	.1520	.1686	.446	.45	.00018
1.0	17.51	8.0	3.305	1.77	9.77	2.879	2.979	26.4	37.7	.00345
3.0	406.2	190.	80.70	43.1	233.1	67.80	71.76	629.	884.	.0814

It may be seen from Figure (2) that the variation of linear attenuation coefficients within the λ range of interest is, for each material, quite small.

Having determined the attenuation of a mono-energetic X-ray beam for a sand-air system - equation (6), and thus with the appropriate substitution for a sand-water system, it was then necessary to determine what useful penetration might be expected in these systems.

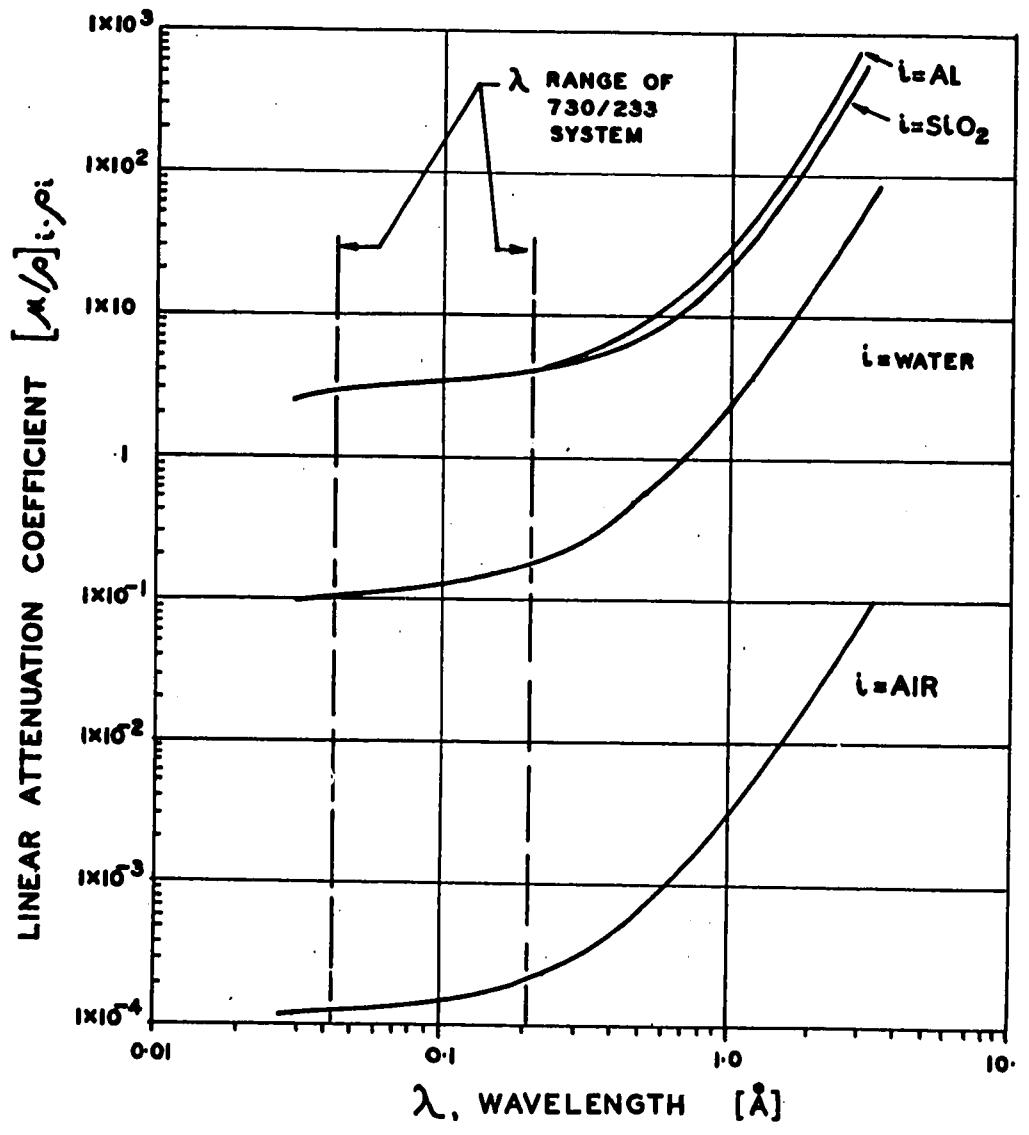


FIGURE [2]: VARIATION OF LINEAR ATTENUATION COEFFICIENT WITH WAVELENGTH & ATTENUATOR (AFTER VICTOREEN, 1949)

APPENDIX II-E2-1 (Cont'd.)

It is first assumed that a mono-energetic pulse passing through 1 cm³ of Aluminum 2SO is reduced from an original intensity of I₀ to I_z. Knowing the void ratio, e, it is possible to set up an equation to determine what approximate thickness of soil, z, produces an equivalent intensity reduction from I₀ to I_z. Since the absorption of aluminum 2SO, as a function of source to film distance, S.F.D., is known for the 300 KV., 730/233 Field Emission system, the ratio z:1 may thus be determined for a variety of soil systems. This ratio is referred to as a Radiographic Equivalence Factor, R.E.F.

For a two phase sand-air system this relationship takes the following form:

$$I_0 e^{-\left(\frac{\mu}{\rho}\right)_{Al} \rho_{Al}} = I_0 e^{-\left\{ \left(\frac{\mu}{\rho}\right)_{SiO_2} \rho_{SiO_2} \left(\frac{1}{1+e}\right) z + \left(\frac{\mu}{\rho}\right)_{air} \left(\frac{e}{1+e}\right) z \cdot (.0012) \right\}}$$

$$\therefore R.E.F. = \frac{z}{1} = \frac{\left(\frac{\mu}{\rho}\right)_{Al} \rho_{Al}}{\left\{ \left(\frac{\mu}{\rho}\right)_{SiO_2} \rho_{SiO_2} \left(\frac{1}{1+e}\right) + \left(\frac{\mu}{\rho}\right)_{air} (.0012) \left(\frac{e}{1+e}\right) \right\}} \quad (7)$$

Assuming a void ratio range of $0.67 \leq e \leq 0.96$ a range of radiographic factors can be calculated from the information contained in Table I. Equation (7) may, with the appropriate substitution, be used to determine the distance, z, for a sand-water system. The computed R.E.F. values are listed below in Table II. These values have also been plotted as Figure (3) which shows the calculated absorption ranges for two 2-phase sand systems as a function of void ratio, moisture content and S.F.D. Table II also shows that for each soil condition the R.E.F.'s are approximately the same for both wavelengths within the effective range ($.042\text{\AA} < \lambda < .20\text{\AA}$). Although not shown, these

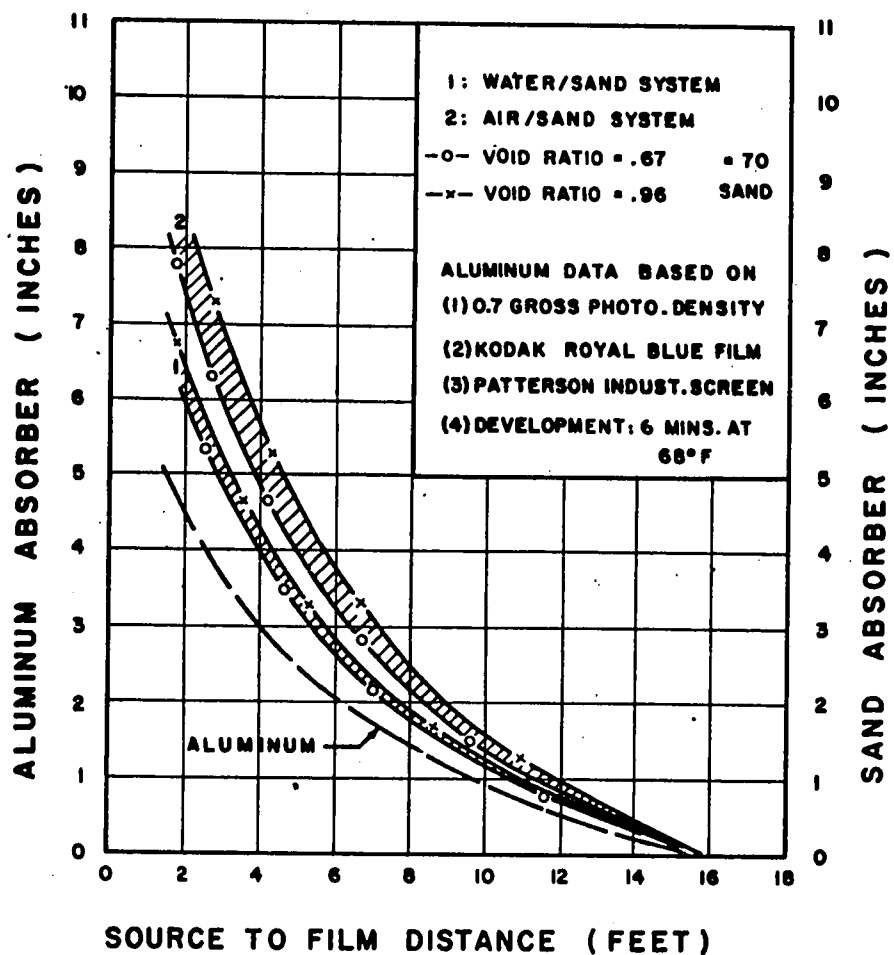


FIG. [3] CALCULATED ABSORPTION RANGES
 FOR SAND AS A FUNCTION OF S.F.D.,
 VOID RATIO, & MOISTURE CONTENT.
 FIELD EMISSION MODEL 730/233, 300 KV.

APPENDIX II-E2-1 (Cont'd.)TABLE II. Calculated R.E.F. Values.

λ	SYSTEM			
	AIR-SAND		WATER-SAND	
	$e = .67$	$e = .96$	$e = .67$	$e = .96$
.08 Å	1.65	1.94	1.32	1.40
.12 Å	1.67	1.97	1.34	1.45

values vary widely for a given sand condition at greater wavelengths.

Figure (3) represents a first approximation of anticipated absorption ranges that has proved indispensable in the development of the ciné-radiographic technique. It is however derived from gross simplifying assumptions:

- i) That a continuous, but bounded, spectral distribution with wide beam geometry, 30° , can be represented by a mono-energetic source (at an equivalent effective λ) and the assumption of a narrow beam.
- ii) That the attenuation law is valid for Flash sources of X-radiation.

In the final analysis the good experimental agreement with calculated values, has been used as a justification for these assumptions.

APPENDIX II-E2-2THE FABRICATION OF TRACER OBJECTS

The tracer-objects were manufactured in the Department Laboratories from a 94% lead, 6% Antimony alloy. The arms of the three dimensional crosses - or 'jacks' - were made from 1.09 mm (= .043 inches) wire, extruded from a simple jacket heated die. The extrusion pressure was applied using the Department's Emery Test Machine.

From this wire four 3 mm and one 7 mm lengths were cut to produce each tracer-object. These components were glued together, with Epoxy resin in a jig, to ensure orthogonality. Since Epoxy resins do not adhere to Teflon the jig was made from this material. Attempts to solder the tracer-object arms did not prove fruitful.

After the initial testing it became apparent that the maximum dimensions of the tracer-objects could be decreased without affecting the resolution of the image centres. However, the glueing technique makes handling of smaller object components difficult and thus a nominal 7 mm. maximum dimension was used for all tracer-objects fabricated.

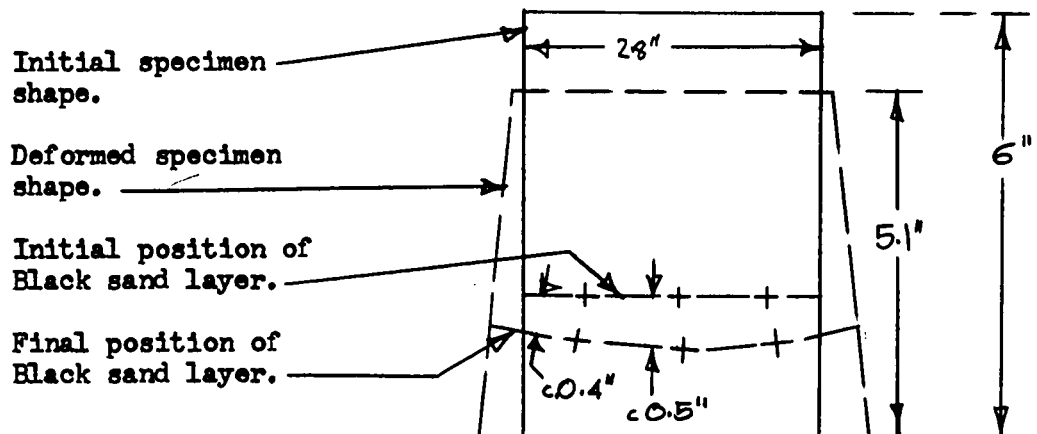
APPENDIX II-E2-3A COMPLEMENTARY STUDY TO DETERMINE WHETHER
THE TRACER-OBJECTS MOVE RELATIVE TO THE
SAND SURROUNDING THEM

The possibility that the tracer-objects might move 'through' rather than 'with' the sand was examined using the following technique.

- METHOD: 1) A sand specimen was prepared using a technique similar to that described by Lambe (1951), for a triaxial compression test with a 6" x 2.8" ϕ sample. After pouring - to ensure a loose initial packing arrangement - two inches of sand, a 0.05" layer of dyed black sand was poured. Five tracer-objects were then placed, with four 'arms' in this dyed layer, in the sample. The remaining four inches of sand was poured, and the final steps taken in the sample preparation (Lambe, 1951).
- 2) The specimen was then transferred to the high strain-rate dynamic loading unit, (Japp, 1967). A controlled strain rate of 30 inches/second was used to deform the specimen, although it should be noted that complete destruction of the specimen is prevented by a built-in restraint (Japp, 1967).
- 3) The deformed specimen was then carefully removed, the top cap taken off, and gelatin at a temperature of 80°C was poured slowly into the open end of the membrane - until it had completely penetrated the depth of the distorted specimen.
- 4) After the gelatin had set, the rubber membrane was removed and slices were cut longitudinally through the 'fixed' specimen.

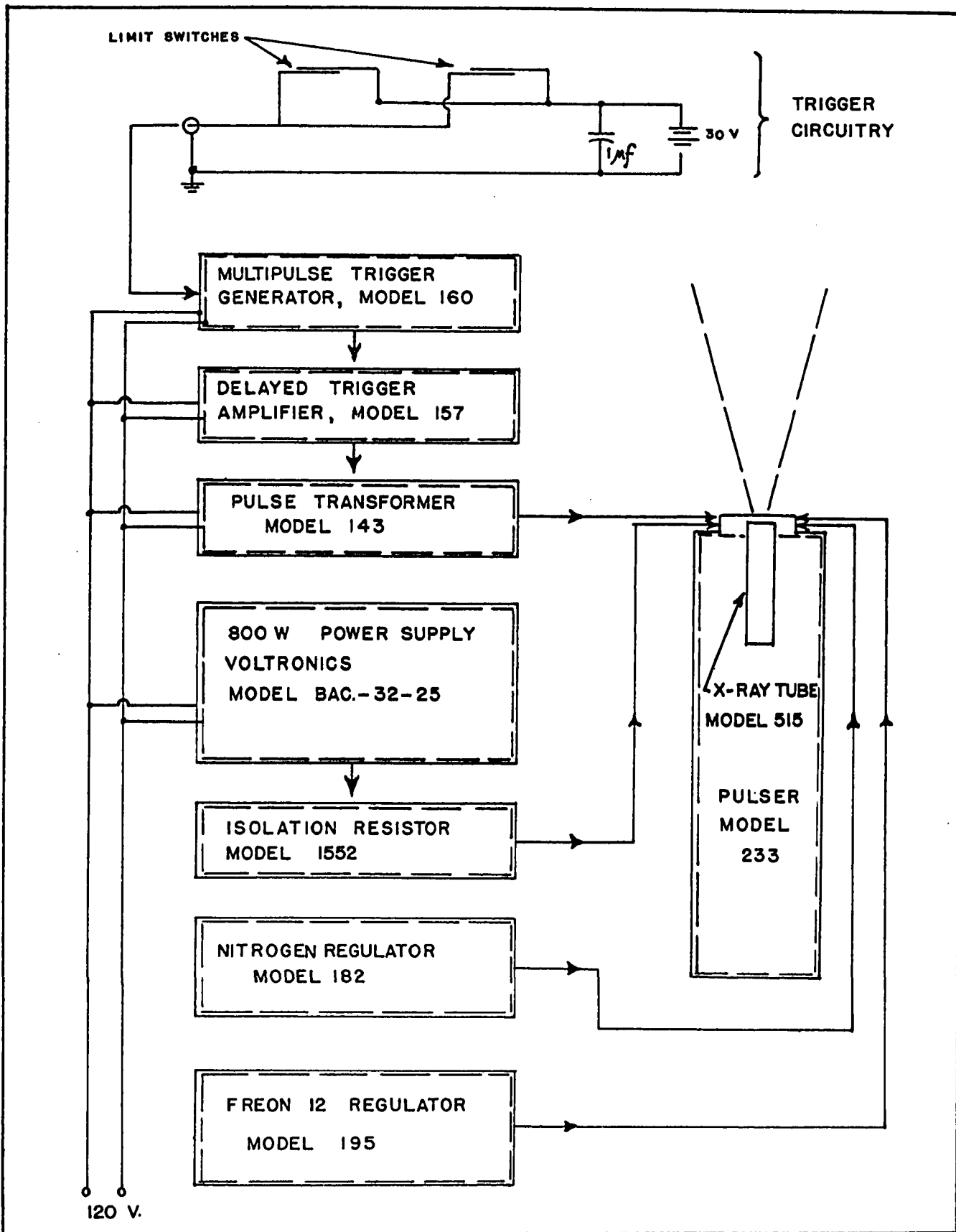
APPENDIX II-E2-3 (Cont'd.)

RESULTS: The slicing process revealed that the black sand layer had been displaced approximately 1/2 inch from the original layer position in a manner shown diagrammatically in Figure (1) below:



Despite this considerable movement the tracer-objects did not 'enjoy' any movement relative to the black sand layer. For all five tracer-objects the four orthogonal arms were seen to have remained within the black, reference, layer. It was thus concluded that for this loading condition there was no measurable differential inertia effect, and thus the tracer-objects moved 'with' rather than 'through' the sand.

For the conditions of the wheel testing the effective strain rates can be considered significantly less than 30 in/sec. and it is thus unlikely that any differential inertia effects occur at a measurable level.



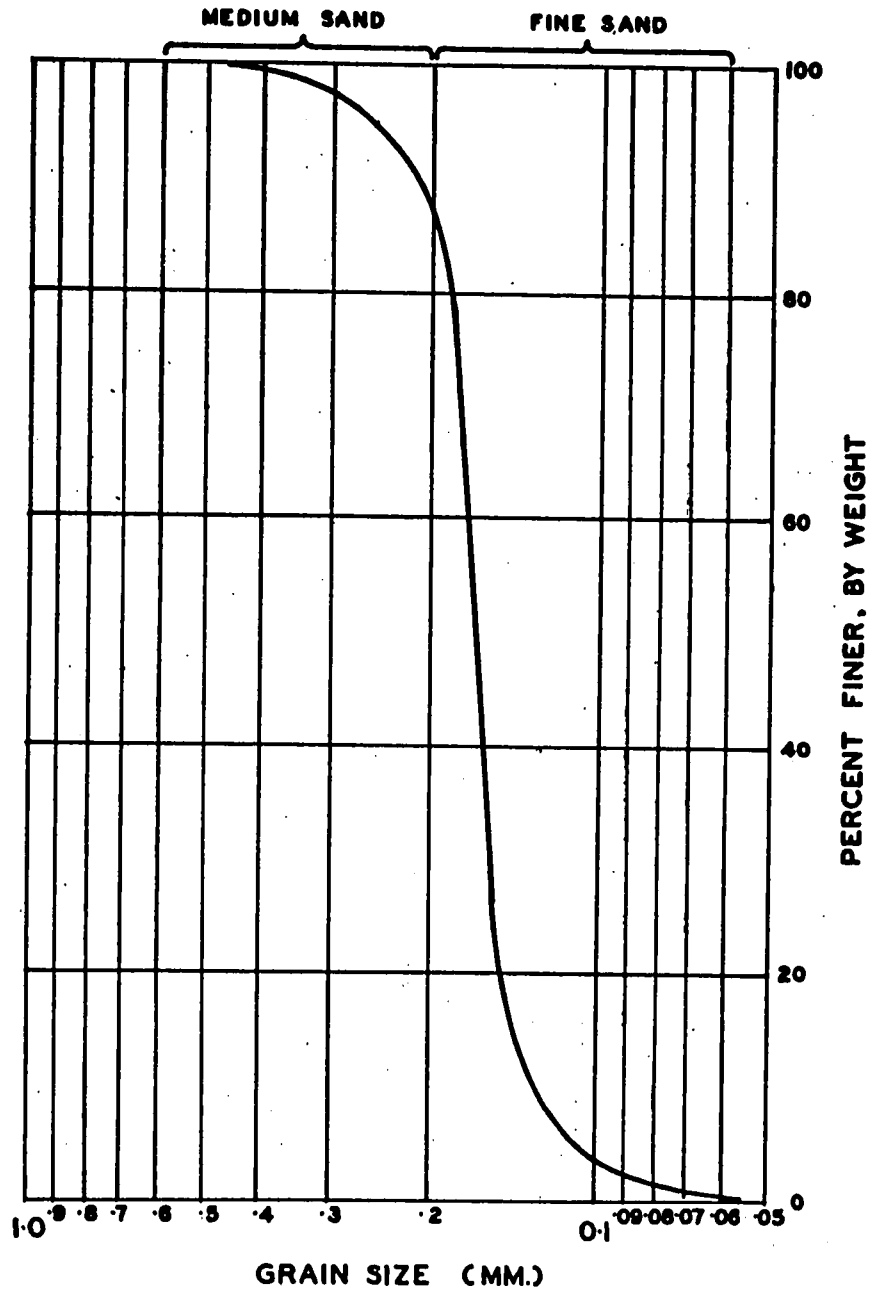
APPENDIX II-E2-4

SCHEMATIC OF CINE-RADIOGRAPHIC SYSTEM

FIELD EMISSION MODEL 730/233, 300 KILO VOLTS.

APPENDIX III

	Page.
III-B1-1	Distribution of Grain Sizes for Test Sand. 153
III-B3-1	Estimates of Tracer-Object Placing Accuracy. 154
III-B3-2	Sand Density Variation with Depth. 155
III-E-1	Contact Print of Radiograph from Test 14 showing undisturbed tracer-object network. 159
III-E-2	The transferred Radiographic Image Centres, Test No. 14, Showing the Identification Markers and the Reference Matrix. 160
III-E-3	A Schematic Circuitry Diagram of the X-Y Plotter- Dymec, System. 161
III-E-4	Editing Necessary to Convert Paper Tape Output to Card Output. 162
III-F-1	Digital Program Description for "Soil-Vehicle Study I". 163
	A. Nomenclature. 163
	B. Notes. 165
	C. Source Listing and Sample Printed Output. 169
III-G-1	Sources and Magnitudes of Radiographic Displace- ments not caused by Movements of the Tracer Objects. 182



APPENDIX III-BI-1 : GRAIN SIZE DISTRIBUTION FOR SAND USED THROUGHOUT TEST SERIES.

APPENDIX III-B3-1ESTIMATES OF TRACER-OBJECT PLACING ACCURACY

Since test Number 14 has been chosen for illustrative purposes, it is convenient to use the results of the same test for estimating the accuracy of the tracer-object placing technique.

From Appendix III-F, the corrected coordinates of the initial tracer-object locations can be used to derive the essential statistics of mean row depth and deviations from the mean. From the "corrected coordinate" listings for Test No. 14 the following Table can be obtained.

ROW	MEAN ROW DEPTH	DEVIATIONS FROM \bar{y} , BY COLUMN i.e. $(y - \bar{y})$						
1	1.491	.009	-.001	.007	-.004	.016	-.004	-.024
2	2.565	-.010	-.010	.007	-.006	.003	-.005	-.013
3	3.667	-.009	.000	.008	-.005	-.025	-.005	.011
4	4.663	-.007	.000	-.001	-.008	-.001	-.002	.003
5	5.709	-.004	.002	.006	-.009	.005	-.016	.013
6	6.723	-.014	-.010	.030	.017	.001	-.028	.006

$$\text{Since } S = \sqrt{\frac{\sum (y - \bar{y})^2}{42}} = \sqrt{\frac{.005570}{42}} = .011$$

From Snedecor's (1956) Text; t_{95} for $(n = 42)$ is 2.02

Thus: best estimate of deviation from mean (for ordinate value)

$$\text{at the 95\% confidence level} = \bar{y} + (2.01 \times .011)$$

$$= \underline{\bar{y} + .022 \text{ inches.}}$$

Considering next the inter - y values i.e. 1.054, 1.102, .966, 1.046 and 1.014, the average distance between rows = 1.042 inches, for this test.

APPENDIX III-B3-2SAND DENSITY VARIATION WITH DEPTH

In order to establish the variation in sand density as a function of a) height of drop and b) height of both drop and overburden, the following technique was used:

METHOD: A plexiglass tray with inside base measuring 12.04 x 20.9 cms and with an effective depth of 1.85 cms was made. The volume of this shallow tray was thus 465 ccs. Using this tray the procedure was as follows:

- 1) The tray was placed at a known distance beneath the orifice of the sand hopper located on the carriage.
- 2) The sand was then poured, the carriage moved at a controlled rate, and the tray filled.
- 3) Excess sand was cleaned from the surface of the tray with a metal blade, and the tray and sand was weighed. This information was entered in a plot of "density vs. height of sand drop from hopper orifice".
- 4) The tray was replaced at the same depth beneath the hopper and 1/2 inch of soil was poured, by moving the carriage and withdrawing the cut-off blade - see Figure III-1.
- 5) A sheet of polythene was placed over this sand and tray, and the additional layers of sand placed in one inch increments to obtain the appropriate overburden sand height.
- 6) The sand contained within the polythene sheet was removed by pulling the polythene sheet vertically (in a 'basket' - like fashion).

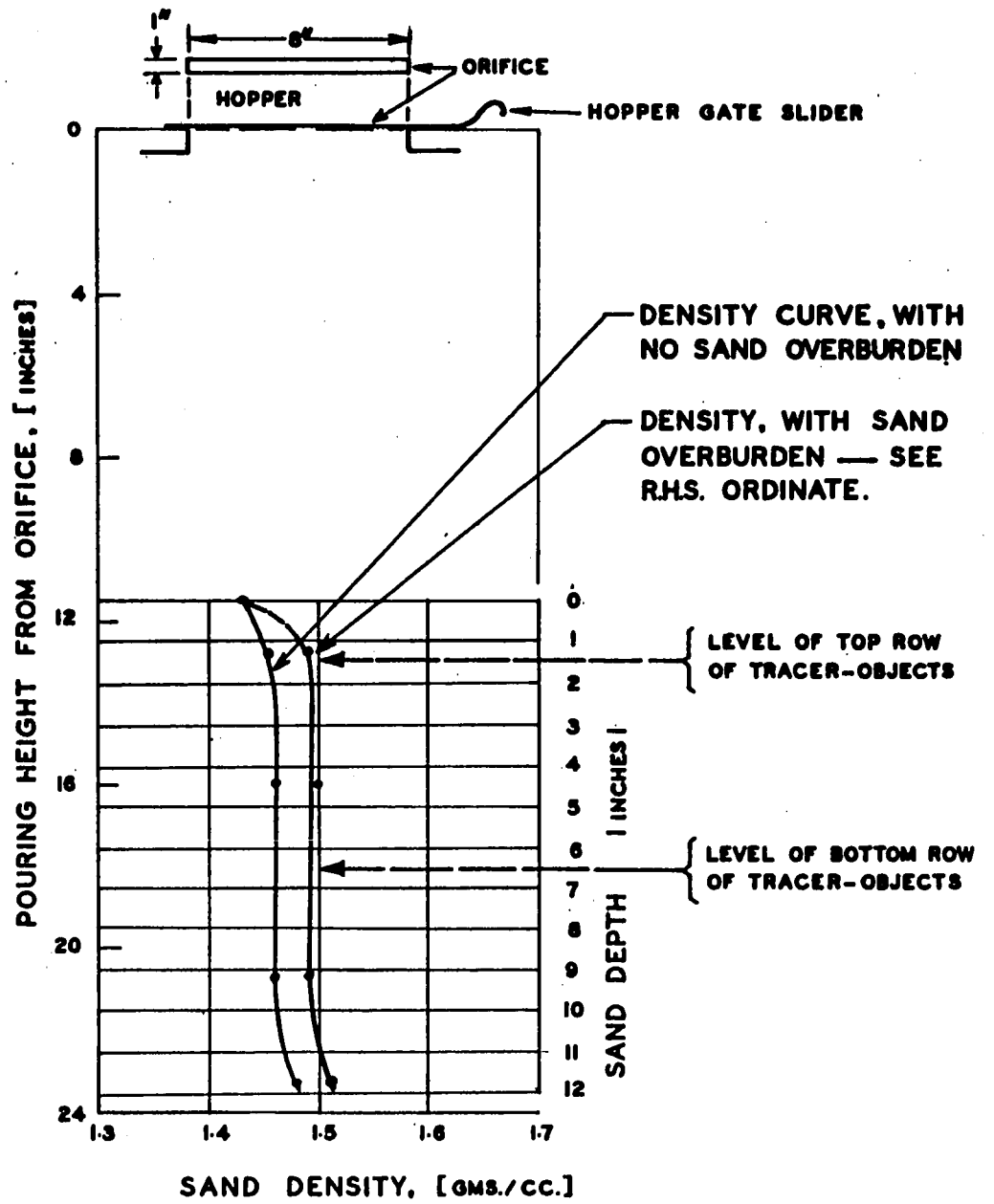
APPENDIX III-B3-2 (Cont'd.)

- 7) The excess sand on the plexiglass tray was scraped clear with a single stroke of a metal blade, and the tray and contents reweighed. This information was plotted on the curve of "density vs. height of drop and overburden".
- 8) The process was repeated at different tray "depths".

RESULTS: (VOL. OF CONTAINER = 465 ccs.)

TEST SPECIFICATIONS		WT. OF SAND	ρ
HT. OF DROP (INCHES)	DEPTH OF SAND OVERBURDEN	gms.	gms/cc.
11.5	N.A.	667	1.43
11.5	N.A.	664	1.43
12.75	N.A.	680	1.46
12.75	1.25"	691	1.49
15.75	N.A.	684	1.47
23.25	N.A.	686	1.48
23.25	11.75"	703	1.51
20.75	N.A.	678	1.46
20.75	9.25"	692	1.49
16.00	N.A.	676	1.46
16.00	4.5"	696	1.50

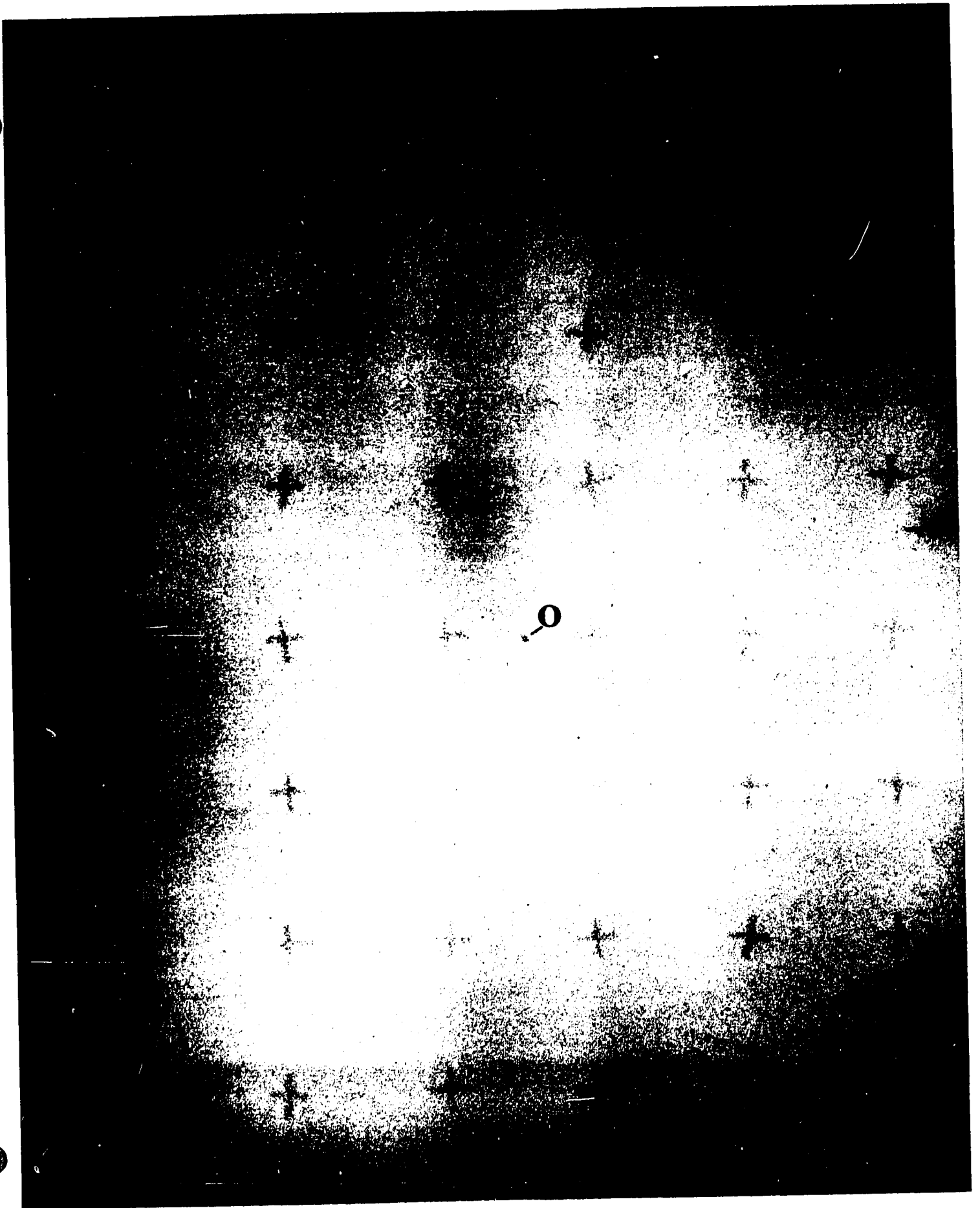
COMMENT: The results plotted on the curve, overpage, show the influence of drop height on the sand density, together with the influence of sand overburden height. The use of a plexiglass tray thus gives a first approximation of the initial density distribution, with depth, of the poured sand



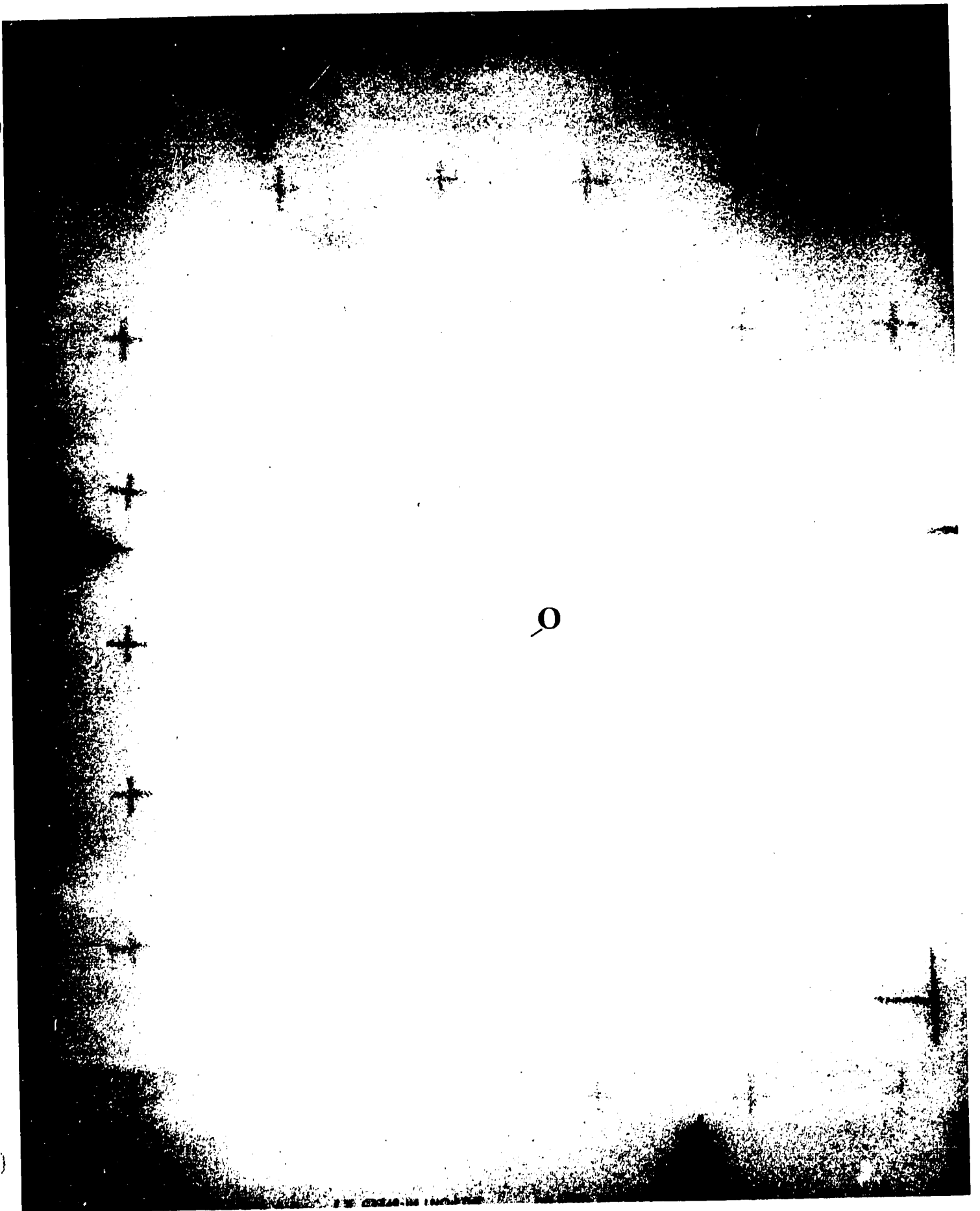
APPENDIX III-B3-2: Poured Sand Density Distributions.

APPENDIX III-B3-2 (Cont'd.)

layers. However, without further experimental information these approximations must not be considered as absolute values. Such influences as the nature of the tray material - in this case, plexiglass - and the influence of scraper action on the resulting density determination have not been evaluated.



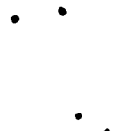
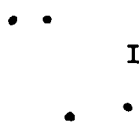
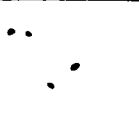
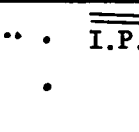
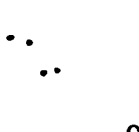
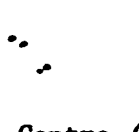
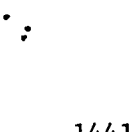
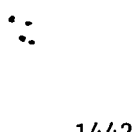
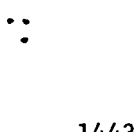
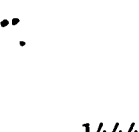
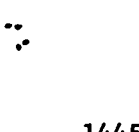
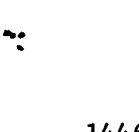
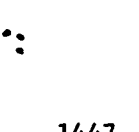
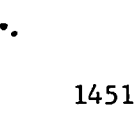
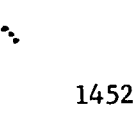
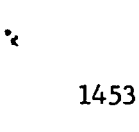
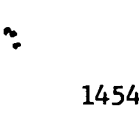
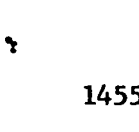
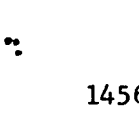
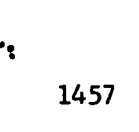
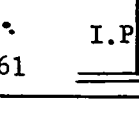
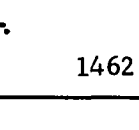
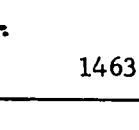
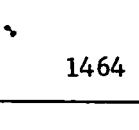
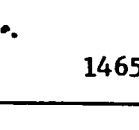
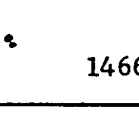
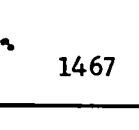
APPENDIX III - D - I: CONTACT PRINT OF RADIOGRAPH FROM TEST NO. I4, SHOWING UNDISTURBED TRACER-OBJECT NETWORK, where 'O' is the optical centre.



APPENDIX III - D - I: CONTACT PRINT OF RADIOGRAPH FROM TEST NO. I4, SHOWING UNDISTURBED TRACER-OBJECT NETWORK, where 'O' is the optical centre.

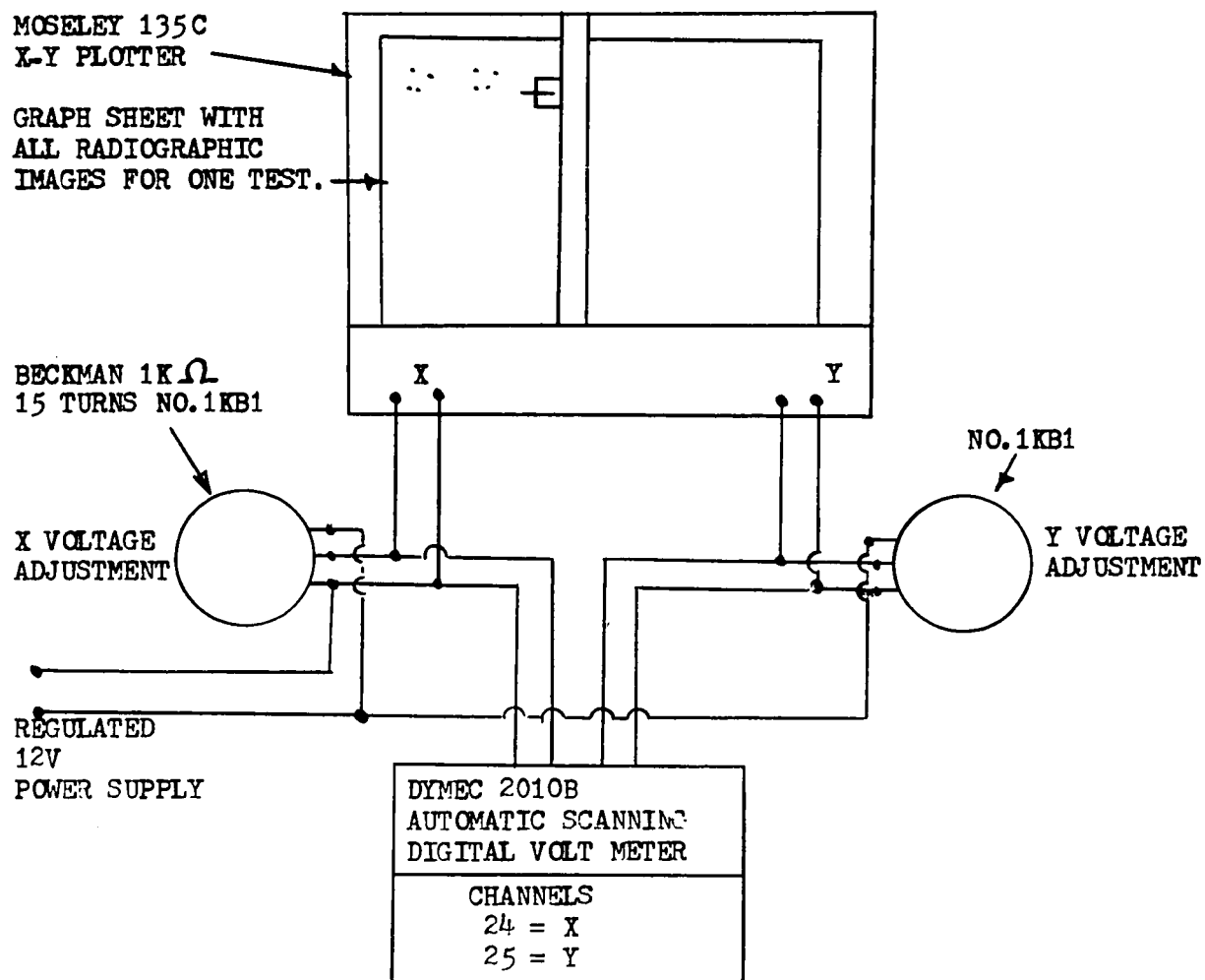
THE TRANSFERRED RADIOGRAPHIC IMAGE CENTRES, TEST NO. 14,
 SHOWING THE IDENTIFICATION MARKERS & REFERENCE MATRIX
 WHERE I.P. REPRESENTS IDENTIFICATION MARKER.

APPENDIX III-E-2

 1411	 1412	 1413	 1414	 1415	 1416	 1417
 1421	 1422	 1423	 1424	 1425	 1426	 1427
 1431	 1432	 1433	 1434	 1435	 1436	 1437
 1441	 1442	 1443	 1444	 1445	 1446	 1447
 1451	 1452	 1453	 1454	 1455	 1456	 1457
 1461	 1462	 1463	 1464	 1465	 1466	 1467

APPENDIX III-E-3

A SCHEMATIC CIRCUITRY DIAGRAM OF THE X-Y PLOTTER - DYMEC SYSTEM



APPENDIX III-E-4EDITING NECESSARY TO CONVERT PAPERTAPE OUTPUT TO CARD OUTPUT

Typical Tape output for Test No. 14, and matrix position 11 i.e. designated as region 1411 read as follows:

1411 T201854
 24 + 0095414
 25 + 0673184
 T 201900
 24 + 0152884
 25 + 0668504
 T 201905
 24 + 0135044
 25 + 0624064
 T 201911
 24 + 0131734
 25 + 0622824
 1412 etc.

Where: 1411 is matrix reference region;
 24 and 25 repeated, are channel numbers; TXXXXX is the time record.

The voltage record corresponding to a coordinate point is followed by the digit 4. This is the negative exponent of the D.V.M. value.

All tape output thus contained redundant information that was eliminated by an editing program and the Pulp and Paper Research Institute of Canada's 1601 IBM Computer. The coordinates of successive radiographic images of each tracer-object were punched on a single IBM card as output from this editing program. For the above case the card output read as follows:

	1411	009541	067318	015288	066850	013504	062406	013173	062282
		X	Y	X	Y	X	Y	X	Y
Identifi- cation Code.		Image of		Image of		Image of		Image of	
		Tracer-object		tracer-object		tracer-object		tracer-object	
		11 from first		11 from 2nd		11 from 3rd		11 from 4th	
		X-ray Pulse.		X-ray Pulse.		X-ray Pulse.		X-ray Pulse.	

Where: X = X coordinate

Y = Y coordinate

APPENDIX III-F-1DIGITAL PROGRAM DESCRIPTION FOR"SOIL-VEHICLE STUDY I"

This program was written in the principal source language of Fortran 4, and was run on McGill Computing Centre's IBM 7044 machine. The operating system used was the \$ IBSYS.

The SOIL-VEHICLE STUDY I, or S.V.S.I., program was written in order to reduce the wheel loading information and radiographic results, of each test, to an organised and meaningful form. The program also contained a statistical control section that was used as a basis for accepting or rejecting the results from any one test series.

PROGRAM DESCRIPTION

A. Nomenclature.

- IXY The matrix of Digital Voltage Values corresponding to the radiographic image locations from the three radiographs.
- XY Optically corrected image locations in adjusted X, Y coordinate system.
- XX Translation of each reduced image centre from its original (first radiograph) location/ to give the 'relative' cartesian reference frame.
- DTVEL Time increments for successive velocity components.
- DUDT $\Delta x / \Delta t$ component of velocity.
- DVDT $\Delta y / \Delta t$ component of velocity.
- XRVEL Relative abscissal value corresponding to DUDT and DVDT value with same subscript.

APPENDIX III-F.1 (Cont'd.)

YRVEL	Relative y coordinate corresponding to DUDT and DVDT value with same subscript.
XVEL	x coordinate corresponding to DUDT and DVDT value with same subscript.
YVEL	y coordinate corresponding to DUDT, DVDT value with same subscript.
TFLOT	Cumulative time increment corresponding to velocity computation with same subscript.
TACC	Cumulative time increment corresponding to acceleration computation with same subscript.
D2UDT	$\Delta(\Delta x)/\Delta t$, component of acceleration.
D2VDT	$\Delta(\Delta y)/\Delta t$, component of acceleration.
BAR(N)	N odd: average x displacement/row from initial to final position. N even: average y displacement/row from initial to final position.
BIAS(N)	N odd: unadjusted standard deviation about BAR(2N+1) position. N even: unadjusted standard deviation about BAR(2N) position.
BES(N)	N odd: BIAS(2N+1) adjusted with small-sample size correction. N even: BIAS(2N) adjusted with small-sample size correction.
A	Uncalibrated angular velocity; cms. on S.E.L.2005 output.
B	Uncalibrated Linear carriage vel., cms. on S.E.L.2005 output.
C	Uncalibrated Drawbar Pull L.H.S., cms. on S.E.L.2005 output.
D	Uncalibrated Drawbar Pull R.H.S., cms. on S.E.L.2005 output.
E	Uncalibrated sinkage; cms. on S.E.L.2005 output.
F	Uncalibrated Torque; cms. on S.E.L.2005 output.
Y (-A, -B, -C, -D, -E, -F)	Calibrated loading information (in appropriate dimensions).
J	Number of Test. (two digit integer).

APPENDIX III-F-1 (Cont'd.)

JJ D.V.M. output matrix identification.
 G Spacing between trigger limit switches, (inches).
 K10 D.V.M. output for x component of optical centre.
 K11 D.V.M. output for y component of optical centre.
 PARAX x coordinate of optical centre.
 PARAY y coordinate of optical centre.
 CORR Optical reduction factor for reducing images from plane of radiograph to plane under centre-line of wheel.

B. Notes.

A listing of the source statement is included as part C. of this Appendix. However the actual instructions are described in some detail, below, where the annotations correspond to the open ended bracketed "notes" of the following section.

NOTE 1. The wheel loading information is converted in this section from S.E.L.2005/.12 output to calibrated values. Appendix II-D contains a listing of the calibration curves and procedures, of the complete test series.

The 'loading' information is listed on the first data card from the recorded galvanometer deflections. For Test No. 14, this card appears as follows:

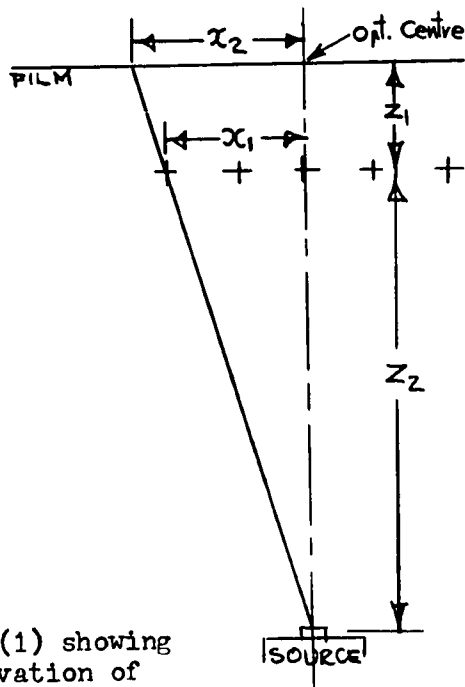
Test No.	A(cms)	B(cms)	C(cms)	D(cms)	E(cms)	F(cms)	G(inches)
14	---	.835	--1.460	--0.570	--0.645	--1.110	--1.865--4.688
	↑						↑
	1st Column						51st Column

The normal slip-rate is computed in this section, as is the optical centre for subsequent corrections to the plane of the tracer-object network.

APPENDIX III-F-1 (Cont'd.)

(Here K10 and K11 are converted to PARAX and PARAY).

NOTE 2. The matrix of D.V.M. values is converted first to a pseudo coordinate system - from the Dymec System Calibrations - and then adjusted by an optical correction factor (CORR) to reduce the pseudo coordinate system to the plane of the tracer-object network. In Figure (1), below, the correction factor (Z_2/Z_1+Z_2) reduces the measured value (x_2, y_2) to the value (x_1, y_1) .



$$\text{CORR} = \frac{Z_2}{Z_1 + Z_2} = \frac{\text{SOURCE TO TRACER-OBJ. DISTANCE}}{\text{SOURCE TO FILM DISTANCE}}$$

This corrected coordinate system is then referred to a reference point, the initial position of tracer-object in the top row and L.H.S., which is assigned the arbitrary coordinates $(0, -1.5)$. The newly defined pt. $(XY(1), XY(2))$ is then used as a pivot for converting the corrected pseudo-coordinate system to what will subsequently be termed the 'Absolute' cartesian reference frame. The allocation of $(0, -1.5)$ to this pivot, is entirely nominal for the 'x' component

Fig (1) showing derivation of correction factor for CORR (x component of pseudo-coordinate system is shown)

but dependent on the accuracy of the placing technique for the ordinate value

- See Appendix III-B3.

Note that $XY(N)$ refers to an abscissal value when N is odd and an ordinate value when the subscript is even valued.

APPENDIX III-F-1 (Cont'd.)

NOTE 3. In order to evaluate the relative movements of each tracer-object the coordinate components of displacement of the 2rd, 3rd and 4th tracer-object locations are subtracted from their initial undisturbed positions. This creates a second Cartesian reference frame - referred to as the 'Relative' coordinate system, $XX(N)$, and given the coordinate designation (r,s) in the text.

NOTE 4. These instructions are used to calculate the statistic of 'net' total displacement from the initial to final tracer-object position and its variability within each row. The mean component values are calculated from the row sample of 7, and tabulated as 'relative' reference coordinates. The standard deviation, s, is then determined, $BIAS(I)$, for each component on a row basis. The s values are then adjusted using the Bessel correction factor for small samples. Thus $BES(I)$ represents the best estimate of the population standard deviation.

$$\text{i.e.} \quad \hat{\sigma}_{(I)} = \sqrt{\frac{n}{(n-1)} \left[\frac{\sum_{i=1}^n x_i^2}{n} - \left(\frac{\sum_{i=1}^n x_i}{n} \right)^2 \right]}$$

where: n = sample size

x represents the chosen statistic

In order to obtain the 95% confidence levels the factor 1.96 is taken from a t distribution with ∞ degree of freedom,

Fisher (1950) to give: $\bar{x} \pm 1.96 \hat{\sigma}_{(x)}$

$\bar{y} \pm 1.96 \hat{\sigma}_{(y)}$

NOTE 5. In the S.V.S. I program the subroutine VELOC is only called three times since it was only possible to resolve four images per tracer-object for the top three rows. In S.V.S. III, four images

APPENDIX III-F-1 (Cont'd.)

per tracer-object were resolved for the top six rows. However, because of the magnitude of translations analyzed by S.V.S. III only six tracer-objects could be resolved in the top row. This necessitated a complete change in the subscript notation and thus a completely revised program.

Using the principles described in Section III - F the velocity computations are generalized on a row by row basis. Thus the VELOC subroutine is called by row. The 'arguments' refer either directly or ultimately to the subscripts.

The cumulative time computations coordinate the results from both intermediate radiographs, through the known G/YB time increment - referred to as ΔT in the text. Corresponding adjustments have been made in the XVEL and YVEL coordinates.

```
0 $IBFIC MAIN
1   COMMON XY,XX,DTVEL,DUOT,DVDT,XRVEL,YRVEL,XVEL,YVEL,TPLOT,D2UDT,
   1D2VDT,TACC,G,YB
2   DIMENSION XY(280),XX(280),DTVEL(36),DUOT(36),DVDT(36),XRVEL(36),
   1YRVEL(36),XVEL(36),YVEL(36),TPLOT(36),D2UDT(30),D2VDT(30),TACC(30)
   2,IXY(280),BAR(12),BIAS(12),BES(12)
3   1 READ 5,J,A,B,C,D,E,F,G
5   5 FORMAT(12,7F7.3)
6   PRINT3,J
7   3 FORMAT(1H1,100X,11HTEST NUMBER,2X,12)
10  READ 15,K10,K11
13  15 FORMAT(4X,217)
14  XK10=K10
15  XK11=K11
16  PARAX=(XK10/10000.)*1.01
17  PARAY=(XK11/10000.)*1.01
20  YA=-0.008+.335*A
21  PRINT 13,YA,PARAX
22  13 FORMAT(1H0,10X,12HLOADING DATA//25X,16HANGULAR VELOCITY,F8.3,2X,
   113HKEVS. PER SEC,20X,7HPARAX ,F5.3)
23  YB=0.1746+5.084*B
24  PRINT 23,YB,PARAY
25  23 FORMAT(1H ,23X,17HCARRIAGE VELOCITY,F7.2,3X,12HINS. PER SEC,
   121X,7HPARAY ,F5.3)
26  YC=.039+3.496*C-.388*C**2+.105*C**3
27  YD=.159+2.752*D-.002*D**2+.023*D**3
30  YE=.048+.513*E
31  YF=(.0208-1.063*F+9.611*F**2-10.439*F**3+5.135*F**4-1.172*F**5
   1+.1006*F**6)*12.
32  FF=(.0208-1.063*F+9.611*F**2-10.439*F**3+5.135*F**4-1.172*F**5
   1+.1006*F**6)*12.
33  PRINT 33,YC,YD,YE,YF,FF
34  33 FORMAT(1H ,24X,16HD.B.P. L.H.S.,F8.3,2X,4HLBS./35X,6HR.H.S.,
   1F8.3,2X,4HLBS./34X,7HSINKAGE,F8.3,2X,6HINCHES/24X,17HTORQUE LOA
   2DING,F7.2,3X,7HIN.LBS./32X,9HUNLOADING,F7.2,3X,7HIN.LBS.)
35  SLIP=(1.-YB/(YA*29.100))*100.
36  PRINT 63,SLIP
37  63 FORMAT(1H ,31X,9HSLIP RATE,F7.2,3X,8HPER CENT)
40  PRINT 73
41  73 FORMAT(1H0,10X,14HD.V.M. OUTPUT //10X,4HCODE,4X,1HX,7X,1HY,7X,1HX,
   1,7X,1HY,7X,1HX,7X,1HY,7X,1HX,7X,1HY/)
42  L=1
43  M=8
44  DO 4 I=1,21
45  READ 10,JJ,(IXY(K),K=L,M)
53  PRINT 83,JJ,(IXY(K),K=L,M)
60  83 FORMAT(1H ,10X,14,818)
61  10 FORMAT(14,817)
62  L=L+8
63  4 M=M+8
65  M=M-2
66  DO 14 I=1,14
67  READ 10,JJ,(IXY(K),K=L,M)
75  PRINT 93,JJ,(IXY(K),K=L,M)
102 93 FORMAT(1H ,10X,14,618)
```

NOTE 1

```

103     L=L+6
104     14 M=M+6
106     M=M-2
107     DO 24 I=1,7
110     READ 10,JJ,(IXY(K),K=L,M)
116     PRINT 103,JJ,(IXY(K),K=L,M)
123     103 FORMAT(1H ,10X,14,4I8)
124     L=L+4
125     24 M=M+4
127     DO 34 K=1,280
130     XAX=IXY(K)
131     34 XY(K)=(XAX/10000.)+1.01
133     CORR=0.835
134     XY1=(XY(1)-PARAX)*CORR+PARAX
135     DO 44 K=1,279,2
136     XY(K)=(XY(K)-PARAX)*CORR+PARAX
137     44 XY(K)=XY(K)-XY1
141     XY2=(XY(2)-PARAY)*CORR+PARAY
142     DO 54 K=2,280,2
143     XY(K)=(XY(K)-PARAY)*CORR+PARAY
144     54 XY(K)=XY(K)-XY2-1.5
146     PRINT 113
147     113 FORMAT(1H1,99X,21HCORRECTED COORDINATES//5X,4HSUBS,3X,1HX,4X,
148     14HSUBS,3X,1HY,5X,4HSUBS,3X,1HX,4X,4HSUBS,3X,1HY,5X,4HSUBS,3X,1HX,
149     24X,4HSUBS,3X,1HY,5X,4HSUBS,3X,1HX,4X,4HSUBS,3X,1HY)
150     DO 64 I=8,280,8
151     L7=I-7
152     L6=I-6
153     L5=I-5
154     L4=I-4
155     L3=I-3
156     L2=I-2
157     L1=I-1
160     PRINT 123,L7,XY(L7),L6,XY(L6),L5,XY(L5),L4,XY(L4),L3,XY(L3),L2,
161     1XY(L2),L1,XY(L1),I,XY(I)
161     123 FORMAT(1H ,6X,13,F7.3,14,F7.3,16,F7.3,14,F7.3,16,F7.3,14,F7.3,16,
162     1F7.3,14,F7.3)
162     64 CONTINUE
164     L=1
165     M=7
166     DO 74 K=1,21
167     DO 84 I=L,M,2
170     XX(I)=XY(I)-XY(L)
171     84 XX(I+1)=XY(I+1)-XY(L+1)
173     L=L+8
174     74 M=M+8
176     M=M-2
177     DO 94 K=1,14
200     DO 104 I=L,M,2
201     XX(I)=XY(I)-XY(L)
202     104 XX(I+1)=XY(I+1)-XY(L+1)
204     L=L+6
205     94 M=M+6
207     M=M-2
210     DO 134 K=1,7

```

NOTE 2

NOTE 3

```

ISN      SOURCE STATEMENT
211      DU 144 I=L,M,2
212      XX(I)=XY(I)-XY(L)
213 144  XX(I+1)=XY(I+1)-XY(L+1)
215      L=L+4
216 134  M=M+4
220      PRINT 133
221 133  FORMAT(1H1,80X,33HUNORDERED LISTING OF TRANSLATIONS//10X,4HSUBS,
        14X,1HX,4X,4HSUBS,4X,1HY,5X,4HSUBS,4X,1HX,4X,4HSUBS,4X,1HY,5X,
        24HSUBS,4X,1HX,4X,4HSUBS,4X,1HY,5X,4HSUBS,4X,1HX,4X,4HSUBS,4X,1HY/)
222      DU 114 I=1,69,2
223      M1=I+1
224      M2=I+70
225      M3=I+71
226      M4=I+140
227      M5=I+141
230      M6=I+210
231      M7=I+211
232      PRINT 143,I,XX(I),M1,XX(M1),M2,XX(M2),M3,XX(M3),M4,XX(M4),M5,
        1XX(M5),M6,XX(M6),M7,XX(M7)
233 143  FORMAT(10X,14,F8.3,15,F8.3,16,F8.3,15,F8.3,16,F8.3,15,F8.3,16,
        1F8.3,15,F8.3)
234 114  CONTINUE
236      I=1
237      K3=7
240      K4=119
241      K5=56
242      K6=8
243      K7=48
244 78  DO 224 K1=K3,K4,K5
245 108  K2=K1+K7
246      SUM=0.
247      SUM2=0.
250      DO 234 N=K1,K2,K6
251      SUM2=SUM2+XX(N)**2
252 234  SUM=SUM+XX(N)
254      BAR(I)=SUM/7.
255      BIAS(I)=SQRT(SUM2/7.-(SUM**2)/49.)
256      BES(I)=1.07*BIAI(I)
257      K16=K1+1
260      K2=K2+1
261      SUM=0.
262      SUM2=0.
263      DO 244 N=K16,K2,K6
264      SUM2=SUM2+XX(N)**2
265 244  SUM=SUM+XX(N)
267      BAR(I+1)=SUM/7.
270      BIAS(I+1)=SQRT(SUM2/7.-(SUM**2)/49.)
271      BES(I+1)=1.07*BIAI(I+1)
272 224  I=I+2
274      IF(I.GT.7) GO TO 88
277      K3=173
300      K4=215
301      K5=42
302      K6=6
303      K7=36

```

NOTE 3 (continued)

NOTE 4

APPENDIX III-E-10

```

ISN      SOURCE STATEMENT

304      GO TO 78
305      88 IF(I.GT.11) GO TO 98
310      K1=255
311      K7=24
312      K6=4
313      GO TO 108
314      98 PRINT 223
315      223 FORMAT(1H1,99X,19HTOTAL DISPLACEMENTS//27X,13HDISPLACEMENTS,20X,
119HSTANDARD DEVIATIONS/17X,3HROW,7X,4HXBAR,6X,4HYBAR,9X,8HBIASED X
2,3X,8HBIASED Y,6X,8HBESSEL X,5X,8HBESSEL Y)

316      K9=1
317      DO 254 I=1,11,2
320      K8=I+1
321      PRINT 233,K9,BAR(I),BAR(K8),BIAS(I),BIAS(K8),BES(I),BES(K8))
322      233 FORMAT(1H0,18X,11,7X,F5.3,5X,F5.3,10X,F6.4,6X,F6.4,7X,F6.4,F11.4)
323      254 K9=K9+1
325      CALL VELOC (48,1,6,1,1)
326      CALL VELOC (104,13,18,13,11)
327      CALL VELOC (160,25,30,25,21)
330      PRINT 163
331      163 FORMAT(1H1,21HVELOCITY CALCULATIONS//15X,20HABSOLUTE COORDINATES,
15X,20HRELATIVE COORDINATES,7X,11HVELOCITIES,8X,15HCUMULATIVE TIME/
25X,7HDELTA T,7X,1HX,9X,1HY,14X,1HX,9X,1HY,10X,5HDX/DT,4X,5HDY/DT,
35X,10HINCREMENTS,11X,5HSUBS./)

332      LP=1
333      NP=12
334      DO 184 J=1,3
335      PRINT 173,(DTVEL(I),XVEL(I),YVEL(I),XRVEL(I),YRVEL(I),DUOT(I),
1UVDT(I),TPlot(I),I,I=LP,NP)
342      173 FORMAT(1H ,5X,F6.3,5X,F6.3,4X,F6.3,9X,F6.3,4X,F6.3,7X,F6.3,2X,
1F6.3,10X,F6.3,12X,12)
343      PRINT 183
344      183 FORMAT(/)
345      LP=LP+12
346      184 NP=NP+12
350      PRINT 193
351      193 FORMAT(1H1,25HACCELERATION CALCULATIONS//5X,5HSUBS.,5X,
115HCUMULATIVE TIME,5X,13HACCELERATIONS/15X,10HINCREMENTS,8X,
27HD2X/DT2,4X,7HD2Y/DT2/)

352      LT=1
353      NT=10
354      DO 194 J=1,3
355      PRINT 203,(I,TACC(I),D2UDT(I),D2VDT(I),I=LT,NT)
362      PRINT 213
363      203 FORMAT(1H ,6X,12,11X,F6.3,8X,F7.3,4X,F7.3)
364      213 FORMAT(/)
365      LT=LT+10
366      194 NT=NT+10
370      GO TO 1
371      PUNCH 7,(XY(I),I=1,280)
376      7 FORMAT(8F7.3)
377      PUNCH 17,(XRVEL(I),YRVEL(I),DUOT(I),DVDT(I),TPlot(I),I=1,36)
404      17 FORMAT(5F7.3)
405      PUNCH 27,(TACC(I),D2UDT(I),D2VDT(I),I=1,30)
412      27 FORMAT(3F7.3)

```

NOTE 4 (continued)

BOYD.-S.v.S.1-

FORTRAN SOURCE LIST MAIN

01/06/67

PAGE 5

ISN	SOURCE STATEMENT
413	NC=3
414	ND=8
415	DD 204 J=1,21
416	PUNCH 37,(XX(L),L=NC,ND)
423	37 FORMAT(6F7.3)
424	NC=NC+8
425	204 ND=ND+8
427	STOP
430	END

APPENDIX III-F-1C

173

```

ISN      SOURCE STATEMENT
0 $IBFTC SPI
1      SUBROUTINE VELOC (LLL,N,M,MA,MZ)
2      COMMON XY,XX,DTVEL,DUOT,DVDT,XRVEL,YRVEL,XVEL,YVEL,TPLOT,DZUDT,
      1DZVDT,TACC,G,YB
3      DIMENSION XY(280),XX(280),DTVEL(36),DUOT(36),DVDT(36),XRVEL(36),
      1YRVEL(36),XVEL(36),YVEL(36),TPLOT(36),DZUDT(30),DZVDT(30),TACC(30)
4      L=LLL
5      DO 124 I=N,M
6      DTVEL(I)=(XY(L+1)-XY(L-7))/YB
7      DUOT(I)=(XX(L-5)-XX(L+3))/DTVEL(I)
10     DVDT(I)=(XX(L-4)-XX(L+4))/DTVEL(I)
11     XRVEL(I)=(XX(L-5)-XX(L+3))/2.+XX(L+3)
12     YRVEL(I)=(XX(L-4)-XX(L+4))/2.+XX(L+4)
13     XVEL(I)=XRVEL(I)+(XY(L-7)+XY(L+1))/2.
14     YVEL(I)=YRVEL(I)+(XY(L-6)+XY(L+2))/2.
15     DTVEL(I+6)=DTVEL(I)
16     DUOT(I+6)=(XX(L-3)-XX(L+5))/DTVEL(I)
17     DVDT(I+6)=(XX(L-2)-XX(L+6))/DTVEL(I)
20     XRVEL(I+6)=(XX(L-3)-XX(L+5))/2.+XX(L+5)
21     YRVEL(I+6)=(XX(L-2)-XX(L+6))/2.+XX(L+6)
22     XVEL(I+6)=XRVEL(I+6)+(XY(L-7)+XY(L+1))/2.-G
23     YVEL(I+6)=YRVEL(I+6)+(XY(L-6)+XY(L+2))/2.
24     124 L=L-8
26     TINV=0.
27     LB=MA+5
30     DO 134 J=MA,LB
31     IF(J.GE.(MA+1)) GO TO 38
34     Z=DTVEL(J)/2.
35     GO TO 48
36     38 Z=DTVEL(J)/2.+DTVEL(J-1)/2.
37     48 TINV=TINV+Z
40     134 TPLOT(J)=TINV
42     TINV=G/YB
43     LA=MA+6
44     LD=MA+11
45     DO 154 J=LA,LD
46     IF(J.GE.(MA+7)) GO TO 58
51     Z=DTVEL(J)/2.
52     GO TO 68
53     58 Z=DTVEL(J)/2.+DTVEL(J-1)/2.
54     68 TINV=TINV+Z
55     154 TPLOT(J)=TINV
57     TINV=0.
60     LC=MZ+4
61     DO 164 J=MZ,LC
62     DZUDT(J)=(DUOT(J+1)-DUOT(J))*2./(DTVEL(J)+DTVEL(J+1))
63     DZVDT(J)=(DVDT(J+1)-DVDT(J))*2./(DTVEL(J)+DTVEL(J+1))
64     Z=DTVEL(J)
65     TINV=TINV+Z
66     164 TACC(J)=TINV
70     TINV=G/YB
71     LE=MZ+5
72     LF=MZ+9
73     DO 174 J=LE,LF
74     DZUDT(J)=(DUOT(J+2)-DUOT(J+1))*2./(DTVEL(J+1)+DTVEL(J+2))

```

NOTE 5

APPENDIX III-F-13

BOYD -S.V.S.I-

FORTRAN SOURCE LIST SP1

01/06/67

PAGE 8

ISN SOURCE STATEMENT

```
75 D2VDT(J)=(DVDT(J+2)-DVDT(J+1))*2./(DTVEL(J+1)+DTVEL(J+2))
76 Z=DTVEL(J+1)
77 TINV=TINV+Z
100 174 TACC(J)=TINV
102 RETURN
103 END
```

NO MESSAGES FOR ABOVE ASSEMBLY

OBJECT PROGRAM IS BEING ENTERED INTO STORAGE.

APPENDIX III-F-1C

175

LOADING DATA

ANGULAR VELOCITY	0.272	REVS. PER SEC
CARRIAGE VELOCITY	7.60	INS. PER SEC
D.B.P. L.H.S.	-2.099	LBS.
R.H.S.	-1.623	LBS.
SINKAGE	0.617	INCHES
TURQUE LOADING	43.97	IN.LBS.
UNLOADING	43.97	IN.LBS.
SLIP RATE	3.92	PER CENT

PARAX	4.627
PARAY	3.576

D.V.M. OUTPUT

CODE	X	Y	X	Y	X	Y	X	Y
1411	9541	67318	15288	66850	13504	62406	13173	62282
1412	21773	67438	25773	67585	25568	61584	25042	62472
1413	34152	67347	36603	67730	38907	61345	37220	62425
1414	46103	67471	47927	67605	52045	62922	48992	62302
1415	58138	67232	59468	67310	64256	64643	61414	62196
1416	70332	67472	71291	67148	75224	66790	73784	62264
1417	82327	67712	82903	67549	85601	67759	85662	62476
1421	9580	54869	12939	53704	11809	51826	11525	51894
1422	21871	54803	24419	53935	24398	51482	23832	51875
1423	34047	54602	35775	53772	36751	51084	36023	51655
1424	45979	54756	47219	54507	49501	51771	48195	51819
1425	58182	54660	59256	54421	61525	52648	60307	51532
1426	70395	54632	70787	54441	73417	53354	72370	51666
1427	82019	54537	82713	54594	84364	54356	84355	51734
1431	9794	41724	11429	40910	11925	39961	11351	39903
1432	22058	41619	23599	40929	23444	39798	23317	39971
1433	34029	41524	35328	41035	35952	39560	35407	39531
1434	46129	41679	47046	41467	48284	40153	47651	39905
1435	58362	41918	58919	41506	60101	40144	59642	40040
1436	70430	41688	70901	41689	72280	40903	71712	39858
1437	82789	41491	83092	41421	84187	41059	83981	39945
1441	9551	29725	10552	29219	10222	28762		
1442	21934	29810	22938	29677	22674	28848		
1443	34198	29830	34951	29735	34950	28715		
1444	46083	29906	46649	29898	46689	28781		
1445	58189	29830	58609	29973	58854	28743		
1446	70190	29792	71031	29535	70856	28972		
1447	82402	29783	83018	29486	83073	28901		
1451	9249	17456	9978	16996	9979	16997		
1452	21807	17382	22179	17035	22325	16739		
1453	34014	17341	34336	16835	34336	16836		
1454	46164	17521	46535	17293	46848	16759		
1455	58300	17350	58515	17121	58809	16530		
1456	70509	17598	70842	17245	71077	16770		
1457	82380	17256	82878	17017	82878	16607		
1461	9311	5180	9746	4988				
1462	21692	5550	21887	5160				
1463	33889	5372	34116	5045				
1464	46205	5503	46460	5172				
1465	58304	5723	58714	5399				
1466	70531	5027	70923	4798				
1467	82646	5314	82949	5017				

CORRECTED COORDINATES

SUBS	X	SUBS	Y	SUBS	X	SUBS	Y	SUBS	X	SUBS	Y	SUBS	X	SUBS	Y
1	-0.000	2	-1.500	3	0.485	4	-1.539	5	0.334	6	-1.914	7	0.306	8	-1.925
9	1.032	10	-1.490	11	1.369	12	-1.477	13	1.352	14	-1.984	15	1.307	16	-1.909
17	2.076	18	-1.498	19	2.282	20	-1.465	21	2.477	22	-2.004	23	2.334	24	-1.913
25	3.083	26	-1.487	27	3.237	28	-1.476	29	3.585	30	-1.871	31	3.327	32	-1.923
33	4.096	34	-1.507	35	4.211	36	-1.501	37	4.614	38	-1.726	39	4.375	40	-1.932
41	5.127	42	-1.487	43	5.208	44	-1.514	45	5.539	46	-1.545	47	5.418	48	-1.926
49	6.138	50	-1.467	51	6.187	52	-1.481	53	6.415	54	-1.463	55	6.420	56	-1.908
57	0.003	58	-2.550	59	0.287	60	-2.648	61	0.191	62	-2.807	63	0.167	64	-2.801
65	1.040	66	-2.555	67	1.255	68	-2.629	69	1.253	70	-2.836	71	1.205	72	-2.802
73	2.067	74	-2.572	75	2.212	76	-2.642	77	2.295	78	-2.869	79	2.233	80	-2.821
81	3.073	82	-2.559	83	3.178	84	-2.580	85	3.370	86	-2.811	87	3.260	88	-2.807
89	4.102	90	-2.568	91	4.193	92	-2.588	93	4.384	94	-2.737	95	4.281	96	-2.831
97	5.132	98	-2.570	99	5.165	100	-2.586	101	5.387	102	-2.678	103	5.299	104	-2.820
105	6.112	106	-2.578	107	6.171	108	-2.573	109	6.310	110	-2.593	111	6.309	112	-2.814
113	0.021	114	-3.658	115	0.159	116	-3.727	117	0.201	118	-3.807	119	0.153	120	-3.812
121	1.056	122	-3.667	123	1.186	124	-3.726	125	1.173	126	-3.821	127	1.162	128	-3.806
129	2.065	130	-3.675	131	2.175	132	-3.717	133	2.227	134	-3.841	135	2.181	136	-3.843
137	3.086	138	-3.662	139	3.163	140	-3.680	141	3.267	142	-3.791	143	3.214	144	-3.812
145	4.117	146	-3.642	147	4.164	148	-3.677	149	4.264	150	-3.792	151	4.225	152	-3.800
153	5.135	154	-3.662	155	5.175	156	-3.661	157	5.291	158	-3.728	159	5.243	160	-3.816
161	6.177	162	-3.678	163	6.203	164	-3.684	165	6.295	166	-3.715	167	6.278	168	-3.809
169	0.001	170	-4.670	171	0.085	172	-4.713	173	0.057	174	-4.752	175	1.045	176	-4.663
177	1.130	178	-4.674	179	1.108	180	-4.744	181	2.079	182	-4.662	183	2.143	184	-4.670
185	2.143	186	-4.756	187	3.082	188	-4.655	189	3.130	190	-4.656	191	3.133	192	-4.750
193	4.103	194	-4.662	195	4.138	196	-4.649	197	4.159	198	-4.753	199	5.115	200	-4.665
201	5.186	202	-4.686	203	5.171	204	-4.734	205	6.145	206	-4.666	207	6.197	208	-4.691
209	6.201	210	-4.740	211	-0.025	212	-5.705	213	0.037	214	-5.744	215	0.037	216	-5.744
217	1.034	218	-5.711	219	1.066	220	-5.741	221	1.078	222	-5.766	223	2.064	224	-5.715
225	2.091	226	-5.757	227	2.091	228	-5.757	229	3.089	230	-5.700	231	3.120	232	-5.719
233	3.146	234	-5.764	235	4.112	236	-5.714	237	4.130	238	-5.733	239	4.155	240	-5.783
241	5.142	242	-5.693	243	5.170	244	-5.723	245	5.190	246	-5.763	247	6.143	248	-5.722
249	6.185	250	-5.742	251	6.185	252	-5.777	253	-0.019	254	-6.740	255	0.017	256	-6.757
257	1.025	258	-6.709	259	1.041	260	-6.742	261	2.053	262	-6.724	263	2.073	264	-6.752
265	3.092	266	-6.713	267	3.114	268	-6.741	269	4.112	270	-6.695	271	4.147	272	-6.722
273	5.144	274	-6.753	275	5.177	276	-6.773	277	6.165	278	-6.729	279	6.191	280	-6.754

APPENDIX III-F-10

UNORDERED LISTING OF TRANSLATIONS

SUBS	X	SUBS	Y	SUBS	X	SUBS	Y	SUBS	X	SUBS	Y	SUBS	X	SUBS	Y
1	-0.000	2	-0.000	71	0.165	72	-0.247	141	0.182	142	-0.129	211	-0.000	212	-0.000
3	0.485	4	-0.039	73	0.000	74	-0.000	143	0.128	144	-0.150	213	0.061	214	-0.039
5	0.334	6	-0.414	75	0.146	76	-0.070	145	0.000	146	-0.000	215	0.062	216	-0.039
7	0.306	8	-0.425	77	0.228	78	-0.297	147	0.047	148	-0.035	217	0.000	218	-0.000
9	0.000	10	-0.000	79	0.167	80	-0.249	149	0.147	150	-0.150	219	0.031	220	-0.029
11	0.337	12	0.012	81	0.000	82	-0.000	151	0.108	152	-0.158	221	0.044	222	-0.054
13	0.320	14	-0.494	83	0.105	84	-0.021	153	0.000	154	-0.000	223	0.000	224	-0.000
15	0.276	16	-0.419	85	0.297	86	-0.252	155	0.040	156	0.000	225	0.027	226	-0.043
17	0.000	18	-0.000	87	0.187	88	-0.248	157	0.156	158	-0.066	227	0.027	228	-0.043
19	0.207	20	0.032	89	0.000	90	-0.000	159	0.108	160	-0.154	229	0.000	230	-0.000
21	0.401	22	-0.506	91	0.091	92	-0.020	161	0.000	162	-0.000	231	0.031	232	-0.019
23	0.259	24	-0.415	93	0.282	94	-0.170	163	0.026	164	-0.006	233	0.058	234	-0.064
25	0.000	26	-0.000	95	0.179	96	-0.264	165	0.118	166	-0.036	235	0.000	236	-0.000
27	0.154	28	0.011	97	0.000	98	-0.000	167	0.101	168	-0.130	237	0.018	238	-0.019
29	0.501	30	-0.384	99	0.033	100	-0.016	169	0.000	170	-0.000	239	0.043	240	-0.069
31	0.244	32	-0.436	101	0.255	102	-0.108	171	0.084	172	-0.043	241	0.000	242	-0.000
33	0.000	34	-0.000	103	0.167	104	-0.250	173	0.057	174	-0.081	243	0.028	244	-0.030
35	0.112	36	0.007	105	0.000	106	-0.000	175	0.000	176	-0.000	245	0.048	246	-0.070
37	0.516	38	-0.216	107	0.059	108	0.005	177	0.085	178	-0.011	247	0.000	248	-0.000
39	0.276	40	-0.425	109	0.198	110	-0.015	179	0.062	180	-0.081	249	0.042	250	-0.020
41	0.000	42	-0.000	111	0.197	112	-0.236	181	0.000	182	-0.000	251	0.042	252	-0.055
43	0.001	44	-0.027	113	0.000	114	-0.000	183	0.064	184	-0.008	253	-0.000	254	-0.000
45	0.413	46	-0.058	115	0.138	116	-0.069	185	0.063	186	-0.094	255	0.037	256	-0.016
47	0.291	48	-0.439	117	0.180	118	-0.149	187	0.000	188	-0.000	257	0.000	258	-0.000
49	0.000	50	-0.000	119	0.131	120	-0.154	189	0.048	190	-0.001	259	0.016	260	-0.033
51	0.049	52	-0.014	121	0.000	122	-0.000	191	0.051	192	-0.095	261	0.000	262	-0.000
53	0.276	54	0.004	123	0.130	124	-0.058	193	0.000	194	-0.000	263	0.019	264	-0.028
55	0.281	56	-0.442	125	0.117	126	-0.154	195	0.035	196	0.012	265	0.000	266	-0.000
57	0.000	58	-0.000	127	0.106	128	-0.139	197	0.056	198	-0.092	267	0.022	268	-0.028
59	0.283	60	-0.096	129	0.000	130	-0.000	199	0.000	200	-0.000	269	0.000	270	-0.000
61	0.188	62	-0.257	131	0.110	132	-0.041	201	0.071	202	-0.022	271	0.035	272	-0.027
63	0.164	64	-0.251	133	0.162	134	-0.166	203	0.056	204	-0.069	273	0.000	274	-0.000
65	0.000	66	-0.000	135	0.116	136	-0.168	205	0.000	206	-0.000	275	0.033	276	-0.019
67	0.215	68	-0.073	137	0.000	138	-0.000	207	0.052	208	-0.025	277	0.000	278	-0.000
69	0.213	70	-0.280	139	0.077	140	-0.018	209	0.057	210	-0.074	279	0.026	280	-0.025

APPENDIX III-F-1C

TOTAL DISPLACEMENTS

ROW	DISPLACEMENTS		STANDARD DEVIATIONS			
	XBAR	YBAR	BIASED X	BIASED Y	BESSEL X	BESSEL Y
1	0.276	-.429	0.0190	0.0096	0.0203	0.0103
2	0.175	-.249	0.0119	0.0075	0.0128	0.0080
3	0.114	-.150	0.0109	0.0115	0.0116	0.0124
4	0.057	-.084	0.0039	0.0093	0.0042	0.0100
5	0.046	-.056	0.0105	0.0114	0.0112	0.0122
6	0.027	-.025	0.0075	0.0052	0.0080	0.0056

APPENDIX III-F-1C

VELOCITY CALCULATIONS

DELTA T	ABSOLUTE COORDINATES		RELATIVE COORDINATES		VELOCITIES,		CUMULATIVE TIME INCREMENTS	SUBS.
	X	Y	X	Y	DX/DT	DY/DT		
0.133	5.697	-1.497	0.065	-0.021	0.243	-0.102	0.067	1
0.135	4.709	-1.508	0.097	-0.010	0.231	0.250	0.201	2
0.134	3.724	-1.488	0.133	0.009	0.312	0.035	0.335	3
0.133	2.760	-1.471	0.180	0.022	0.399	0.158	0.468	4
0.137	1.826	-1.471	0.272	0.022	0.951	-0.145	0.603	5
0.136	0.927	-1.508	0.411	-0.014	1.085	-0.302	0.740	6
0.133	1.289	-1.504	0.344	-0.027	1.025	-0.462	0.684	7
0.135	0.389	-1.635	0.464	-0.138	0.764	-1.188	0.818	8
0.134	-0.589	-1.798	0.509	-0.301	-0.111	-1.237	0.952	9
0.133	-1.657	-1.937	0.451	-0.445	-0.755	-0.924	1.086	10
0.137	-2.774	-1.994	0.361	-0.500	-0.589	0.091	1.221	11
0.136	-3.845	-1.949	0.327	-0.454	0.104	0.585	1.357	12
0.129	5.668	-2.580	0.046	-0.006	-0.197	-0.162	0.065	13
0.136	4.679	-2.587	0.062	-0.018	0.424	-0.030	0.197	14
0.135	3.685	-2.584	0.098	-0.021	0.103	-0.006	0.332	15
0.132	2.695	-2.611	0.125	-0.045	0.311	-0.370	0.466	16
0.135	1.734	-2.636	0.180	-0.072	0.512	-0.024	0.600	17
0.136	0.771	-2.638	0.249	-0.086	0.501	-0.184	0.736	18
0.129	1.161	-2.635	0.226	-0.062	0.442	-0.717	0.682	19
0.136	0.198	-2.707	0.268	-0.139	0.200	-0.457	0.814	20
0.135	-0.811	-2.774	0.289	-0.211	0.111	-0.606	0.949	21
0.132	-1.856	-2.840	0.263	-0.274	-0.521	-0.339	1.083	22
0.135	-2.914	-2.852	0.221	-0.288	-0.110	0.123	1.217	23
0.136	-3.966	-2.821	0.201	-0.268	-0.184	0.172	1.353	24
0.137	5.689	-3.673	0.033	-0.003	0.103	0.044	0.069	25
0.134	4.670	-3.669	0.043	-0.017	0.054	-0.260	0.204	26
0.136	3.664	-3.678	0.062	-0.026	0.224	0.124	0.339	27
0.134	2.669	-3.698	0.093	-0.030	0.240	-0.174	0.474	28
0.133	1.680	-3.721	0.120	-0.050	0.154	-0.128	0.608	29
0.136	0.672	-3.726	0.134	-0.063	0.058	-0.077	0.742	30
0.137	1.105	-3.721	0.137	-0.051	0.278	-0.217	0.686	31
0.134	0.090	-3.760	0.151	-0.108	-0.070	-0.623	0.821	32
0.136	-0.922	-3.791	0.164	-0.139	0.258	0.154	0.956	33
0.134	-1.941	-3.816	0.172	-0.147	-0.146	-0.275	1.091	34
0.133	-2.988	-3.831	0.140	-0.160	-0.341	0.091	1.225	35
0.136	-4.001	-3.814	0.148	-0.151	0.462	0.036	1.359	36

APPENDIX III-F-1C



ACCELERATION CALCULATIONS

SUBS.	CUMULATIVE TIME INCREMENTS	ACCELERATIONS	
		D2X/DT2	D2Y/DT2
1	0.133	-0.085	2.625
2	0.269	0.600	-1.600
3	0.402	0.652	0.923
4	0.535	4.088	-2.245
5	0.672	0.984	-1.736
6	0.750	-1.944	-5.410
7	0.886	-6.506	-0.360
8	1.019	-4.833	2.356
9	1.152	1.225	7.513
10	1.289	5.077	3.618
11	0.137	5.077	3.618
12	0.273	-2.279	-5.643
13	0.402	4.698	0.999
14	0.538	-2.366	0.174
15	0.673	1.548	-2.715
16	0.752	-0.076	-1.177
17	0.889	-0.443	-4.018
18	1.018	-1.635	1.968
19	1.153	-0.651	-1.101
20	1.289	-4.720	1.989
21	0.135	-4.720	1.989
22	0.268	3.067	3.455
23	0.403	-0.543	0.360
24	0.540	2.101	-0.937
25	0.677	-0.352	-2.240
26	0.753	0.120	-2.207
27	0.887	-0.646	0.347
28	1.020	-0.709	0.377
29	1.156	1.607	-1.026
30	1.293	-2.565	-2.992

END-OF-DATA ENCOUNTERED ON SYSTEM INPUT FILE.

APPENDIX III-R-1C

APPENDIX III-G-1SOURCES & MAGNITUDES OF RADIOGRAPHIC DISPLACEMENTSNOT CAUSED BY MOVEMENTS OF THE TRACER-OBJECTS

Any discussion of the reliability of measurements obtained from radiographs must include a consideration of what Roscoe et al (1963) have termed 'fictitious displacements'. In the technique described in Chapter III, three main sources of 'fictitious displacements' are present.

- 1) Movement of the X-ray source.
- 2) Misalignment of the X-ray cassette.
- 3) Departures from the assumed co-planar tracer-object matrix. This includes departures resulting from initial misplacements and from movements away from the assumed plane that occur during the wheel loading cycle.

1) Movements of the X-Ray Source:

The Flash X-ray tube and pulser are mounted on a dolly which is in turn mounted on guide rails. This limits possible movements to the single case of departures in the Z direction - see Fig. (1) below. Because the primary X-ray beam may be considered as unrefracted, simple optics can be used to obtain the image-centre displacement, $(\delta x_2)_1$, caused by a source displacement, δz_2 :

$$(\delta x_2)_1 = x_1 \frac{(z_1+z_2)}{z_2} - \frac{x_1(z_1+z_2+\delta z_2)}{z_2+\delta z_2} \quad (1)$$

The difference on the tracer-object, reduced, plane would be:

APPENDIX III-G-1 (Cont'd.)

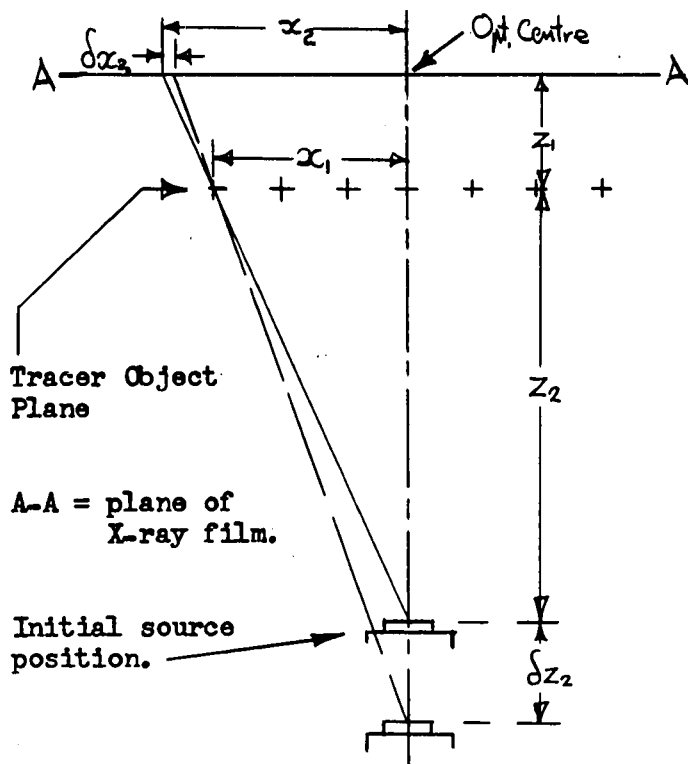


Figure (1): The Influence of X-ray Source Movements on Image Location.

where: O.C. is the Optical Centre.

$$(\delta x_2)_1^1 = \frac{z_2}{z_1 + z_2} (\delta x_2)_1 \quad (2)$$

Since the X-ray pulser position was checked frequently it is unlikely that δz_2 values greater than .25 inches occurred. From equation (2) this corresponds to a displacement in the tracer-object, T.O., plane of $(\delta x_2)_1^1 = .019$ inches, for a maximum $x_1 = 3$ inch value. ($z_1 = 3.5$ inches, $z_2 = 13.0$ inches unless otherwise stated). For $x_1 < 3''$, $(\delta x_2)_1^1 < .019$ inches. The same reasoning holds for $(\delta y_2)_1^1$ displacements in the y direction in the T.O. plane.

Since the reference grid on the inside of the Cassette holder forms an image pattern uninfluenced by δz_2 movements of the pulser the resulting errors are manifest in the translation and velocity calculations.

2) Misalignment of the X-Ray Cassette:

As the Cassette holder is bolted to the floor and surrounded by sand

APPENDIX III-G-1 (Cont'd.)

it may be considered to occupy a constant, unmoveable, position for the duration of the testing. However, the locating of the Cassette within the holder is performed three times during each Test and thus represents a source of 'fictitious displacement'. This source can be divided into the following possible components, caused by:

a) Rotations about the vertical, y, axis:

With reference to Fig. (2), below, the greatest potential cause of fictitious displacements from this source is represented by a rotation $\delta\theta$ from the correct film plane A.A. to the displaced plane B.A. This causes a corresponding displacement of images in the x coordinate direction, on the radiograph, equal to:

$$(\delta x_2)_{2a} = x_3 \sin \delta\theta (\tan(\delta\theta + \theta_2) - \tan \delta\theta/2) \quad (3)$$

This is equivalent to a displacement on the T.O. plane of:

$$(\delta x_2)_{2a}^1 = \frac{z_2}{z_1 + z_2} (\delta x_2)_{2a} \quad (4)$$

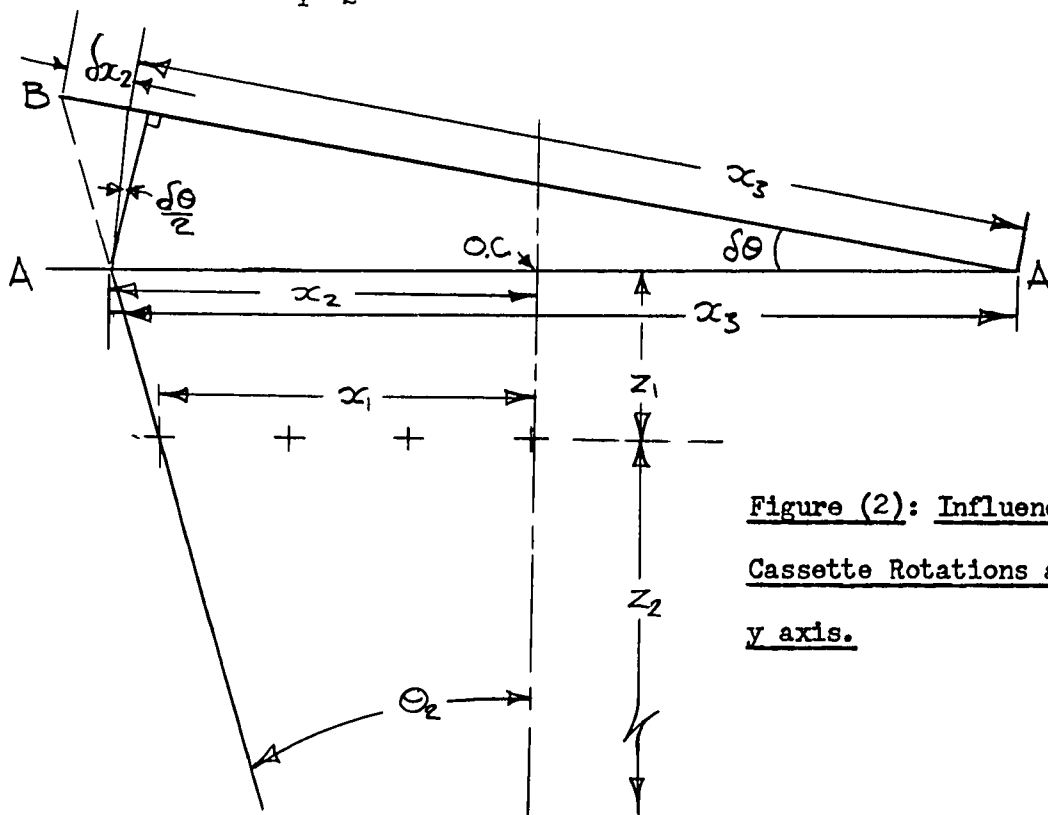


Figure (2): Influence of Cassette Rotations about y axis.

APPENDIX III-G-1 (Cont'd.)

Assuming the worst condition to be: $\Theta_2 = 13^\circ$ and $\Delta\Theta = 1^\circ$, where $x_3 = 9''$, equation (4) gives:
 $(\delta x_2)_{2a}^1 = .031$ inches. This value does, however, represent an overestimate since the reference grid images will suffer corresponding displacements thus tending to compensate for this 'fictitious displacement'.

b) Rotations about the horizontal, x, axis.

This source of image displacement may be calculated using a similar formulation to equation (4). It should be noted that the y dimension of the Cassette is only 8 inches and thus errors in the T.O. plane will be less than .031 inches - assuming the same maximum rotation of 1 degree.

c) Displacements of the Cassette in the Z direction.

Assuming that the Cassette remains in the X-Y plane, displacements in the Z direction of $< .1$ inch can possibly occur. With reference to Figure (3), below,

$$(\delta x_2)_{2c}^1 = \frac{x_1 \delta z_1}{z_2} \quad (5)$$

$$\text{or: } (\delta x_2)_{2c}^1 = \frac{z_2}{z_1+z_2} (\delta x_2)_{2c} \quad (6)$$

for a displacement of the image on the T.O. plane. For $\delta z_1 = .1$ inch with $x_1 = 3$ inches, the maximum anticipated displacement from this source is equal to .018 inches.

APPENDIX III-G-1 (Cont'd.)

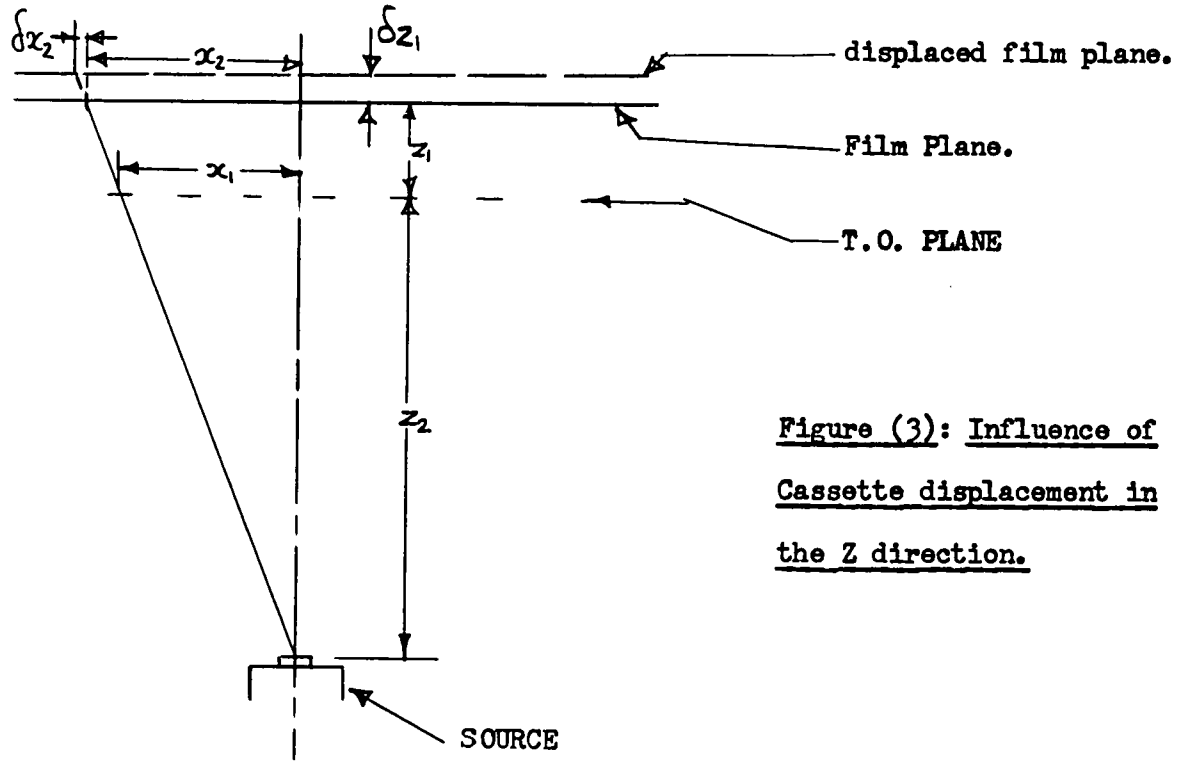


Figure (3): Influence of Cassette displacement in the Z direction.

3) Departures from the Assumed Co-Planar Tracer-Object 'Matrix'.

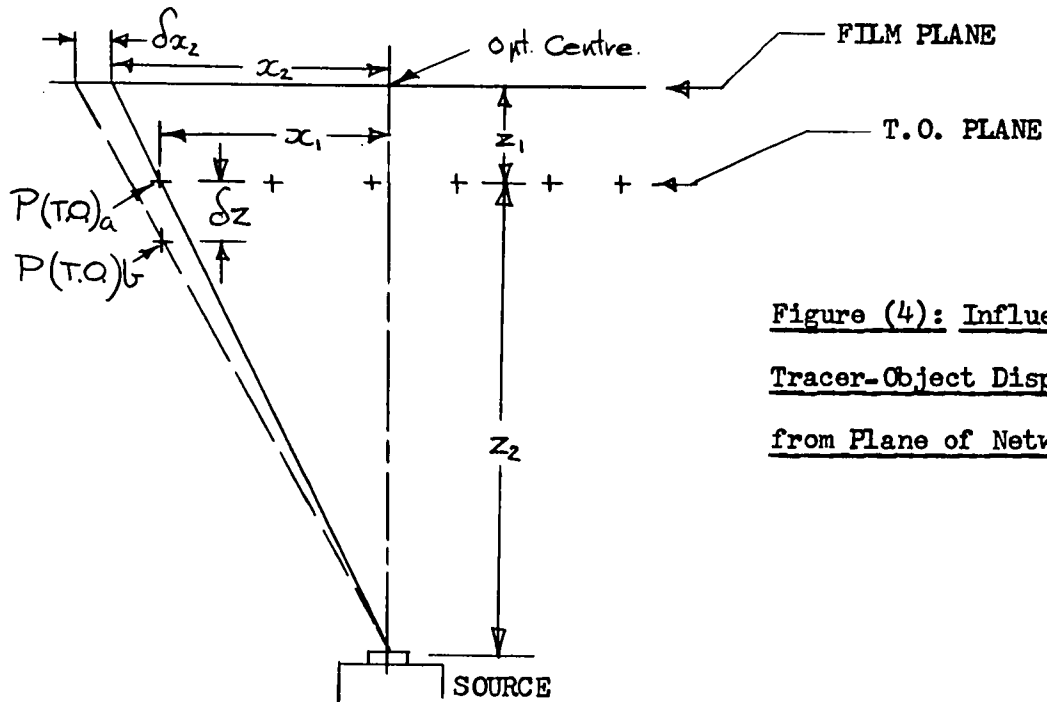


Figure (4): Influence of Tracer-Object Displacement from Plane of Network.

APPENDIX III-G-1 (Cont'd.)

The displacement, or misplacement, of a tracer-object from position (T.O.)_a to (T.O.)_b results in a radiographic image displacement.

$$(\delta x_2)_3 = x_1(z_1+z_2) \left[\frac{1}{(z_2-\delta z)} - \frac{1}{z_2} \right] - \quad (7)$$

which causes a corresponding change in the Tracer-object plane of:

$$(\delta x_2)_3^1 = \frac{z_2}{z_1+z_2} (\delta x_2)_3 \quad (8)$$

For a displacement $\delta z = .05$ inches, $(\delta x_2)_3^1 = .015$ inches.

It should be noted that the net effect of such a displacement is small if the T.O. was originally misplaced and describes a translation path parallel to the T.O. plane. If z components of translation occur then this source of variation becomes important.

SUMMARY:

From the forgoing considerations it is evident that the magnitude of all sources of 'fictitious displacements' are directly proportional to the magnitude of the dimension z_2 . In this particular application, where maximum penetration was required, z_2 was limited to a maximum value of 13 inches. The 'fictitious displacements' are thus correspondingly high. Since displacements from equations (2), (4), (6) and (8) can not be added algebraically the total scatter from these sources can not be obtained directly. However as a first approximation a value of .08 inches for the maximum possible 'fictitious displacement' may be obtained from: $((\delta x_2)_1^1 + (\delta x_2)_{2a}^1 + 2(\delta x_2)_3^1)$. This corresponds to an approximate value of .02 inches for the associated standard deviation.

APPENDIX IV-A1

SURFICIAL LOADING INFORMATION (BY TEST)*

	APPLIED TORQUE	WHEEL LOAD	TRANSLAT. VELOC.	ANGULAR VEL.	D.B.P.	NORMAL SLIP	DYNAMIC SINKAGE	WHEEL DIAMETER
TEST NO.	M (In-lbs)	W (lbs)	V (ins/sec)	ω (rads/sec)	F (lbs)	S (%)	y_0 (ins)	D (ins)
4	41.54	23.8	7.75	1.9	-3.845	9.2	.689	9
5	49.51	"	7.8	2.58	-5.25	32.95	.874	"
6	33.4	"	7.9	1.78	-4.946	1.5	.651	"
8	57.89	"	5.23	1.37	-1.863	15.29	.776	"
9	68.9	"	4.8	1.8	-4.188	40.87	.923	"
10	55.7	"	5.0	1.17	-3.536	5.01	.680	"
11	42.68	24.2	4.9	1.04	-2.704	-2.4	.592	9.25
12	62.05	"	4.83	1.23	+0.391	14.8	.748	"
13	70.61	"	4.75	1.54	-1.753	33.35	1.010	"
14	43.97	"	7.6	1.72	-3.713	3.92	.617	"
15	56.53	"	7.72	1.92	-0.868	13.03	.682	"
16	68.69	"	7.65	2.56	-2.933	35.49	.894	"
19	56.26	28.2	4.93	1.02	-2.099	-3.99	.605	"
20	72.98	"	5.06	1.36	-3.736	19.74	.733	"
21	75.38	"	4.90	1.54	-4.142	31.21	.935	"
22	56.53	"	7.79	1.78	-4.316	4.99	.692	"
23	65.33	"	7.70	1.92	-2.636	13.32	.774	"
24	75.72	"	7.67	2.64	-4.482	37.58	.912	"
29	41.30	24.2	7.67	1.73	+0.11	4.14	.608	"
30	51.02	"	7.88	2.02	+1.592	15.49	.505	"
31	70.61	"	7.55	2.66	+0.236	38.37	.643	"
33	47.05	"	7.90	1.73	-2.061	1.28	.582	"

APPENDIX IV-A1 (Cont'd.)

TEST NO.	M	W	V	ω	F	S	y_0	D
34	60.46	24.2	7.55	1.9	+1.259	13.62	.661	9.25
35	71.45	"	7.6	2.61	-1.174	36.7	.751	"
LARGE WHEEL (Prototype)								
39	96.69	80.2	7.24	.975	-20.11	-10.43	.850	13.5
40	139.78	"	7.24	1.05	-8.354	-2.64	.938	"
41	173.84	"	7.39	1.3	4.39	15.61	1.195	"
42	130.75	"	9.55	1.43	-6.716	.63	.839	"
43	63.17	"	9.45	1.57	.255	10.91	1.107	"
44	200.51	"	9.53	1.95	.951	27.25	1.312	"
45	147.57	"	6.05	.97	9.926	6.78	.896	"
46	85.20	"	6.86	.84	-17.009	-21.78	.817	"
47	211.59	"	6.40	1.32	3.176	28.09	1.415	"
48	160.29	80.7	6.58	1.01	16.785	5.49	.979	13.75
49	193.95	"	6.58	1.11	13.668	13.57	1.153	"
50	224.31	"	6.22	1.25	3.445	27.85	1.516	"
51	123.77	"	9.45	1.39	-4.7	1.20	.875	"
52	174.25	"	10.04	1.53	12.922	4.48	1.024	"
53	214.05	"	9.76	1.92	8.926	26.0	1.387	"
54	117.62	"	9.10	1.42	-12.531	6.34	1.066	"
55	195.18	"	9.55	1.55	-8.345	10.31	1.162	"
56	248.52	"	9.43	1.98	-2.606	30.41	1.558	"
57	208.31	"	6.61	1.01	17.765	5.13	1.115	"
58	282.17	"	6.28	1.22	19.796	24.73	1.457	"

* Note: The broken sequence in the test numbering is due to the fact that one group of experiments have not been included. These were carried out in a lower velocity range ($\ll V_1$) where it was not possible to control the slip rate, s , and translational wheel velocity, V , within acceptable limits.

APPENDIX V

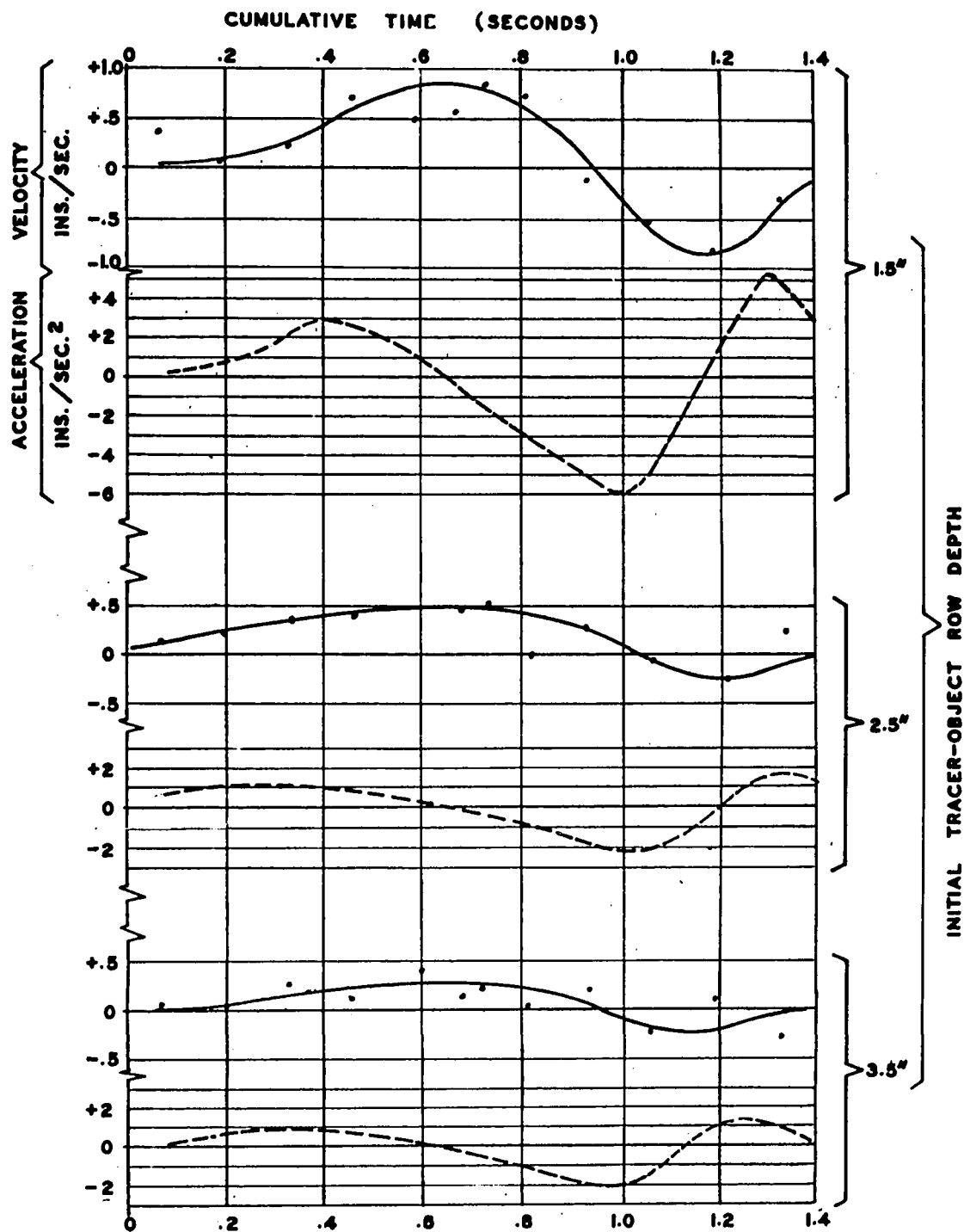
<u>APPENDIX</u>	<u>TITLE</u>	<u>Page.</u>
V-B-1	A listing of the Torque Energy Coefficients η , and the Dimensionless Sinkage Ratio, y_0/D , by Test.	191
V-C-1	Component Velocity and Acceleration Results; plotted by row, vs. Cumulative Time, Test 29.	192
V-C-2	Tracer-Object Matrices Corresponding to Four Sequential X-Ray Pulses.	194
V-C-3	Evaluation of Equation (V-14) for Test 29.	195

APPENDIX V-B-1

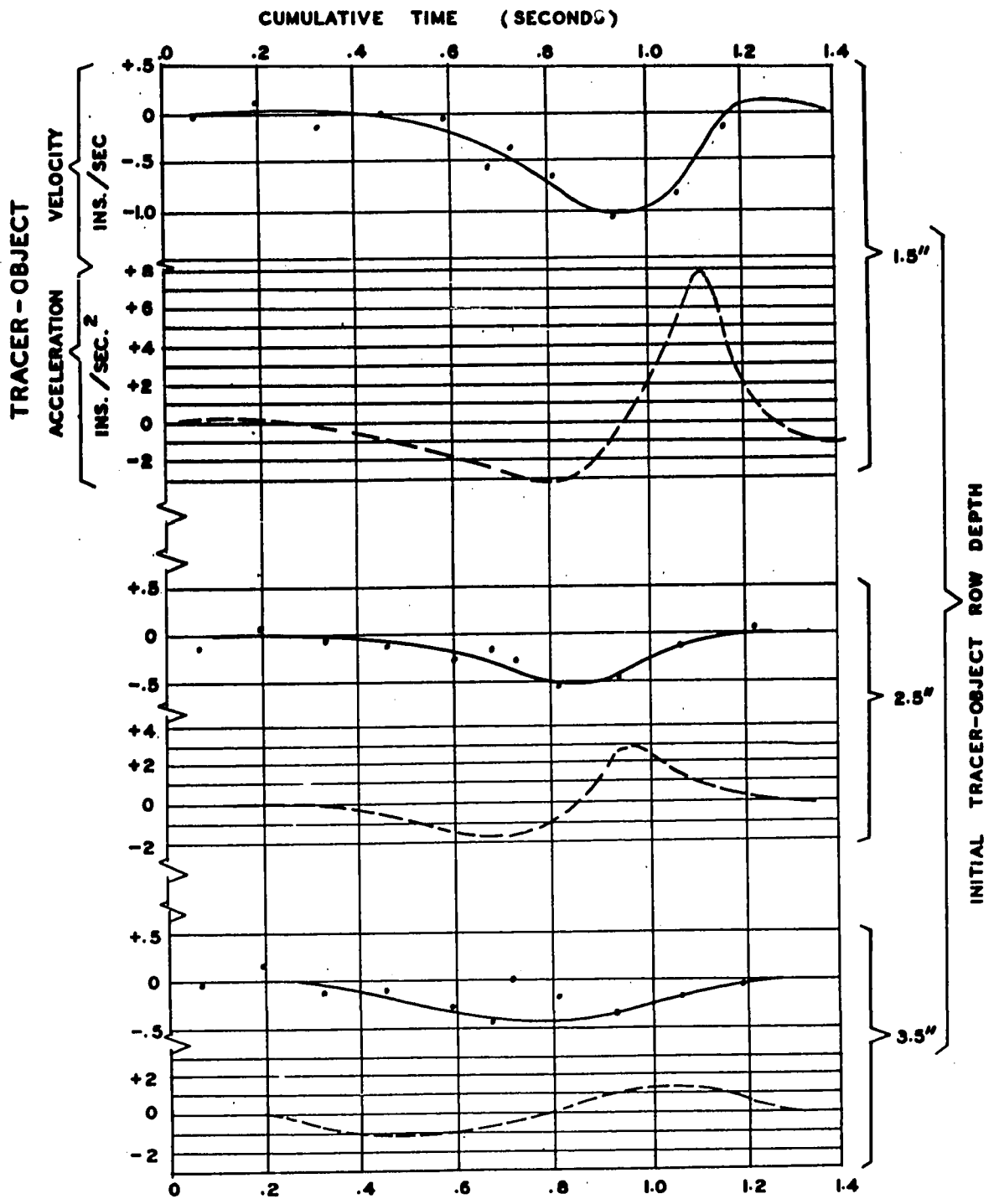
A LISTING OF THE TORQUE ENERGY COEFFICIENT, η ,
AND THE DIMENSIONLESS SINKAGE RATIO $\frac{y_0}{D}$, BY TEST

TEST NUMBER	$\eta = \frac{M\omega}{W\dot{x}}$	$\frac{y_0}{D}$
4	.430	.0765
5	.690	.0971
6	.316	.0725
8	.640	.0865
9	1.090	.102
10	.550	.0735
11	.376	.064
12	.662	.081
13	.940	.109
14	.410	.067
15	.574	.073
16	.950	.099
19	.412	.0655
20	.692	.0792
21	.841	.101
22	.46	.0750
23	.576	.0837
24	.925	.0986
29	.385	.066
30	.54	.0516
31	1.10	.0695
33	.426	.063

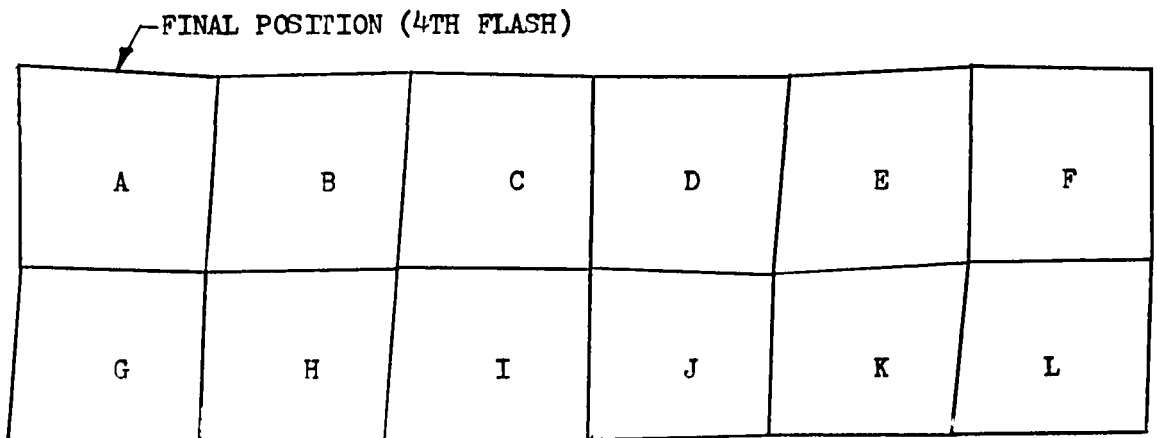
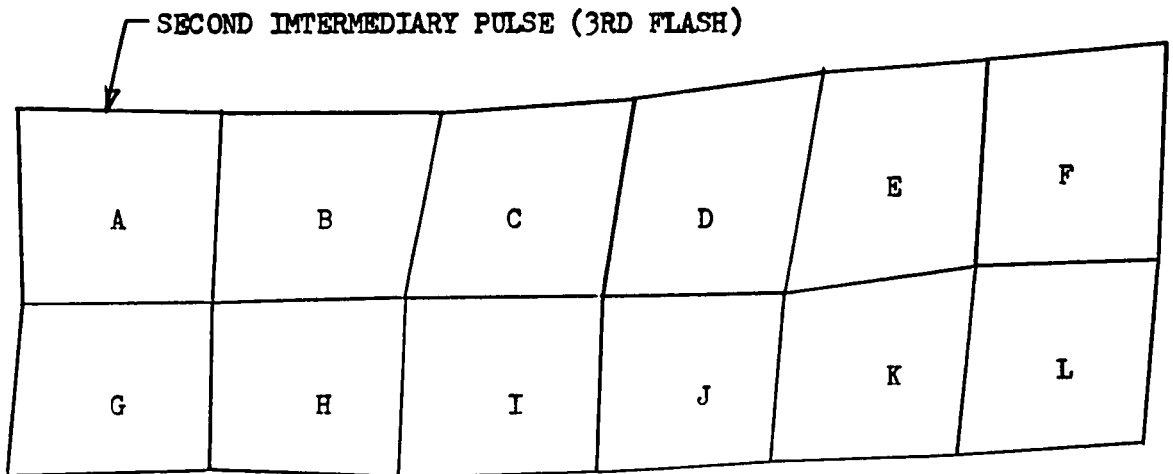
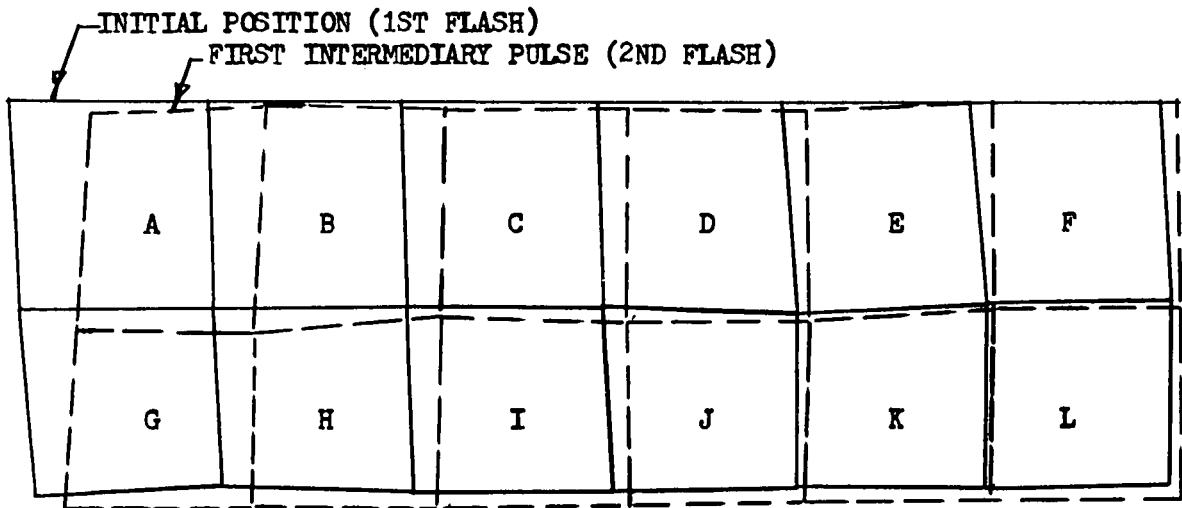
TEST NUMBER	$\eta = \frac{M\omega}{W\dot{x}}$	$\frac{y_0}{D}$
34	.626	.0715
35	1.01	.0815
39	.163	.0630
40	.254	.0695
41	.383	.0886
42	.244	.062
43	.338	.0820
44	.527	.0975
45	.320	.0665
46	.130	.061
47	.540	.104
48	.310	.071
49	.406	.084
50	.564	.110
51	.225	.0646
52	.327	.0745
53	.524	.101
54	.195	.0775
55	.338	.0845
56	.555	.113
57	.336	.0812
58	.584	.106



APPENDIX V-C-1: THE 'X' COMPONENTS OF THE VELOCITY & ACCELERATION HISTORIES OF TEST 29, FOR THE FIRST THREE ROWS.



APPENDIX V-C-1: THE 'Y' COMPONENTS OF THE VELOCITY & ACCELERATION HISTORIES OF TEST 29, FOR THE FIRST THREE ROWS.



The Tracer-Object Matrices for Subsequent Density Determinations

- Test No. 29.

APPENDIX V-C-3

THE EVALUATION OF EQUATION (V-14) FOR TEST 29

		I	II	III	IV	V	VI	VII	VIII	IX	X
	FACTOR	$\frac{\partial \bar{y}}{\partial x}$	$\left \frac{\Delta \bar{y}}{\Delta x} \right $	$\bar{\rho}$	$\bar{x}' \bar{\rho} dV \times 10^{-3}$	$(\bar{x})' \Delta x \times 10^{-3}$	\bar{y}'	$\left \frac{\Delta \bar{x}}{\Delta y} \right $	$\bar{\rho}$	$\bar{y}' \bar{\rho} dV \times 10^{-3}$	$(\text{VII}) \cdot \text{IX} \cdot \Delta y \times 10^{-3}$
Row I	1	.4	0	.0538	.341	0	0	0	.0538	0	0
	2	.7	.01	.0544	.6	.00150	.1	.01	.0544	.085	.00021
	3	1.1	.01	.0544	.94	.00234	.1	.05	.0544	.085	.00106
	4	2	.01	.0545	1.71	.00420	-.1	.05	.0544	.085	.00106
	5	2.5	.03	.0545	2.13	.0159	-.4	.02	.0544	.341	.0017
	6	2.1	.01	.0545	1.8	.00450	-.7	.06	.0544	.6	.0090
	7	1.4	.04	.0545	1.19	.0118	-1.	.08	.0544	.85	.0170
	8	.6	.05	.0545	.54	.0067	-1.6	.1	.0545	1.44	.036
	9	-.1	.07	.0545	.09	.0015	-2.1	.1	.0545	1.88	.047
	10	-1.2	.08	.0580	1.07	.0216	-2.7	.08	.0580	2.42	.048
	11	-2.5	.1	.0580	2.24	.056	-3.0	1.	.0580	2.7	.0675
	12	-3.6	.2	.0570	3.24	.162	-2.0	.01	.0570	1.81	.0045
	13	-4.9	.06	.0570	4.66	.07	-.5	.1	.0570	.47	.0117
	14	-6.	.06	.0604	5.7	.086	1.9	.15	.0604	1.8	.0675
	15	-4.6	.1	.0604	4.18	.104	5	.12	.0604	4.5	.135
	16	-2	.2	.0578	1.82	.091	9	.1	.0578	8.1	.203
	17	.8	.1	.0604	.7	.0174	4	.1	.0604	3.5	.087
	18	5.2	.01	.0604	4.55	.0113	.5	.1	.0604	.44	.011
	19	4.5	.01	.0604	4.2	.0105	-.5	.1	.0604	.47	.013
Row II	7	.7	.02	.0545	.60	.003	-.9	.08	.0545	.78	.0156
	8	.4	.03	"	.341	.0026	-1.5	.08	"	1.28	.0254
	9	0	.05	.057	-	0	-2	.08	.057	1.71	.0242
	10	-.6	.07	"	.540	.0094	-2.2	.08	"	1.96	.0392
	11	-1.	.12	"	.896	.0269	-1.8	.09	"	1.61	.0362
	12	-2.	.15	"	1.792	.067	-1	.01	"	.9	.0022
	13	-3	.08	.0604	2.84	.057	.5	.03	.0604	.475	.0035
	14	-3.5	.1	"	3.32	.083	3	.08	"	2.84	.057
	15	-3.5	.1	.0578	3.18	.0795	4.1	.15	.0578	3.73	.140
	16	-3.5	.15	"	3.18	.104	3	.15	"	2.72	.102
	17	-.2	.02	.0556	1.75	.0088	1	.2	.0556	.875	.044
	18	1.5	0	"	-	0	.4	.15	"	.35	.013
19	2.5	0	.0604	-	0	-.1	.1	.0604	.095	.00023	

APPENDIX V-C-3 (Cont'd.)

		I	II	III	IV	V	VI	VII	VIII	IX	X
	δ	\bar{x}'	$ \frac{\Delta y}{\Delta x} $	\bar{y}	$\bar{x}' \bar{y} dV$ $\times 10^{-3}$	(II)(IV) Δ $\times 10^{-3}$	\bar{y}'	$ \frac{\Delta x}{\Delta y} $	\bar{y}	$\bar{y}' \bar{y} dV$ $\times 10^{-3}$	(III)(V) Δ $\times 10^{-3}$
Row III	7	.55	.02	.0554	.48	.0024	-1	.02	.0554	.872	.00436
	8	.35	.02	.057	.312	.0015	-1.4	.03	.057	1.25	.0094
	9	0	.03	"	-	0	-1.6	.03	"	1.43	.0106
	10	-.5	.05	.058	.45	.0056	-1.5	.03	.058	1.36	.0102
	11	-.8	.05	"	.715	.0089	-1	.02	"	.91	.0045
	12	-1.2	.03	.057	1.07	.0080	0	.01	.057	-	0
	13	-2	.05	.0595	1.85	.023	1.5	.01	.0595	1.4	.0035
	14	-2.5	.15	"	2.33	.076	3	.01	"	2.8	.0070
	15	-2.3	.05	.059	2.13	.027	2.5	0	.059	-	0
	16	-2	.04	"	1.85	.0185	1	.15	"	.925	.0348
	17	-.5	.02	.058	.456	.0023	.4	.1	.058	.365	.00915
	18	.8	0	"	-	0	.2	.08	"	.182	.00364
	19	1.6	0	.057	-	0	0	.06	.057	-	0
Row IV	7	.55	.02	.0554	.47	.0024	-1.1	.08	.0554	.96	0.0193
	8	.3	.04	.057	.268	.0027	-1.1	.08	.057	1.00	.020
	9	0	.02	"	-	0	-1.1	.08	"	1.00	.020
	10	-.6	.03	.058	.546	.0041	-1.0	.07	.058	.91	.016
	11	-.9	.02	"	.82	.0041	-0.3	.06	"	.273	.0041
	12	-1.3	.02	.057	1.16	.0058	.2	.05	.057	.178	.0022
	13	-1.8	.03	.0595	1.68	.0126	1.1	.03	.0595	1.02	.0076
	14	-2.3	.03	"	2.14	.016	2	.02	"	1.80	.0090
	15	-2.1	.05	.059	1.94	.0242	1.8	.05	.059	1.66	.0083
	16	-1.5	.02	"	1.39	.007	1.2	.02	"	1.12	.0056
	17	-.1	.02	.058	.091	.0004	.6	.02	.058	.545	.0027
	18	1.2	.01	"	1.1	.0027	.2	.02	"	.183	.0009
	19	1.2	0	.057	-	0	0	.02	.057	-	0

BIBLIOGRAPHY

* denotes bibliography addendum on page 203

- Arthur, J.R.F., James, R.G., & Roscoe, K.H., (1964) "The Determination of Stress Fields During Plane Strain of a Sand Mass", Géotechnique Vol. XIV, pp. 283-308.
- Barden, L., & Khayatt, A., (1966) "Incremental Strain Rate Ratios and Strength of Sand in the Triaxial Test", Géotechnique Vol. XVI; 4; pp. 338-357.
- Bekker, M.G., (1956) "Theory of Land Locomotion", University of Michigan Press, Ann Arbor.
- Bekker, M.G., (1960) "Off-the-Road Locomotion; Research and Development in Terramechanics", University of Michigan Press, Ann Arbor.
- Bekker, M.G., (1959) "Mobility of Cross Country Vehicles", Machine Design Vol. 31; No. 26; pp. 92-96 and Vol. 32, No. 1; (1960) pp. 145.
- Berlyn, R., (1961) D.I.C. Dissertation
Imperial College, London.
- Bernstein, R., (1913) "Probleme zur Experimentellen Motorplug-Mechanik", Vol. 16.
- Birkhoff, G., (1955) "Hydrodynamics, a Study in Logic, Fact and Similitude", Princeton University Press, N.Y.
- Blagovashchensky, S., (1954) "Theory of Ship Motions", Translated from 1st Russian Edition. 2 Vols. Dover, N.Y. (1962).
- Bloedow, F.H., (1962) "Radiographic Instrumentation Study", Report No AFSWC-TDR-62-44, U.S. Air Force Special Weapons Centre, Kirtland Air Force Base, New Mexico.
- Boyd, C.W., & Windisch, S.J., (1966) "A Technique for Measuring Deformations Within a Sand Under Controlled Wheel Loads", Proc. 2nd Int. Conf. I.S.T.V.S., Quebec.
- Boyd, C.W., Japp, R.D., Leitch, H.C. (1966) "A Discussion of Yield Criteria", Unpublished Report, McGill University.
- Buchard, G.H., (1962) "Measurement of Bremsstrahlung Dose and Spectrum from a 600 K.V.P. Pulsed X-ray Generator Using Photographic Film", Sandia Corporation Report.
- * Cornforth, D.H., (1964) "Some Experiments on the Influence of Strain Conditions on the Strength of Sand", Géotechnique Vol. XIV; p. 143.

- Davis, H.E., & Woodward, R.J. (1949) "Some Laboratory Studies of Factors Pertaining to the Bearing Capacity of Soils", Proc. Highway Res. Bd. Vol. 29, pp.467-476.
- Dickson, W.J., (1962) "Ground Vehicle Mobility on Soft Soils", Proc. A.S.C.E. Vol. 88, SM4; pp. 69-83.
- Drucker, D.C., (1954) "Coulomb Friction, Plasticity & Limit Loads", ASME Vol. 21, Journal of App. Mech. p. 71.
- Drucker, D.C., Gibson, R.E., & Henkel, D.J. (1957) "Soil Mechanics and Work Hardening Theories of Plasticity", Trans. A.S.C.E., Vol. 122, p. 338.
- Drucker, D.C., (1961) "On Stress-strain Relations for Soil and Load Carrying Capacity", Proc. 1st Int. Conf. I.S.T.V.S., Turin, pp. 15-23.
- Dyke, W.P., Grundhauser, F.J., Collins, F.M., & Stunkard, N.W., (1962) "Recent Developments in Flash Radiography at Hyper-Velocities", (Editor A.M. Krill) Plenum Press.
- Dyke, W.P., (1964) "Advances in Field Emission", Scientific American, January.
- *₂
- Evans, R.D., (1955) "The Atomic Nucleus", McGraw Hill, New York.
- Fisher, Sir R.A., (1950) "Statistical Methods for Research Workers", Oliver & Boyd, Edinburgh.
- Freitag, D.R., & Knight, S.T., (1962) "Stresses in Yielding Soils Under Moving Wheels and Tracks", Highway Research Board Bull. 342, p. 24.
- Freitag, D.R., & Smith, M.E., (1966) "Centre Line Deflection of Pneumatic Tires Moving in Dry Sand", J. Terramechanics Vol. 3, No. 1, pp. 31-46.
- Freitag, D.R., (1966) "A Dimensional Analysis of the Performance of Pneumatic Tires on Clay", J. Terramechanics Vol. 3, No. 3, pp. 51-68.
- Gerber, E., (1929) "Untersuchungen uber die Druckverteilung im Oertlich Belasteten Sand", Dissertation, Technische Hochschule, Zurich.
- Habib, P., (1953) "Influence de la Variation contrainte Principale Moyenne Sur La Resistance au Cisaillement Des Sols", 3rd Int. Conf. of Soil Mech. & Foundation Eng. Vol. 1, p. 131
- Haythornthwaite, R.M., (1960) Discussion on: "Failure Hypotheses for Soils" by N.M. Newmark. Proceedings A.S.C.E. Research Conference on Shear Strength of Cohesive Soils, Boulder, Colorado, p. 992.

- Hegedus, E., (1965) "Plate Sinkage Study by Means of Dimensional Analysis",
J. Terramechanics, Vol. 2, No. 2, pp. 25-32.
- Hill, R., (1950) "The Mathematical Theory of Plasticity",
Oxford University Press.
- Horne, M.R., (1966) "The Behaviour of an Assembly of Rotund, Rigid,
Cohesionless Particles", Parts I and II,
Proc. Roy. Soc. A, Vol. 286; pp. 62-97.
- Inglis, Sir Charles (1951) "Applied Mechanics for Engineers",
Cambridge University Press.
- Japp, R.D., (1967) "An Investigation of the Dynamic Behaviour of Inelastic
Materials", Ph.D. Thesis, McGill University.
- Jeffreys, Sir H., & Swirles, B., (1962) "Methods of Mathematical Physics",
Cambridge University Press.
- Kirkpatrick, W.M., (1957) "The Conditions for Failure of Sands",
4th Int. Conf. on Foundation Eng. Vol. 1.
- Lambe, T.W., (1951) "Soil Testing for Engineers",
John Wiley, N.Y.
- Langhaar, H.L., (1951) "Dimensional Analysis and Theory of Models",
John Wiley & Sons, N.Y.
- Leflaive, E.M., (1966)a "Mechanics of Wheels on Soft Soils - a Method
for Presenting Test Results",
J. Terramechanics No. 1. Vol. 3; pp. 13-22.
- Leflaive, E.M., (1966)b "Description of Wheel Performance on Dry Sand
in Terms of Energy Parameters",
paper presented at 2nd Int. Conf. I.S.T.V.S., Quebec.
- Long, R.R., (1963) "Engineering Science Mechanics",
Prentice Hall, New Jersey.
- Morganstern, N.R., (1963) "Maximum Entropy of Granular Materials",
Nature Vol. 200; pp. 559-560.
- McKibben, E.G., (1938) "Some Kinematic and Dynamic Studies of Rigid
Transport Wheels for Agricultural Equipment",
Iowa State College of Agriculture,
Research Bulletin 231, Ames, Iowa.
- McMaster, R.C., (1959) "Non Destructive Testing Handbook",
Volume I, Ronald Press, New York.
- Nadai, A., (1950) "Theory of Flow & Fracture of Solids",
Vol. I, McGraw Hill, New York.

- Nicholson, D.A., & Booker, G.E., (1963) "Variations in the Performance of a Tracked Model Vehicle On Loose Sand due to Changes in the Longitudinal Position of its Centre of Gravity", CARDE Tech. Memo 715/63, Valcartier, Quebec.
- Poletayev, A.F., (1964) "The Compaction of Soil Under a Rolling Wheel", J. Terramechanics Vol. 1, No. 3; pp. 7-17.
- Prager, W., (1961) "Introduction to Mechanics of Continua", Ginn & Co., Boston.
- Rayleigh, J.W.S., 3rd Baron (1945) "The Theory of Sound", 2 Vols. 2nd Ed. Rev. & Enlarged, Dover publications.
- Reece, A.R., (1965) "Principles of Soil-Vehicle Mechanics" Proc. Inst. Mech. Eng., London, Vol. 180, part 2A.
- Reynolds, O., (1876) "On Rolling Friction", Phil. Trans. of Roy. Soc. London. 166; 155-174.
- Richtmyer, F.K., & Kennard, E.H., (1947) "Introduction to Modern Physics", McGraw Hill, New York, 4th Edition.
- Roscoe, K.H., Arthur, J.R.F., & James, R.G., (1963) "The Determination of Strains in Soils by an X-ray Method", Civ. Eng. and Pub. Wks. Rev. 58; 873-876 and 1009-1012.
- Roscoe, K.H., Schofield, A.N., & Thurairajah, A., (1963) "Yielding of Clays in States Wetter than Critical", Géotechnique Vol. XII: 3: p. 211.
- Rowe, P.W., (1954) "A Stress-Strain Theory for Cohesionless Soil Applications to Earth Pressures at Rest and Moving Walls", Géotechnique Vol. IV: No. 1: p.70.
- (1962) "The Stress-dilatancy Relation for Static Equilibrium of an Assembly of Particles in contact", Proc. Roy. Soc. Ser.A. Vol. 269. p. 501.
- (1963) "Stress Dilatancy, Earth Pressures and Slopes", A.S.C.E. Journal of Soil Mech. & Fnd. Divi. Vol. 89. No. SM3. p. 37.
- Savage, S.B., (1966) "Gravity Flow of Cohesionless Bulk Solid in a Converging Conical Channel", Ind. Jnl. of Mech. Sciences (in press).
- Schuring, D., (1961) "Zur Mechanik des Starren Rades Auf Weichem Boden", VDI Zeitschrift No. 16. Vol. 103. pp. 693-732. Translation No. 63-1, W.E.S. (1963) by J.C. van Tienhoven.
- Schuring, D., (1966) "The Energy Loss of a Wheel", Proc. 2 Int. Conf. I.S.T.V.S., Quebec, pp. 391-424.

- Sedov, L.I., (1959) "Similarity and Dimensional Methods in Mechanics Translation from the 4th Russian Edition", Academic Press, New York.
- Selig, E.T., Hofer, K.E., Weil, N.A., (1961) "Elastic Response of Soil to Tracked Vehicles", Proc. 1st. Int. Conf. I.S.T.V.S. Turin, pp. 97-106.
- Selig, E.T., (1964) "Shock Induced Stress Wave Propagation in Sand", Illinois Inst. of Technology, Ph.D Thesis.
- Shibata, T., & Karube, D., (1965) "Influence of the Variation of the Intermediate Principal Stress on the Mechanical Properties of Normally Consolidated Clays", 6th Int. Conf. Soil Mech. & Fdn. Eng., Montreal, p. 359.
- Sitkei, G., (1966) "The Bull Dozing Resistance of Towed Rigid Wheels in Loose Sand", J. Terramechanics Vol. 3, No. 2. pp. 25-38.
- Snedecor, G.W., (1956) "Statistical Methods", Iowa State University Press, Ames, Fifth Edition.
- Sohne, W., & Sonnen, F.J., (1961) "Messungen von Rollwiderstand und Zugkraft von Luftbeverftten Ackerschleppern Sowie Mechanischen Boden-kenngrossen und Versuch einer Zuordnung", Proc. 1st Int. Conf. I.S.T.V.S., Turin, pp. 506-540.
- *₃
Terzaghi, K. and Peck, R.B., (1948) "Soil Mechanics in Engineering Practice", John Wiley & Sons Inc., New York.
- Thomsen, E.G., Yang, C.T., & Kobayashi, S., (1965) "Mechanics of Plastic Deformations in Metal Processing", MacMillan, New York, p. 486.
- *_{4,6}
Uffelmann, F.L., (1961) "The Performance of Rigid Cylindrical Wheels on Clay Soil", Proc. 1st Int. Conf. I.S.T.V.S., Turin, pp. 111-125.
- Ul'yanov, N.A., & Mikhaylov, B.I., (1965) "The Work of the Driving Elastic Wheel on a Deforming Surface", J. Terramechanics, Vol. 2, No. 2, pp. 11-16.
- Victoreen, J.A., (1948) "The Absorption of Incident Quanta by Atoms as Defined by the Mass Photoelectric Absorption Coefficient and the Mass Scattering Coefficient", J. App. Phys. Vol. 19, p. 855.
- _____ (1949) "The Calculation of X-Ray Mass Absorption Coefficients", J. App. Phys. Vol. 20, p. 1141.
- Vincent, E.T., (1960) "Pressure Distribution On and Flow of Sand Past a Rigid Wheel", University of Michigan, Dept. of Mech. Eng., T.M. 03026-1-T.

- Wills, B.M.D., Barret, F.M., & Shaw, G.J., (1965) "An Investigation into Rolling Resistance Theories for Towed Rigid Wheels", J. Terramechanics Vol. 2, No. 1. pp. 24-53.
- Wills, B.M.D., (1966) "The Load Sinkage Equation in Theory and Practice", Proc. 2nd Int. Conf. I.S.T.V.S., Quebec. pp. 199-246.
- Wilson, N., & Krzywicki (1965) "Deformations in a Peat Soil Under Dynamic Load", J. Terramechanics, Vol. 2, No. 1. pp. 54-62.
- Windisch, S.J., (1967), Ph.D. Thesis in preparation, McGill University.
- Wong, J.Y., & Reece, A.R. (1966) "Soil Failure Beneath Rigid Wheels", Proc. 2nd Int. Conf. I.S.T.V.S., Quebec, pp. 425-445.
- Wroth, C.P., & Bassett, R.H., (1966) "A Stress-Strain Relationship for the Shearing Behaviour of a Sand", Géotechnique, Vol. XVI. pp. 32-56.
- Wu, T.H., Loh, A.K. & Malvern, L.E., (1963) "Study of Failure Envelope of Soils", A.S.C.E. Vol. 89: SM1: p. 145.
- Yong, R.N., Boyd, C.W., & Simonsen, O.F., (1964) "Fundamental Research Considerations in Soil-Vehicle Interaction", McGill University, Soil Mechanics Series, No. 11.
- Yong, R.N., Boyd, C.W., & Windisch, S.J., (1965) "Soil Vehicle Interaction Study", Paper presented to 5th Meeting, Quadripartite Working Group on Ground Mobility, Royal Military College, Kingston, Ont.
- Yong, R.N., & Warkentin, B.P., (1966) "Introduction to Soil Behaviour", MacMillan, N.Y.
- Yong, R.N., & Osler, J.C., (1966) "On the Analysis of Soil Deformation Under a Moving Rigid Wheel", Proc. 2nd Int. Conf. I.S.T.V.S., Quebec, pp. 339-352.
- Yong, R.N., & McKyes (1967) "Yielding of Clay in a Complex Stress Field". Preprint of paper to be published in Proceedings of Pan-American Conference.
- Yong, R.N., & Japp, R.D., (1967) "A Flow Law for Clays in Dynamic Compression", Preprint of paper to be presented at Symposium on Wave propagation & Soil Dynamics, Albuquerque, New Mexico.
- Young, D.F., (1966) "Similitude of Soil-Machine Systems", J. Terramechanics Vol. 3, No. 2, pp. 57-70.
- Ziegler, H., (1963) "Some Extremum Principles in Irreversible Thermodynamics with Application to Continuum Mechanics", Prog. in Solid Mechanics. Vol. IV. North-Holland Pub. Comp., Amsterdam.

BIBLIOGRAPHY ADDENDUM

- *₁ Coleman, B.D. and W. Noll (1961) "Foundations of Linear Viscoelasticity", *Revs. of Modern Phys.*, Vol. 33, pp. 239-249
- *₂ Eringen, A.C., (1962) "Non-linear Theory of Continuous Media", McGraw-Hill, New York.
- *₃ Spain B., (1956) "Tensor Calculus", 2nd Ed., Interscience Publishers Inc., New York.
- *₄ Toupin, R.A., (1956) "The Elastic Dielectric", *J. Rational Mech. and Analysis* Vol. 5, pp. 849-915.
- *₅ Truesdell C. and R.A. Toupin, (1960) "The Classical Field Theories" in "Handbuck der Physik", Vol. III/1 Springer-Valag, Berlin.